SYNTHETIC APPROACHES FOR THE DEVELOPMENT OF ORGANIC MOLECULES AND THEIR APPLICATION IN SOLAR CELLS

Dora Alejandra González Ruiz

UNIVERSITAT ROVIRA i VIRGILI

Synthetic Approaches for the Development of Organic Molecules and their Application in Solar Cells

DORA ALEJANDRA GONZÁLEZ RUIZ

DOCTORAL THESIS
2024

UNIVERSITAT ROVIRA I VIRGILI
SYNTHETIC APPROACHES FOR THE DEVELOPMENT OF ORGANIC MOLECULES AND THEIR APPLICATION IN SOLAR CELLS
Dora Alejandra González Ruiz

UNIVERSITAT ROVIRA I VIRGILI
SYNTHETIC APPROACHES FOR THE DEVELOPMENT OF ORGANIC MOLECULES AND THEIR APPLICATION IN SOLAR CELLS
Dora Alejandra González Ruiz

UNIVERSITAT ROVIRA I VIRGILI
SYNTHETIC APPROACHES FOR THE DEVELOPMENT OF ORGANIC MOLECULES AND THEIR APPLICATION IN SOLAR CELLS
Dora Alejandra González Ruiz

Doctoral Thesis

Synthetic Approaches for the Development of Organic Molecules and their Application in Solar Cells

Dora Alejandra González Ruiz

INSTITUT CATALÀ D'INVESTIGACIÓ QUÍMICA

UNIVERSITAT ROVIRA I VIRGILI

TARRAGONA

2024

UNIVERSITAT ROVIRA I VIRGILI
SYNTHETIC APPROACHES FOR THE DEVELOPMENT OF ORGANIC MOLECULES AND THEIR APPLICATION IN SOLAR CELLS
Dora Alejandra González Ruiz

Prof. Dr. Emilio J. Palomares Gil, group leader at the Institute of Chemical Research of Catalonia (ICIQ) in Tarragona and Research Professor at the Catalan Institution for Advanced Studies (ICREA) in Barcelona.

I STATE that the present study, entitled "Synthetic Approaches for The Development of Organic Molecules and their Application in Solar Cells", presented by Dora Alejandra González Ruiz for the award of the degree of doctor, has been carried out under my supervision at the Institute of Chemical Research of Catalonia (ICIQ) and that he fulfills the requirements to obtain the distinction of international doctor.

Tarragona, 2024

73559843R EMILIO JOSE PALOMARES (R: G43619550)
Digitally signed by 73559843R EMILIO JOSE PALOMARES (R: G43619550)
Date: 2024.03.19 13:41:59 +01'00'

Prof. Dr. Emilio J. Palomares Gil

Doctoral thesis supervisor

UNIVERSITAT ROVIRA I VIRGILI

ICIQ Institut Català d'Investigació Química

UNIVERSITAT ROVIRA I VIRGILI
SYNTHETIC APPROACHES FOR THE DEVELOPMENT OF ORGANIC MOLECULES AND THEIR APPLICATION IN SOLAR CELLS
Dora Alejandra González Ruiz

UNIVERSITAT ROVIRA I VIRGILI
SYNTHETIC APPROACHES FOR THE DEVELOPMENT OF ORGANIC MOLECULES AND THEIR APPLICATION IN SOLAR CELLS
Dora Alejandra González Ruiz

ACKNOWLEDGEMENTS

I was thinking a lot about how to be as brief as possible, but it turned out to be impossible. I couldn't even express it how I want. That said, I hope you know that these thanks are forever, since in some way you have contributed to making this work possible. So, without any sense or order let's begin.

THANKS TO ALL OF YOU!

Todo pasa por algo.

Everything happens for a reason.

A mis padres y mis hermanos

Para mi hermosa hija, Paola

Para Augusto

Para Maria

ABSTRACT

Renewable energy has emerged as the foremost alternative for energy supply, driven by the increasing energy demand and addressing concerns over climate change. Solar energy utilization has experienced gradual growth over the past 11 years, making it as one of the fastest-growing renewable energy technologies. Perovskite solar cells have shown remarkable progress in converting sunlight energy into electricity, with efficiency increasing from 3.8% in 2009 to a recent peak of 26.1%. However, several challenges hinder their commercialization, including the optimization of perovskite materials, deposition methods, device architecture, and the development of cost-effective charge-transporting materials. Hole-transporting materials (HTMs) are critical components of perovskite solar cells, playing a pivotal role in achieving high efficiencies, enhancing device stability, and overall performance. Moreover, they are responsible in reducing production costs, making HTMs essential for advancing perovskite solar cells towards commercial viability. The intricate relationship between these materials and the surrounding layers, particularly the perovskite layer, has been examined.

The overall objective of this thesis is to design and synthesise novel hole-transporting materials to explore the intricate relationship between their molecular structure and its effects on the surrounding layers. Through this, the research aims to gain a fundamental understanding of the requirements for effective hole-transporting materials and contribute to enhancing the overall performance of perovskite solar cells.

First, eleven new organic carbazole-based hole-transporting molecules (HTMs) have been synthesised through rational design and molecular engineering, and subsequently characterised. The new HTMs are obtained from relatively inexpensive starting materials employing a simple preparation method, avoiding the need for expensive and complex purification techniques. Their chemical structures were verified by ^{1}H and ^{13}C NMR spectroscopy and mass spectrometry. We evaluated their optical, thermal and electrochemical properties using various techniques such as TGA, UV-vis, CV and PL.

The HTMs were used in regular or inverted perovskite solar cells (iPSCs). The fabrication methodology of the devices consisted of the deposition of

the different layers comprising the device via spin-coat deposition and evaporation in high vacuum, complemented by thermal treatments. The characterisation of the solar cells was carried out by measuring current-voltage (JV) curves using a solar simulator and advanced optoelectronic techniques. In addition, the interfaces between the substrate/HTM and HTM/perovskite were studied via charge transfer processes, field emission scanning electron microscopy (FESEM), X-ray photoelectron spectroscopy and surface wettability. The new carbazole derivatives showed interesting differences in their behaviour in perovskite-based devices.

In summary, the thesis explores numerous molecules, demonstrating how subtle modifications of their molecular structure –such as replacing electron-donating groups or adjusting the length of the π-conjugated system by incorporating phenyl groups– can significantly influence material properties and improve photovoltaic performance. To obtain high-performance results in perovskite solar cells, it is necessary to tune several desirable characteristics of the hole-transporting materials, such as steric effects, well-aligned energy levels, hydrophobicity, and stability. The thesis outlines rational design strategies using simple synthetic schemes with straightforward procedures. These findings contribute to the advancement of various materials, serving as a basis for the development of even more efficient alternatives and accelerating the commercialisation of innovative solar cell technologies.

Resumen

Las energías renovables se han convertido en la principal alternativa para el suministro de energía, impulsadas por la creciente demanda y las preocupaciones sobre el cambio climático. La utilización de la energía solar ha experimentado un crecimiento gradual en los últimos 11 años, lo que la convierte en una de las tecnologías de energía renovable de más rápido crecimiento. Las células solares de perovskita han sido una de las tecnologías que han mostrado avances notables en la conversión de la energía solar en electricidad, con una eficiencia que ha aumentado del 3,8% en 2009 al reciente 26,1%. Sin embargo, varios desafíos obstaculizan su comercialización, incluida la optimización de los materiales de perovskita, los métodos de deposición, la arquitectura del dispositivo y el desarrollo de materiales de transporte de carga eficientes. Los materiales transportadores de huecos (HTM) son componentes críticos de las células solares de perovskita y desempeñan un papel fundamental para lograr altas eficiencias, mejorar la estabilidad del dispositivo y el rendimiento general. Además, son responsables de reducir los costos de producción, lo que hace que los HTM sean esenciales para hacer avanzar las células solares de perovskita hacia la viabilidad comercial.

El objetivo general de esta tesis es diseñar y sintetizar nuevos materiales transportadores de huecos para explorar la intrincada relación entre su estructura molecular y sus efectos en las capas circundantes. A través de esto, la investigación ha tenido como objetivo mejorar la comprensión fundamental de los requisitos esenciales para obtener materiales eficaces para el transporte de huecos y contribuir a mejorar el rendimiento general de las células solares de perovskita.

En primer lugar, se han sintetizado once nuevas moléculas transportadoras de huecos (HTM) orgánicas basadas en carbazol mediante el diseño racional e ingeniería molecular, y posteriormente se han caracterizado. Los nuevos HTM se han obtenido a partir de materiales de partida relativamente económicos empleando un método de preparación simple, evitando la necesidad de técnicas de purificación costosas y complejas. Sus estructuras químicas se han verificado mediante espectroscopia de RMN de ^{1}H y ^{13}C y espectrometría de masas. Además, se han evaluado sus propiedades ópticas, térmicas y electroquímicas utilizando diversas técnicas como TGA, UV-vis, CV y PL.

Finalmente, los HTM se han utilizado en células solares de perovskita (PSC) de estructura regular o invertida. La metodología de fabricación de los dispositivos consistió en la deposición de las diferentes capas que componen el dispositivo mediante deposición por *spin-coating* y evaporación en alto vacío, complementadas con tratamientos térmicos. La caracterización de las células solares se ha llevado a cabo midiendo curvas corriente-tensión (JV) mediante un simulador solar y técnicas optoelectrónicas avanzadas. Además, las interfaces entre sustrato/HTM y HTM/perovskita se han estudiado mediante procesos de transferencia de carga, microscopía electrónica de barrido (FESEM), espectroscopia fotoelectrónica de rayos X e hidrofobicidad de la superficie. Los nuevos derivados de carbazol mostraron diferencias interesantes en su comportamiento en dispositivos basados en perovskita.

En resumen, la tesis explora numerosas moléculas, demostrando cómo modificaciones sutiles de su estructura molecular –como la sustitución de grupos donadores de electrones o el ajuste de la longitud del sistema conjugado π mediante la incorporación de grupos fenilo– pueden influir significativamente en las propiedades de los materiales y mejorar el rendimiento fotovoltaico. Para obtener resultados de alto rendimiento en células solares de perovskita, es necesario ajustar varias características deseables de los materiales transportadores de huecos, como efectos estéricos, niveles de energía bien alineados, hidrofobicidad y estabilidad. La tesis describe estrategias de diseño racional utilizando esquemas sintéticos simples con procedimientos sencillos. Estos hallazgos contribuyen al avance de diversos materiales, sirviendo como base para el desarrollo de alternativas aún más eficientes y acelerando la comercialización de tecnologías innovadoras de células solares.

RESUM

Les energies renovables s'han convertit en la principal alternativa per al subministrament d'energia, impulsades per la creixent demanda i les preocupacions sobre el canvi climàtic. La utilització de l'energia solar ha experimentat un creixement gradual en els últims 11 anys, la qual cosa la converteix en una de les tecnologies d'energia renovable de més ràpid creixement. Les cèl·lules solars de perovskita han estat una de les tecnologies que han mostrat avanços notables en la conversió de l'energia solar en electricitat, amb una eficiència que ha augmentat del 3,8% en 2009 al recent 26,1%. No obstant això, diversos desafiaments obstaculitzen la seva comercialització, inclosa l'optimització dels materials de perovskita, els mètodes de deposició, l'arquitectura del dispositiu i el desenvolupament de materials de transport de càrrega eficients. Els materials transportadors de buits (HTM) són components crítics de les cèl·lules solars de perovskita i exerceixen un paper fonamental per a aconseguir altes eficiències, millorar l'estabilitat del dispositiu i el rendiment general. A més, són responsables de reduir els costos de producció, la qual cosa fa que els HTM siguin essencials per a fer avançar les cèl·lules solars de perovskita cap a la viabilitat comercial.

L'objectiu general d'aquesta tesi és dissenyar i sintetitzar nous materials transportadors de buits per a explorar la intricada relació entre la seva estructura molecular i els seus efectes en les capes circumdants. A través d'això, la recerca ha tingut com a objectiu millorar la comprensió fonamental dels requisits essencials per a obtenir materials eficaços per al transport de buits i contribuir a millorar el rendiment general de les cèl·lules solars de perovskita.

En primer lloc, s'han sintetitzat onze noves molècules transportadores de buits (HTM) orgàniques basades en carbazole mitjançant el disseny racional i enginyeria molecular, i posteriorment s'han caracteritzat. Els nous HTM s'han obtingut a partir de materials de partida relativament econòmics emprant un mètode de preparació simple, evitant la necessitat de tècniques de purificació costoses i complexes. Les seves estructures químiques s'han verificat mitjançant espectroscòpia de RMN de ^{1}H i ^{13}C i espectrometria de masses. A més, s'han avaluat les seves propietats òptiques, tèrmiques i electroquímiques utilitzant diverses tècniques com TGA, UV-vis, CV i PL.

Finalment, els HTM s'han utilitzat en cèl·lules solars de perovskita (PSC) d'estructura regular o invertida. La metodologia de fabricació dels dispositius va consistir en la deposició de les diferents capes que componen el dispositiu mitjançant deposició per *spin-coating* i evaporació a buit, complementades amb tractaments tèrmics. La caracterització de les cèl·lules solars s'ha dut a terme mesurant corbes corrent-tensió (JV) mitjançant un simulador solar i tècniques optoelectròniques avançades. A més, les interfícies entre substrat/HTM i HTM/perovskita s'han estudiat mitjançant processos de transferència de càrrega, microscòpia electrònica d'escombratge (FESEM), espectroscòpia fotoelectrònica de raigs X i hidrofòbia de la superfície. Els nous derivats de carbazole van mostrar diferències interessants en el seu comportament en dispositius basats en perovskita.

En resum, la tesi explora nombroses molècules, demostrant com modificacions subtils de la seva estructura molecular –com la substitució de grups donadors d'electrons o l'ajust de la longitud del sistema π conjugat mitjançant la incorporació de grups fenil– poden influir significativament en les propietats dels materials i millorar el rendiment fotovoltaic. Per a obtenir resultats d'alt rendiment en cèl·lules solars de perovskita, és necessari ajustar diverses característiques desitjables dels materials transportadors de buits, com a efectes estèrics, nivells d'energia ben alineats, hidrofòbia i estabilitat. La tesi descriu estratègies de disseny racional utilitzant esquemes sintètics simples amb procediments senzills. Aquests resultats contribueixen a l'avanç de diversos materials, servint com a base per al desenvolupament d'alternatives encara més eficients i accelerant la comercialització de tecnologies innovadores de cèl·lules solars.

CONTRIBUTIONS TO SCIENTIFIC LITERATURE

The following publications are based on the work described in this thesis:

- **Dora A González**, Carlos E Puerto Galvis, Wenhui Li, Maria Méndez, Ece Aktas, Eugenia Martínez-Ferrero, Emilio Palomares; "Influence of the carbazole moiety in self-assembling molecules as selective contacts in perovskite solar cells: interfacial charge transfer kinetics and solar-to-energy efficiency effects", Nanoscale Adv., 2023, 5, 6542-6547.

  DOI: 10.1039/d3na00811h

- Carlos E Puerto Galvis, **Dora A González**, Eugenia Martínez-Ferrero, Emilio Palomares; "Challenges in the design and synthesis of self-assembling molecules as selective contacts in perovskite solar cells", Chem. Sci., 2024, 15, 1534-1556.

  DOI: 10.1039/d3sc04668k

- **Dora A. González**, Carlos E. Puerto Galvis, Wenhui Li, Maria Méndez, José Sánchez, Eugenia Martínez-Ferrero, Emilio Palomares; "Exploring the Interactions at the Interface: Tailoring Carbazole-Based SAMs with Varying Functional Groups for Enhancing the Performance of Inverted Perovskite Solar Cells", Solar RRL, 2024, submitted Article.

The following publications are not included in this thesis:

- Ece Aktas, Nga Phung, Hans Ko¨bler, **Dora A. González**, Maria Méndez, Ivona Kafedjiska, Silver-Hamill Turren-Cruz, Robert Wenisch, Iver Lauermann, Antonio Abate and Emilio Palomares; Understanding the perovskite/self-assembled selective contact interface for ultra-stable and highly efficient p-i-n perovskite solar cells. Energy Environ Sci 14, 3976–3985 (2021).

  DOI:10.1039/D0EE03807E

- Sarika Kumari, José G. Sánchez, Muhammad Imran, Ece Aktas, **Dora A. González**, Liberato Manna, Eugenia Martinez-Ferrero and Emilio Palomares; "Self-assembled molecules as selective contacts in $CsPbBr_3$ nanocrystal light emitting diodes", J. Mater. Chem. C, 2023,11, 3788-3795.

  DOI: 10.1039/d2tc03536g

- Giuseppina Anna Corrente, **Dora A González**, Ece Aktas, Agostina Lina Capodilupo, Francesco Ruighi, Gianluca Accorsi, Daniela Imbardelli, Cristina Rodriguez-Seco, Eugenia Martinez-Ferrero, Emilio Palomares, Amerigo Beneduci.; "Reversible vis-NIR electrochromic/electrofluorochromic switching in dual-functional devices modulated by different benzothiadiazole-arylamine anodic components", J. Mater. Chem. C, 2023, 11, 17115-17127.

  DOI: 10.1039/d3tc03577h

- Giuseppina Anna Corrente, **Dora A González**, Ece Aktas, Agostina Lina Capodilupo, Gloria Mazzone, Francesco Ruighi, Gianluca Accorsi, Daniela Imbardelli, Cristina Rodriguez Seco, Eugenia Martinez Ferrero, Emilio Palomares, Amerigo Beneduci.; "Vis–NIR Electrochromism and NIR–Green Electroluminochromism in Dual Functional Benzothiadiazole Arylamine Mixed Valence Compounds", Adv Opt Mater, 2023, 11, 2201506.

  DOI: 10.1002/adom.202201506

ORAL AND POSTER PRESENTATIONS AT CONFERENCES

- **International Conference on Spectral Shaping for Biomedical and Energy Applications:** Oral Presentation "Novel Carbazole-based Conjugated Molecules as Self-Assembled Hole Transporting Monolayers for Inverted Perovskite Solar Cells". Canary Islands, Universidad de la Laguna. October 2022.

- **International symposium Vth PhD day ICIQ:** Oral Presentation "Novel Carbazole-based Conjugated Molecules as Self-Assembled HTM for Inverted Perovskite Solar Cells". Tarragona, Spain, ICIQ. October 2022.

- **31st International Materials Research Congress:** Poster Presentation "Analysing the Functional Group Effect of Carbazole-Based Compounds as Self-Assembled Molecules in Inverted Perovskite Solar Cells", Cancún, México. August 2023.

- **International symposium VII ICIQ-URV PhD Day:** Oral Presentation, Analysing the functional group effect of carbazole-based compounds as self-assembled molecules in inverted perovskite solar cells. Tarragona, Spain, ICIQ. October 2023.

LIST OF ACRONYMS

ACN	acetronirile
c-	compact
CB	Chlorobenzene
CsFA	(Cs,FA)PbI3 perovskite
CsMAFA	$Cs_{0.1}(MA_{0.15}FA_{0.85})_{0.9}Pb(I_{0.85}Br_{0.15})_3$ perovskite
DCM	dichloromethane
DFT	Density Functional Theory
DMF	4,4-Dimethyl formamide
DMSO	Dimethyl sulfoxide
Eg	Bandgap
ETL	Electron transport layer
FA	Formamidinium
FAPI	$FAPbI_3$
FF	Fill factor
FTO	Fluorine tin oxide
fwd	Forward scan
HTM	Hole transport material
ITO	Indium tin oxide
J_{SC}	Short circuit current density
JV	Current density – voltage curve
m-	mesoporous
MA	Methylammonium
MPP	Maximum power point
PCE	Power conversion efficiency
PEA	Phenethylammonium
PL	Photoluminescence
PSC	Perovskite solar cell
PV	Photovoltaic
rev	Reverse scan
TOL	Toluene
SEM	Scanning electron microscopy
SJ	Single junction
spiro-OMeTAD	2,2′,7,7′-Tetrakis[N,N-di(4-methoxyphnyl)amin]-9,9′-spirobifluorene
SQ	Shockley-Queisser

TCO	Transparent conductive oxide
TRPL	Time resolved photoluminescence
UV-VIS	Ultraviolet-visible
V_{OC}	Open circuit voltage
w/o	without
XPS	X-ray photoelectron spectroscopy
XRD	X-ray diffraction
CBM	conduction band maximum

CONTENTS

CHAPTER 1

INTRODUCTION

As the world attempts to mitigate environmental pollution, particularly CO_2 emissions and their association with global warming, the increase in global electricity demand becomes an important concern. This rise in electricity consumption is directly related to significant CO_2 emission, where almost 80% of electricity generation comes from fossil fuels (see **Figure 1.1**).[1] Understanding this connection is crucial in addressing the environmental challenges posed by our escalating energy needs while maintaining our standards of living and overall development.

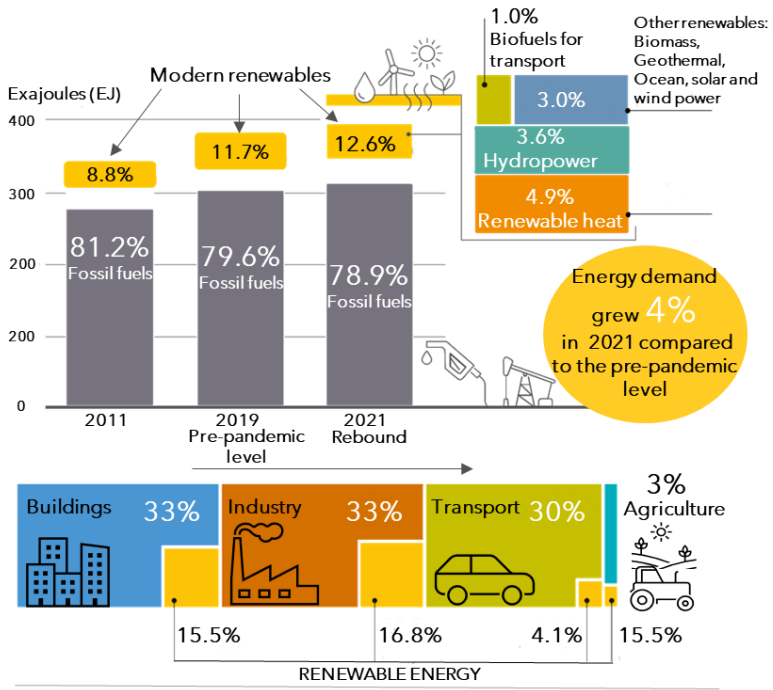

Figure 1.1 Comparison of total final energy consumption (TFEC) by source in 2011, 2019 and 2021. Illustration from *REN21 Renewables 2023 Global Status Report Collection, Global Overview*.

In addition, the growing contribution of renewable energies has led to a decline in the intensity of fossil fuels and emissions, driven by the

rapid deployment of solar photovoltaic (PV) and wind renewables, primarily. Between these, PV stands out as the superior alternative, showcasing the highest contribution among all technologies offered as depicted in Figure 1.2.

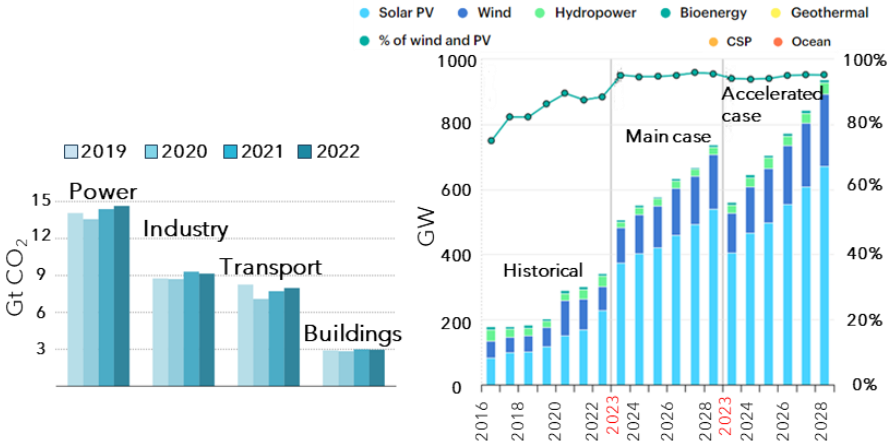

Figure 1.2 Global CO_2 emissions by sector and renewable electricity capacity additions by technology and segment.

Therefore, this thesis aims to develop new hole-transporting materials (HTMs) that significantly improve the efficiency and cost-effectiveness of perovskite solar cells (PSCs) in order to overcome these problems. Since the main objective of this work is not solely the synthesis of new HTMs but also their application in PSCs, the upcoming part is divided in two main sections. Firstly, it offers a brief introduction covering general concepts of photovoltaic devices and the requisite properties for achieving considerably high performance. The subsequent section delves into the state-of-the-art of HTMs, providing a detailed chronological overview focused on their design and their impact on PSCs. This contributes valuable insights toward achieve this goal outlined in this thesis.

1.1 Overview of Photovoltaics

Solar radiation, as a self-sustaining and clean energy source, is an attractive renewable energy source to provide sufficient electrical energy for human activity by way of the photovoltaic effect. Since the commercialization of the first silicon-based solar cell in the 1950s, solar cell technology has been the subject of intense research, recognized as one of the most promising candidates for the next generation of alternative energy sources.[2] Depending on materials and progress through time, PV technologies were divided into several generations.

The initial power efficiency (PCE) of the first generation of silicon p-n junction solar cells (SCs) reached 6%, and it has been developed and commercialized for several years, mainly due to its long-term stability. The second generation consists of inorganic thin-film SCs that utilize alternative semiconductor materials, such as cadmium, telluride or copper indium gallium selenide (CIGS), making them flexible and lightweight, ideal for scale-up applications. Emerging photovoltaic technologies, also well known as next generation SCs, utilize abundant and cost-effective materials, including organic materials, quantum dots and perovskites (hybrid organic-inorganic materials). These materials are solution-processable, reducing the fabrication cost for large-area applications and enabling future cost-effective energy generation. However, reducing the cost and improving the performance and stability of all these systems for making them competitive with primary fossil fuel sources has proven challenging.[3,4]

Among all these emerging PV technologies, the increase in the efficiency of perovskite solar cells (PSCs) is remarkable, taking just over 12 years to progress from 3.8% to the current 26.1%, making them the hottest topic in PV (see **Figure 1.3**).[5,6] In addition to their high efficiency, PSCs are easy to fabricate as single-junction thin-film SCs and can be easily integrated with other PV technologies to create hybrid cells, making them cost-effective. [4,7–9]

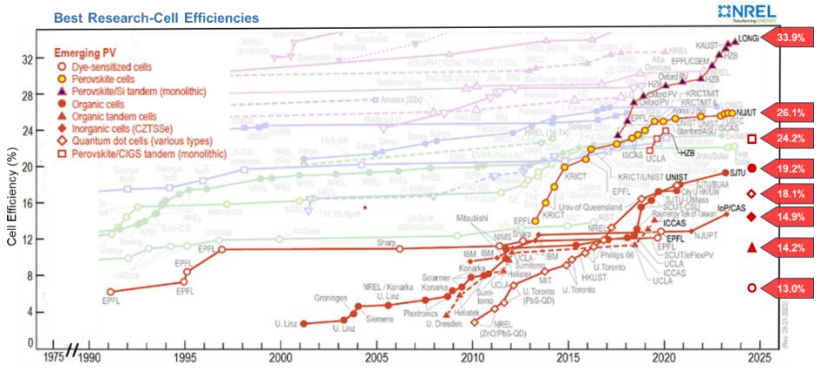

Figure 1.3 Certified best power conversion efficiencies over time for various PV technology.

1.1.1 Perovskite Solar Cells

Perovskite materials are attractive due to their rare properties and interdisciplinary nature, involving the fields of chemistry, physics, and optoelectronics. This has resulted in tremendous progress in many applications (light-emitting diodes, photodetectors, batteries, and so on) beyond PSCs.[10] In brief, perovskite material refers to a group of compounds with a general ABX_3 structure, derived from the crystal structure found in calcium titanate ($CaTiO_3$), named "perovskite".

As shown in **Figure 1.4**, the ideal perovskite crystal presents a cubic face, where A stands for an organic cation such as methylammonium ($CH_3NH_3^+$), formamidinium (FA^+), or metal cation Cs^+, Rb^+ and K^+. B is an inorganic cation, typically lead (Pb^{2+}) or tin (Sn^{2+}) and X is a halogen anion, usually chloride (Cl^-), iodine (I^-) or bromide (Br^-). Indeed, the band gap can be easily tuned by varying or mixing these halide ions, owing to the simultaneously ionic and semiconducting nature of perovskite material [4,11]

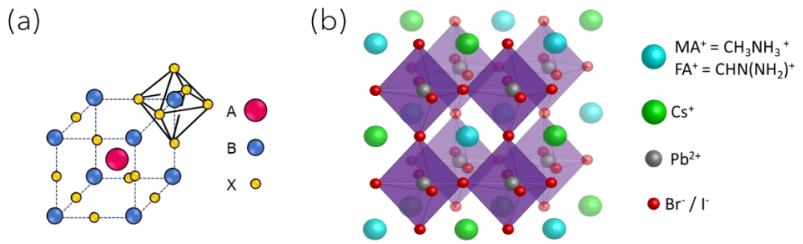

Figure 1.4 a) Ideal crystal ABX_3 structure of perovskite; b) projected view of cubic triple cation perovskite.

Since the first use of perovskite as absorbing material in 2009, more complex compositions involving multi-cations and mixed-anions

have been employed in the perovskite absorber layer in order to improve the performance and stability of PSCs. The use of a triple cation (Cs/MA/FA) mixture stands out among other strategies and has made an important contribution in terms of reproducibility and stability, becoming as standard for the development of PSCs (see Figure 1.4b).[12,13]

1.1.1.1 Perovskite Device Architectures and Working Mechanisms

Different PSC device architectures have been developed, with the general device architecture, typically called regular or standard, composed of five main layers: transparent electrode, n-type electron-transporting layer (ETL), perovskite light absorbing, p-type hole-transporting layer (HTL) and metallic electrode, allowing several combinations. According to the position of the charge transport layers in relation to the substrate, the planar configuration can be divided into two well-known architectures: regular (n-i-p) and inverted (p-i-n), where the incident light passes through the electron-transporting layer (ETL) or hole-transporting layer (HTL), respectively. Figure 1.5 illustrate the configurations and the working mechanism of PSCs (regular and inverted).

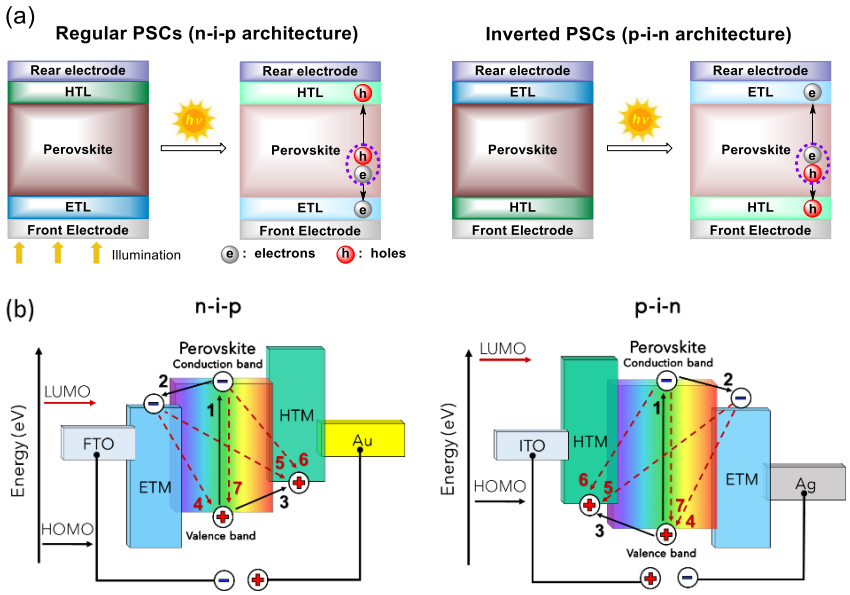

Figure 1.5 a) Illustration of common device architecture for PSC[14] and b) schematic representation of energy levels and their working mechanism in different PSC architectures. The first step is the generation of charge (electron and hole), while their transport to their respective charge-selective contact is represented by steps 2 and 3. The different recombination processes that can take place in the operational device are depicted as dash-lines (4-7).

For both structures, a simplified PSC mechanism consists of a light absorption by the perovskite generating photoexcited charges (electron and hole), which are then transferred from the perovskite to their respective selective contacts and connected to electrodes to complete the electrical circuit.[13–15]

Despite all the effort, there remains a gap in understanding the undesirable mechanisms occurring during charge transfer processes and their relationships among the different PSC architectures. Figure 5b depicts the main undesirable processes, including charge recombination processes at the three interfaces ETM/perovskite/HTL (4-6), non-radiative recombination (7) and the energy level alignment of the charge selective contacts with the perovskite, which also determines the charge transfer/transport and carrier recombination.[16,17]

To date, both the regular and the inverted architectures have achieved a remarkable performance above of 25%. This seems that high performance is not limited to any specific device configuration.[6,8] However, inverted perovskite solar cells (iPSCs) have attracted significant attention for their superior stability, negligible hysteresis, potential for integration with other PV devices, and simpler fabrication methods compared to regular PSCs, and so on. These outstanding advantages have triggered a research fever aimed at improving iPSCs' performance.[18–20]

1.1.1.2 Essential Components of n-i-p and p-i-n PSC

Electrodes

Front electrodes, commonly known as substrates, are typically based on a transparent conductive oxide deposited on glass. So far, fluorine-doped tin oxide (FTO) and indium tin oxide (ITO) have been the most used in PSC. These materials not only influence the final performance but also impact the film quality, including the fill factor (FF) and the photocurrent density, in charge transporting/collecting and in long-term stability, principally.[21]

Back electrodes play a crucial role in the transportation of charge carriers and the device protection of the PSCs, influencing their overall performance. In the case of regular structure, where the back electrode serves as an anode, its work function should match the HOMO level or valence band of the HTM. In contrast, serving as a cathode, the work function of the back electrode should match the LUMO level or conduction band of ETM. The most used back electrodes for PSCs are Au and Ag for regular and inverted architectures, respectively. Despite the high cost of both materials, they continue to be the best options because they are thermally stable, have good electrical conductivities, exhibit a well-matched work function with several materials and yield high-performance

PSCs, among others. Therefore, for cost competitiveness, a major requirement is that their efficiency should significantly surpass that of current commercial technology.[22,23]

Charge transporting materials (CTMs)

The main role of HTMs (p-type) and ETMs (n-type) is the effective separation and transport of charge carriers (hole and electron) in PSCs to their respective electrodes. Despite the ambipolar nature of perovskite material, charge collection can occur in the absence of CTMs, i.e., HTM-free or ETM-free. Nevertheless, CTM enhance charge transport while also acting as a blocking barrier for electrons or holes, prevent recombination and contribute to improve the device's stability. In this context, their use is critical to ensuring good performance in PSCs.[24,25]

Electron transporting materials (ETMs)

There are various types of ETMs including metal oxides such as TiO_2, SnO_2, ZnO or Al-doped ZnO (AZO), typically used for n-i-p devices, and fullerene derivatives for p-i-n devices. PSCs using these materials have achieved high performance and extensive research has been done to improve perovskite based-ETL. However, challenges persist in advancing the development of ETM, like straightforward synthetic routes, the optimization of the electron-extraction from the perovskite layer, and enhancement in the morphology and coverage of the ETL film.[26,27]

Hole transporting materials (HTMs)

HTMs are essential components to fabricate stable and efficient PSCs, as well as the aforementioned materials. To date, a wide variety of HTMs are available, making the selection of an appropriate one a challenging task. However, the PCE has been a focal point of research in PSCs, guiding the selection of HTMs with the primary aim of developing highly efficient PSCs. On the other hand, a significant research interest has been dedicated to design new HTM candidates, aiming to gain a better understanding of the relationship between HTM structure and PSC performance, including interfaces such as HTM/perovskite and HTM/substrate for both structures n-i-p and p-i-n.[20,28-31]

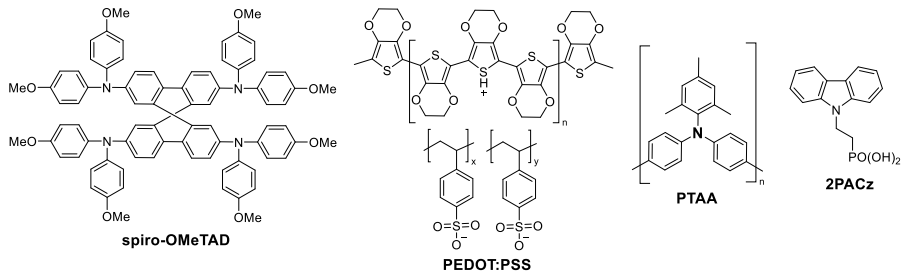

Figure 1.6 Molecular structures of the most popular HTMs. The full names are indicated in the text.

The most popular HTMs used in PSCs include 2,2′7,7′-tetrakis-(*N,N*'-di-*p*-methoxyphenyl amine)-9,9'-spirobifluorene (spiro-OMeTAD), poly(3,4-ethylenedioxythiophene)-poly(styrenesulfonate) (PEDOT:PSS), polytriarylamine (PTAA), nickel oxide (NiO_x) and recently [2-(9H-carbazol-9-yl)ethyl]phosphonic acid (2PACz) derivatives, among others (Figure 1.6). While these HTMs are widely used as a reference for reliable and reproducible results in PSCs, it is important to note that none of them excel in all the characteristics requested for an optimal HTM. The reason for these disadvantages lies in their hygroscopic nature, lack of profitability, typically requiring doping or additives, susceptibility to chemical degradation, and poor stability, presenting one or more of these challenges.[15,28,30,32]

1.1.2 Electron Donor Groups in HTMs

In simple terms, the design of organic HTMs involves a type of chemical selection that remains incompletely understood. However, it is clear that design engineering includes considerations such as simple synthetic procedures, well-aligned energy levels (specially with those of perovskite), lateral interactions among the groups and their surrounding layers, tuneable properties, sufficient solubility, among other factors.

In the context of designing HTMs, the selection of electron donor groups often involves the substitution with various functional groups, such amino groups ($-NH_2$), amine groups ($-NR_2$), hydroxyl groups (-OH), thiol groups (-SH), simple alkyl groups, etc. Nevertheless, identifying the ideal combination among these groups has proven challenging, mainly due to the introduction of additional moieties or extra π–bridge conjugation. This not only leads to tunning energy levels and affecting optical and electronic properties but also highlights the importance of steric effects. Steric considerations are

crucial as they can influence the molecular geometry, as well as effects interactions among its constituent and with the adjacent layers.

The majority of organic small molecules (SMs) used as HMT utilized electron-donor moieties, such as diphenylamine, carbazole, thiophen or triphenylamine, often in a strategic combination among them. These moieties frequently feature alkyl or methoxy groups as auxiliary electron donor. Figure 1.7 shows different electron-donating groups. These types of molecules exhibited minimal visible absorption, avoiding interference with the absorption of light by perovskite. They also assist in adjusting the energy levels according to the donor strength trend.[14,28,30]

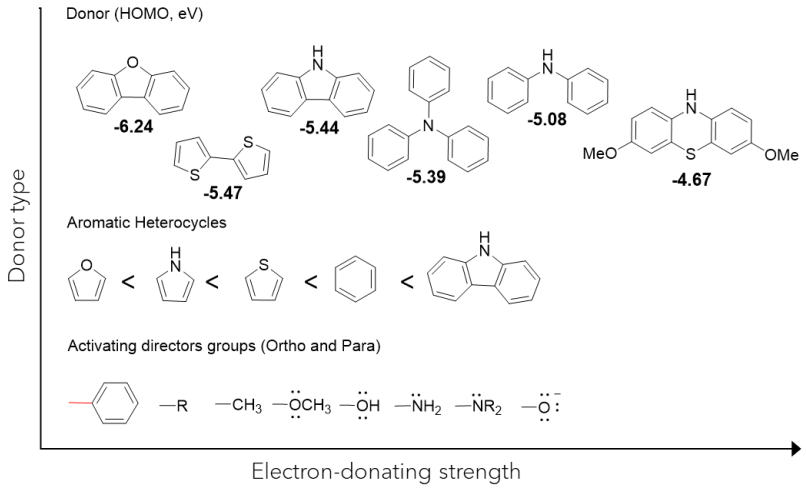

Figure 1.7 Molecular structures of different types of electron-donating units.

1.1.3 Energy Level Alignment

The strategy to achieve an appropriate energy level alignment requires the incorporation of HTMs between the perovskite and electrode, facilitating the efficient extraction and transport charge carriers. Figure 1.8 illustrates the HOMO/LUMO energy levels for the synthetised compound used in this thesis in a p-i-n structure device (detailed information will be provided in the following chapters). This is crucial for PSCs, as the mismatch energy levels can lead to energy barriers, non-radiative recombination or contact resistance, all of them which significantly impact the overall performance of the device. On the other hand, chemical doping is a common method to introduce additional mobile charges, enhancing the conductivity HTMs and aligning the energy levels at the interface. Nevertheless, the use of additives and dopants has a negative impact on the stability

of the entire device, as well as HTM degradation and interfacial recombination processes.[17,21,33]

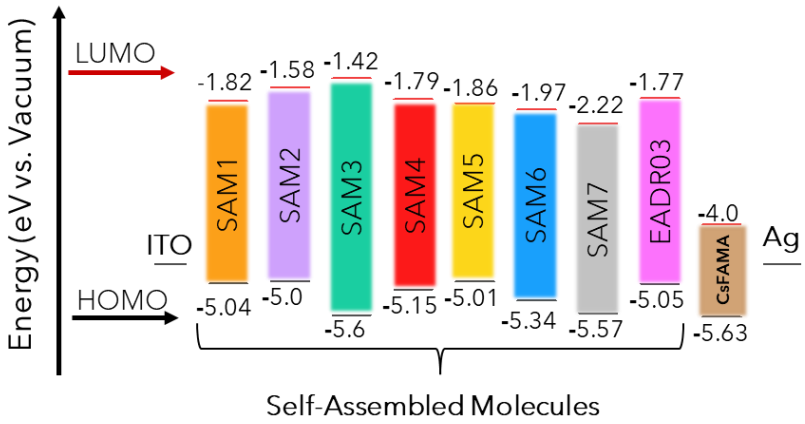

Figure 1.8 Energy level diagram of the different self-assembled molecules (SAMs) used as hole-transporting materials in inverted perovskite solar cells. The related materials are compared with triple cation perovskite (labeled CsFAMA) and EADR03 utilized as a reference.

43

1.2 Overview of Organic Hole Transporting Materials for Perovskite Solar Cells

Since the introduction of the first solid-state devices in 2012,[4] the configuration of PSCs has not changed considerably.[34] The growing interest in PSCs is attributed not only to their PCEs but also lies in their stability for commercial applications.[13,35] As a result, several approaches are used to improve perovskite cells' performance, e.g., changes in the perovskite composition, the addition of interfacial layers, the synthesis of many different charge transporting materials (CTM, i.e., HTM and ETM), among other parameters.[28,36,37] Based on the aforementioned, where the general architecture of the PSC device is composed of five main layers, one of the most interesting strategies is to optimize these layers already integrated into the device architecture, with a focus on the hole transport material (HTM), which plays a crucial role in the extraction and transport of holes from the perovskite material to the electrode, achieving better performance.[28,31,38]

Currently, there are three main categories of HTMs: low molecular weight organic molecules (frequently known as “small molecules”, SMs), conjugated polymers and inorganic salts. Several SMs have been tested as HTMs for the preparation of PSCs to identify the characteristics that pave the way for establishing efficient design and fundamental principles for these compounds in their application in PSCs.[30] Regarding the accelerated advancement of the SMs, organic chemistry plays an essential role in both their design and the synthesis. Thus, in this thesis we aim to tackle current PSCs challenges by designing and synthesizing new materials, specifically focusing on organic SMs as HTMs. In the context of photovoltaics, the term “SMs” typically refers to organic semiconductors with relatively low molecular weight compared to large polymers, ranging from few hundred to a few thousand. Additionally, their synthesis can be easier to control, enabling precise manipulation of their properties due to their well-defined and regular structures.[28]

1.2.1 Background

In PSCs, an ideal HTM candidate must possess some features such as excellent thermal and photochemical stability, well-aligned energy levels (in this work especially with those of perovskite), as well as hydrophobic character. Additionally, it should be soluble in nonpolar and aprotic solvents, among other criteria.[30,31,39]

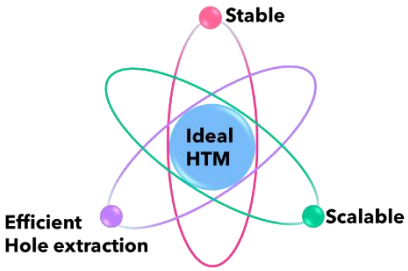

Figure 1.9 The key features of a hole-transporting material (HTM) required in an ideal case for the efficient production of PSCs.

Through chemical modifications, organic chemistry provides an endless number of precisely defined structural alternatives, facilitating the deliberate adjustment of optoelectronic properties, molecular functionality and intermolecular interactions.[28] This versatility enables the achievement of a wide range of properties required for high performance of HTMs in PSCs. On the other hand, to facilitate the cost-effective production of PSCs for future commercialization, an optimal HTM must be easily affordable through a simple synthesis with a reduced number of steps. In addition, it should involve easy workup and purification procedures, promoting relatively inexpensive scaling (Figure 1.9).

In this context, SMs stand out as promising candidate due to their easy synthesis and process, and the ability to tune their desired properties by modifying the chemical structure. To date, impressive approaches have been employed in the development of such SMs, which can be used as HTM in two different ways as depicted in Figure 1.10: 1) SMs randomly distributed as a layer (hereafter referred to as random distribution small molecules, RD-SM) and 2) SMs as an ordered and oriented forming a layer known as a self-assembled molecule (SAM).[19,20,28,31,40]

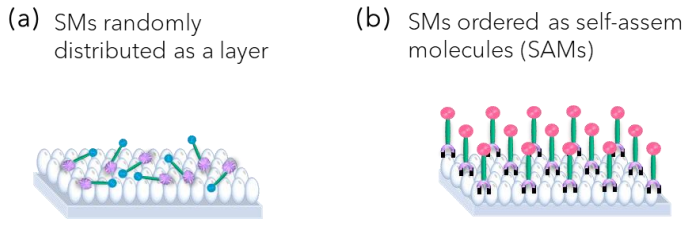

Figure 1.10 Different ways to compose a layer of an organic SMs as HTMs.

Many opportunities still exist for a fundamental understanding of the relationship between chemical structure and photovoltaic performance. It is important to note that there are significant differences in the design and characteristics of the currently employed HTMs between regular (n-i-p) and inverted (p-i-n) architectures. For example, it is well known that spiro-OMeTAD has been the most employed RD-SM as HTM for regular PSCs.[41] In the case of inverted perovskite solar cells (iPSCs), among all SMs, the emerging SAMs have received a special attention due to its ability to bond to the substrate surface (Figure 1.11).[42] Brief, SAMs are mainly composed of an anchoring group that facilitates chemical bonding onto the surface, a linker moiety which not only serves to connect the anchor group and the functional group but also helps to maintain the structural integrity of the SAM by allowing the molecules to organize in an orderly manner on the surface. Finally, the functional group that plays and important role in interactions with the overlayer or surrounding environment.[14,19] A detailed description of SAMs can be found in section 1.2.3.

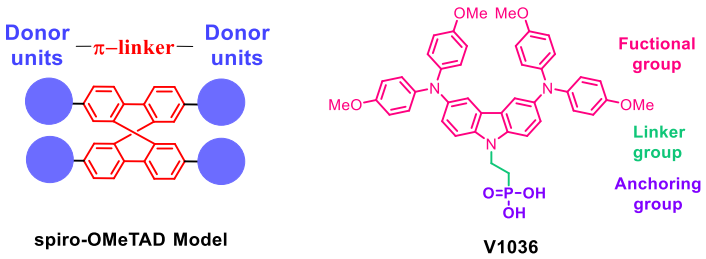

Figure 1.11 General model of simplified spiro-OMeTAD structure and chemical structure of (2-{3,6-bis[bis(4-methoxyphenyl)amino]-*9H*-carbazol-9-yl}ethyl)phosphonic acid (V1036).

The next section, inspired by the aforementioned SMs, aims to explore the impact of various SM structures on photovoltaics performance to pave the way for a more informed approach in designing and configuring new molecules as HTMs. In order to do so, the section is divided into two parts focusing on SMs used as HTM: 1) an overview of RD-SMs in regular PSCs, and 2) a discussion on SAMs in iPSC.

1.2.2 Random distribution Small Molecules (RD-SMs) for Regular PSCs

Spiro type RD-SMs

After the emergence of spiro-OMeTAD, several studies have focused on the spiro-OMeTAD structure as a general model with slight structural modifications in an effort to improve the performance of PSCs and produce low-cost HTM.[31,32] In this typical model, the spiro-OMeTAD structure consists of a central core of spirobifluorene as a π–linker (π), encircled by diphenylamine as terminal electron-donating (D) groups, resulting in a wide range of D–π–D molecular HTMs. Figure 1.12 illustrate some representative examples of this model.

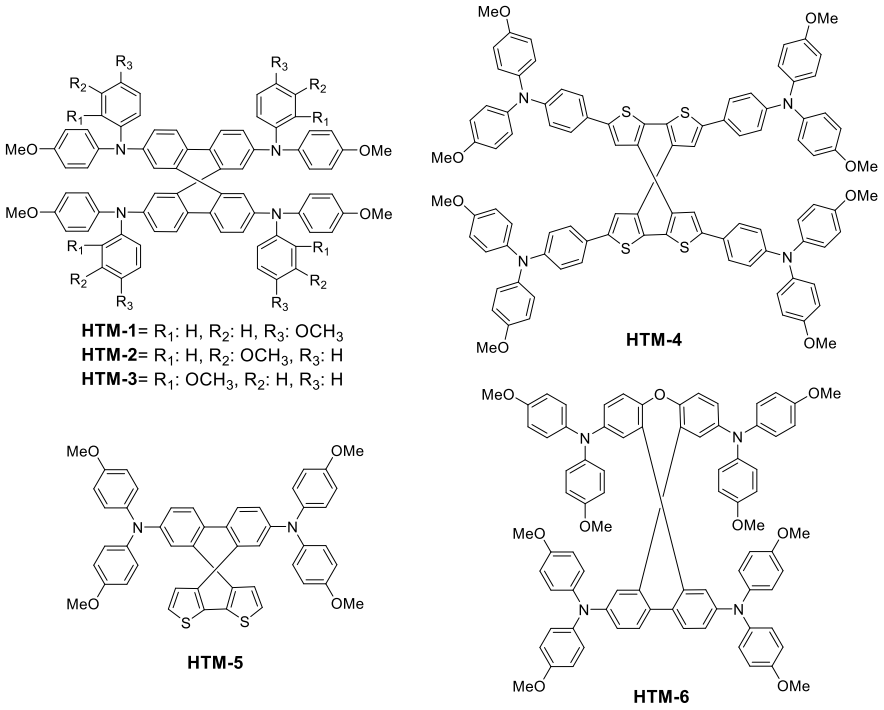

Figure 1.12 Chemical structure of spiro-type and triphenylamine (TPA)-based small molecule HTMs.

In 2014, Jeon et al. [43] demonstrated a simple strategy for fine-tuning the electronic properties of spiro-OMeTAD derivatives (HTM 1-3) by changing the position of the methoxy (-OMe) substituents at its diphenylamine moieties. According to the result, when the methoxy is in the *meta* position, it exhibits electron-withdrawing behaviour, leading to an increased oxidation potential. Meanwhile, in the *para*

and *ortho* positions, it shows an electron-donating effect, as previously reported.[44] However, the *ortho* position due to steric effects results in a higher LUMO compared to the *para* position. In addition, *ortho* position achieves greater efficiency (16.7%) than *para* (spiro-OMeTAD, 15.2%) and *meta* position (13.9%).

Later, a novel dopant-free spiro-cyclopentadithiophene (s-CPDT) core-based connected by 4-methoxy-*N*-(4-methoxyphenyl)-*N*-phenylaniline as terminal group was synthetized and tested in perovskite solar cells using a sequential deposition method. The HTM-4 show red-shifted absorption, ascribed to the s-CPDT unit, this was compared with spiro-OMeTAD in both solution and thin films. A remarkable PCE of 13.4% was obtained without the use of any dopants, which were very close to doped spiro-OMeTAD with a PCE of 15%.[45]

On the other hand, Saliba et al. presented an attractive low-cost HTM-5 for cost effective upscale or as alternative of spiro-OMeTAD. Despite HTM-5 having energy levels similar to spiro-OMeTAD, it showed a slightly higher PCE of 20.2% compared to 19.7% of spiro-OMeTAD. This was attributed to the additional interaction between thiophene-iodine, which enhances the hole transfer at the HTM/perovskite interface. Both unencapsulated devices based on HTM-5 and spiro-OMeTAD exhibited stability for two months under dry conditions in the dark.[46] Xu et al. reported a low-cost spiro-type HTM (HTM-6) a few months later, showing a high PCE of 19.8%.[47] HTM-6 was obtained in just two steps (overall yield >70%) by synthesizing the spiro[fluorene-9,9'-xanthene] (SFX) core using a one-pot method,[48] confirming that HTM-6 has great potential for large scale production. Besides, many compounds of SFX-based structures have been reported in the literature.[31]

N,N,N′,N′-Tetraphenylbenzidine (TPB) derivatives as RD-SMs

Additives also play a crucial role in the preparation of the hole-transporting layer (HTL) to achieve high efficiency in PSCs. Taking this into account, Song et al. synthesized two asymmetric doping-free HTMs based on *N,N,N′,N′*-tetraphenyl-benzidine (TPB) additive, as illustrated in Figure 1.13.

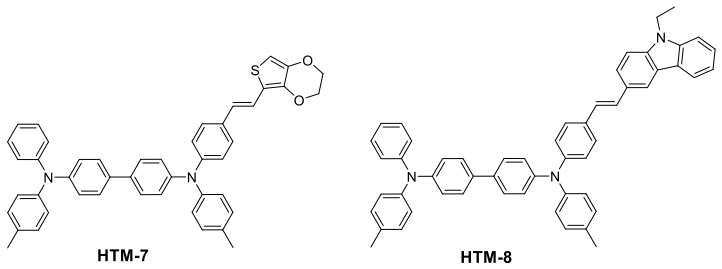

Figure 1.13 Chemical structure of HTM-7 and HTM-8

In their study, it was found that the energy levels of TPB-core as HTM were fine-tuned to align with the perovskite by incorporating 3,4-ethilene dioxythiophene (EDOT) and *N*-ethylcarbazol (NEC) into TPB structure, HTM-7 and HTM-8, respectively. HTM-7 exhibited a higher hole mobility than that of spiro-OMeTAD, leading to a device performance of 13.1%, comparable to that of doped spiro-OMeTAD (13.3%) Additionally, the introduction of electron-donating groups (EDOT and NEC) demonstrated a straightforward synthetic process with lower cost compared to spiro-OMeTAD, good solubility in organic solvents and reliable reproducibility of the cells' performance.[49] These TPB-based HTMs not only exhibited good performance as novel dopant-free materials but also introduced the potential for a new class of linear HTMs.

Diverse π-bridges in RD-SMs

The strategic modification of the structure of the central fragment (π) provide a wide range of HTMs. In addition, the π-bridge has an important role in regulating both photovoltaic performance and synthetic cost.[28] Rakstys et al. presented another interesting strategy to enhance the multi-step synthesis of spiro-like derivatives. The authors employed molecular engineering to obtain HTM-9, incorporating a twisted double bond (C=C) between the two fluorene moieties substituted with 4,4'-dimethoxydiphenylamine through a one-step reaction.

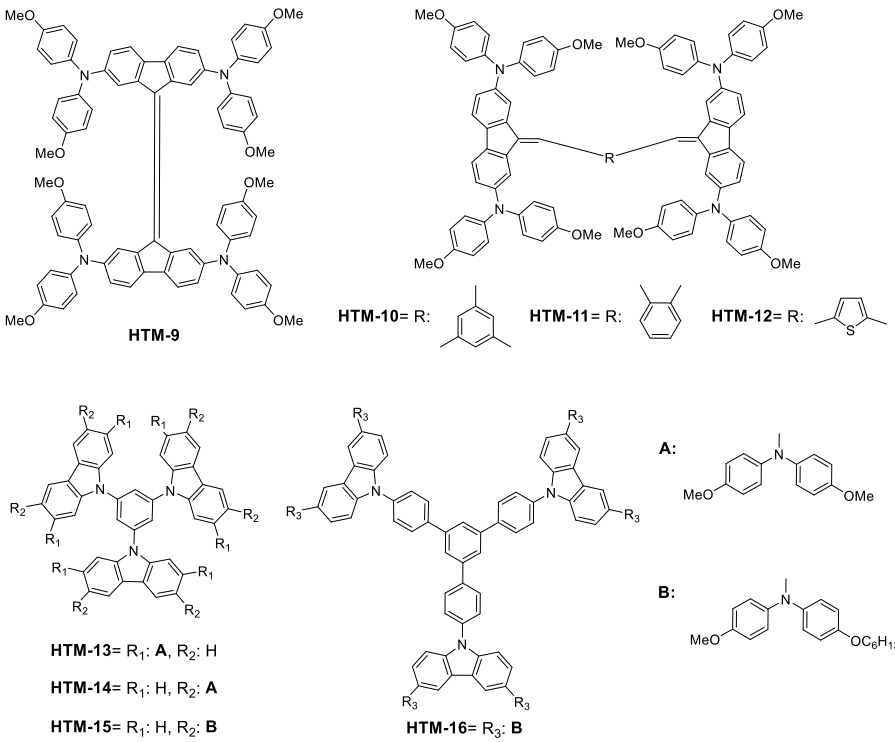

Figure 1.14 Chemical structure of related spiro-type and starburst small molecule HTMs.

Further, they compared the spiro-OMeTAD synthesized by them with the high-purity commercially available to clarify the influence of the "impurities" derived from standard laboratory procedures (lab-grade). Both lab-grade HTM-9 and lab-grade spiro-OMeTAD showed PCE of 17.8% and 17.4% respectively, while commercial spiro-OMeTAD reached 18.4%. The results confirmed that HTM-9 is a promising candidate for being use in PSCs, whereas spiro-OMeTAD requires high purity to achieve high performance.[50] Inspired by their work, Malinauskas et. al reported the introduction of benzene (HTM-10 and HTM-11) or thiophene (HTM-12) as central units in the structure. HTM-12 displayed an additional absorption band attributed to the increased of π-conjugated system through the thiophene-core. Despite this, the energy levels of the new series of branched HTMs showed negligible variations. Moreover, both HTM-11 and HTM-12 achieved a similar impressive PCE up to 19%. However, the increase in the number of fluorene moieties in HTM-10 had an evident negative impact on the performance, charge mobility and conductivity.[51] Furthermore, Lu et al. designed analogous star-shaped molecules based on their previous work (HTM-13)[52] by

replacing the central core and the conjugated side arms, resulting in HTM-14 to HTM-16.[53] The three carbazole-based HTMs were synthesized *via* tuning the substitution position from *ortho* to *para* in the carbazole moiety. This not only simplified the synthesis route, reducing costs, but also improved their hole-transporting properties. The superior smoothness and uniformity observed in the layer of HTM-14 compared to spiro-OMeTAD, can be attributed to its twisted non-planar molecular structure.

Additionally, to improve the solubility, long alkyl chains were introduced in HTM-15 and HTM-16 molecules, which not only enhance solubility but also contributes to the homogeneity of the HTM layer. However, inevitable sphere-shaped islands formed as a result of van der Waals interactions derived from the long alkyl chains, negatively affecting the performance. The device prepared with HTM-14 achieved the highest efficiency of 18.8% among the carbazole-based HTM and spiro-OMeTAD (17.1%) under the same fabrication conditions. Moreover, several types of star-shaped SM have been used in PSCs as HTM, unfortunately, dopants and additives are required to achieve high performance in regular structure.[28,29,32,54–56]

Linear RD-SMs featuring di- or tri- phenylamine groups

Despite the numerous attempts to mimic the spiro-OMeTAD structure, some authors have directed their research employing "linear" HTMs. For example, a new and successful HTM-18, was developed by making a slight structural modification, replacing the triphenylamine (TPA) core of HTM-17[57] with a carbazole-core. It was found that the molecular structure of HTM-18 exhibited a greater planarity, resulting in improved uniformity and complete coverage on the perovskite layer. This characteristic effectively prevented the degradation of the perovskite, contributing to enhance the long-term stability. HTM-18 presented a lower HOMO compared to HTM-17, favouring a higher open-circuit voltage (Voc) in PSCs and consequently leading to superior overall performance. In addition, it was demonstrated that the carbazole-unit not only improved the molecular structure but also contributed to increase the efficiency, from 14.7% (HTM-17) to 17.4% (HTM-18).[58]

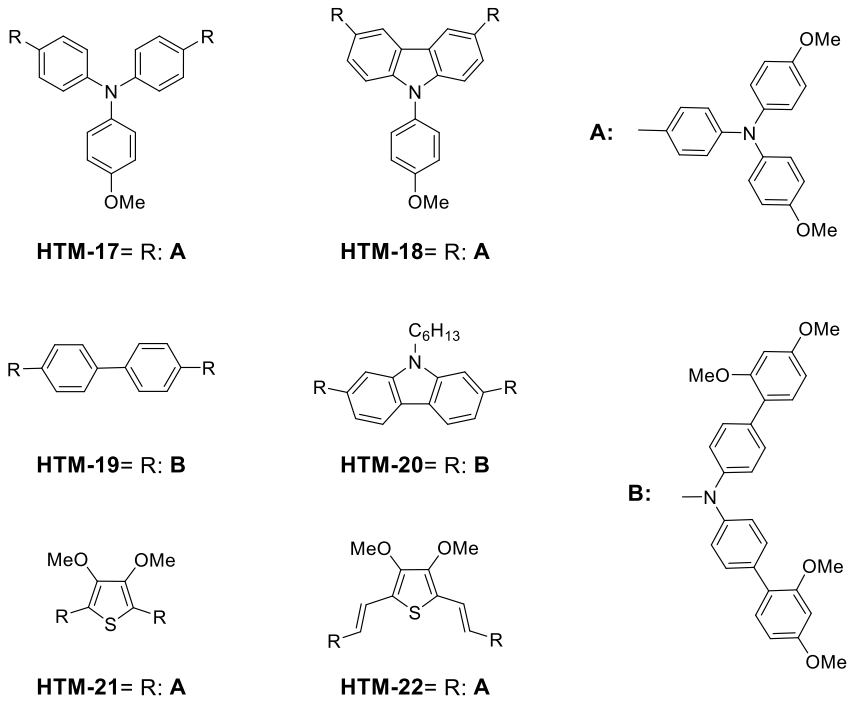

Figure 1.15 Chemical structures of bi- or tri-phenylamine-based HTMs.

Li et al., also have synthesized a new small molecule based on carbazole-core, HTM-20.[59] They enhanced the solubility and improved the interfacial properties between the HTM and perovskite by introducing alkyl groups at the nitrogen atom on the carbazole-core and *o,p*-dimethoxyphenyl units on the TPA side-arms, respectively. Also, the carbazole unit has been introduced to replace the biphenyl-core in HTM-19.[60] This modification aimed to achieve an impressive PCE of 18.3% in HTM-20, while HTM-19 exhibited 16.1%. This is mainly attributed to the carbazole core, which enhances the dihedral angle of the diphenylamine and the π-bridge, as well the steric hindrance effect caused by the long hexyl chain. These improvements not only enhance the quality of the perovskite film surface but also improve the hole-transporting properties, thereby boosting stability.[61]

Another interesting approach was reported by Zhang et al., involving the introduction of two novel thiophene-based HTMs functionalized with *p*-methoxytriphenylamine (TPA-OMe) and connected by a single (HTM-21) or double (HTM-22) bond. Both molecules exhibited suitable energy levels and demonstrated good alignment with the perovskite. The PSCs based on HTM-22 showed an impressive PCE of

20.1%, which is very similar to the 20.6% achieved with spiro-OMeTAD. On the other hand, devices using HTM-22 demonstrated better stability compared to those employing HTM-21 and spiro-OMeTAD under relative humidity. This was attributed to its morphology, which involves the introduction of double bonds, resulting in a more hydrophobic character compared to HTM-21 and spiro-OMeTAD. This characteristic leads to fewer pinholes and homogeneous surface. In addition, the improved interfacial coupling between HTM-22 or HTM-21 and perovskite *via* the sulphur-iodine interactions increases the hole-transporting properties.[62]

Family of branched HTMs with carbazole fragments

The integration of carbazole units in the design of new HTMs have been widely used for photovoltaics applications. Since carbazoles can be easily functionalized into the nitrogen atom or the benzene rings, and are cost-effective as starting material, they exhibit favorable properties such as chemical stability, charge transporting ability and the facility to fine-tune the optical and electronic attributes.[63] As an example of carbazole-based HTMs,[72] in 2018 Magomedov et al., synthesized a series of SM based on HTM-23 structure, taking inspiration from their prior work.[64] The purpose was to investigate structural influences on their HTM properties, focused on three aspects: i) the position of the side arms, ii) the influence of the terminal group, and iii) the number of the side arms.

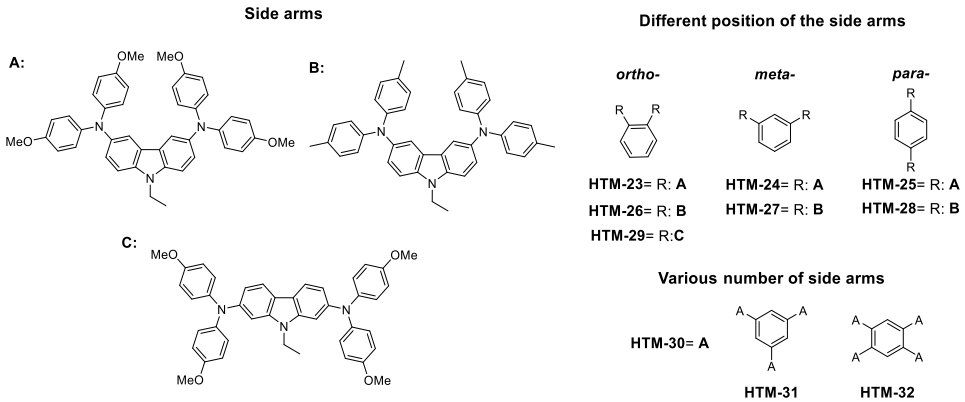

Figure 1.16 Chemical structures of carbazole-based HTMs.

The nine compounds were synthesized through a straightforward two-step process with a simple purification procedure, resulting in high yields. Thermal analysis revealed an increase in the temperature of decomposition (T_{dec}) for compounds in both series at the

para>meta>ortho positions linked with A or B. However, the compound linked with C (HTM-29) exhibited a T_{dec} higher than its homologues. There is only a minor T_{dec} increase for compounds with varying numbers of moieties from one to four substitutions. The change in the central nucleus does not influence the optical properties or the ionization potential. In contrast, regarding hole mobility and PCE, both the core and the terminal group play crucial roles in influencing molecular interactions and molecular packing in terms of hole mobility and PCE. Device performance results indicate that HTMs containing A moieties show better results, achieving a PCE over 18%, compared to the other molecules. On the other hand, the addition of side arms did not lead to higher efficiency.[65]

1.2.3 Self-Assembled Molecules (SAMs) for iPSCs

Since the first report as new class of HTM known as self-assembled molecules (SAMs) for iPSCs in 2018, with our group being among the pioneers in this area, SAMs continue to attract attention in the quest to develop new candidates and understand the complex relationship between the HTM and device performance. Besides, low-consumption material, a simplicity in processing and large versatility, SAMs offer a cost-effective and efficient means of interfacial engineering of PSC, boosting their overall performance.[42,66,67]

One distinguishing characteristic of conventional HTMs is that SAMs are composed of molecules that spontaneously organize and arrange themselves in an ordered structure on a specific surface through a self-assembly process. The molecules that form a SAM typically consist of three main groups: 1) an anchoring or head group, 2) a linker o spacer group and 3) the functional or terminal group, each group having a specific chemical functionality, making them the most attractive feature of the SAMs.[19,36]

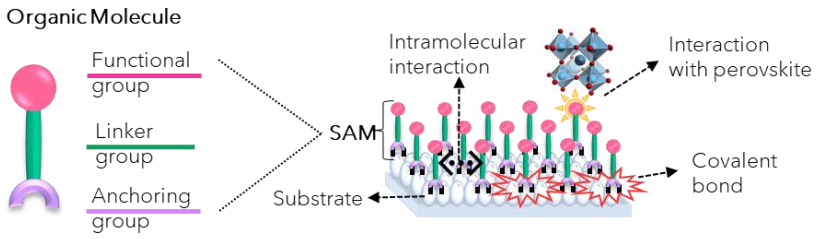

Figure 1.17 Structural components of SAM and the schematic diagram illustrate the ideal arrangement of SAMs showing the mechanisms and chemical interactions.

1.2.3.1 Structural Components of SAMs

Anchoring or head group: This group is the part of the molecule that allows the chemical adsorption onto the surface through chemical reactions such as hydrolysis and condensation to form a strong and uniform monolayer providing stability. The most used anchoring groups are the carboxylic acids (-COOH) and phosphonic acids (-$PO(OH)_2$) among the Brønsted-Lowry acids, that can allow mono-, bi- and tridentate binding modes on the surface.[68]

Linker or spacer group: In addition to connecting the anchor group to the functional groups, the linker group influences charge transport properties, controls molecular packing, and determines geometry *via* Van der Waals interaction. Frequently, alkyl chains and conjugated benzene rings of different sizes and lengths are chosen as spacer groups.[69-71]

Functional or terminal group: These groups define the new surface for the deposition of next layer, commonly the perovskite layer, influencing its structure and morphology. They become a key feature that makes SAMs highly versatile and adaptable, some inspired by previous HTMs. These characteristics allow the generation of well-defined organic surfaces exhibiting useful chemical and physical properties at exposed surface.[67,72,73]

Due to the aforementioned characteristics in the combination of these groups, the utilization of SAMs represents a straightforward and effective engineering approach for interfaces (i.e., substrate/SAM and SAM/perovskite). It stands as an important area of research required for the development of efficient and stable solar cells. Therefore, organic chemistry plays a key role in the development of SAMs, involving making and breaking "bonds" to design the optimal combination of these three groups. This allows researchers to precisely tune the properties of SAMs in the quest for the ideal HTM candidate.[14]

Progress of SAM in iPSCs

In this part, we provide a summary of the advances in the field, highlighting the most relevant SAMs from 2018 to the present (Figure 1.18). These novel SAMs commonly exhibit the characteristics previously mentioned, essential for their effectiveness as HTMs in iPSCs. Our emphasis is specifically on flagship SAMs serving as HTMs, noteworthy for not only exhibiting superior performance but also inspiring the development of innovative SAMs.

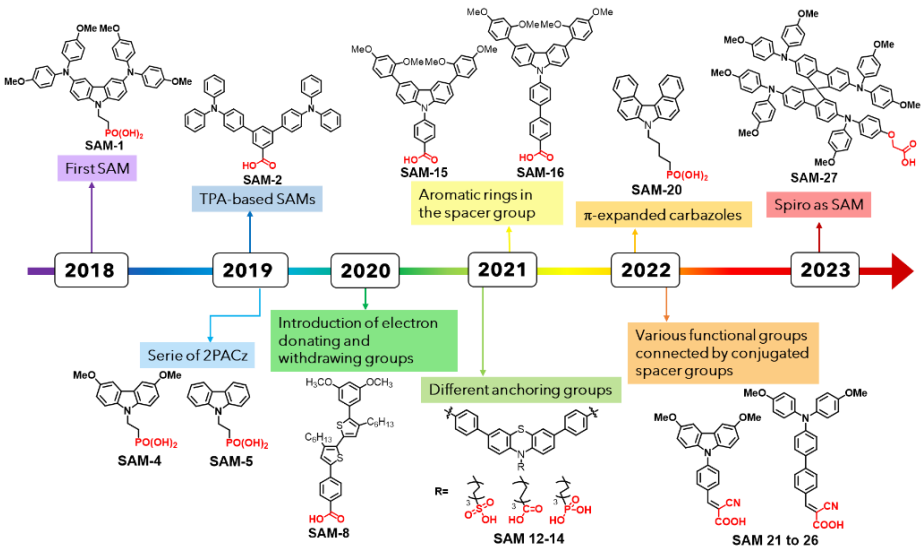

Figure 1.18 Key developments in SAM-based HTMs for iPSCs from their beginning to 2023, along with their corresponding chemical structures.

In 2018, Magomedov and coworkers published for the first time the use of self-assembled molecules (SAMs) as HTM for inverted perovskite solar cells (iPSCs).[42] followed by publications from our research group (Figure 1.19).

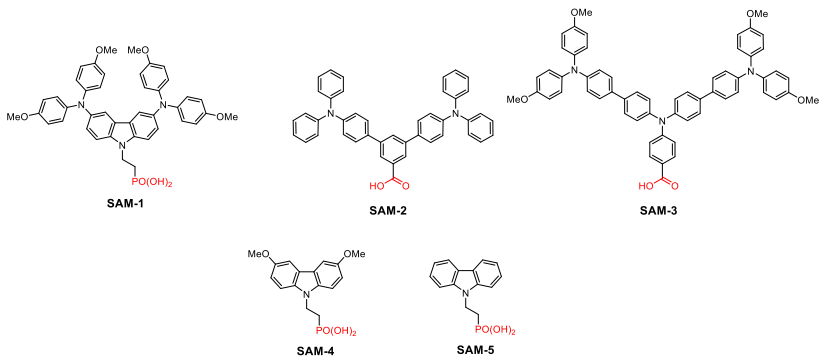

Figure 1.19 First self-assembled molecules (SAMs) applied as HTM for inverted PSCs.

SAM-1 known as a V1036 shares a similar structure with HTM-30, differing only from the introducing of propylphosphonic acid at the nitrogen atom on the carbazole core, leading to an increase in the synthetic route from two to five steps. Despite this, SAM-1 offered a variety of advantages including the spontaneous formation of the SAM on the ITO by immersing the substrate in a SAM solution, with a minimal material consumption, it serves as a dopant-free HTM, is easy to tune in terms of optical and photoelectrical properties and exhibits slight hysteresis. They employed the approach by mixing a SAM solution with phosphonic acid, which was linked to aliphatic chains of two (C2), four (C4), and six carbons (C6). This approach aimed to enhance the quality of the formed monolayer, improve the solubility, and have a positive impact on the overall performance. The best performance was achieved with SAM-based of 10% SAM-1 and 90% C4, successfully incorporated into iPSCs as a self-assembled monolayer, showing a PCE of 17.8% with average FF values close to 80%. Instead, using only SAM-1, the devices achieved a PCE of 15.3%, owing to slight solubility and poor surface coverage.

Our group performed a similar study using SAMs in 2019, where PCE of 17.3% and 15.9% was achieved with SAM-2 and SAM-3, respectively. These SAMs feature TPA-based moieties with a carboxylic acid as an anchoring group and were synthesized through a simple three-steps route. Furthermore, these compounds contributed to fine-tuning the work function (WF) of the ITO, offering a distinct advantage in minimizing charge losses and ensuring selective contact.[66] By changing the side arm on SAM-1 with (SAM-4) and without (SAM-5) methoxy groups by Al-Ashouri, Magomedov et. al., resulted in enhanced properties such as improved the dense film-formation, superior hole-selectivity, efficient hole-extraction and optimized energy alignment with three different types of perovskites. Certainly, the use of SAM-4 and SAM-5 (well known as MeO-2PACz and 2PACz, respectively) in 2019 represented a significant advancement in the progress of PSCs, showing performances of 20.8% and 20.2% in iPSCs, respectively. Furthermore, the utilization of SAM-5 achieved a PCE of 21.1% in co-evaporated perovskite and a certified efficiency of 23.26% in perovskite-based tandem solar cells. Additionally, MeO-2PACz (SAM-4) and 2PACz (SAM-5) are now commercially available and are used in various applications, serving

as HTMs, starting materials and references in photovoltaic devices, among other uses.[67]

All these studies into SAMs not only paved the way for a new category of SM as potential attractive dopant-free HTM candidates among all compounds but have also encouraged organic researchers to take an active part in the molecular design of novel SAMs, investigating different anchoring, linker and functional groups. Although over the last 5 years, there has been a particular focus on the development of new SAMs, as well documented in the literature.[14,74]

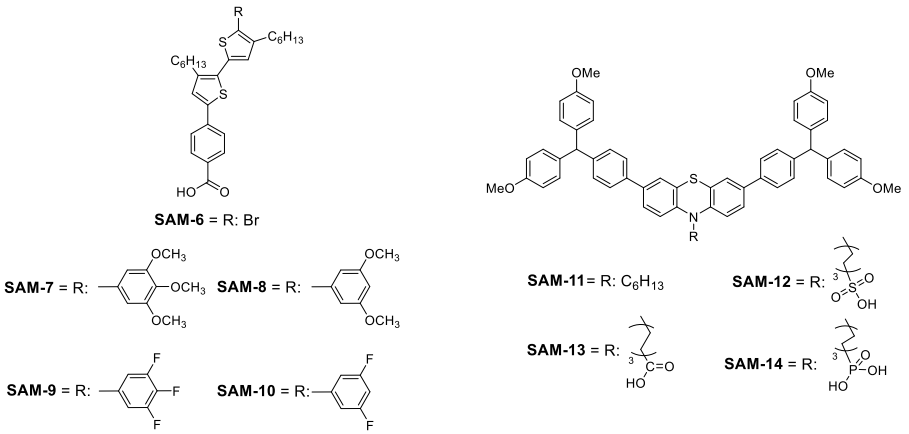

Figure 1.20 Introduction of diverse functional groups in SAM-6and anchoring groups in SAM-11 as self-assembled molecules.

Arkan et al.in 2020, introduced five new SAMs featuring electron donating and withdrawing groups demonstrating that SAMs are an effective method for the permanent alteration of the WF of ITO. Devices prepared with SAM-8 showed the highest efficiency of 12% among the SAMs. However, the introduction of electron withdrawing groups lead to increased WF values and a deeper HOMO, resulting in a negative impact on charge extraction and the performance of iPSCs.[75] Li et al. reported another interesting study in this direction, strategically designing three different anchoring groups linked to phenothiazine bodies to investigate their adsorption on ITO. It was observed that incorporating anchoring groups into the molecule SAM-11 improves the coverage, compactness and adhesion to the substrate, resulting in dense and well-crystalized perovskite films on all of these SAMs. The chemical adsorption and bonding strength of SAMs on the ITO surface follow the same trend SAM-14> SAM-13> SAM-12, resulting in a surprising increase in the contact angle compared with SAM-11 molecule without anchoring group, which

also exhibits the same trend. The champion iPSCs based on $PO(OH)_2$ anchoring group (SAM-14) show an impressive performance with a PCE of 21.4%, maintained at over 90% under illumination after 200 h in ambient atmosphere with 35% humidity. In contrast, devices prepared with SAM-11, SAM-12 and SAM-13, exhibit PCEs of 12%, 16.2%, and 18.9%, respectively. In addition, SAM-14 demonstrate a PCE of 20.1% with a working area of 1 cm^2 in iPSCs.[68]

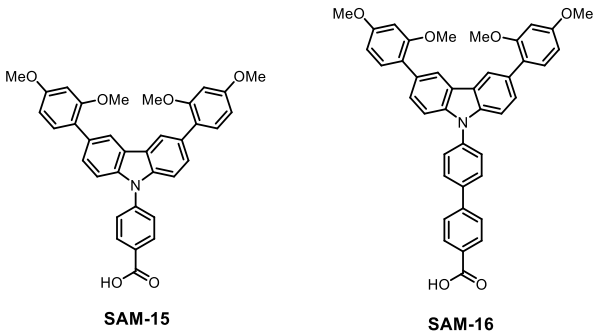

Figure 1.21 Chemical structure of SAM-15 and SAM-16 as SAMs.

Recently, inspired by our previous works,[66,76] we designed and synthesized two simple molecules with 2,4-dimethoxyphenyl functionalized-carbazole core, linked by either one or two phenyl groups to a carboxylic acid anchoring group. Here, the methoxy and carboxylic groups increase the solubility, while the extra phenyl in SAM-16 makes the compound less soluble and more hydrophobic, however both compounds formed good quality films on ITO. Despite SAM-15 and SAM-16 exhibiting slight differences in performance, both showing outstanding PCE over to 21%, SAM-16 demonstrates higher stability, exceeding 2000 h with a UV-filter at 80 °C. This enhanced stability is attributed to the high thermal decomposition resulting from the presence of the two linked phenyl groups. Currently, SAM-15 and SAM-16, known as EADR03 and EADR04, respectively, are commercially available and have been successfully utilized in QDLEDs.[70,77]

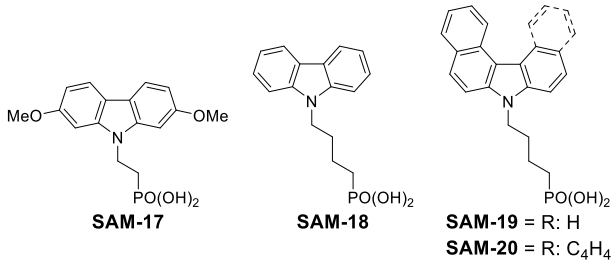

Figure 1.22 Molecular structure of SAMs as 2PAC derivatives.

In 2022, Jen's group reported two studies using 2PACz derivatives. On one hand, they introduced methoxy (MeO-) groups at position 2 and 7 resulting in a favorable dipole moment. In addition, to cover the sites with no SAMs on the substrate, SAM-17 was combined with 6-(iodo-λ^5-azanyl) hexanoic acid (IAHA) to form a co-assembled monolayer, leading to an improvement in film quality and an impressive PCE of 23.6% in iPSCs.[78]

On the other hand, they designed two novel SAMs through asymmetric and helical p-expansion molecular strategies, obtaining a higher dipole moment compared to SAM-18. This facilitated their dense assembly and the fine-tune of the ITO work function. As a result, the PCE of SAMs significantly improved: from 14.5% for SAM-50 to 19.2% and 21.4% for SAM-19 and SAM-20, respectively. Furthermore, devices based on SAM-20 were treated with top surface passivation and antireflection coating, resulting in a champion device with a remarkable PCE of 24.1%.[69]

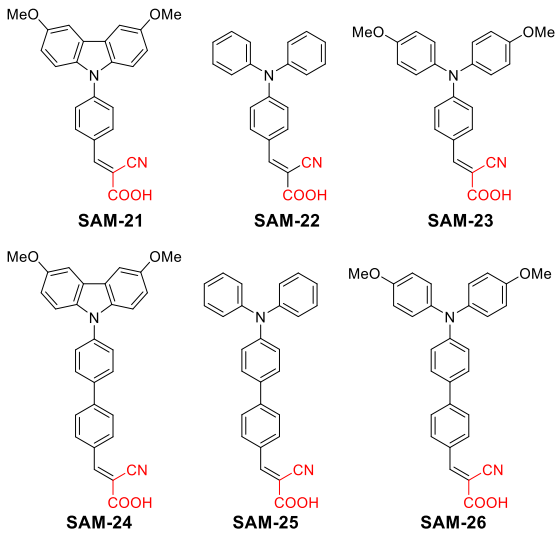

Figure 1.23 Chemical structure of SAMs with conjugated spacer groups

Zhang et al., reported a series of conjugated SAMs inspired by our previously work, employing different carbazole and triphenylamine units connected to cyanoacetic acid anchoring group by conjugated linkers. In their studies, they found that introducing a phenyl moiety into the linker group not only increase the PCE but also enhanced long-term stability. These improvements are attributed to the effective delocalization of electron/charge distribution, contributing to fine-tune energy levels and the improvement of photostability. Most of the SAMs showed PCE values of over 20%, while SAM-26 achieved an exceptionally high PCE of 22.5% (certified PCE of 22.12%).[73]

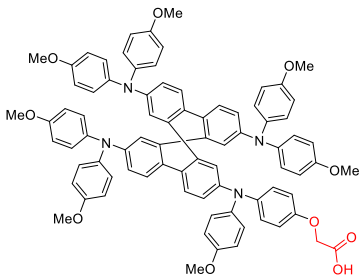

Figure 1.24 Chemical structure of SAM-27 (spiro-acid).

Further, in collaboration with Michele Cariello et al., our group implemented a strategy to transform the spiro-molecule into a self-assembled molecule by introducing a carboxylic acid unit as an anchoring group, named spiro-acid (SAM-27) and tested in iPSCs. Our result demonstrated that SAM-27 provides a simple methodology for reducing the manufacturing cost of spiro-OMeTAD without compromising the device performance. The devices based on SAM-27 achieved a PCE of 18.1%, demonstrating excellent long-term illumination stability and minimal energy loss.[79] This opened the possibility of studying HTMs previously investigated in regular structure for implementation in various approaches with minor structural modifications, aiming to improve the performance in photovoltaic devices without the use of additives or dopants.

It is worth mentioning that, until now, we cannot always compare the performance of studies utilizing different synthesized HTMs, mainly due to the use of different materials and structures in constructing the devices.

Due to the promising application of several carbazole-based SMs in photovoltaic devices and inspired by their easy synthesis and performance compared to commonly used HTMs like spiro-OMeTAD, in this thesis, three groups of SMs, based on carbazole HTMs are designed and synthesized with the aim of exploring the effects and interactions at the interfaces of HTMs, both above and below (principally, HTM/perovskite interface), through the strategic engineering of HTM molecular structures.

1.3 Motivation and Outline of the Thesis

Renewable energy is becoming the hottest alternative for energy supply due to the growth in energy demand and climate change. Over the last 11 years, among of renewable energy technologies, the utilization of solar energy sources has experienced a gradual growth. Perovskite solar cells are promising candidates to transform the sunlight energy into electrical energy and have made a significant progress, increasing from 3.8% efficiency in 2009 to a very recent of 26.1%. However, there are still different challenges limiting commercialization such as the optimization of perovskite materials, deposition methods, device architecture and cost-effective charge transporting materials. Among the components of the perovskite solar cell, the hole-transporting materials play a pivotal role in achieving high efficiencies, contributing significantly to the enhancement of device stability and overall performance. Additionally, they serve as a key factor in reducing production costs, making HTMs a compelling choice for advancing the perovskite solar cell towards commercialization.

The general aim of this thesis is to design and synthesize new hole-transporting materials in order to investigate the complex relationship between the molecular structure and their surrounding layers specially perovskite layer, leading to a fundamental understanding of the requisites for effective hole transporting materials and further contributing to the enhancement of the overall performance of perovskite solar cells.

This section provides a brief description of each chapter's objectives and contents:

Chapter 1 provides an overview of perovskite solar cells, delving into fundamental knowledge, diverse structures, and operational mechanisms. It also outlines the main components of these solar cells, along with a brief summary of the evolution of hole transporting materials employed in perovskite-base devices since the introduction of spiro-OMeTAD.

Chapter 2 gives a detailed description of the methods, techniques and experimental procedures used for characterizing the synthesized compounds and for the fabrication of perovskite solar cells.

Chapter 3 present the design, the synthesis and basic characterization of the new hole transporting materials based on carbazole. This chapter is

divided into three different sections corresponding to the projects, where the objectives of each project are described in the subsequent chapters.

Chapter 4, is focused on the synthesis of three new self-assembling molecules based on carbazole, aiming to comprehend the SAM/perovskite interface in inverted perovskite solar cells. This investigation provides a deeper insight of the impact of the diverse molecular structures on both their overlayers and power conversion efficiency. A comparison of the linker groups (phenyl or biphenyl) reveals that the shorter linker demonstrated a superior performance in this type of device and molecular structure. Furthermore, varying terminal groups does not yield significant differences in cells performance.

Chapter 5, the main objective of this chapter was to obtain an easy and cost-effective self-assembling molecules with functional groups engineered substituents. A total of four new compounds were obtained with affordable starting materials in a few and simple synthetic procedures. The impact on different side arms in the SAM structure was explored through different techniques, as well the performance. A power conversion efficiency of 19.8% was achieved utilising SAM5 which is containing a phenylthiophene moieties attached to the carbazole core, demonstrated comparable efficiency to the reference (EADR03).

In Chapter 6, derivatives of thiophen-core hole transporting materials based on spiro-type (D-π-D) architecture are explored, presenting a potential lower cost advantage compared to the widely used spiro-OMeTAD. The aim of this chapter is to investigate the impact on the different electron-rich methoxy-engineered donor units (D) in comparison to D units of spiro. In another hand, their potential used as a dopant free hole transporting molecule.

Finally, Chapter 7 summarizes the conclusions based on the preceding chapters' results and poses the perspectives opened by them for further advances on the field.

CHAPTER 2

EXPERIMENTAL TECHNIQUES AND PROCEDURES

This chapter is organized into three sections where we detail the experimental techniques and methods employed to acquire the data reported in the results. The first section includes the characterization of the synthesized hole-transporting molecules (structural, thermal, electrochemical, optical and optoelectrical), along with their characterization in film form. The second section describes the completed characterization of PSC devices, which are used for deep comprehension of HTM-based devices and demonstrates that the newly developed molecules are promising HTMs for PSCs. Finally, the third section describes the fabrication procedures of the PSCs employed in this thesis.

General Materials

All the chemical materials and solvents were purchased from Sigma-Aldrich, TCI Europe, MERCK, Fluorochem, Dyenamo, Lumtec, Apollo Scientific, Emplura, Panreac or Alfa Aesar and they were used without further purification unless otherwise mentioned. Common solvents are purchased from VWR chemicals BDH.

The Patterned indium tin oxide (ITO) and fluorine tin oxide (FTO) glass substrates (1.5 cm × 1.5 cm, 15 Ω sq^{-1}) were purchased from Xin Yan Technology Ltd.

2.1 Organic Synthesis

General Methods

All sensitive reactions were carried out under nitrogen or argon atmosphere using standard Schlenk techniques (under high-vacuum, ~10^{-2} mbar) with distilled and dried solvents, unless otherwise stated. The course of the reactions was monitored using analytical thin layer chromatography (TLC) using Merck silica gel 60 F_{254} precoated plates (0.25 mm) and subsequently visualized with a UV lamp. All workup and purification procedures were carried out with reagents and solvents with analytical grade. All the solvents were removed by rotary evaporation under reduced pressure. Column chromatography was performed using spherical silica gel 70 Å, 40–75 mm.

General Instrumentation and Characterization

^{1}H and ^{13}C Nuclear Magnetic Resonance (NMR)

NMR spectra were recorded on a Bruker Avance spectrometer (400 and 500 MHz). Chemical shifts (δ) are reported in ppm referenced with the solvent resonance as the internal standard. All deuterated solvents used are indicated. Coupling constants (*J)* are given in Hz. Data have been reported as follows: chemical shift, multiplicity (standard abbreviations), coupling constants and integration.

High-Resolution Mass Spectra (HR-MS)

HR-MS were recorded on Waters Micromass LCT Premier using electrospray ionization (ESI) Mass Spectrometer or on a Bruker Daltonics Autoflex using matrix-assisted laser desorption/ionization (MALDI), and

matrix-assisted laser desorption/ionization time-of-flight (MALDI-TOF) techniques and are reported as m/z (relative intensity).

Thermal Measurements

The thermal stability of the molecules is essential for the long-term stability of solar cell devices, which could be determined by thermogravimetric analysis (TGA) and differential scanning calorimetry (DSC).

Thermogravimetric Analysis (TGA)

TGA technique was used to determine the weight loss of a material as a function of temperature or time under a controlled atmosphere. The decomposition temperature (T_{dec}) was determined as the temperature where 5% of the weight is lost by heating the sample from 30 to 1000 °C at a scan rate of 10 °C/min under an N_2 atmosphere. The measurements were carried out in a TGA/SDTA851 Mettler Toledo equipment.

Differential scanning calorimetry (DSC)

DSC analysis provide information about physical and chemical changes such as melting (T_m), glass transition (T_g), and crystallization (T_c) temperatures (See Figure 2.1). DSC measurements were recorded on DSC822e from Mettler Toledo instrument with a heating rate of 10 °C/min under N_2 atmosphere by heating from 30 to 600 °C.

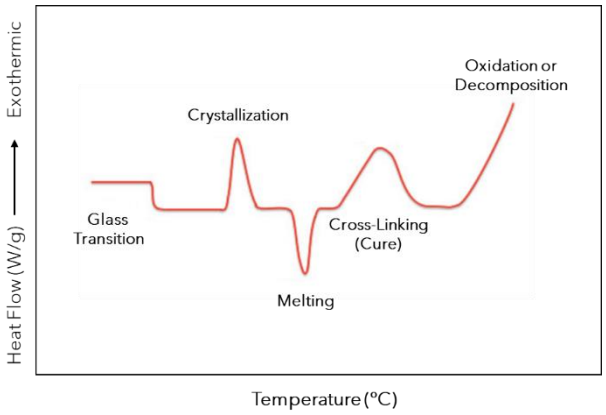

Figure 2.1 Illustration of a differential thermogram showing material transitions as a function of time and temperature.

Electrochemical Characterization

The electrochemical properties of the HTMs were studied by cyclic voltammetry (CV), performed using an SP-150e potentiostat electrochemical workstation from BioLogic. The main purpose of conducting CV measurements was to determine the oxidation and reduction potentials of the HTM to estimate its energy levels.

The measurements were performed with a conventional three-electrodes electrochemical cell (**Figure 2.2**): 0.1 M for tetrabutylammonium hexafluorophosphate ($TBAPF_6$) in DCM as electrolyte; Ag/AgCl (3 M potassium chloride) in a 0.5 mM acetonitrile solution as the reference electrode; a glassy carbon as the working electrode; a platinum wire as the counter electrode with Fc/Fc^+ as an internal standard. The scan rate was set up as 100 mV/s at room temperature. The potentials (E) were corrected to the potential of Fc/Fc^+ (E_{Fc}).

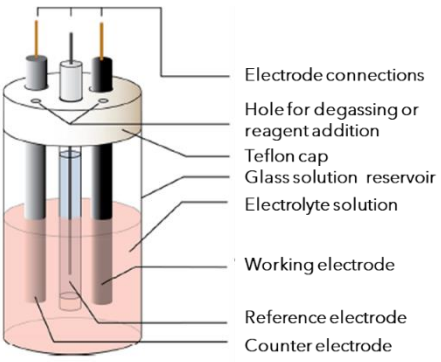

Figure 2.2 Schematic illustration of an electrochemical characterization setup.[80]

Optical Measurements

Ultraviolet-visible (UV-vis) absorption spectroscopy was performed to measure the absorbance of HTMs in solution. UV-vis was measured using Shimadzu UV spectrophotometer 1700 with an optical range from 190 to 1100 nm.

Steady-state fluorescence emission (PL) spectra were recorded on Horiba Jobin Yvon Ltd. Width a PMT (UV-vis) and InGaAs (NIR) detectors with wavelengths ranging from 250 to 1600 nm.

All samples were measured using a 1 cm path-length quartz cell at room temperature with a concentration of ~10^{-5} M in dichloromethane (DCM), tetrahydrofuran (THF) and toluene (TOL).

Energy Level Calculations

One of the crucial parameters influencing the functioning of the solar cell is the energy levels alignment of the HTM, among other factors. When the HOMO (highest occupied molecular orbital) level is higher than the edge valence band (VB) of the perovskite, and its LUMO (lowest unoccupied molecular orbital) level is sufficiently high to avoid charge recombination, the HTM is considered a suitable material for use in PSCs. The energy levels were calculated using the determined parameters obtained from CV and UV-vis measurements.

The HOMO was calculated using **Equation 1**, where the halfway potentials ($E_{1/2}$) of the corresponding molecules were calculated by averaging the points of minimum and maximum current during the first oxidation and reduction potential, these potentials were determined graphically by means of the CV measurements.

$$\mathrm{E_{HOMO}(eV)} = -(4.8 - \mathrm{E_{1/_2Fc}} + \mathrm{E_{1/_2sample}}) \qquad \text{EQUATION 1}$$

The band gap energies (E_g) for the organic molecules were calculated using equation 2:

$$\mathrm{E_g} = \frac{1242}{\lambda_{\mathrm{onset}}} \qquad \text{EQUATION 2}$$

where the λ_{onset} corresponds to the intersection point between the absorption and emission normalized plots.

Finally, the LUMO level was calculated by equation 3:

$$\mathrm{E_{LUMO}(eV)} = (\mathrm{E_g} + \mathrm{E_{HOMO}}) \qquad \text{EQUATION 3}$$

Ultraviolet Photoelectron Spectroscopy (UPS)

Ultraviolet photoelectron spectroscopy (UPS) is one of the conventional methods to determine the ionization energy (I), which is equal to the HOMO level of the material in film form. In this work, UPS was used to

estimate the HOMO level for HTMs deposited onto the substrate. In addition, UPS analysis permited the comparison of the HOMO levels of HTM obtained from CV (HTM_{film} vs. $HTM_{solution}$, respectively).

The HOMO energy level is given by:

$$E_k = h\nu - E_{HOMO} \qquad \text{EQUATION 4}$$

Where E_k is the highest kinetic energy of the electron, hv is the energy of the ultraviolet photon (where h=Plank's constant and v=frequency of the ionizing light). As a photon source, we used a helium lamp corresponding to an energy of 21.2 eV ($E_{He\ I}$) and the data obtained with a -10 V was applied to the samples to facilitate the emission of the secondary electrons (SECO).

Film Characterization

Contact Angle

Contact angle measurements were used to investigate the surface wettability of ITO substrates before and after modification with SAMs, confirming the successful adsorption of each SAM onto the ITO substrate. As it is shown in Figure 2.3 a small angle (less than 90°) indicates that the surface is favorable for wetting.

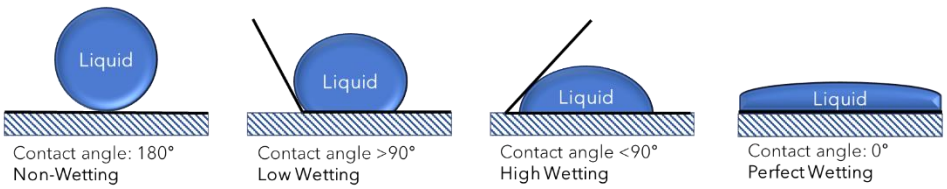

Figure 2.3 Examples of contact angles formed by a drop of water on the substrates in the static state.

To value the surface wettability of the prepared films before (ITO treated with UV-O_3) and after modification with SAMs (ITO treated + SAMs), contact angle measurements were performed with the Attention Theta Flex optical tensiometer, using sessile water drop analysis. In the experiments, 10 μL of water was placed on the film surfaces, meanwhile, the images were collected simultaneously. Figure 4 depicts the contact angle measured on ITO used as a reference to evaluate the surface properties after SAM deposition.

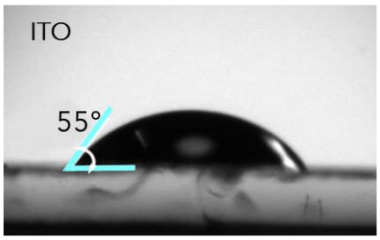

Figure 2.4 Image of contact angle measurement on ITO surface after UV-O_3 treatment.

X-ray Photoelectron Spectroscopy (XPS)

XPS measurements were performed at room temperature with a SPECS PHOIBOS 150 hemispherical analyser (SPECS GmbH, Berlin, Germany) at a base pressure of $5x10^{-10}$ mbar. Monochromatic Al K alpha radiation (1486.74 eV) was used as an excitation source operated at 300 W. The energy resolution as measured by the FWHM of the Ag 3d5/2 peak for a sputtered silver foil was 0.62 eV. **Figure 2.5** displays an XPS measurement of ITO used as a reference in this work, where no nitrogen atoms were observed on the surface.

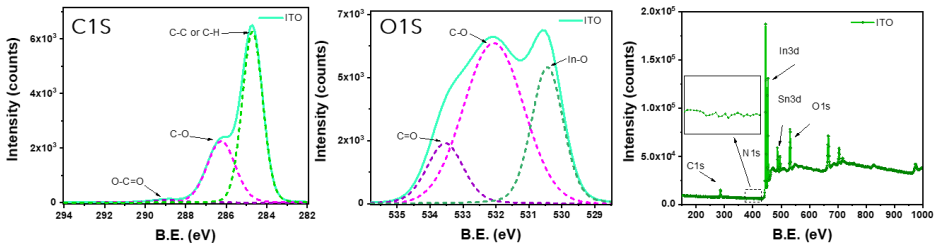

Figure 2.5 XPS of C1s, O1s and survey spectrum for the treated ITO.

2.2 Characterization of Perovskite Solar Cell Devices

The photovoltaic performance of solar cell devices is crucial to determine the abilities of the HTMs. The photovoltaic properties were evaluated by measuring the current (J) flowing through the device under applied voltage (V), both with and without illumination, resulting in current density-voltage (JV) curves. Using the maximum power point (P_{max} = J·V) we can calculate the produced power and compare it to the incoming power to approximate power conversion efficiency (PCE) of the solar cell efficiency. Furthermore, from the JV curve, the following parameters are obtained: short-circuit current (J_{sc}), open-circuit voltage (V_{oc}) and fill factor (FF). JV curves were recorded using a Solar Simulator (ABET 11000) and a source

meter (Keithley 2400). The curves were registered under 1 Sun standard conditions (100 mW/cm^2, AM 1.5G) calibrated with a silicon reference cell.[81]

The photovoltaic parameters were extracted from the J-V curves under both forward (from J_{sc} to V_{oc}) and reverse (V_{oc} to J_{sc}, respectively) scans. As shown in Figure 2.6, the J_{sc} can be obtained when the voltage equals zero, and V_{oc} can be obtained with a zero net current through the device.

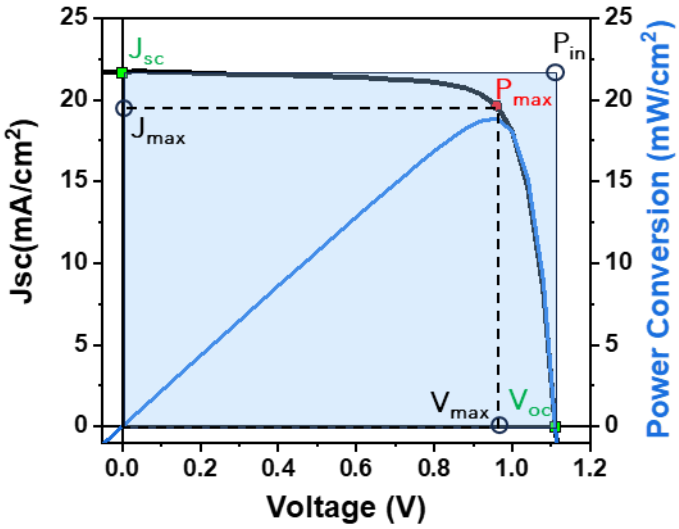

Figure 2.6 Typical JV curve of a PCS (black line) displaying its important parameters and its power conversion output (blue line).

The FF is an important parameter used to calculate the deviation of the measured solar cell efficiency from the theoretical (P_{in}) of the cell, which corresponds to the ratio of the maximum power and the product of J_{sc} and V_{oc}, as expressed by the following equation:

$$FF = \frac{J_{max} \cdot V_{max}}{J_{sc} \cdot V_{oc}} \qquad \text{EQUATION 5}$$

The PCE is defined by the ratio of the maximum power output (P_{max}) to the power of the incident light (P_{in}, 100 mW/cm^2) as the following equation,

$$PCE = \frac{P_{max}}{P_{in}} = \frac{J_{SC} \cdot V_{OC} \cdot FF}{P_{in}} \qquad \text{EQUATION 6}$$

Morphology Characterization

Scanning Electron Microscopy

The film morphology and the grain size distribution of the perovskite layer on top of the small molecules (SMs) film were analysed using a Field-Emission Scanning Electron Microscope (FESEM), where the various topologies of the sample resulted in different contrast colours in the final image. The FESEM images are acquired with FEI Quanta 600 microscopy. The average grain size values for perovskite film were determined by calculating the sizes of at leats 50 individual grains through the ImageJ program.

Photophysical Measurements

To investigate the impact at the interface between SAM/perovskite, integrated photoluminescence (PL) and time-resolved photoluminescence (TRPL) experiments were conducted by exciting the samples from the perovskite side under ambient conditions, unless otherwise mentioned. PMMA films were deposited on perovskite layers to protect them from the environment. Both techniques offer insights into carrier recombination at the SAM/perovskite interface. The PL and TRPL spectra were performed on an Edinburgh Instruments LifeSpec-II apparatus with excitation by a 635 nm laser. TRPL decay curves were fitted with the biexponential decay function:

$$y = A_1 \exp\left(-\frac{t}{\tau_1}\right) + A_2 \exp\left(-\frac{t}{\tau_2}\right) \qquad \text{EQUATION 7}$$

Where A_n is an amplitude and τ_1 and τ_2 represent the decay time components.

Effect of Light Intensity

The study of light dependence of J_{SC} and V_{OC} with different light intensities (P_{light}) was conducted using optical filters from 1 sun to dark. The study of the light dependence of J_{SC} allows us to estimate the photocurrent losses due to recombination mechanisms. It is fitted to a power-law: $J_{SC} \propto P_{light}^{\alpha}$,

where α = 1 at short circuit conditions indicates that there aren't photocurrent losses, whereas higher values suggest that charges might be trapped in the perovskite layer. For the case of V_{OC} dependence with light intensity, it is possible to calculate the ideality factor (n_{id}) which shows how much the solar cell deviates from the ideal diode behavior. Typically, the value of n_{id} = 1 indicates band-band recombination, whereas the value of n_{id} closer to 2 means Shockley-Read-Hall (SRH) recombination is predominant. The value of n_{id} closer to 1 indicates a lower degree of defect-assisted recombination. The non-ideal diode equation is described in Equation 8.

$$J = J_{SC} - J_0(e^{\frac{qV}{n_{id}k_B}} - 1) \qquad \text{EQUATION 8}$$

Where J is net current, J_0 is a constant, k_B is the Boltzmann constant, q is the elementary charge, V is the applied voltage and T is the device temperature.

As the J_{SC} increments linearly with the P_{light} at open-circuit conditions (J = 0) a final approximation to derivate the ideality factor from Equation 9 is as follows,

$$V_{oc} = \frac{n_{id}k_B T}{q} \mathrm{Ln}\,(P_{light}) \qquad \text{EQUATION 9}$$

Long-Term Illumination Stability

The stability tests were conducted on a home-made setup including a Keithley 2400 Source Measure Unit and an LED lamp. The stability of the unencapsulated devices was performed in a sealed holder filled with nitrogen under continuous white-light LED. The light intensity was adjusted to ensure that devices achieved equivalent Jsc values to that under standard 1 Sun AM1.5G illumination at room temperature. The photovoltage measurements were recorded every 60 min and a custom C++ code was developed for the automated data recording and pre-processing.

External Quantum Efficiency Measurement

The external quantum efficiency (EQE), also known as the incident Photon-to-Current Conversion Efficiency (IPCE), is a characterization technique

that quantifies the relationship between the number of free electrons collected by the solar cell and the number of incident photons.

EQE measurements record the short-circuit photocurrent by changing the light wavelength (λ). EQE can be calculated by the following equation:

$$\mathrm{EQE} = \frac{hv * \mathrm{J_{sc}}}{\mathrm{I_{in}} * e} \qquad \text{EQUATION 10}$$

Where *hv* is the photon energy, I_{in} is the incident light intensity and *e* is the absolute value of electron charge.

The J_{sc} can be calculated by integrating the EQE over the spectral photon flux (*S*) at standard one sun illumination if the J_{sc} shows a linear response with the light intensity with Equation 11,

$$J_{SC_{EQE}} = \int \mathrm{qEQE}(\lambda)\mathrm{S}(\lambda)\mathrm{d}\lambda \qquad \text{EQUATION 11}$$

where S(***λ***) is photons per second (photon flux density), and by integrated the EQE spectra of this is obtained as $J_{SC,EQE}$ that is relatively lower than the $J_{SC,JV}$ for the solar devices.

EQE measurements are recorded by an Oriel Instruments QEPVSI-by system with a Xenon lamp (Newport 300 W). The white light is chopped at a frequency of 78 Hz by a Newport Cornerstone 260 monochromator. Before each measurement, a Si diode with a known spectrum is used as a reference. The response from the solar cells is measured with a Stanford Research SR830 Lock-In amplifier and evaluated by a commercial software named TracQ.

Optoelectronic Transient Techniques

The transient techniques, such as charge extraction (CE), transient photovoltage (TPV) and transient photocurrent (TPC) are powerful techniques to study both carrier transport accumulation and recombination kinetics under close to operando conditions. The CE, TPV and TPC measurements were performed in a sealed holder filled with nitrogen and carried out using a white LED controlled by a programmable power supply and a box that switches from open to short-circuit states. All the signals are recorded using a Yokogawa DLM2052 oscilloscope registering drops in voltage. Light perturbation pulses for TPV and TPC

were provided by nanosecond PTI GL-3300 nitrogen laser and using a 580 nm laser pulse wavelength with a duration of 1.5 ns.

Charge Extraction (CE)

CE is a technique designed to quantify the charge stored in the solar cell under operational conditions. In this order, the device is illuminated while is kept at open-circuit conditions until a stable open-circuit voltage (Voc) is obtained. Subsequently, the device is promptly switched to short-circuit and the light is switched off. The current transient obtained from the discharge of the device is integrated to obtain the charge in the device. In this thesis, the measurements were obtained at different light intensities to obtain the charge stored in the device at different Voc. Using Ohm's law, it is possible to obtain the charge stored in the device by integrating the transient voltage over time (Equation 12).

$$Q = {}^{1}/_{R} \int_{t=0}^{t=t} V(t)dt \qquad \text{EQUATION 12}$$

Where Q represents the charge, R is the resistance (50 Ω), and V(t) is the voltage at a given time. From these measurements, two different regions are obtained. The first is a constant part which is directly related to the charges stored at the electrodes called geometrical capacitance (C_{geo}), following a parallel plate capacitor model and increasing proportionally with the applied V, as depicted in Equation 13.

$$Q = C_{geo} \cdot V = \frac{\varepsilon_0 \cdot \varepsilon_r A}{d} V \qquad \text{EQUATION 13}$$

Where ε_0 is the electric constant, ε_r is the relative permittivity, A the active area of the plate of the capacitor and d is the distance between the two plates.

The second is the exponential part, linked to the chemical capacitance, or the accumulation of charges at the perovskite/selective contact interface, following the Maxwell-Boltzmann distribution (Equation 14)

$$Q = Q_0 \left[\exp\left(\frac{q \cdot V}{m \cdot k_B T} \right) - 1 \right] \qquad \text{EQUATION 14}$$

Where Q_0 is the charge density in equilibrium and m is a factor related to the deviation from the thermal voltage (k_BT/q). By subtracting 1 from the exponential factor, we obtain a result of zero charge when V = 0. Equation 15 derives an expression for charge extraction as a function of V, resulting from the combination of Equations 13 and 14.

$$Q = C_{geo} \cdot V + Q_0 \left[\exp\left(\frac{q \cdot V}{m \cdot K_B T} \right) - 1 \right] \qquad \text{EQUATION 15}$$

For an accurate analysis, CE needs to efficiently capture all types of charges (ionic carriers and geometrical charges) which are presented at the device at a specific V. This rapid extraction is essential to surpass carrier recombination, preventing charge losses before the solar cell reaches a short-circuit state. Thus, the charge density in the perovskite bulk can be directly estimated.

Transient Photovoltage (TPV) and transient photocurrent (TPC)

TPV is a technique employed to investigate carrier recombination. It relies on utilizing a laser pulse while maintaining the device under open circuit conditions during continuous illumination. The laser pulse induces a small perturbation in the Voc, resulting in a number of charges, directly related to a small perturbation in the quasi-Fermi level. Then, we observe the decay of the Voc to its steady state value associated with the light illumination and from the kinetics associated with this decay, we can determine the carrier lifetime, which corresponds with the major recombination rate in the solar cell. In this context, it is possible to compare small perturbation lifetime ($\tau_{\Delta n}$) with Voc (Equation 16).

$$\tau_{\Delta n} = \tau_{\Delta n0} \cdot \exp\left(\frac{q \cdot Voc}{m \cdot K_B T} \right) \qquad \text{EQUATION 16}$$

Where $\tau_{\Delta n0}$ is the equilibrium carrier lifetime. In the case of TPV decay is faster than CE at the same light bias, the combination of TPV and transient photocurrent (TPC) allows obtaining the differential capacitance (DC) as another option for CE. TPC use DC analysis to measure the extra carriers in the solar cell generated by the laser pulse (ΔQ), which should be the same at different light intensities, inducing perturbation in short-circuit conditions Equation 17.

$$C(\mathrm{Voc}) = \frac{\Delta Q}{\Delta V} \qquad \text{EQUATION 17}$$

TPC presents two different regimes like CE, which was previously described and the stored charges in the device can be correlated with the increasing voltage using the following equation,

$$\mathrm{Q(Voc)} = \int_0^{\mathrm{Voc}} \mathrm{C(Voc)dVoc} \qquad \text{EQUATION 18}$$

TPV as a function of the charge density

The comparison of the small perturbation lifetime as a function of the charge density calculated from the CE or DC experiments allows obtaining the recombination order (δ) facilitating the calculation of the total carrier lifetime (τ) which can be fitted with a power law dependence (Equation 19).

$$\tau_{\Delta n} = \tau_{\Delta n0}\left(\frac{\mathrm{Q}}{\mathrm{Q_0 T}}\right)^{-\lambda} \qquad \text{EQUATION 19}$$

Where λ is the slope which is correlated with the recombination order ($\delta = \lambda + 1$), and Q_0 is the charge density in the equilibrium.

2.3 Fabrication of Perovskite Solar Cell Devices

This thesis explores the use of synthetised-HTMs in both regular (n-i-p) or inverted (p-i-n) configurations of PSCs, aiming to understand the relationship between the molecular structure of these new HTMs and their impact on the performance of PSCs. The different architectures are illustrated in Figure 2.7.

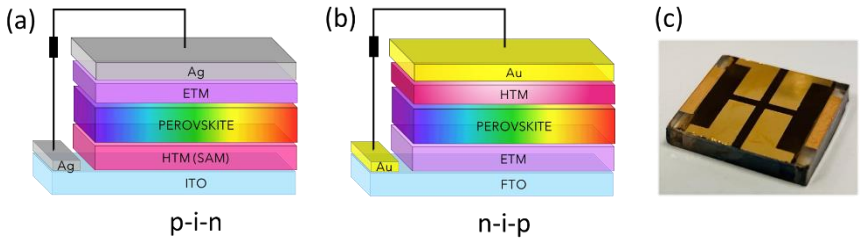

Figure 2.7 Schematic illustration of the main layers in a) p-i-n and b) n-i-p perovskite solar cells, and c) a picture of a complete PSCs device taken from the metal-electrode side.

This section will outline the fabrication procedure for both type of PSCs, including the steps applicable to both configurations as follows:

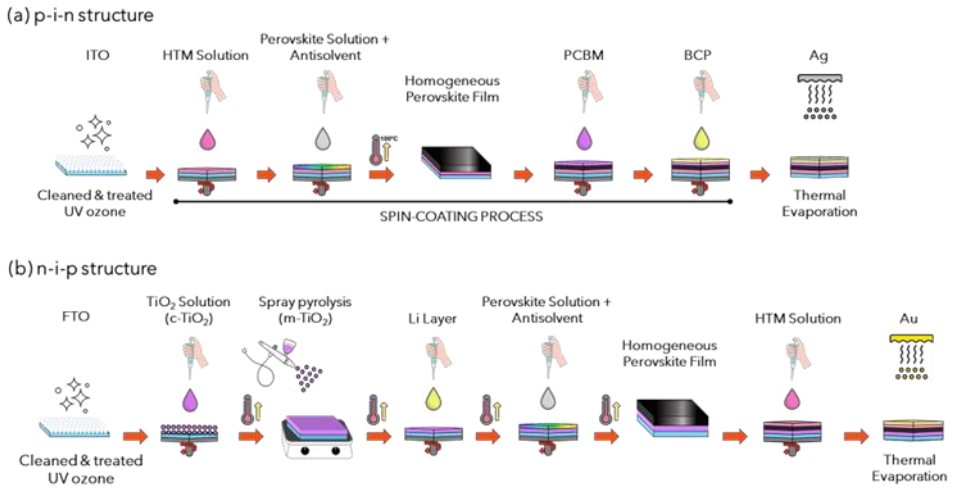

Scheme 2.1 Device fabrication steps for PSC in (a) p-i-n and (b) n-i-p structures.

2.3.1 Inverted Solar Cell Fabrication

Cleaning the patterned glass substrate

ITO substrates were sequentially cleaned with EtOH and IPA within an ultrasonic bath for 15 minutes each, followed by drying with N_2 gas. Subsequently, the substrates were treated with ultraviolet ozone (UV-O_3) for 30 minutes. Once cleaned and treated the substrates were transferred in an N_2 globe box. This basic step demands careful execution to prevent detrimental consequences in the final operation.

Self-Assembled Molecules deposition

A SAM solution optimized to 0.1 M in THF anhydrous was filtered and deposited by one step on the treated ITO by spin-coating. The spin coating sequence was at 3000 rpm for 30 s with an acceleration of 2000 rpm·s^{-1} without thermal annealing. For the dip-coating method, ITO substrates were immersed into SAM solution at 50 ºC for 6-10 h in a sealed container. Afterward, they were washed with THF anhydrous three times at 3000 rpm for 30 s under nitrogen atmosphere.

Triple-cation perovskite deposition

The triple-cation perovskite (onwards labelled as CsFAMA) solution reported by Li W. et al.,[79] was prepared from a precursor solution of $(Cs_{0.05}(FA_{0.85}MA_{0.15})_{0.95}Pb(I_{0.85}Br_{0.15})_3$ by mixing formamidinium iodide (FAI, 1.1 M), PbI_2 (1.15 M), methylammonium bromide (MABr, 0.2 M) and $PbBr_2$ (0.2 M) and dissolved in anhydrous DMF:DMSO (4:1 volume ratio). Finally, once the mixture was dissolved, 42 µL of CsI solution (1.5 in DMSO) was added to obtain the CsFAMA perovskite solution. Next, 80 µL of CsFAMA solution was dropped onto SAM layer by spin-coating with two step deposition method; step 1) at 2000 rpm for 10 s with an acceleration of 2000 rpm s^{-1}, and step 2) 4000 rpm for 25s, where 110 µL of chlorobenzene (CBZ) was dispensed onto the spinning substrate in the last 12 s. Following this, samples were transferred to a preheated hot plate at 100 ºC for 40 minutes.

Deposition of the ETM

After CsFAMA deposition, a 70 µL of a $PC_{61}BM$ solution (20 mg in 1 mL of CBZ) was dynamically deposited at 1000 rpm for 1 min with an acceleration of 1000 rpm·s^{-1}. After that, a solution of BCP (1 mg·mL^{-1})

dissolved in IPA, was spin-coated at 4000 rpm for 30 s with an acceleration of 2000 rpm s^{-1}. We also used an electron selective layer with an optimised thickness, C_{60} (23 nm) and BCP (9 nm). C_{60} and BCP were thermally evaporated at low pressure (1×10^{-6} bar) on top of the perovskite layer.

Thermal evaporation of metal electrodes

Finally, 100 nm of a metal (Ag) was evaporated under high vacuum (1×10^{-6} bar) as a counter electrode defining the active area of the devices at 0.09 cm^2.

2.3.2 Regular Solar Cell Fabrication

The PSCs were fabricated with device structure of:

FTO/c-TiO_2/ m-TiO_2)/CsFAMA)/HTM/Au,

where FTO substrates were cleaned and treated by using the same protocol of iPSC. The TiO_2 compact layer (c-TiO_2) was made by spray pyrolysis. The precursor solution was prepared by mixing 0.480 mL acetylacetone, 0.780 mL titanium diisopropoxide bis(acetylacetonate) (75% in 2-propanol) and 10.8 mL of ethanol. The whole solution was filtered and sprayed, maintaining a distance of ~20 cm with an inclination of the spray-gun at 45°. The substrates were thermally annealed at 450 °C for 30 minutes. Once the substrates cooled down, 40 µL of mesoporous TiO_2 (m-TiO_2) solution was deposited on top by spin coating at 4000 rpm, 2000 rpm·s^{-1} for 10 s. After that, samples were thermally annealed at 100 °C for 5 minutes and 450 °C for 30 minutes to obtain a m-TiO_2 layer around 150-200 nm. The m-TiO_2 solution was prepared using 0.3 g of commercial TiO_2 paste in 2 mL of absolute ethanol. Additionally, the lithium surface treatment was deposited onto m-TiO_2, using 40 µL of LiTFSI solution (10 mg per 1 mL of acetonitrile) by spin coating at 3000 rpm, 1000 rpm·s for 10 s followed by sintering at 450 °C for 30 min. After cooling down to ~100 °C, the substrates were immediately transferred to an N_2 glovebox for depositing the perovskite layer. The CsFAMA was deposited following the same procedures as iPSCs. For regular PSC, a 50 µL of HTM solution (28.4 mM) in chlorobenzene (CBZ) was deposited on top of the perovskite layer dynamically by spin coating at 4000 rpm for 30 s with an acceleration of 2000 rpm s^{-1}. After the substrates had been cooled down for a few min, a 50 µL of HTM solution (28.4 mM) in CBZ was deposited on top of the

perovskite layer dynamically by spin coating at 4000 rpm for 30 s with an acceleration of 2000 rpm s^{-1}. For doped HTMs we used bis(trifluoromethylsulfonyl)imide lithium salt (LiTFSI), tris(2-(1H-pyrazol-1-yl)-4-tert-butylpyridine)cobalt(III)-tris(bis(trifluoro-methylsulfonyl)imide) (FK209) and 4-tert-Butylpyridine (tBP). The molar ratio of the solution is 1, 0.5, 0.03 and 3.3 for HTM, LiTFSI, FK209 and tBP, respectively. It worth noting that these conditions are well optimised for spiro-OMeTAD. Finally, 100 nm of Au were deposited by thermal evaporation under high vacuum.

CHAPTER 3

Design and Synthesis of New Carbazole-based Organic Molecules as Hole Transporting Materials

Carbazole-based small molecules have shown promising application as hole-transporting materials in perovskite-based devices due to their easy synthesis and astounding performance. Inspired on that, in this chapter we focused our efforts on the design and synthesis of new carbazole-based HTMs with three different groups. They were synthesized through a straightforward route featuring diverse electron donor groups, permitting a deep exploration of the impact of HTM molecular structure on perovskite-based devices performance.

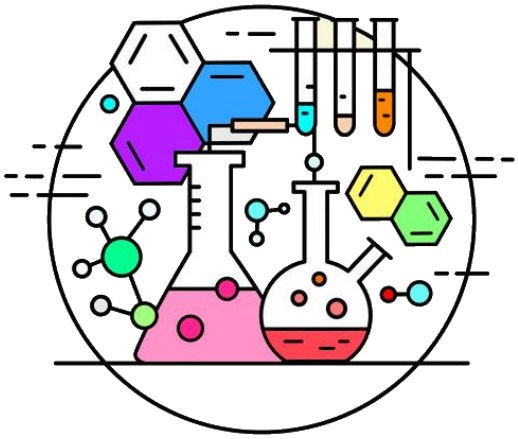

3.1 INTRODUCTION

This chapter is focused on the synthesis of novel HTMs utilising simple synthetic methods and techniques. Their chemical structures were verified by ^{1}H and ^{13}C NMR spectroscopy and mass spectrometry. These groups of molecules are presented in three separated and consecutive projects. The obtained results after their implementation on perovskite-based devices are reported in chronological order in Chapter 4, 5 and 6.

The first group of SMs consists of three self-assembling molecules (SAM 1, SAM 2 and SAM 3). The aim is to explore how the variation on the linker and functional groups impact their chemical, optical, electrical properties, and, as well as the effects on the interfaces of both ITO/SAM and SAM/perovskite. To do so, the chemical design involved the addition of a phenyl ring either as a linker or as side-arm into the carbazole-core, for higher degree of π-conjugation,[66,70] which was further functionalized with a carboxylic acid (COOH-) as the anchoring group (see Scheme 3.1). In contrast, di-*p*-tolylamine was introduced as a side-arm to fine-tune the electron-donor properties and energy-level alignment.[82] In addition, both functional groups were selected to induce a partially negative charge centred on the COOH- group, facilitating the transport of the charges. These new SMs involved a simple reaction procedure, as illustrated in Scheme 3.1 by adapting bromination, C-N coupling, Buchwald-Hartwig amination and Suzuki coupling reactions. Subsequently, their performance in iPSCs was assessed, as detailed in Chapter 4.

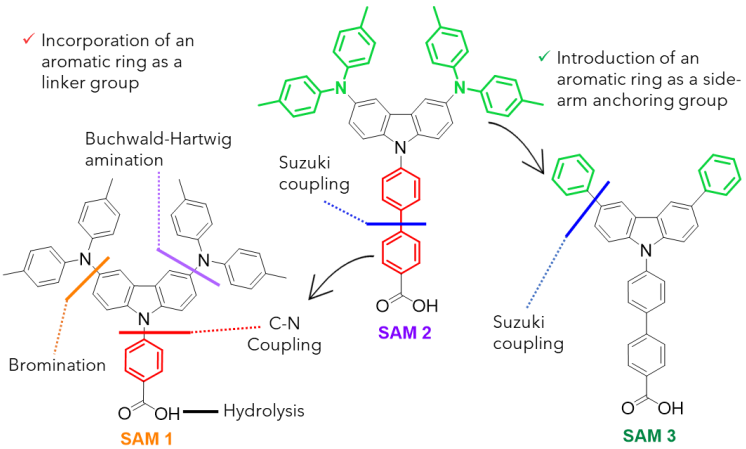

Scheme 3.1 Molecular engineering and final structure of carbazole-based SAMs

The inspiration for the second group of SMs stems from the observed advantages and impact of the SAM/perovskite interfaces demonstrated with SAM 2 and SAM 3. To further explore these results, we designed four new SAMs (molecular structures are shown in Figure 3.1). They are derivatives of the compound ethyl 4'-(*9H*-carbazol-9-yl)-[1,1'-biphenyl]-4-carboxylate (11).

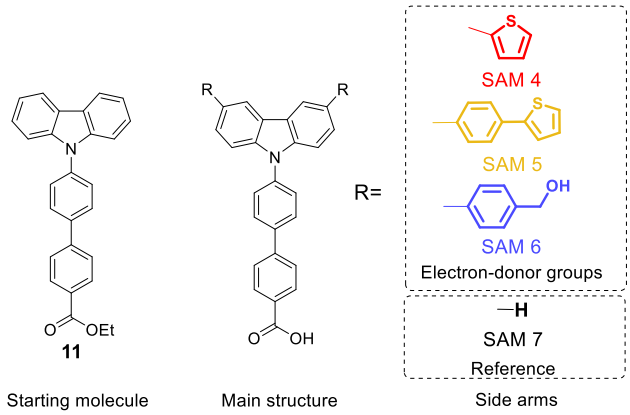

Figure 3.1 Molecular structure of the carbazole-based SAMs functionalized with electron-donor groups and without side arm using as reference SAM 7.

We tuned their chemical and physical properties, particularly, their electron-donor nature by introducing electron-rich groups into the carbazole core in a simple two or three steps. We have selected the thiophene unit because of the efficient passivation effect from S–Pb interaction and efficient hole-extraction.[83,84] Based on our previous results, the units 2-phenylthiophene and phenylmethanol were chosen to enhance the degree of π-conjugation by introducing a phenyl ring. Additionally, we have considered the incorporation of S (same as the previous unit) or O atoms to form stronger coordination with the Pb of the perovskite material, which could lead to enhanced surface properties.[85,86] The compounds were synthesised and tested in iPSCs (refer to Chapter 5 for detailed information). In particular, SAM 7 has been developed as a reference to gain a better understanding of the introduction of the aforementioned units to the carbazole core and to examine the role of the carbazole unit as a functional group in these kinds of compounds.

Finally, the third group of SMs is formed by four HTMs for regular PSC. Although there is a wide variety of SM used as HTMs in PSCs, challenges persist in understanding the relationship between the chemical structure of HTMs and perovskite, among other factors.[21,28,30]

In contrast to the previously prepared SAMs, these molecules are randomly distributed on surface, lacking of any anchoring group in their molecular structure. This work shares the same objective as the previous ones, aiming to further elucidate the phenomena at the interfaces concerning the molecular structure of HTMs, particularly focusing on the HTM/perovskite interface. The results about their performance are shown in Chapter 6. For the design of these HTMs, we decided to create a linear D–π–D molecular structures mimicking the spiro-model. They feature one or two thiophene central cores (π) linked to different carbazole-based (D) moieties through a facile synthetic route. This is inspired by our previous studies with the aforementioned thiophene-based groups, as well as other work involving these types of electron-donor groups.[70,76] Their molecular structure is presented in Figure 3.2.

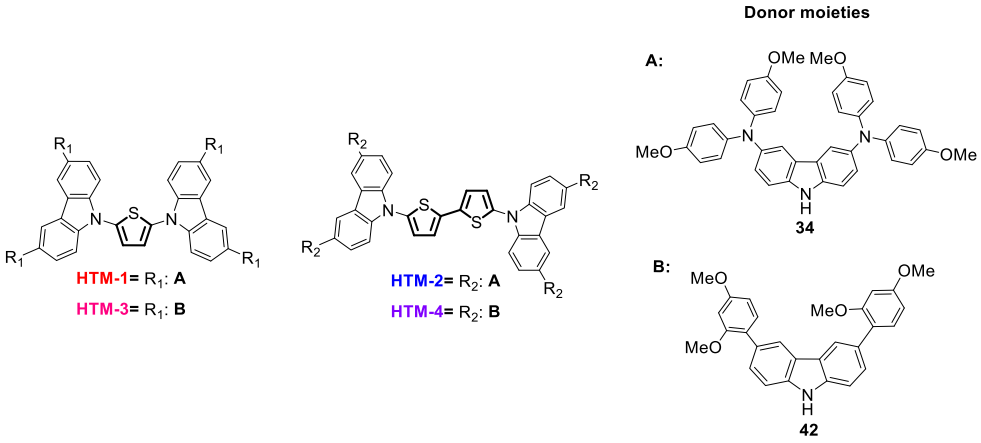

Figure 3.2 Molecular structure of the new thiophene-based HTMs.

The following section provides details on the synthesis and characterization of the aforementioned SMs, and in the subsequent chapters the results obtained for each group applied in PSCs are presented.

3.2 Experimental section of the synthetic methods and procedures

General Methods. Reagents and chemicals were purchased from commercial suppliers and were used as received unless mentioned otherwise. Air-sensitive reactions were carried out under nitrogen or argon atmosphere. All workup and purification procedures were carried out in air using reagent grade solvents. ^{1}H and ^{13}C NMR spectra were performed at 298 K using deuterated solvents as internal standards: chloroform-d 7.26 ppm and 77.16 ppm, acetone-d6 at 2.05 ppm and 29.84 ppm, tetrahydrofuran-d8 at 1.72, 3.58 ppm and 25.31, 67.21 ppm, dimethyl sulfoxide-d6 2.50 ppm and 39.51 ppm for ^{1}H and ^{13}C, respectively. Chemical shifts (δ) are reported in ppm and coupling constants (J) in Hz. Data are reported as follows: chemical shift, multiplicity (s: singlet, d: doublet, t: triplet, m: multiplet), coupling constant and integration. High resolution mass spectra (HRMS) were obtained by electrospray ionisation (ESI) and reported as m/z (relative intensity). For more detailed information see **Chapter 2** (Experimental Techniques and Procedures).

3.3 Group 1: Synthesis of SAM 1, SAM 2 and SAM 3

Synthesis of SAM 1

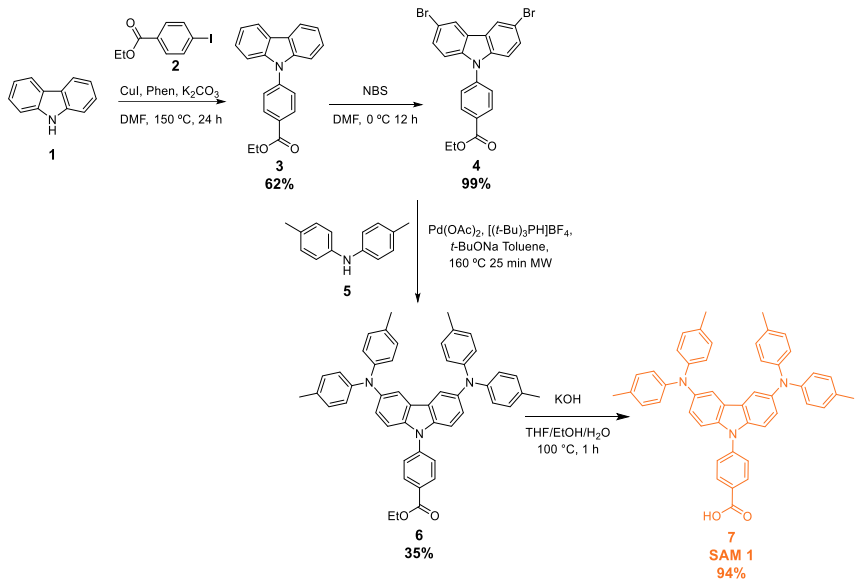

Scheme 3.2 Synthetic pathway for the synthesis of SAM 1

Synthesis of ethyl 4-(9*H*-carbazol-9-yl)benzoate (3)

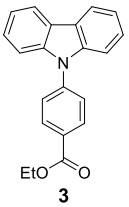

Procedure 1a: A mixture of CuI (160 mg, 0.83 mmol), 1, 10-Phenanthroline (150 mg, 0.83 mmol), K_2CO_3 (1.73 g, 12.55 mmol) and ethyl 4-iodobenzoate (**2**) (2.50 g, 9.21 mmol), was dissolved in dry DMF (15 mL) and the mixture was stirred for one hour under argon atmosphere at room temperature. Then, 9*H*-carbazole (**1**) (1.40 mg, 8.37 mmol) was added and the reaction mixture was stirred at 150 °C for 24 h. After cooling down, was filtered through celite to remove insoluble solids and solvents were evaporated under reduced pressure. The resulting solid was purified by silica gel column chromatography to obtain **3** as a white powder (1.61 g, 62%). **^{1}H NMR** (500 MHz, $CDCl_3$) $\delta_{(ppm)}$: 8.30 (2H, d, *J* = 8.5 Hz, 3 and 16-H_{Ar}), 8.15 (2H, d, *J* = 7.8 Hz, 7 and 14-H_{Ar}), 7.69 (2H, d, *J* = 8.5 Hz, 4 and

15-H_{Ar}), 7.51 – 7.41 (4H, m, 8, 10, 11 and 13-H_{Ar}), 7.32 (2H, t, *J* = 7.4 Hz, 9 and 12-H_{Ar}), 4.46 (2H q, *J* = 7.2 Hz, O*C*H_2), 1.46 (3H t, *J* = 7.1 Hz, -*C*H_3). **^{13}C NMR** (126 MHz, $CDCl_3$) $\delta_{(ppm)}$: 165.9, 141.9, 140.3, 131.3, 129.1(2C), 126.4(2C), 126.2(2C), 123.8(2C), 120.5(2C), 120.5(2C), 120.5(2C), 109.8(2C), 61.3, 14.4.

Synthesis of ethyl 4-(3,6-dibromo-9*H*-carbazol-9-yl)benzoate (4)

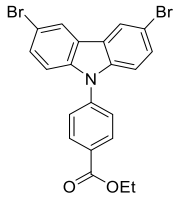

4

Procedure 1b: A solution of NBS (1.73 g, 9.75 mmol) in 7 mL DMF was dropwised into a solution of **3** (0.7 g, 2.32 mmol) in DMF (20 mL). The mixture was shielded from light and stirred for 12 h at 0 °C. The reaction mixture was quenched with crushed ice and the formed precipitated was filtered, washed with water and dried, giving **4** as a white solid (1.06 g, >99%). **^{1}H NMR** (500 MHz, $CDCl_3$) $\delta_{(ppm)}$: 8.30 (2H, d, *J* = 8.5 Hz, 3 and 16-H_{Ar}), 8.20 (2H, d, *J* = 2.0 Hz, 10 and 11-H_{Ar}), 7.60 (2H, d, *J* = 8.6 Hz, 4 and 15-H_{Ar}), 7.52 (2H, dd, *J* = 8.7, 1.9 Hz, 7 and 14-H_{Ar}), 7.30 (2H, d, *J* = 8.7 Hz, 8 and 13-H_{Ar}), 4.46 (2H, q, *J* = 7.1 Hz, O*C*H_2), 1.45 (3H, t, *J* = 7.1 Hz, *C*H_3). **^{13}C NMR** (126 MHz, $CDCl_3$) $\delta_{(ppm)}$: 166.0, 142.0, 140.3 (2C), 131.4, 129.1 (2C), 126.4 (2C), 126.2 (2C), 123.8 (2C), 120.5 (2C), 120.5 (2C), 109.8 (2C), 61.3, 14.4.

Synthesis of Ethyl 4-(3,6-bis(di-p-tolylamino)-9*H*-carbazol-9-yl)benzoate (6)

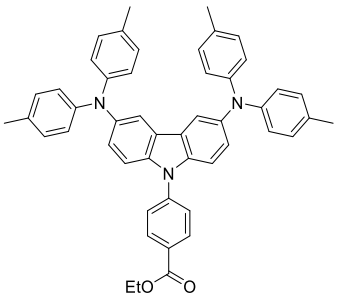

6

Procedure 1c: In the presence of argon atmosphere, **5** (0.35 g, 1.77 mmol), $Pd(OAc)_2$ (38 mg, 0.164 mmol), [(*t*-Bu)$_3$PH]BF_4 (TTBP) (69 mg,

0.338 mmol) and *t*-BuONa (0.28 g, 3 mmol) were mixed in anhydrous toluene (10mL). After 30 min, **4** was added in one portion and the solution was heated under MW irradiation for 25 min at 160 ºC. The crude was filtered through celite and the solvent was removed under reduced pressure. Finally, the crude product was purified using silica gel column chromatography (HEX:EtOAc, 20:1, v//v) to obtain a pale-yellow solid (0.21 g 35%). **^{1}H NMR** (500 MHz, THF) $\delta_{(ppm)}$: 8.27 (2H, d, *J* = 8.8 Hz, 1 and 26-H_{Ar}), 7.77 – 7.74 (4H, m, 3, 4, 23 and 24-H_{Ar}), 7.40 (1H, s, 13-H_{Ar}), 7.38 (1H, s, 14-H_{Ar}), 7.14 (2H, dd, *J* = 8.8, 2.2 Hz, 2 and 25-H_{Ar}), 6.97 (8H, d, *J* = 8.1 Hz, 5, 8, 9, 12, 15, 18, 19, and 22-H_{Ar}), 6.89 (8H, d, *J* = 8.5 Hz, 6, 7, 10, 11, 16, 17, 20, and 21-H_{Ar}), 4.39 (2H, q, *J* = 7.1 Hz, O*C*H_2), 2.23 (12H, s, -*C*H_3), 1.40 (3H, t, *J* = 7.1 Hz, -*C*H_3). **^{13}C NMR** (101 MHz, THF) $\delta_{(ppm)}$: 166.1, 147.6 (4C), 143.0, 142.9 (2C), 138.6 (2C), 132.2 (8C), 131.8 (4), 130.5, 127.2, 126.5 (2C), 125.8 (2C), 124.0 (2C), 123.8 (8C), 119.0 (2C), 111.6 (2C), 61.8, 20.9 (4C), 14.8.

Synthesis of 4-(3,6-bis(di-p-tolylamino)-9*H*-carbazol-9-yl)benzoic acid (SAM 1)

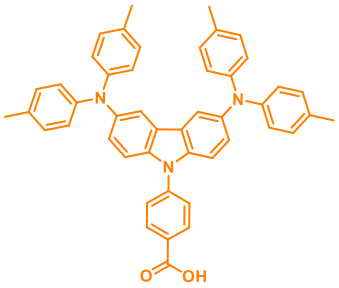

7
SAM 1

Procedure 1d: A solution of compound **6** (0.2 g, 0.289 mmol) in THF (6 mL) was added in one portion to a solution of KOH (48.6 mg, 0.86 mmol) in EtOH:H_2O (1 mL, 1:1, v/v). The mixture was refluxed at 100 ºC for one hour. After cooling it to room temperature, the workup was performed using ethyl acetate (2 x 100 mL). Then, 20 mL of HCl solution (5 M) were added to neutralize the mixture. The combined organic layers were filtered and concentrated under reduced pressure. The final product was obtained via crystallization from hexane as light-green solid (0.184 g, 94%). **SAM 1** was characterized by ^{1}H and ^{13}C NMR spectrometry as well by HRMS. **^{1}H NMR** (400 MHz, Acetone) $\delta_{(ppm)}$: 8.31 (2H, d, *J* = 8.6 Hz, 1 and

26-H_{Ar}), 8.02 (1H, s, -OH), 7.84 (2H, d, *J* = 8.6 Hz, 2 and 25-H_{Ar}), 7.80 (2H, d, *J* = 2.3 Hz, 13 and 14-H_{Ar}), 7.49 (2H, d, *J* = 8.8 Hz, 4 and 23-H_{Ar}), 7.20 (2H, dd, *J* = 8.8, 2.2 Hz, 3 and 24-H_{Ar}), 7.04 (8H, d, *J* = 8.4 Hz, 5, 8, 9, 12, 15, 18, 19, and 22-H_{Ar}), 6.91 (8H, d, *J* = 8.5 Hz, 6, 7, 10, 11, 16, 17, 20, and 21-H_{Ar}), 2.25 (12H, s, -CH_3). **^{13}C NMR** (101 MHz, Acetone) $\delta_{(ppm)}$: 165.7, 146.4 (5C), 141.9 (2C), 137.3 (2C), 131.3 (2C), 131.1 (3C), 129.7 (8C), 126.2 (4C), 125.3 (2C), 124.5 (2C), 122.9 (8C), 117.5 (2C), 110.8 (2C), 19.8 (4C). m/z calculated for $C_{47}H_{39}N_3O_2$ [M^+] exact mass= 677.3042, found MS (MALDI-TOF) = 677.3041.

Synthesis of **SAM 2**

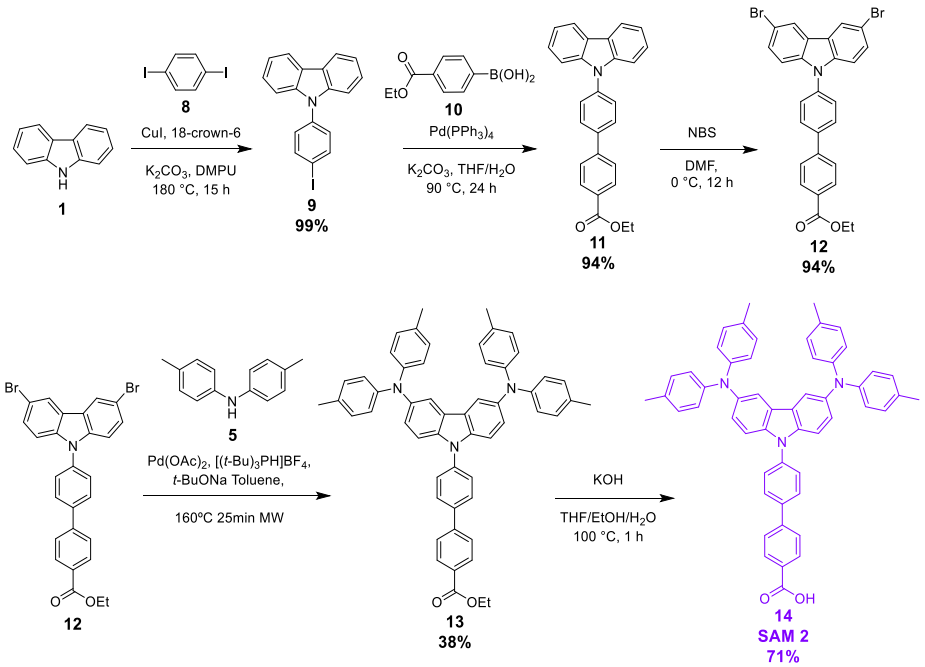

Scheme 2.2 Pathway of **SAM 2**

Synthesis of 9-(4-iodophenyl)-9*H*-carbazole (9)

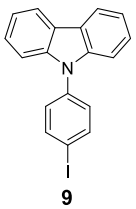

Procedure 2a: To a 50 mL vial charged with a stir bar, CuI (28 mg, 0.14 mmol), 18-crown-6 (13 mg, 0.04mmol), *9H*-carbazole **1** (500 mg, 2.99

mmol) and K_2CO_3 (826 mg, 5.97 mmol) were added and dissolved in 20 mL of DMPU. The mixture was stirred for one hour at room temperature under Ar atmosphere and then, 1,4-diiodobenzene (1.99 g, 5.98 mmol) was added. The mixture was heated at 140 °C for another hour, after that at 180 °C for 12 h. The crude was filtered through celite and the solvent was removed under reduced pressure. The residue was purified by column chromatography using silica gel with HEX:EtOAc (20:1, v/v) as eluent, yielding compound **9** as a light-yellow solid (1.09 g, 99%). **^{1}H NMR** (500 MHz, $CDCl_3$) $\delta_{(ppm)}$: 8.15 (2H d, *J* = 7.7 Hz,6 and 7-H_{Ar}), 7.93 (2H d, *J* = 8.6 Hz, 1 and 2-H_{Ar}), 7.45 – 7.37 (4H, m, 2, 3, 4, and 5-H_{Ar}), 7.37 – 7.28 (4H, m, 8, 9, 10 and 11-H_{Ar}). **^{13}C NMR** (126 MHz, $CDCl_3$) $\delta_{(ppm)}$: 140.7, 139.2 (2C), 137.7, 129.1 (2C), 126.2 (2C), 123.7 (2C), 120.5 (2C), 120.4 (2C), 109.7 (2C), 92.2.

Synthesis of Ethyl 4'-(9*H*-carbazol-9-yl)-[1,1'-biphenyl]-4-carboxylate (11)

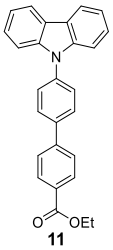

11

Procedure 2b: Compound **9** (0.462 g, 1.25 mmol), K_2CO_3 (0.346 g, 2.5 mmol), $Pd(PPh_3)_4$ (58 mg, 0.005 mmol) and **10** (0.315 g, 1.58 mmol) were dissolved in 9 mL of THF:H_2O (2:1) and stirred at 90 °C for 24 hours. Once the reaction was cooled down to room temperature, was extracted with EtOAc (3 x 50 mL), washed with a saturated brine solution (3 x 15 mL), dried over anhydrous Na_2SO_4 and filtered. The organic mixture was evaporated under reduced pressure and the residue was purified by silica-gel column chromatography using hexane and EtOAc as eluents (20:1, v:v) to obtain a 0.452 g of **11** (94%). **^{1}H NMR** (400 MHz, $CDCl_3$) $\delta_{(ppm)}$: 8.21 – 8.15 (4H, m, 1, 8, 9 and 16-H_{Ar}), 7.86 (2H, d, *J* = 8.6 Hz, 5 and 12-H_{Ar}), 7.77 (2H, d, *J* = 8.6 Hz, 4 and 13-H_{Ar}), 7.68 (2H, d, *J* = 8.6 Hz, 3 and 14-H_{Ar}), 7.51 – 7.41 (4H, m, 6, 7, 10 and 11-H_{Ar}), 7.35 – 7.29 (2H, m, 2 and 15-H_{Ar}), 4.44 (2H, q, *J* = 7.1 Hz, OCH_2), 1.45 (3H, t, *J* = 7.1 Hz, -CH_3). **^{13}C NMR** (101 MHz, $CDCl_3$) $\delta_{(ppm)}$: 166.6, 144.6, 140.9, 139.2 (2C), 137.8, 130.4, 129.8

(2C), 128.8 (2C), 127.5(2C), 127.1 (2C), 126.2 (2C), 123.7 (2C), 120.5 (2C), 120.3 (2C), 109.9 (2C), 61.2, 14.5.

Ethyl 4'-(3,6-dibromo-9*H*-carbazol-9-yl)-[1,1'-biphenyl]-4-carboxylate (12)

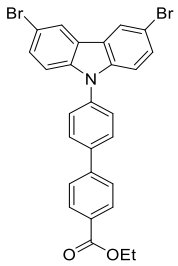

12

Following the procedure **1b**, compound **12** was obtained as a white solid (0.72 g, 94%). **^{1}H NMR** (500 MHz, $CDCl_3$) $\delta_{(ppm)}$: 8.22 – 8.15 (4H, m, 1, 7, 8 and 14-H_{Ar}), 7.85 (2H, d, *J* = 7.7 Hz, 3 and 12-H_{Ar}), 7.74 (2H, d, *J* = 8.7 Hz, 2 and 13-H_{Ar}), 7.59 (2H, d, *J* = 8.7 Hz, 5 and 10-H_{Ar}), 7.52 (2H, dd, *J* = 8.7, 1.9 Hz, 4 and 11-H_{Ar}), 7.31 (2H, d, *J* = 8.7 Hz, 6 and 9-H_{Ar}), 4.43 (2H, q, *J* = 7.1 Hz, -O*C*H_2), 1.44 (3H, t, *J* = 7.1 Hz, -*C*H_3). **^{13}C NMR** (126 MHz, $CDCl_3$) $\delta_{(ppm)}$: 173.2, 166.5, 144.3, 139.9 (2C), 136.8, 130.4, 129.9 (2C), 129.6 (2C), 129.1 (2C), 127.4 (2C), 127.1 (2C), 124.2 (2C), 123.4 (2C), 113.4 (2C), 111.6 (2C), 61.3, 14.5.

Ethyl 4'-(3,6-bis(di-p-tolylamino)-9*H*-carbazol-9-yl)-[1,1'-biphenyl]-4-carboxylate (13)

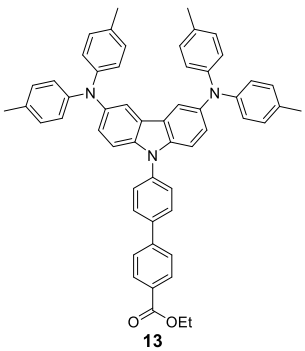

13

Following the procedure **1c**, the product **13** was obtained and purified by column chromatography (HEX:EtOAc, 15:1) to obtain 67 mg (38%) of pale green solid. However, due to its poor solubility, it was not possible to confirm its structure by NMR. Therefore, the next synthetic step

(procedure **1d**) was carried out without further analysis, yielding **SAM 2** and confirming the structure of compound **13**.

4'-(3,6-bis(di-p-tolylamino)-9*H*-carbazol-9-yl)-[1,1'-biphenyl]-4-carboxylic acid (SAM 2)

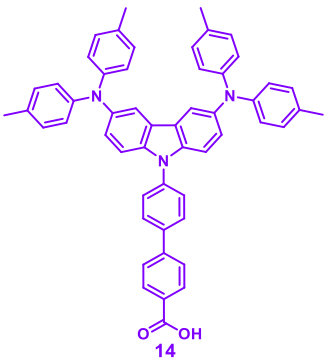

14
SAM 2

SAM 2 was synthesized following the procedure **1d**. A light-green solid (231 mg, 92%) was obtained. **SAM 2** was characterized by ^{1}H and ^{13}C NMR spectrometry as well by HRMS. **^{1}H NMR** (400 MHz, acetone) $\delta_{(ppm)}$: 8.21 – 8.14 (2H, m, 1 and 30-H_{Ar}), 8.07 (2H, d, *J* = 8.7, 2.3 Hz, 5 and 26-H_{Ar}), 7.95 (2H, d, *J* = 8.6 Hz, 16 and 15-H_{Ar}), 7.80 (4H, dd, *J* = 7.1, 1.7 Hz, 4, 5, 26 and 27-H_{Ar}), 7.45 (2H, d, *J* = 2.5 Hz, 6 and 25-H_{Ar}), 7.21 (2H, d, 3.7 Hz, 3 and 28-H_{Ar}), 7.04 (8H, d, *J* = 8.3 Hz, 7, 10, 11, 14, 17, 20, 21 and 24-H_{Ar}), 6.91 (8H, d, *J* = 8.5 Hz, 8, 9, 12, 13, 18, 19, 22 and 23-H_{Ar}), 2.25 (12H, s, -CH_3). **^{13}C NMR** (101 MHz, acetone) $\delta_{(ppm)}$: 147.5 (3C), 142.5, 138.9, 132.0 (4C), 131.4 (2C), 131.1 (2C), 130.7 (8C), 129.8 (4C), 128.2 (2C), 128.0 (4C), 126.4 (2C), 125.3 (2C), 123.9 (8C), 118.7 (2C), 111.8 (4C), 20.8 (4C). m/z calculated for $C_{53}H_{43}N_3O_2$ [M^+] exact mass= 753.3355, found MS (MALDI-TOF) = 753.3331.

Synthesis of SAM 3

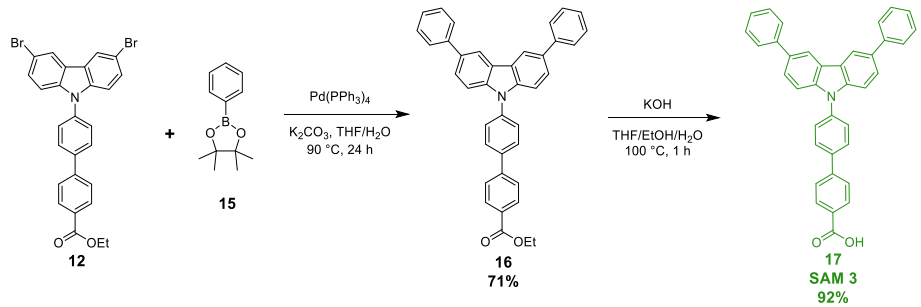

Scheme 3.3 Synthetic route of **SAM 3**

Ethyl 4'-(3,6-diphenyl-9*H*-carbazol-9-yl)-[1,1'-biphenyl]-4-carboxylate (16)

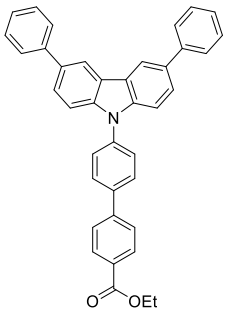

16

Following the procedure **2b,** product **16** was obtained and purified by column chromatography (HEX:EtOAc, 15:1) to give a 0.289 g of **16** (71%). **^{1}H NMR** (500 MHz, $CDCl_3$) $\delta_{(ppm)}$: 8.44 (2H, d, *J* = 1.8 Hz, 1 and 24-H_{Ar}), 8.20 (2H, d, *J* = 8.4 Hz, 12 and 13-H_{Ar}), 7.86 (2H, d, *J* = 8.5 Hz, 5 and 20-H_{Ar}), 7.79 -7.74 (6H, m, 8-10-H_{Ar} and 15-17-H_{Ar}), 7.70 (4H, td, *J* = 5.2, 2.6 Hz, 3, 6, 19 and 22-H_{Ar}), 7.56 – 7.49 (6H, m, 2, 7, 11, 14, 18 and 23-H_{Ar}), 7.38 (2H, t, *J* = 7.4 Hz, 4 and 21-H_{Ar}), 4.46 (2H, q, *J* = 7.1 Hz, -O*C*H_2), 1.47 (3H, t, *J* = 7.1 Hz, -*C*H_3). **^{13}C NMR** (126 MHz, $CDCl_3$) $\delta_{(ppm)}$: 166.6, 144.5, 141.9, 140.7 (2C), 139.2, 137.7, 134.0 (2C), 130.4 (2C), 129.8 (2C), 128.9 (2C), 128.9 (4C), 127.4 (4C), 127.3 (2C), 127.1 (2C), 126.8 (2C), 125.9 (2C), 124.3 (2C), 119.0 (2C), 110.3 (2C), 61.2, 14.3.

4'-(3,6-diphenyl-9*H*-carbazol-9-yl)-[1,1'-biphenyl]-4-carboxylic acid (SAM 3)

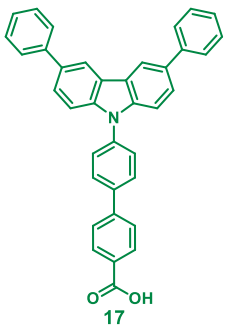

17
SAM 3

SAM 3 was obtained as a light-green solid (0.25 g, 92%), following procedure **1d**. **SAM 3** was characterized by ^{1}H and ^{13}C NMR spectrometry as well by HRMS. **^{1}H NMR** (400 MHz, DMSO) $\delta_{(ppm)}$: 8.76 (2H, d, *J* = 2.0 Hz, 1 and 24-H_{Ar}), 8.08 (4H, m, 5, 6, 19 and 21-H_{Ar}), 7.95 (2H, d, *J* = 8.6 Hz, 12

and 13-H_{Ar}), 7.86 – 7.78 (8H, m, 3, 8-10-H_{Ar} and 15-17, 22-H_{Ar}), 7.58 – 7.48 (6H, m, 2, 7, 11, 14, 18 and 23-H_{Ar}), 7.37 (2H, t, *J* = 7.4 Hz, 4 and 21-H_{Ar}). ^{13}C NMR (101 MHz, DMSO) $\delta_{(ppm)}$: 167.1, 143.3, 140.7, 140.0 (2C), 138.4, 138.1 (2C), 132.7 (4C), 130.1, 129.9 (4C), 128.9 (6C), 128.8 (4), 126.9 (2C), 126.7 (2C), 125.5 (2C), 123.9 (2C), 119.1 (2C). m/z calculated for $C_{37}H_{25}NO_2$ [M^+] exact mass = 515.1885, found MS (MALDI-TOF) = 518.1886.

3.4 Group 2: Synthesis of SAM 4, SAM 5, SAM 6 and SAM 7

Synthesis of SAM 4

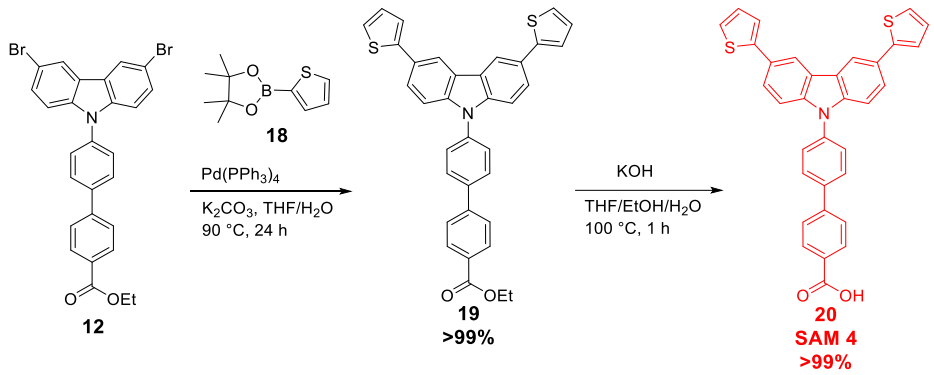

Scheme 3.4 Synthetic route of SAM 4

Ethyl 4'-(3,6-di(thiophen-2-yl)-9*H*-carbazol-9-yl)-[1,1'-biphenyl]-4-carboxylate (19)

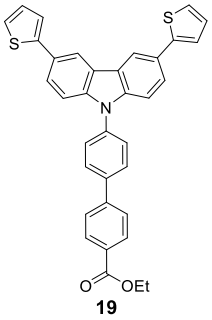

Following the procedure **2b**, compound **19** was obtained and purified by silica gel column chromatography (HEX:THF, 10:1) to afford 0.19 g, (>99%) of light yellow solid. **^{1}H NMR** (400 MHz, $CDCl_3$) $\delta_{(ppm)}$: 8.40 (2H, d, *J* = 1.3 Hz, 10 and 11-H_{Ar}), 8.19 (2H, d, *J* = 8.5 Hz, 1 and 20-H_{Ar}), 7.88 (2H, d, *J* = 8.6 Hz, 5 and 16-H_{Ar}), 7.77 (2H, d, *J* = 8.6 Hz, 6 and 15-H_{Ar}), 7.73 – 7.67 (4H, m, 3, 4, 17 and 18-H_{Ar}), 7.47 (2H, d, *J* = 8.5 Hz, 2 and 19-H_{Ar}), 7.39 (2H, d, *J* = 1.1 Hz, 9 and 14-H_{Ar}), 7.30 (2H, d, *J* = 1.1 Hz, 7 and 12-H_{Ar}), 7.16 – 7.12 (2H, m, 8 and 13-H_{Ar}), 4.44 (2H, q, *J* = 7.1 Hz, OCH_2), 1.44 (3H, t, -CH_3). **^{13}C NMR** (101 MHz, $CDCl_3$) $\delta_{(ppm)}$: 166.6, 145.4 (2C), 144.5, 140.8 (2C), 139.5, 137.4, 130.4 (2C), 129.9, 129.0 (2C), 128.2 (2C), 127.4 (2C), 127.4 (2C), 127.2 (2C), 125.7, 125.1, 124.2 (2C), 124.1 (2C), 122.6 (2C), 118.1 (2C), 110.5 (2C), 61.2, 14.5.

4'-(3,6-di(thiophen-2-yl)-9*H*-carbazol-9-yl)-[1,1'-biphenyl]-4-carboxylic acid (SAM 4)

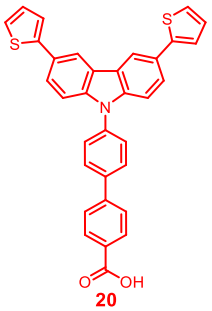

20
SAM 4

Following the procedure **1d**, **SAM 4** was obtained as a light-white solid (0.19 g, >99%). **SAM 4** was characterized by ^{1}H NMR and ^{13}C NMR spectrometry as well by HRMS. **^{1}H NMR** (400 MHz, THF) $\delta_{(ppm)}$: 8.54 (2H, d, *J* = 1.4 Hz), 8.16 (2H, d, *J* = 8.5 Hz), 8.02 (2H, d, *J* = 8.5 Hz), 7.87 (2H, d, *J* = 8.5 Hz), 7.78 – 7.72 (4H, m), 7.50 – 7.44 (4H, m), 7.33 (2H, d, *J* = 1.1 Hz), 7.09 (2H, d, *J* = 3.6 Hz). **^{13}C NMR** (101 MHz, THF) $\delta_{(ppm)}$: 166.4, 145.1 (2C), 144.0, 140.7 (2C), 139.3, 137.3 (2C), 130.2 (2C), 130.2 (2C), 128.7 (2C), 127.7 (2C), 127.4 (2C), 127.1 (2C), 126.7 (2C), 124.6 (2C), 124.0 (2C), 123.7 (2C), 122.2 (2C), 117.6, 110.2. m/z calculated for $C_{33}H_{21}NO_2S_2$ [M^+] exact mass = 527.1014, found MS (MALDI-TOF) = 527.1008.

Synthesis of SAM 5

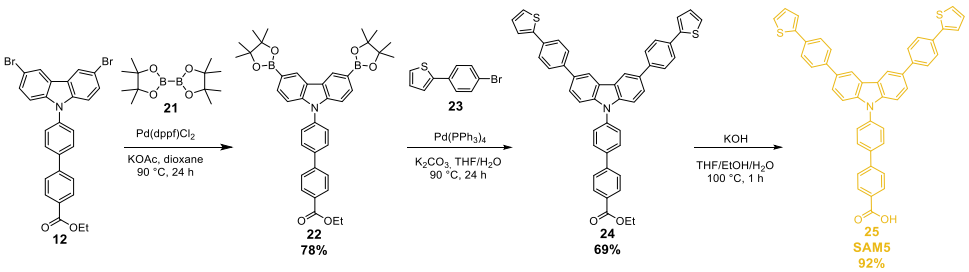

Scheme 3.5 Synthetic route of **SAM 5**

Synthesis of ethyl 4'-(3,6-bis(4,4,5,5-tetramethyl-1,3,2-dioxaborolan-2-yl)-9*H*-carbazol-9-yl)-[1,1'-biphenyl]-4-carboxylate (22)

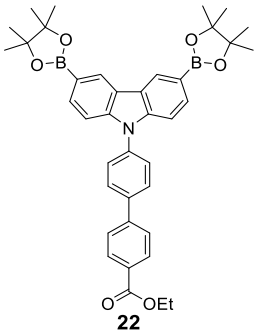

22

Procedure 3a: Compound **12** (1 g, 1.55 mmol) was mixed with bis(pinacolato)diboron **21** (1.18 g, 4.65 mmol), $Pd(dppf)Cl_2$ (169 mg, 15% mmol) and KOAc (0.91 g, 9.3 mmol). The reagents were purged with argon for 30 min. After, 10 mL of dioxane anhydrous were added. The resulting solution was heated to 90 °C for 12 hours under argon atmosphere. The reaction mixture was gradually cooled down to room temperature, filtered through celite and washed with ethyl acetate (3 x 20 mL). The crude product was recovered in a 100 mL round-bottom flask and the solvent was removed by rotary evaporation. The isolated compound was dissolved with Et_2O and recrystallized from cold hexene. The product **22** was obtained as a pale brown solid (0.78 g, 78 %). **^{1}H NMR** (500 MHz, $CDCl_3$) $\delta_{(ppm)}$: 8.74 (2H, s, 7 and 8-H_{Ar}), 8.18 (2H, d, *J* = 8.3 Hz, 1 and 14-H_{Ar}), 7.87 (4H, t, *J* = 7.9 Hz, 4, 5, 10 and 11-H_{Ar}), 7.77 (2H, d, *J* = 8.3 Hz, 3 and 12-H_{Ar}), 7.66 (2H, d, *J* = 8.4 Hz, 2 and 13-H_{Ar}), 7.44 (2H, d, *J* = 8.3 Hz, 6 and 9-H_{Ar}), 4.43 (2H, q, *J* = 7.1 Hz, O*C*H_2), 1.46 – 1.37 (27H, m, -CH_3). **^{13}C NMR** (126 MHz, $CDCl_3$) $\delta_{(ppm)}$: 166.6, 144.6, 143.1, 139.4 (2C), 137.4, 132.5, 130.4 (4C), 129.8 (2C), 128.9 (2C), 128.2 (2C), 127.5 (2C), 127.1 (2C), 123.5 (2C), 109.3 (2C), 83.8 (4C), 61.2, 25.1 (8C), 14.5.

Ethyl 4'-(3,6-bis(4-(thiophen-2-yl)phenyl)-9*H*-carbazol-9-yl)-[1,1'-biphenyl]-4-carboxylate (24)

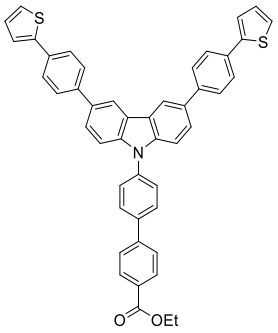

24

Following the procedure **2b**, compound **24** was obtained via crystallization from ethyl acetate (0.153 g, 69%) as a light-white solid. However, due to the poor solubility of **24**, it was not possible to confirm its structure by NMR. Therefore, procedure **1d** was carried out to obtain **SAM 5**, confirming the structure of compound **24**.

4'-(3,6-bis(4-(thiophen-2-yl)phenyl)-9*H*-carbazol-9-yl)-[1,1'-biphenyl]-4-carboxylic acid (SAM 5)

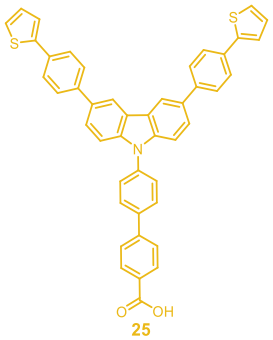

25
SAM 5

Following the procedure **1d**, **SAM 5** was obtained as a light-white solid (0.95 g, 92%). **SAM 5** was characterized by ^{1}H and ^{13}C NMR spectrometry as well by HRMS. **^{1}H NMR** (400 MHz, THF) $\delta_{(ppm)}$: 8.62 (2H, d, *J* = 1.4 Hz), 8.17 (2H, d, *J* = 8.5 Hz), 8.04 (2H, d, *J* = 8.6 Hz), 7.89 (2H, d, *J* = 8.6 Hz), 7.85 – 7.73 (13H, m), 7.57 (2H, d, *J* = 8.5 Hz), 7.44 (2H, d, *J* = 1.1 Hz), 7.37 (2H, d, *J* = 1.1 Hz), 7.11 – 7.07 (2H, m). **^{13}C NMR** (101 MHz, THF) $\delta_{(ppm)}$: 167.6, 145.2 (2C), 141.9 (2C), 141.9, 140.3, 138.7 (2C), 134.1 (2C), 134.0 (2C), 131.4 (2C), 131.3 (2C), 129.8 (2C), 129.0 (2C), 128.4 (2C), 128.3 (4C), 127.8 (2C), 127.1 (4C), 126.3 (2C), 126.1 (2C), 125.6 (2C), 125.6 (2C),

124.0 (2C), 119.6, 111.3. m/z calculated for $C_{45}H_{29}NO_2S_2$ [M^+] exact mass = 679.1640, found MS (MALDI-TOF) = 679.1634.

Synthesis of SAM 6

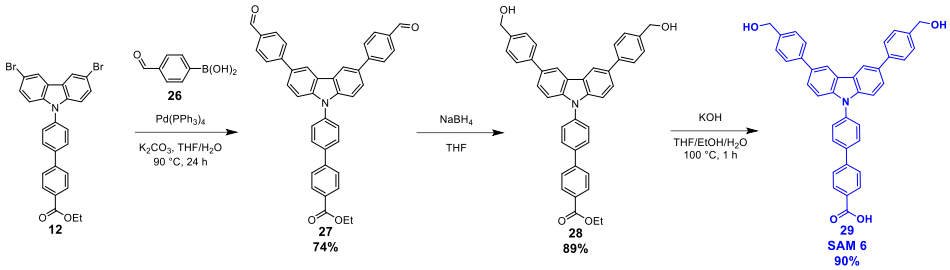

Scheme 3.6 Synthetic route of SAM 6

Ethyl 4'-(3,6-bis(4-formylphenyl)-9*H*-carbazol-9-yl)-[1,1'-biphenyl]-4-carboxylate (27)

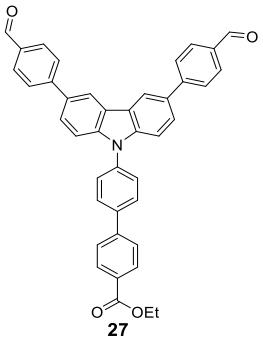

Following the procedure 2b product 27 (0.28 g, 74%) was obtained as a white powder. ^{1}H NMR (500 MHz, DMSO) $\delta_{(ppm)}$: 10.08 (2H, s, 1 and 22-H_{Ar}), 8.95 (2H, s, 11 and 12-H_{Ar}), 8.27 – 7.76 (16H, m), 7.60 (2H, s, -C*H*), 4.36 (2H, s, OCH_2), 1.36 (3H, s, $-CH_3$). ^{13}C NMR (101 MHz, THF) $\delta_{(ppm)}$: 191.8 (2C), 166.5, 148.3, 145.3, 142.6 (2C), 136.5 (2C), 133.4 (2C), 131.1 (4C), 131.0 (4C), 129.9 (4C), 128.4 (2C), 128.3 (4C), 127.9 (2C), 126.9 (2C), 125.5 (2C), 120.5 (2C), 111.5 (2C), 54.8, 14.9.

Ethyl 4'-(3,6-bis(4-(hydroxymethyl)phenyl)-9*H*-carbazol-9-yl)-[1,1'-biphenyl]-4-carboxylate (28)

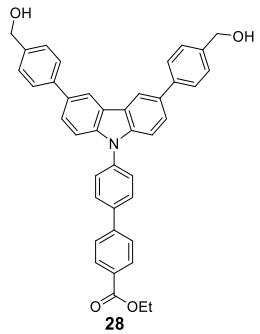

28

Procedure 4a: Compound **27** (0.28g, 0.47 mmol) and 4 equiv. (0.071 g, 1.86 mmol) of sodium borohydride ($NaBH_4$) were dissolved in 10 mL of THF. The mixture was stirred for 19 hours at room temperature. After evaporation of the solvent, the mixture was purified by column chromatography on silica gel (1:1 v/v, HEX:EtOAc) affording a 0.25 g of compound **28** (89% yield). **^{1}H NMR** (400 MHz, Acetone/THF) $\delta_{(ppm)}$: 8.65 (2H, d, *J* = 1.6 Hz, 11 and 12-HAr), 8.18 (2H, d, *J* = 8.2 Hz, 1 and 22-H_{Ar}), 8.09 (2H, d, *J* = 8.4 Hz, 5 and 18-H_{Ar}), 7.96 (2H, d, *J* = 7.0 Hz, 4 and 19-H_{Ar}), 7.84 – 7.76 (8H, m, 7-10 and 13-16-H_{Ar}), 7.58 (2H, d, *J* = 8.5 Hz, 6 and 17-H_{Ar}), 7.49 (4H, d, *J* = 8.1 Hz, 2, 3, 20 and 21-H_{Ar}), 4.69 (4H, d, *J* = 5.7 Hz, -CH_2), 4.41 (2H, q, *J* = 7.1 Hz, OCH_2), 1.42 (3H, t, *J* = 7.1 Hz, -CH_3). **^{13}C NMR** (101 MHz, Acetone/THF) $\delta_{(ppm)}$: 142.3, 141.7, 141.3, 134.8 (2C), 131.2 (4C), 130.0 (2C), 128.4 (2C), 128.2 (4C), 128.1 (8C), 127.8 (8C), 125.6, 119.8, 111.3 (2C), 64.8 (2C), 61.8, 14.9.

4'-(3,6-bis(4-(hydroxymethyl)phenyl)-9*H*-carbazol-9-yl)-[1,1'-biphenyl]-4-carboxylic acid (SAM 6)

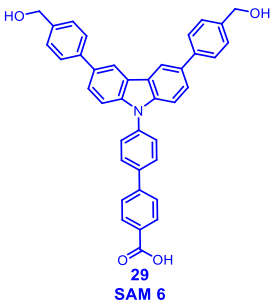

29
SAM 6

Following the procedure **1d**, **SAM 6** was obtained as a white solid (300 mg. 90%). The molecule was characterized by ^{1}H and ^{13}C NMR

spectrometry as well by HRMS. **^{1}H NMR** (400 MHz, THF) $\delta_{(ppm)}$: 8.55 (2H, s, 11 and 12-H_{Ar}), 8.16 (2H, d, *J* = 8.3 Hz, 1 and 22-H_{Ar}), 8.02 (2H, d, *J* = 8.5 Hz, 5 and 18-H_{Ar}), 7.87 (2H, d, *J* = 8.4 Hz, 4 and 19-H_{Ar}), 7.81 – 7.71 (8H, m, 7-10 and 13-16-H_{Ar}), 7.54 (2H, d, *J* = 8.5 Hz, 6 and 17-H_{Ar}), 7.44 (4H, d, *J* = 8.1 Hz, 2, 3, 20 and 21-H_{Ar}), 4.63 (4H, s, -CH_2). **^{13}C NMR** (101 MHz, THF) $\delta_{(ppm)}$: 167.6, 145.2, 142.5 (2C), 141.7 (2C), 141.3 (2C), 140.2, 138.9 (2C), 138.3 (2C), 134.8 (2C), 131.4 (2C), 131.3, 129.8 (2C), 128.2 (2C), 127.8 (4C), 127.8 (2C), 127.7 (4C), 126.4, 126.1, 125.5, 119.6, 111.1, 64.8 (2C). m/z calculated for $C_{39}H_{29}NO_4$ [M^+] exact mass = 575.2097, found MS (MALDI-TOF) = 575.2091.

Synthesis of SAM 7

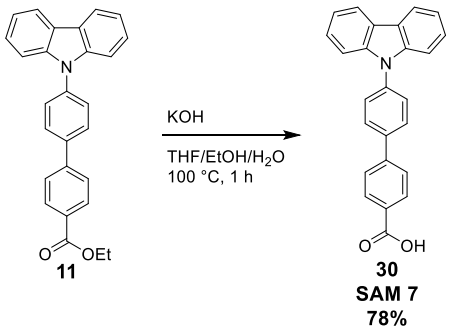

Scheme 3.7 Synthetic route of **SAM 7**

4'-(*9H*-carbazol-9-yl)-[1,1'-biphenyl]-4-carboxylic acid (SAM 7)

Following the procedure **1d,** 100 mg of **SAM 7** was obtained as a pale brown solid (78% yield). **SAM7** was characterized by ^{1}H and ^{13}C NMR spectrometry as well by HRMS. **^{1}H NMR** (400 MHz, THF) $\delta_{(ppm)}$: 8.15 (4H, d, *J* = 8.6 Hz, 1, 5, 12 and 16-H_{Ar}), 8.00 (2H, d, *J* = 8.6 Hz, 4 and 13-H_{Ar}), 7.86 (2H, d, *J* = 8.6 Hz, 2 and 15-H_{Ar}), 7.73 (2H, d, *J* = 8.6 Hz, 8 and 9-H_{Ar}), 7.46 (2H, d, *J* = 8.3 Hz, 3 and 14-H_{Ar}), 7.38 (2H, t, *J* = 7.0 Hz, 6 and 11-H_{Ar}), 7.25 (2H, t, *J* = 6.9 Hz, 7 and 10-H_{Ar}). **^{13}C NMR** (101 MHz, THF) $\delta_{(ppm)}$: 167.5, 145.2, 141.9, 140.2 (C2), 138.9, 131.4, 131.2 (2C), 129.7 (2C), 128.4 (2C), 127.8 (2C), 126.9 (2C), 124.7 (2C), 121.2 (2C), 121.0 (2C), 110.7 (2C). m/z calculated for $C_{25}H_{17}NO_2$ [M^+] exact mass = 363.1259, found MS (MALDI-TOF) = 363.1253.

3.5 Group 3: Synthesis of HTM-1, HTM-2, HTM-3 and HTM-4

The synthesis begins with the production of the conjugated side arms **35** and **42**.

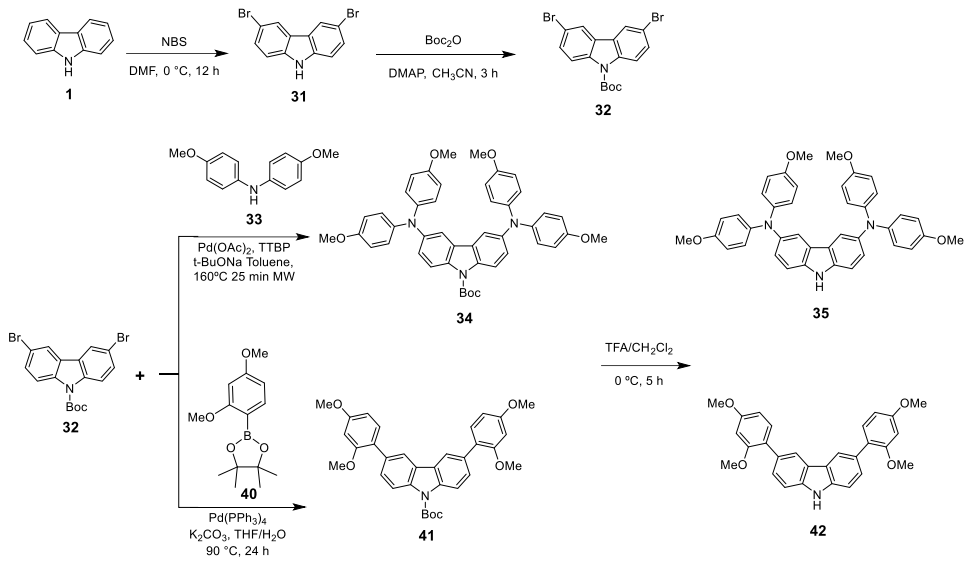

Scheme 3.8 Synthetic route and conditions for the obtention of carbazole-based derivatives **35** and **42**.

3,6-dibromo-9*H*-carbazole (31)

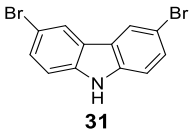

Following the procedure **1b**, compound **31** was obtained as a white solid (1.92 g, ≥99%). **^{1}H NMR** (300 MHz, DMSO) $\delta_{(ppm)}$: 11.59 (1H, s, -NH), 8.43 (2H, d, *J* = 1.9 Hz, 3 and 4-H_{Ar}), 7.57 – 7.50 (2H, m 1 and 6-H_{Ar}), 7.47 (2H, d, *J* = 8.6 Hz, 2 and 5-H_{Ar}). **^{13}C NMR** (101 MHz, $CDCl_3$) $\delta_{(ppm)}$: 137.3 (2C), 127.0 (2C), 121.8 (2C), 121.4 (2C), 111.4 (2C), 109.5 (2C).

Tert-butyl 3,6-dibromo-*9H*-carbazole-9-carboxylate (32)

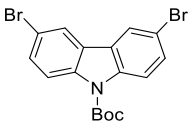

32

Procedure 5a: To a solution of compound **31** (1.94 g, 5.99 mmol) and di-*tert*-butyl decarbonate, **Boc_2O** (2.4 g, 1.9 equiv.) in acetonitrile (25 mL), and 4-(dimethylamino)pyridine, **DMAP** (0.735 g, .6.01 mmol) was added and the reaction was stirring for 4 hours at room temperature. The reaction mixture was extracted with DCM (3x20 mL) and the organic phase was dried over anhydrous magnesium sulphate. The solvent was removed under reduced pressure and the crude product was washed several times with cold methanol. After filtering, the extra solvent was evaporated to afford compound **32** (2.49 g, 98%) as a light yellow solid, without the need of further purification. **^{1}H NMR** (400 MHz, $CDCl_3$) $\delta_{(ppm)}$: 8.15 (2H, d, *J* = 8.8 Hz, 1 and 6-H_{Ar}), 8.03 (2H, s, 3 and 4-H_{Ar}), 7.57 (2H, d, *J* = 6.9 Hz, 2 and 5-H_{Ar}), 1.75 (9H, s, -CH_3). **^{13}C NMR** (101 MHz, $CDCl_3$) $\delta_{(ppm)}$: 150.6, 137.6, 130.7 (2C), 126.4 (2C), 122.7 (2C), 118.0 (2C), 116.5 (2C), 85.0 (2C), 28.5 (3C).

Tert-butyl 3,6-bis(bis(4-methoxyphenyl)amino)-9*H*-carbazole-9-carboxylate (34)

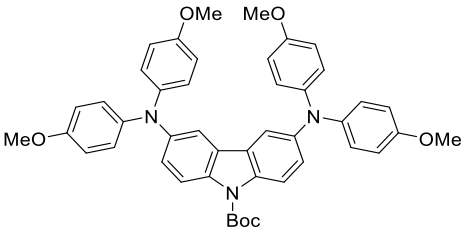

34

Following the procedure **1c**, the crude product **34** was obtained and purified by column chromatography (silica gel, HEX:EtOAc, 9:1). Compound **34** was obtained as a white solid (563 mg, 76%). Since product **34** has a similar retention factor to **33**, this reaction crude was used directly in future reactions without prior purification. **^{1}H NMR** (400 MHz, Acetone) $\delta_{(ppm)}$: 8.14 (2H, d, *J* = 9.0 Hz, 1 and 22-H_{Ar}), 7.43 (2H, s, 11 and 12-H_{Ar}), 7.05 (2H, d, *J* = 11.4 Hz, 2 and 21-H_{Ar}), 6.91 (8H, d, *J* = 9.1 Hz, 3, 6, 7, 10, 13,

16, 17, 20-H_{Ar}), 6.80 (8H, d, *J* = 9.1 Hz, 4, 5, 8, 9, 14, 15, 18, 19-H_{Ar}), 3.73 (12H, s, -O*CH*$_3$), 1.72 (9H, s, -*CH*$_3$). **^{13}C NMR** (101 MHz, Acetone) $\delta_{(ppm)}$: 156.4 (4C), 151.5, 145.7 (2C), 142.6 (4C), 134.9, 127.3 (2C), 126.3 (8C), 123.8 (2C), 117.8 (2C), 115.5 (8C), 114.3 (2C), 84.4 (2C), 55.7 (4C), 28.4 (3C).

N^3,*N*^{3},*N*^{6},*N*^{6}-tetrakis(4-methoxyphenyl)-9*H*-carbazole-3,6-diamine (35)

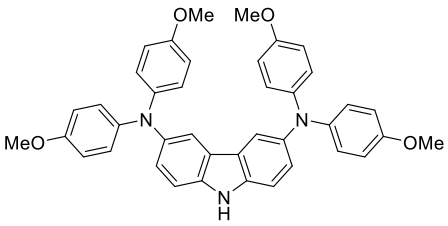

35

Procedure 5b: To a dry round bottom flask equipped with a stirrer bar, compound **34** (0.50 g, 0.69 mmol) was dissolved in 15 mL of TFA:DCM (30% v/v). The reaction was stirred for 5 h at 0 ºC. Next, the solvent was evaporated, the residue was extracted with dichloromethane (DCM) (3X20 mL) and neutralized by adding sodium bicarbonate. The organic phase was dried over anhydrous magnesium sulphate and filtered. The solvent was removed under reduced pressure and the crude product was purified by column chromatography (silica gel, HEX:EtOAc, 6:1). Compound **35** was obtained as a white solid (0.194 g, 45%). NMR data were in good agreement with those reported in the literature.[76] **^{1}H NMR** (500 MHz, Acetone) $\delta_{(ppm)}$: 10.20 (1H, s, -NH), 7.63 (2H, s, 11 and 12-H_{Ar}), 7.42 (2H, d, *J* = 8.6 Hz, 1 and 22-H_A), 7.11 (2H, d, *J* = 8.6, 2.2 Hz 2 and 21-H_{Ar}), 6.93 (8H, d, *J* = 8.0 Hz, 3, 6, 7, 10, 13, 16, 17, 20-H_{Ar}), 6.80 (8H, d, *J* = 7.7 Hz, 4, 5, 8, 9, 14, 15, 18, 19-H_{Ar}), 3.74 (12H, d, *J* = 1.4 Hz, -O*CH*$_3$). **^{13}C NMR** (126 MHz, Acetone) $\delta_{(ppm)}$: 155.8 (4C), 143.6 (4C), 141.7 (2C), 125.8 (2C), 125.7 (8C), 125.1, 124.5, 116.0, 115.9 (8C), 115.3, 114.7, 113.2, 112.6, 112.0, 57.4, 56.2, 55.7, 55.1.

Tert-butyl 3,6-bis(2,4-dimethoxyphenyl)-9*H*-carbazole-9-carboxylate (41)

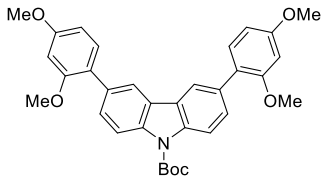

41

Following the procedure **2b**, crude compound **41** was obtained and purified by silica gel column chromatography (HEX:EtOAc, 6:1) to afford 0.289 g, (76%) of white solid. Since, compound **41**, has a retention factor similar to its side arm **40**, the reaction crude was used directly in future reactions without prior purification. **^{1}H NMR** (400 MHz, $CDCl_3$) $\delta_{(ppm)}$ = 8.30 (2H, d, *J* = 8.6 Hz, 1 and 12-H_{Ar}), 8.09 (2H, d, *J* = 1.8 Hz, 6 and 7-H_{Ar}), 7.61 (2H, d, *J* = 8.7, 1.9 Hz, 2 and 11-H_{Ar}), 7.35 (2H, d, *J* = 8.7 Hz, 5 and 10-H_{Ar}), 6.62 (4H, d, *J* = 6.2, 2.3 Hz, 3, 4, 8 and 9-H_{Ar}), 3.88 (6H, s, -O*CH*$_3$), 3.82 (6H, s, -O*CH*$_3$), 1.78 (9H, s, -*CH*$_3$). **^{13}C NMR** (101 MHz, $CDCl_3$) $\delta_{(ppm)}$: 160.4 (2C), 157.7 (2C), 151.3, 137.8, 133.4 (2C), 131.6 (2C), 128.8 (2C), 126.1 (2C), 123.9 (2C), 120.5 (2C), 115.8 (2C), 104.8 (2C), 99.3 (2C), 83.9 (2C), 55.8 (2C), 55.6 (2C), 28.6 (3C).

3,6-bis(2,4-dimethoxyphenyl)-9*H*-carbazole (42)[70,76]

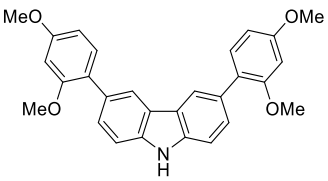

42

Following the procedure **5b**, crude compound **42** was obtained and purified by silica gel column chromatography (HEX:EtOAc, 6:1) to afford 0.226 g, (81%) of white solid. **^{1}H NMR** (400 MHz, $CDCl_3$) $\delta_{(ppm)}$: 8.17 (2H, d, *J* = 1.7 Hz, 1 and 12-H_{Ar}), 8.04 (1H, s, -NH), 7.56 (2H, d, *J* = 1.7 Hz, 2 and 11-H_{Ar}), 7.43 (2H, d, *J* = 0.7 Hz, 6 and 7-H_{Ar}), 7.37 – 7.33 (2H, m, 5 and 10-H_{Ar}), 6.64 – 6.59 (4H, m, 3, 4, 8 and 9-H_{Ar}), 3.88 (6H, s, -O*CH*$_3$), 3.82 (6H, s, -O*CH*$_3$). **^{13}C NMR** (101 MHz, $CDCl_3$) $\delta_{(ppm)}$: 160.0 (2C), 157.7 (2C), 138.9 (2C), 131.7 (2C), 129.9 (2C), 127.8 (2C), 124.7 (2C), 123.8 (2C), 121.3 (2C), 110.1 (2C), 104.8 (2C), 99.3 (2C), 55.8 (2C), 55.6 (2C).

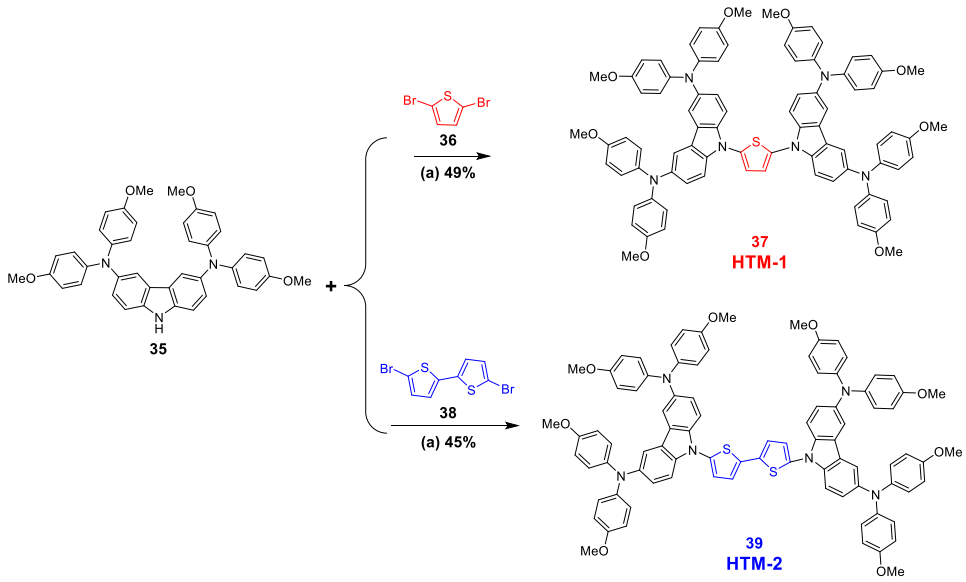

Scheme 3.9 Synthesis of carbazole-based HTM-1 and HTM-2 and conditions: a) $Pd_2(dba)_2$, $[(t\text{-}Bu)_3PH]BF_4$ (TTBP), *t*-BuONa, 110 °C, Toluene, 24 h.

9,9'-([2,2'-bithiophene]-5,5'-diyl)bis(N3,N3,N6,N6-tetrakis(4-methoxyphenyl)-9*H*-carbazole-3,6-diamine) (HTM-1)

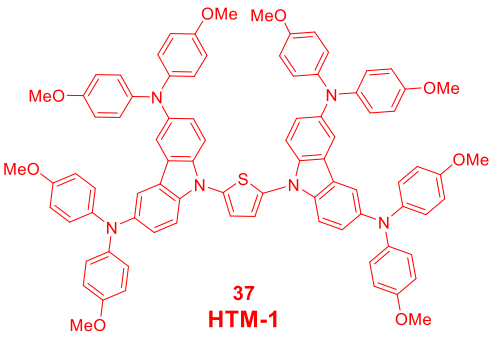

Procedure 6a: In a glass reactor vessel, compound **35** (200 mg, 0.32 mmol), $Pd_2(dba)_2$ (58.6 mg, 0.06 mmol), TTBP (34.82 mg, 0.12 mmol) and *t*-BuONa (76.88 mg, 0.8 mmol) were dissolved in anhydrous toluene (30 mL). The reaction mixture was degassed for 30 minutes with argon. Finally, **36** (38.7 mg, 0.16 mmol) was added and the mixture was heated to reflux under an argon atmosphere for 24 h. The crude was filtered through celite and the solvent was removed under reduced pressure. The residue was extracted with EtOAc (3 x 20 mL) and washed with brine (3 x 20 mL). The organic phase was dried over anhydrous magnesium sulphate and

filtered. The crude product was purified by column chromatography with HEX:EtOAc (silica gel, 8:3, v/v). **HTM-1** was obtained as a light yellow solid (104 mg, 49%), which was characterized by ^{1}H and ^{13}C NMR spectrometry as well by HRMS. **^{1}H NMR** (500 MHz, Acetone) $\delta_{(ppm)}$: 7.65 (4H, d, *J* = 2.2 Hz, 11 and 12-H_{Ar}), 7.55 (4H, d, *J* = 8.8 Hz, 1 and 22-H_A), 7.46 (2H, s, 23 and 24-*CH*-), 7.17 (4H, d, *J* = 8.8, 2.2 Hz, 2 and 21-H_{Ar}), 6.98 – 6.93 (16H, m, 3, 6, 7, 10, 13, 16, 17, 20-H_{Ar}), 6.84 – 6.79 (16H, m, 4, 5, 8, 9, 14, 15, 18, 19-H_{Ar}), 3.74 (24H, s, -O*CH*$_3$). **^{13}C NMR** (101 MHz, Acetone) $\delta_{(ppm)}$: 165.2 (2C), 160.6 (2C), 155.2 (8C), 143.1 (4C), 142.3 (4C), 138.2 (4C), 136.2 (4C), 124.8 (16C), 124.3 (4C), 124.0 (4C), 115.5 (4C), 114.6 (16C), 111.0 (4C), 54.8 (8C). MS-ESI (m/z): [M^+] calculated for $C_{84}H_{70}N_6O_8S$ 1322.5, found MS (MALDI-TOF) = 1322.4979.

9,9'-([2,2'-bithiophene]-5,5'-diyl)bis(N3,N3,N6,N6-tetrakis(4-methoxyphenyl)-9*H*-carbazole-3,6-diamine) (HTM-2)

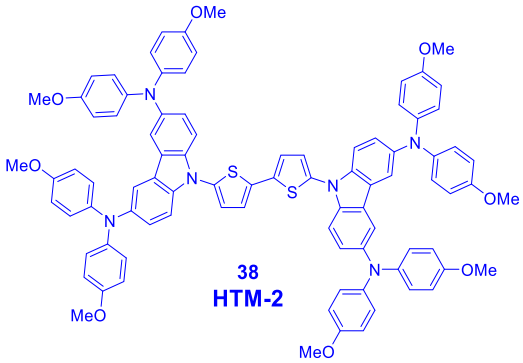

HTM-2 was obtained following the procedure **6a** as a light orange solid (195 mg, 45%). **HTM-2** was characterized by ^{1}H and ^{13}C NMR spectrometry as well by HRMS. **^{1}H NMR** (500 MHz, DMSO) $\delta_{(ppm)}$: 7.66 (4H, d, *J* = 2.2 Hz, 1 and 22-H_A), 7.46 (6H, d, *J* = 8.8 Hz, 11-12-H_{Ar} and 23-*CH*-), 7.35 (2H, d, *J* = 4.0 Hz, 24-*CH*-), 7.15 (4H, d, *J* = 2.2 Hz, 2 and 21-H_{Ar}), 6.94 (16H, d, *J* = 9.0 Hz, 3, 6, 7, 10, 13, 16, 17, 20-H_{Ar}), 6.85 (16H, d, *J* = 9.0 Hz, 4, 5, 8, 9, 14, 15, 18, 19-H_{Ar}), 3.74 (24H, s, O*CH*$_3$). **^{13}C NMR** (126 MHz, DMSO) $\delta_{(ppm)}$: 154.4 (8C), 142.1 (4C), 141.5 (8C), 140.4 (2C), 137.6 (4C), 136.8 (2C), 133.8 (4C), 125.4 (2C), 124.0 (16C), 123.5 (4C), 123.1 (2C), 115.5 (4C), 114.6 (16C), 110.7 (4C), 55.0 (8C). MS-ESI (m/z): [M^+] calculated for $C_{88}H_{72}N_6O_8S_2$ 1404.49, found MS (MALDI-TOF) = 1404.4841.

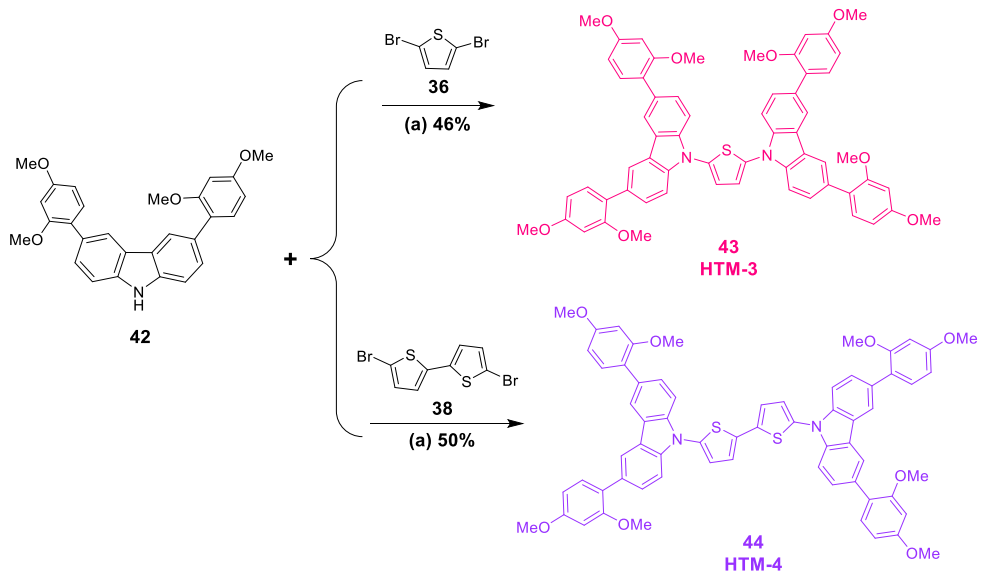

Scheme 3.10 Synthesis of carbazole-based **HTM-3** and **HTM-4** and conditions: a) $Pd_2(dba)_2$, [(*t*-Bu)$_3$PH]BF_4 (TTBP), *t*-BuONa, 110 ºC, Toluene, 24 h.

2,5-bis(3,6-bis(2,4-dimethoxyphenyl)-9*H*-carbazol-9-yl)thiophene (HTM-3)

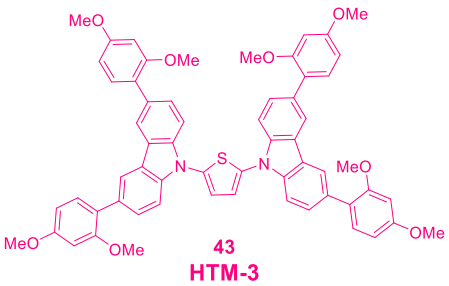

HTM-3 was obtained following the procedure **6a** as a yellow solid (140 mg, 46%). **HTM-3** was characterized by ^{1}H and ^{13}C NMR spectrometry as well by HRMS. **^{1}H NMR** (400 MHz, Acetone) $\delta_{(ppm)}$: 8.31 (4H, d, *J* = 6.9 Hz, 6 and 7-H_{Ar}), 7.72 (2H, d, *J* = 8.5 Hz, 13 and 14-*CH*-), 7.69 – 7.63 (4H, m, 1 and 12-H_{Ar}), 7.63 – 7.56 (4H, m, 2 and 11-H_{Ar}), 7.40 – 7.36 (4H, m, 5 and 10-H_{Ar}), 6.72 – 6.64 (8H, m, 3, 4, 8 and 9-H_{Ar}), 3.86 (24H, d, *J* = 10.2 Hz).

^{13}C NMR (101 MHz, Acetone) $\delta_{(ppm)}$: 160.4 (4C), 157.7 (4C), 140.9 (4C), 133.1 (4C), 133.1 (4C), 131.9 (4C), 131.4 (4C), 123.7 (2C), 109.5 (4C), 105.1 (4C), 98.9 (4C), 55.1 (4C), 54.8 (4C). m/z calculated for $C_{60}H_{50}N_2O_8S$ [M^+] exact mass = 958.3288, found MS (MALDI-TOF) = 958.3251.

5,5'-bis(3,6-bis(2,4-dimethoxyphenyl)-9*H*-carbazol-9-yl)-2,2'-bithiophene (43, HTM-4)

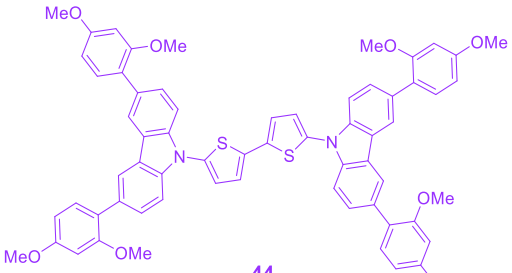

44
HTM-4

HTM-4 was obtained following the procedure **6a** as a light orange solid (195 mg, 50%). **HTM-4** was characterized by ^{1}H and ^{13}C NMR spectrometry as well by HRMS. **^{1}H NMR** ($CDCl_3$, 500 MHz) $\delta_{(ppm)}$: 8.21 (4H, s, 6 and 7-H_{Ar}), 7.64 – 7.58 (8H, m, 2, 5, 10 and 11-H_{Ar}), 7.37 (4H, d, *J* = 8.7 Hz, 1 and 12-H_{Ar}), 7.30 (2H, d, *J* = 3.9 Hz, 14-*CH*-), 7.19 (2H, d, *J* = 3.8 Hz, 13-*CH*-), 6.64 – 6.61 (8H, m, 3, 4, 8 and 9-H_{Ar}), 3.88 (12H, s, -OCH_3), 3.83 (12H, s, -OCH_3).

^{13}C NMR (126 MHz, $CDCl_3$) $\delta_{(ppm)}$: 160.2 (4C), 157.7 (4C), 141.1 (2C), 138.3 (4C), 131.7 (2C), 131.4 (4C), 128.3 (4C), 125.4 (4C), 124.4 (4C), 124.0 (4C), 122.8 (4C), 121.3 (4C), 109.9 (4C), 104.9 (4C), 99.3 (4C), 55.8 (4C), 55.6 (4C). m/z calculated for $C_{64}H_{52}N_2O_8S_2$ [M^+] exact mass = 1040.3165, found MS (MALDI-TOF) = 1040.3164

CHAPTER 4

INFLUENCE OF THE CARBAZOLE MOIETY IN SELF-ASSEMBLING MOLECULES AS SELECTIVE CONTACTS IN PEROVSKITE SOLAR CELLS: INTERFACIAL CHARGE TRANSFER KINETICS AND SOLAR-TO-ENERGY EFFICIENCY EFFECTS

In this first work, three new self-assembled molecules (SAMs) have been designed and synthesised as hole transport materials (HTMs) for their application in inverted perovskite solar cells (iPSCs). These compounds were obtained using relatively simple and versatile synthetic procedures with high yields. They are based on carbazole-core and incorporate modified electron-donor groups, which have been selected for their efficient charge transfer capabilities. The SAMs were employed to investigate interactions at both the ITO/SAM and SAM/perovskite interfaces, providing insights into the relationship between the SAM molecular structure and the performance of perovskite-based devices. The champion cells exhibited efficiencies between 17.5% and 18.9%.

The work of this chapter has been published: *D. A. González et al. Nanoscale Adv* **2023**, *5, 6542–6547. DOI:10.1039/d3na00811h*[72]

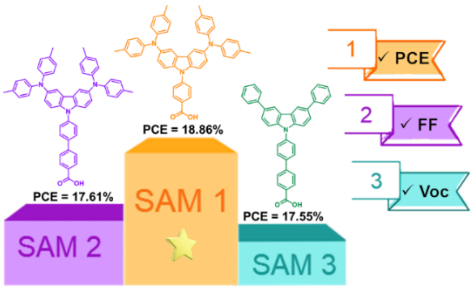

4.1 Introduction

Over the last decade, the hole transporting material (HTM) play a crucial role in achieving high performance and stability in perovskite-based devices.[15,28] However, the widely used HTMs involve complex synthesis and doping process, impacting their cost-effectiveness, long-term stability, and overall performance in the device.[28,39,87] In 2018, a new family of HTM, known as self-assembled molecules (SAMs) have emerged as a novel approach for fabricating efficient inverted perovskite solar cells (iPSCs).[42] Specially, the synthesis and design of SAMs offer numerous advantages, including low-cost, reproducibility, stability and the ability of easily tune their optoelectronic properties. This, sharply contrasts with the widely used Poly[bis(4-phenyl) (2,4,6-trimethylphenyl)amine] (PTAA) polymer, making SAMs as HTM a highly promising candidate for large-scale production.[66,67]

One of the most attractive features of SAMs is their ability for each molecule to chemically bond to the desired surface via its anchoring group, resulting in the formation of a uniform monolayer with defined packing facilitated by the linker group. This arrangement allows the terminal group to determine both surface properties and coverage. Through simple chemical structure modifications of these three components comprising a SAM (anchoring group, linker group and terminal or functional group), it is possible to tackle the actual challenges including passivation of defects, proper alignment of the energy levels, stability, efficient charge transport and increase overall performance of enhancement of PSCs.

Moreover, in just 5 years, SAM-based p-i-n structure have achieved efficiencies of over 25%, making them comparable to their n-i-p structure counterparts and demonstrating that SAMs represent an optimal strategy for high-performance devices.[6,8,88]

Considering the aforementioned advantages, three new SAMs have been designed in this work using a synthetical strategy, employing carbazole-derivative functional groups linked to a phenyl or biphenyl units, with a carboxylic acid (-COOH). Three new molecules labeled **SAM1**, **SAM2** and **SAM3**, as well the commercial molecule EADR03[70], which our lab synthesised and utilised as a reference in this work, are shown in **Figure**

4.1. It is noteworthy that, as an alternative approach within this study, the synthesis of the new compounds and EADR03 were optimized, resulting in high yields (see Scheme 4.1).

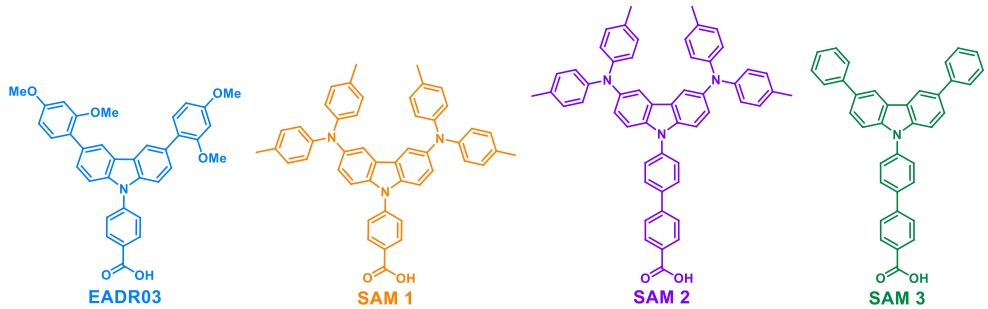

Figure 4.1 Molecular structure of EADR03 and the three new SAM molecules used as hole selective contacts in iPSCs.

Finally, to gain a deeper understanding of the interfacial processes between the three new molecules and their adjacent layers (perovskite and ITO), iPSCs were fabricated, providing additional insight on the impact of the different molecular structures on device performance.

4.2 Results and Discussion

Design and Synthesis

The general synthesis scheme for the preparation of SAM1, SAM2 and SAM3 is depicted in Scheme 4.1. The synthesis begins with the construction of the linker group containing a -COOH on the carbazole core by C-N and Suzuki coupling reactions. Then, the reaction is followed by a bromination reaction using NBS for further Buchwald-Hartwig amination or Suzuki coupling reactions. Finally, a reduction was carried out to obtain the desire compounds. Chapter 2 provides synthetic methods and procedures and Chapter 3 includes a general scheme of the synthesis of the three SAMs,the measurements to determine their structures using ^{1}H and ^{13}C NMR spectroscopy, as well by High-Resolution Mass Spectra (HRMS), the thermal and optoelectronic characterization, and their use as HTM in iPSCs

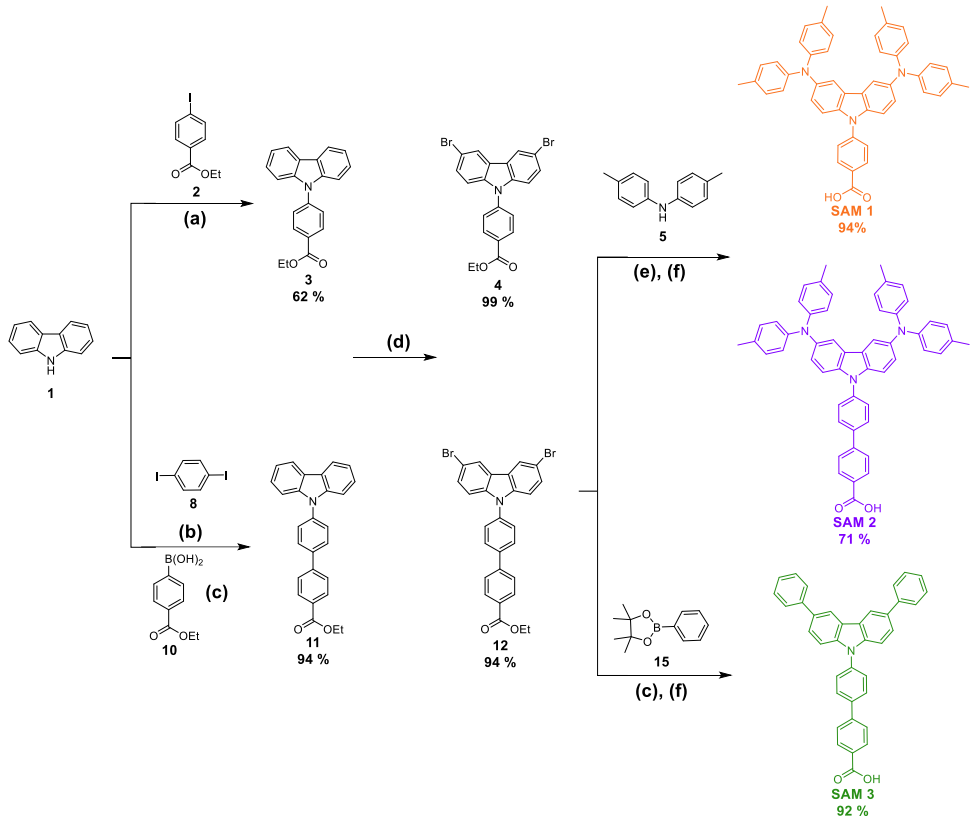

Figure 4.2 Synthetic route for carbazole-based SAMs.(**a**) CuI, Phen, K_2CO_3, DFM, 150 °C, 24 h; (**b**) CuI, 18-crown-6, K_2CO_3, DMPU, 180 °C, 15 h; (**c**) $Pd(PPh_3)_4$ K_2CO_3, THF/H_2O, 90 °C, 24 h; (**d**) NBS/DFM, 0 °C, 12 h; (**e**) $Pd(OAc)_2$, $[(t\text{-}Bu)_3PH]BF_4$ (TTBP), *t*-BuONa, Toluene 160 °C, 25 min MW; (**f**) KOH, THF/EtOH/H_2O, 100 °C, 1 h.

Thermal, Optical and Photophysical Properties

The initial step involved calculating the molecular geometry in its most stable conformation. From this optimized molecular geometry, the electrostatic potentials (ESP) were derived and depicted, ranging from red (indicating positive regions) to blue (indicating negative regions), with green representing neutral EPS. **Figure 4.3** depicts the molecular electrostatic potentials (MEP) from **SAM 1**, **SAM 2** and **SAM 3**. Here, it is evident that the three molecules exhibit a comparable EPS, characterized by partial neutrality across the entirety of the molecule. However, notable deviations are observed at the anchoring group, where the oxygen exhibits a negative (δ^-) electron density, while the -OH moiety of the carboxylic acid (anchoring group) demonstrates a positive (δ^+) electron density. A persistent dipole moment (δ^-/δ^+) of SAM/ITO surface is

expected after SAM binding to ITO.[21] However, the molecules with two phenyl linker groups, SAM 2 and SAM 3, shows an increase in the negative (δ^-) EPS within the functional group. This is attributed to the presence of an extra electron-rich phenyl unit in the linker group. Besides inducing steric effects, this extra phenyl unit induces the delocalisation of π-electrons, resulting in a higher electron density.[69,89] Hence, it becomes evident that in such compounds, the electron density is more influenced by the size of the linker group rather than the side arm.

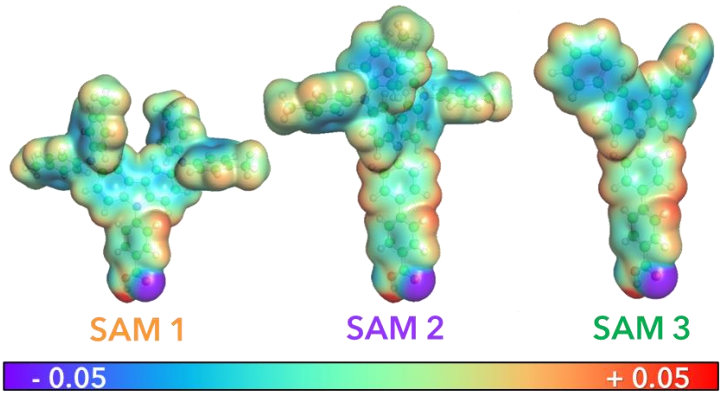

Figure 4.3 The electrostatic surface potentials of SAMs

Thermogravimetric analysis (TGA) was employed to investigate the thermal behaviour of SAM 1, SAM 2 and SAM 3, as illustrated in Figure 4.4a. Notably, both SAM 2 and SAM 3 demonstrate nearly identical decomposition temperatures (T_{dec}, with a weight loss of 5%) of approximately 270 °C, while T_{dec} of SAM 1 is 246 °C, suggesting enhanced thermal stability in compounds featuring a biphenyl linker group. Nevertheless, it is noteworthy that the T_{dec} of all SAMs surpasses the annealing temperature used in device fabrication, making them suitable for their application in iPSC. Furthermore, to gain insight into their optical properties, ultraviolet-visible (UV-vis) absorption and steady-state fluorescence emission (PL) spectroscopy were performed on the synthetised SAMs in solution (10^{-5} M in dichloromethane, DCM). The data derived from these measurements are displayed in Figure 4.4b and summarised in Table 4.1. Comparing the absorption spectra of SAM 1 and SAM 2, an additional peak emerged around 357 nm for SAM 1, together with reduced emission. This phenomenon could be ascribed to an enhanced conjugation facilitated by the presence of only one phenyl

linker group. Additionally, the optical band gap was determined from the intersection of the normalised UV-vis and PL spectra (λ_{onset}), ranging from 2.99 nm to 3.36 nm.

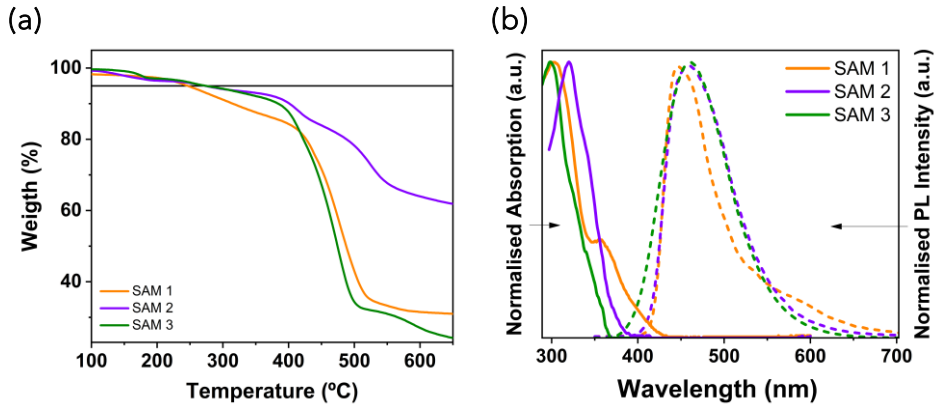

Figure 4.4 (a) TGA of SAM molecules at a scan rate of 10 °C/min under N_2 atmosphere. **(b)** UV-vis absorption and emission spectra of conjugated SAMs in DCM solution.

Table 4.1 Thermal and optical properties of SAMs.

	T_{dec} (°C)[(a)]	λ_{abs}(nm)	λ_{onset} (nm)	E_g [(b)]	E_{HOMO} (eV)[(c)]	E_{LUMO} (eV)[(d)]
SAM 1	246	299	414	2.99	-5.4	-1.82
SAM 2	273	304	393	3.13	-5.0	-1.58
SAM 3	274	320	369	3.36	-5.6	-1.42

[(a)] The decomposition temperature was determined from TGA (5 % weight loss) and the experiment was carried out under N_2 atmosphere, scan rate of 10 °C/min. [(b)] The optical band gap (E_g) was calculated using the formula $E_g = 1240/\lambda_{onset}$, ($\lambda_{onset}$ estimated from the intersection point of the normalized absorbance and PL spectra).

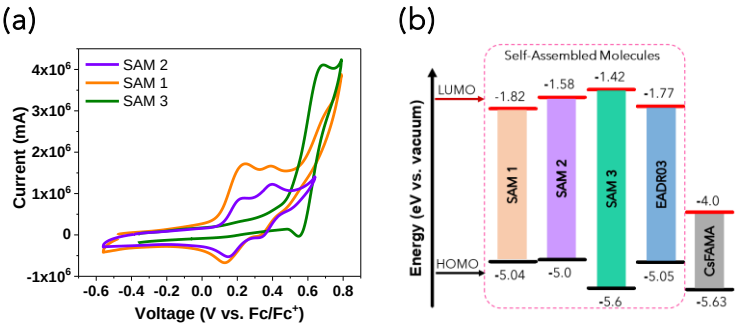

Figure 4.5 a) Cyclic voltammetry results of conjugated SAMs in the supporting electrolyte ($TBAPF_6$ in DCM), measured using ferrocene (Fc/Fc+) as an internal reference and (**b**) the energy levels of the SAMs, EADR03[70] and perovskite.[76]

To calculate the relative energy levels of the new compounds, cyclic voltammetry (CV) was performed to obtain the Highest Molecular Orbital

(HOMO), while the Lowest Unoccupied Molecular Orbital (LUMO) was estimated from the optical band gap. The summarised values of HOMO and LUMO energy levels are presented in Table 4.1. The HOMO energy values of SAM 1 (-5.04 eV) and SAM 2 (-5.0 eV) are very similar, primarly attributed to the di *p*-tolylamine terminal groups, exhibiting two reversible oxidation waves (Figure 4.5a). In contrast, SAM 3 presents only one reversible oxidation wave, assigned to the carbazole-core and phenyl terminal groups, resulting in a deeper HOMO value of -5.6 eV versus vacuum, respectively. These HOMO levels of all the SAMs align closely with the energy levels of the triple cation perovskite ($Cs_{0.05}(FA_{0.85}MA_{0.15})_{0.95}Pb(I_{0.85}Br_{0.15})_3$ onwards labeled as CsFAMA). Moreover, the estimated LUMO values of SAMs, ranging from -1.4 to -1.8 eV, should effectively block the electron transfer from CsFAMA to SAM. Additionally, as can be seen in Figure 4b, the energy levels of the new SAMs closely resemble those ofEADR03.

SAM's Influence on the ITO Surface and the Perovskite Interface

It is well-established that SAMs change the properties of ITO surfaces prior the deposition, consequently impacting the quality of the perovskite film.[75] To investigate both the ITO/SAM and SAM/perovskite films, contact angle measurements and field emission scanning electron microscopy (FESEM) were performed. The contact angles of SAM 1 (60°), SAM 2 (70°) and SAM 3 (66°) were found to be higher than that of the ITO (55°), indicating that SAMs bond to the ITO surface by altering its hydrophobicity (see top images in Figure 4.6). In Figure 4.6, (middle images) the homogeneous deposition of the perovskite solution on SAM layers is evident. The data from the grain size distribution extracted from FESEM images is summarised in Table 4.2. Notably, ITO/SAM 1 and ITO/SAM 2, which have the same functional group, exhibit a slight decrease in grain size distribution, while ITO/SAM 3 demonstrates a grain size distribution similar to bare ITO.

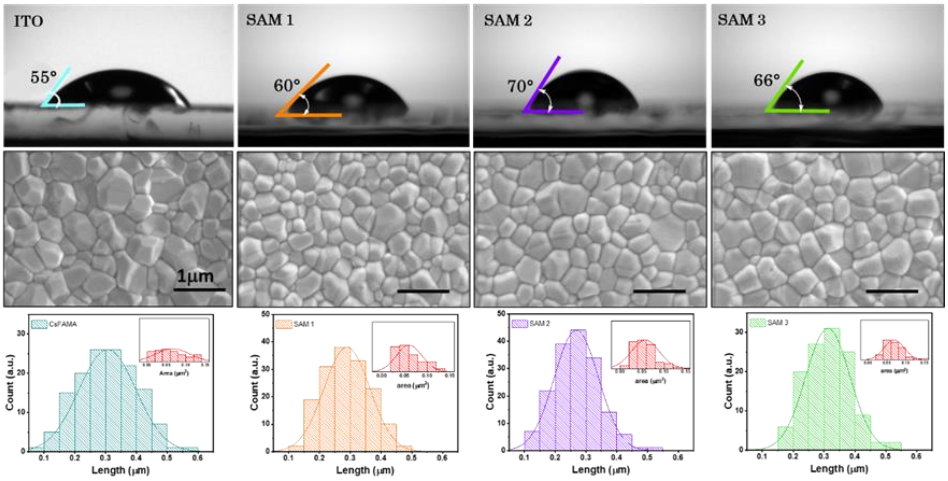

Figure 4.6 Contact angle measurements of ITO/SAMs surfaces and ITO surface after UV-O_3 treatment.(top), FESEM top view of perovskite films deposited on **(a)** ITO, **(b)** ITO/**SAM1**, **(c)** ITO/**SAM2** and, **(d)** ITO/**SAM3** (middle), and their gran size distribution (bottom). All scale the bars are 1 μm.

Table 4.2 Average grain size in perovskite films determined from FESEM images.

	Mean	
Sample	Length (nm)	Area (nm^2)
ITO/SAM 1/CsFAMA	289	61
ITO/SAM 2/CsFAMA	269	57
ITO/SAM 3/CsFAMA	312	69
ITO/CsFAMA	306	66

Furthermore, X-ray photoelectron spectroscopy (XPS) was carried out to confirm the atomic bonds of SAMs on ITO surface (**Figure 4.7** and **Table 4.3**). The C1s spectra were decomposed into three peaks at 285, 286 and 289 eV assigned to C–C or C–H, C–O and COOCH bonds, respectively (see **Figure 4.7a**). The O1 spectra shows similar peaks corresponding to In-O bonds around 531 eV for all the SAMs, wheras for bare ITO, the peak was observedat 532 eV (**Figure 4.7b**). Finally, in **Figure 4.7c**, the N1 spectra confirmed the successful anchoring of SAMs on the ITO surface, as all SAMs presented a consistent peak at 400 eV assigned to C-N bond, which was not observed on bare ITO.

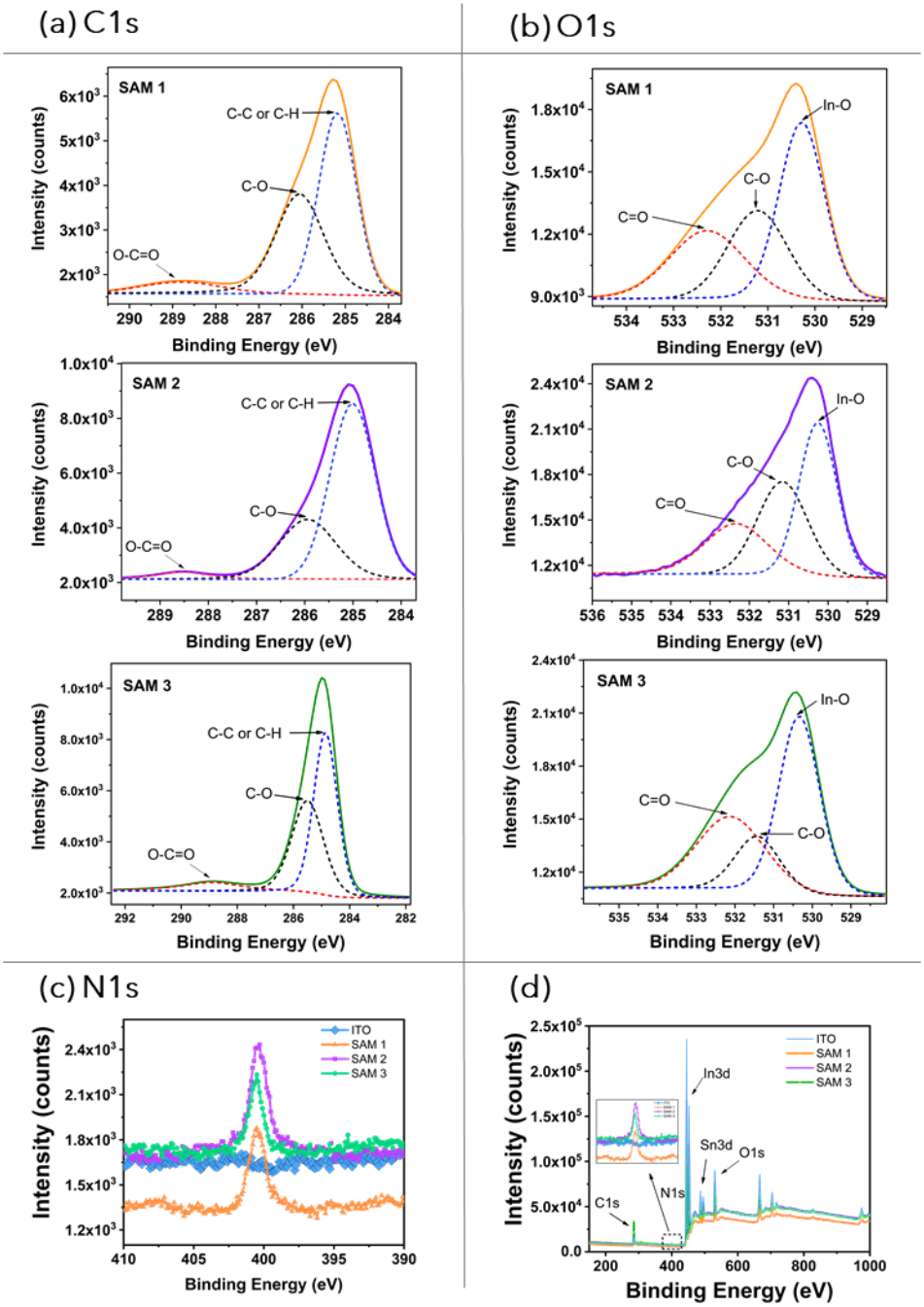

Figure 4.7 High-resolution XPS surface spectra of (a) C1s, (b) O1s, (c) N1s and (d) survey spectrum for bare ITO and the SAMs used in this study.

Table 4.3 The functional groups and their related binding energies extracted from XPS spectra of SAM1, SAM2 and SAM3.

	C1s (eV)		O1s (eV)		N1s (eV)
Samples	C-C/C-H	O=C-O	O_2^-	C=O	C-N
ITO/SAM 1	286.1	288.8	531.2	532.3	400.5
ITO/SAM 2	285.9	288.5	531.1	532.4	400.3
ITO/SAM 3	285.5	288.9	531.5	532.1	400.5
ITO	286.3	289.0	532.1	536.5	-

Photoluminescence Properties

To investigate the effect of the new compounds on interface processes, in particular, on hole transfer at the perovskite/SAM interface, and to confirm the role of SAMs as hole acceptor/transporter materials, steady-state photoluminescence (PL) and time-resolved photoluminescence (TrPL) analyses were performed (see **Figure 4.8**). Perovskite films were prepared on bare ITO, on the new SAMs, and on EADR03 for comparison (see **Chapter 2**, for detailed information). The results demonstrate a considerable PL quenching in all SAM/perovskite films compared to the bare perovskite (**Figure 4.8a**). This reduction confirms the injection of holes from the valence band of the CsFAMA layer to the HOMO of the SAM, as was observed in earlier studies.[66,79,90] Interestingly, the PL spectrum of perovskite films based on **SAM 1** and **SAM 2** exhibited stronger PL emission than those based on **SAM 3**. This observation suggests that the inclusion of the phenyl unit in carbazole-core enhances hole transfer more effectively, even in comparison to the reference molecule.

The TRPL decay curves depicted in **Figure 4.8b** were fitted using a double-exponential model, attributed to charge transfer from CsFAMA to SAM, as well as interfaces or surfaces recombination, as discussed in **Chapter 2**. The parameters obtained from the fitting are provided in **Table 4.4**, where A1 and A2 represent the amplitudes of the respective components. Additionaly, τ_1 and τ_2 represent the lifetimes corresponding to the fast and slow components, ascribed to charge transfer recombination from CsFAMA to SAM and interface, and radiative charge recombination in the perovskite bulk, respectively.[79,91]

In Figure 4.8b, it is observed that perovskite film shows a lower PL decay (τ_1 = 88.83 ns and τ_2 = 874.4 ns) compared to those based on our SAMs, consistent with the trend observed in PL quenching. This correlation is further confirmed by the PL decays at a fixed time of 300 s, as shown in Figure 4.8c. The τ_1 lifetimes follow the trend: 22.65 ns (SAM 2) > 23.55 ns (SAM 1) > 24.37 ns (SAM 3). These results suggest that the efficiency of hole transfer from the perovskite to the SAM is dependent on their structural characteristics. Our analysis of TRPL decay curves further supports the efficient hole transfer from the perovskite to SAM.

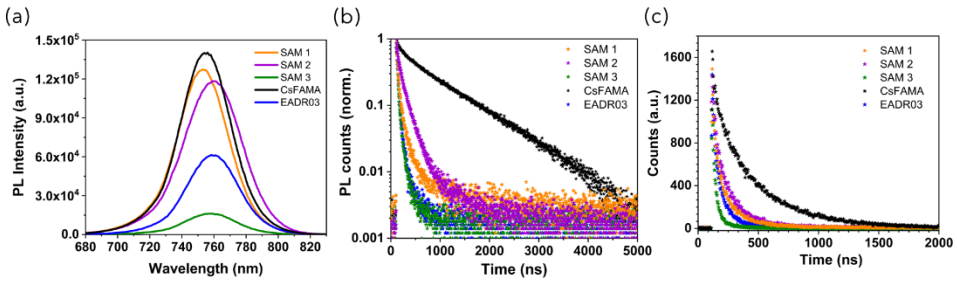

Figure 4.8 (a) Steady-state photoluminescence spectra, (b) normalized time-resolved photoluminescence decays with fixed 5000 acquisition counts and, (c) with a fixed time at 300 seconds. The films have been protected with a transparent PMMA layer to prevent degradation. The samples were excited from the glass side (635 nm) at 770 nm (maximum emission band of the perovskite).

Table 4.4 Decay fitting parameters obtained from the TrPL curves.

Films	A_1	τ_1	A_2	τ_2	Counts [a]
ITO/SAM1/CsFAMA	1.13	23.55	0.17	132.38	1491
ITO/SAM2/CsFAMA	0.54	22.65	0.53	151.44	1423
ITO/SAM3/CsFAMA	1.12	24.37	0.04	151.40	1112
ITO/CsFAMA	1.12	88.83	0.74	874.40	1656
ITO/EADR03/CsFAMA	1.15	29.48	0.03	214.31	1438

[a] Counts collected within a fixed time of 300 s.

Photovoltaic Properties

Once we have corroborated that the new compounds possess suitable characteristics as HTM, as well as understanding the impact/effect of their structures on the ITO/SAM and SAM/perovskite interfaces, the next step was to study their implementation in the iPSC device. Chapter 2 provides detailed information on device fabrication. We evaluated the photovoltaic

performance of optimised devices fabricated with the three SAMs using the following schematic configuration:

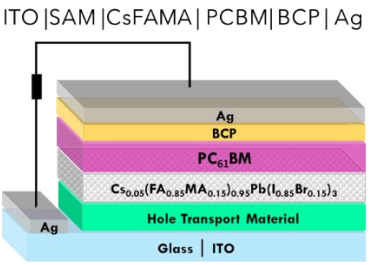

Figure 4.9 The architecture of the p-i-n device used in this work

Figure 4.10 and Table 4.5 show the comparison between the forward (fwd) and reverse (rev) scan and the statistical distribution of the device parameters using SAM 1, SAM 2, SAM 3 and EADR03 as HTM. The efficiencies of devices employing SAMs demonstrate that these new SAMs can be successfully employed in iPSCs, yielding devices with PCEs very similar to our reference. It is noteworthy that EADR03 exhibits a champion device efficiency of 20.18%, which is comparable to those reported in the literature,[70] confirming the suitability of our process for comparison purposes.

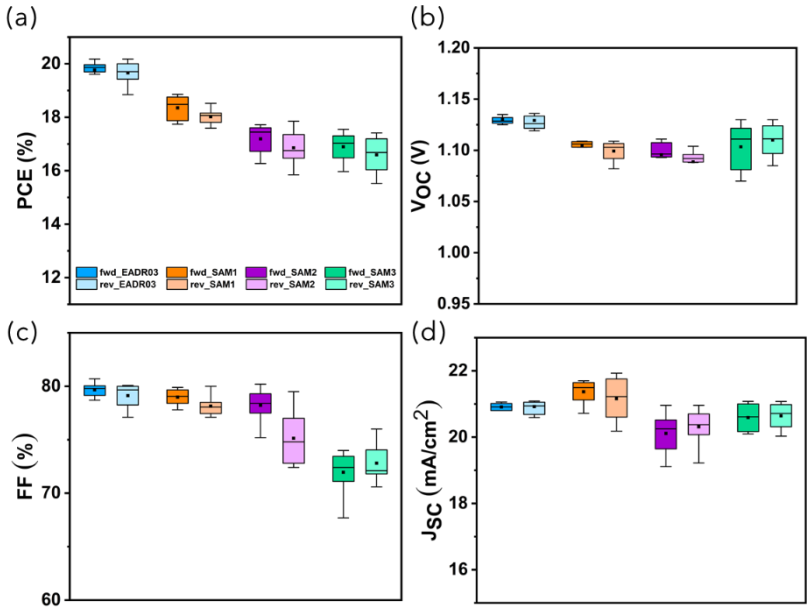

Figure 4.10 Comparison of iPSCs performance statistics with all the SAMs.

Table 4.5 The photovoltaic parameter statistics of an average of 8 devices based on SAM 1, SAM 2, SAM 3 and EADR03.

HTM	Scan direction	Jsc (mA/cm²)	Voc (V)	FF (%)	Efficiency (%)
SAM 1	fwd	21.37 ± 0.37	1.10 ± 0.005	79.0 ± 0.7	18.35 ± 0.46
	rev	21.16 ± 0.68	1.09 ± 0.009	78.1 ± 0.9	18.02 ± 0.28
SAM 2	fwd	20.11 ± 0.63	1.09 ± 0.025	78.2 ± 1.6	17.19 ± 0.55
	rev	20.31 ± 0.56	1.09 ± 0.015	75.1 ± 2.9	16.86 ± 0.67
SAM 3	fwd	20.59 ± 0.42	1.10 ± 0.023	71.9 ± 2.0	16.89 ± 0.55
	rev	20.64 ± 0.40	1.10 ± 0.016	72.8 ± 1.7	16.59 ± 0.69
EADR03	fwd	20.91 ± 0.47	1.13 ± 0.006	79.67 ± 1.7	19.02 ± 0.56
	rev	20.92 ± 0.54	1.13 ± 0.011	79.12 ± 1.1	19.00 ± 0.43

The current density.voltage (JV) curves in forward and reverse scans for the champion iPSCs using the new compounds and EADR03 are shown in Figure 4.11, with the photovoltaic parameters summarised in Table 4.6. Clearly, SAM 1 and EADR03 have similar structures, however, the differences in terms of PCE can be related to the observed decrease in charge transfer, as indicated by the PL decays. Consequently, the substituents di-p-tolylamine (SAM 1) and (1,3-dimethoxybenzene) (EADR03) on the carbazole core play a critical role in the electron-donating effect. Unfortunately, the substituent in SAM 1 creates undesired effects, including steric hindrance and a deeper LUMO, among others. Nonetheless, this substituent, also present in SAM 2, has comparable PCE to the phenyl substituent in SAM 3, both of which share similar structures. Although SAM 3 shows an increase in J_{SC} and V_{OC}, its PCE decreases due to a lower FF. Regarding the addition of a second phenyl group in the linker, as in SAM 2 compared to SAM 1, a 6% reduction in PCE is observed, however, a decrease in hysteresis is noted.

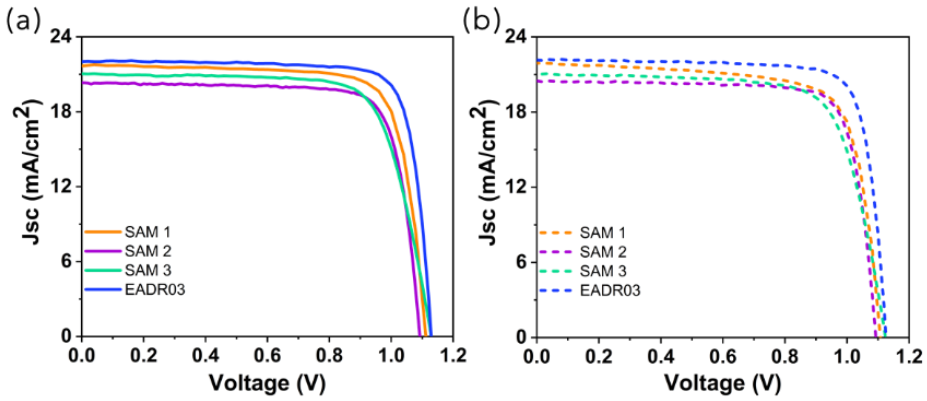

Figure 4.11 JV curves of the champion cells in forward and reverse scan direction for the different SAMs and the reference (EADR03).

Table 4.6 Photovoltaic parameters of the champion devices of the different SAMs and EADR03.

HTM	Scan direction	Jsc (mA/cm^2)	Voc (V)	FF (%)	Efficiency (%)
SAM 1	fwd	21.70	1.109	78.3	**18.86**
	rev	21.91	1.105	74.7	18.09
SAM 2	fwd	20.32	1.093	79.3	**17.61**
	rev	20.46	1.093	79.9	17.85
SAM 3	fwd	21.03	1.130	73.8	**17.55**
	rev	21.04	1.127	73.3	17.40
EADR03	fwd	21.89	1.149	80.24	**20.18**
	rev	21.83	1.144	80.66	20.15

Figure 4.12 shows the stability of the tested devices over a duration of 20 min at room temperature under 1 Sun AM1.5G light. After 20 minutes, Jsc decreases by only 2% for SAM 1 and EADR03, and 6% for SAM 2 and SAM 3 (Figure 12a). Prior to stabilisation, the Voc of SAM 2 and SAM 3 decreases from 1.07 V to 0.92 V, and from 1.10 V to 1.03 V, respectively (see Figure 12b). Given that SAM 1 shows a stable Voc similar to EADR03, further investigation into the device stability was conducted using SAM 1 and EADR03 for 100 hours to gain deeper insight (refer to Figure 4.12c and d). As depicted in Figure 4.12c, after 94 hours, the EADR03-based devices had dropped to 80% of their initial Jsc level. In contrast SAM 1

gradually reduces to 88% of the initial J_{SC} after approximately 100 hours. In particular, the SAM 1-based device shows a higher stability with a slight decreasing trend in J_{SC} and V_{OC} within 100 h, indicating better long-term illumination stability than EADR03 within that time interval.

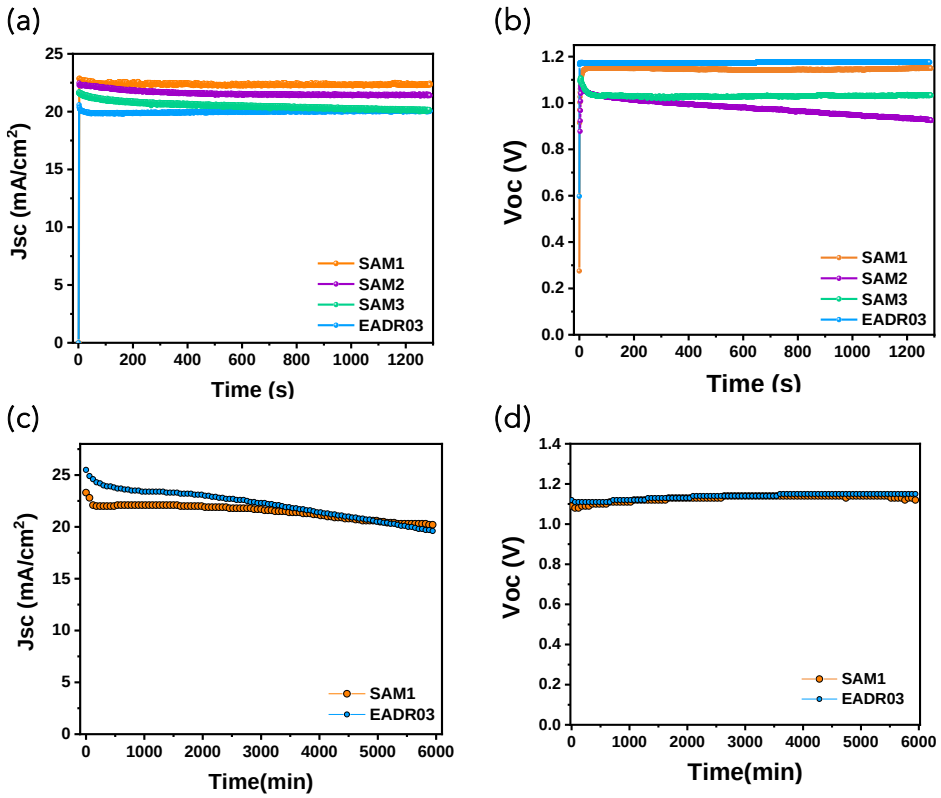

Figure 4.12 Effect of the long-term continuous illumination of iPSCs based on the new SAMs and the reference on the (a) Jsc and on the (b) Voc. And iPSC based on SAM 1 and EADR03 (c) Jsc and (d) Voc at around 100 h, using a Solar Simulator under standard 1 Sun AM1.5G.

Optoelectronic transient techniques

After that, devices with SAM 1, SAM 2, SAM 3, and the EADR03 were further analysed in-operando conditions utilising charge extraction (CE) and transient photovoltaic (TPV) as advanced optoelectronic techniques in order to gain a better understanding of the impact of their molecular structures and the losses in device efficiency. When all types of charges are removed before they recombine, the CE technique, which quantifies the charge stored in the solar cell under various light intensities is generally valid technique. In contrast, the carrier recombination mechanism is studied using the TPV technique (see Chapter 2). With the

same light bias, carrier recombination can occasionally be faster than CE.[79] Then, as an alternative to CE, differential capacitance (DC) combines data obtained from TPV and transient photocurrent (TPV/TPC) measurements.[92] The comparison of the normalized CE and TPV decays at 1 Sun illumination settings is shown in **Figure 4.13** and **Table 4.7**, demonstrating that the CE is a valid technique to assess the charge carrier kinetics for all SAMs.

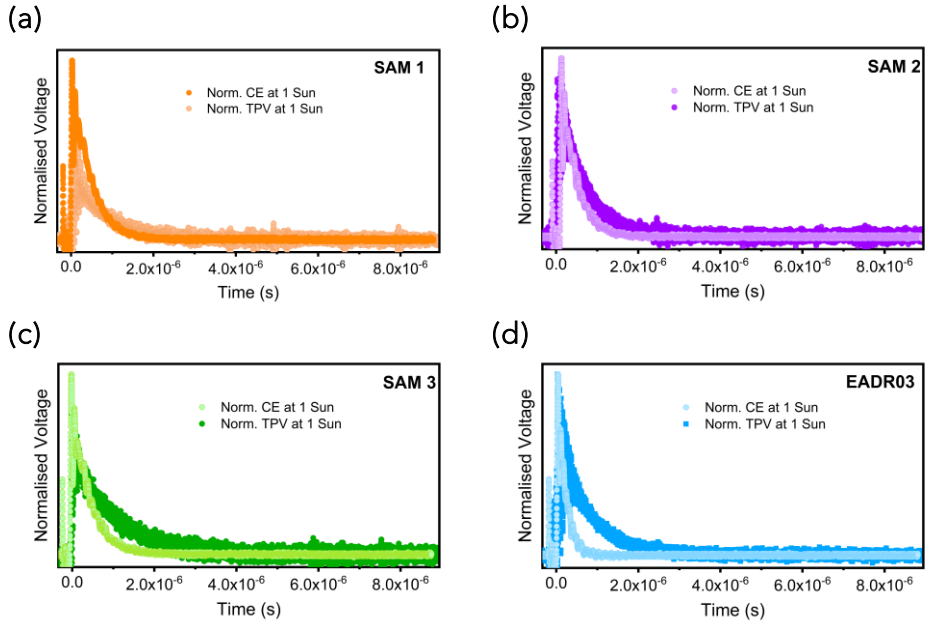

Figure 4.13 The CE and TPV decays under 1 Sun illumination conditions for (a) **SAM 1**, (b) **SAM 2**, (c) **SAM 3** and (d) EADR03.

Table 4.7 CE and TPV decays lifetime at 1 Sun illumination conditions. Two diodes of every molecule are shown, indicating reproducible results.

	CE (μs)	TPV (μs)
SAM1	0.497	0.82
SAM2	0.353	0.493
SAM3	0.447	1.055
EADR03	0.226	0.785

The photo-generated charges that are stored in the cells at equilibrium at various V_{OC} levels are displayed in **Figure 4.14**, which was obtained by adjusting the background illumination between 1 Sun and the dark. The charge density found for each sample is in line with the earlier JV findings,

which show that SAM 1 devices have a larger photocurrent than SAM 2 and SAM 3 devices. The charges that accumulated at the interfaces (also referred to as geometrical capacitance, C_{geo}) and within the bulk (chemical capacitance) are often responsible for the linear and exponential parts of charge density. When comparing SAM1, SAM2, and SAM3 to EADR03, the charges in the bulk (solid lines) exhibit a more marked slope at lower voltages. This indicates that the voltage vs. chemical capacitance trend is SAM 1 < SAM 2 ≈ SAM 3 < EADR03. These variations in charge versus voltage point to modifications in the energy offsets concerning the valence band (VB) of the perovskite.

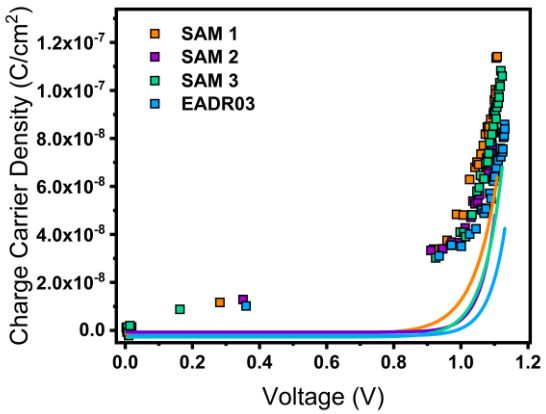

Figure 4.14 Charge density under different open circuit voltages due to the different illumination conditions with Cgeo and without Cgeo. The solid lines at the bottom are the experimental part of the fits: y= Be^{Cx} (chemical capacitance) after subtracting the Cgeo (linear part).

Next, we used TPV measurements to analyse the impact of interfacial carrier losses for the various solar cells. For each sample, the carrier lifetime is plotted vs V_{OC}, and vs charge in Figure 4.15. Because each SAM has a unique photocurrent and the carrier lifetime is directly correlated with the charge density, Figure 4.15b allows for the analysis of the recombination kinetics. The variations in carrier lifetime at the same charge value are compared using the dashed vertical black line. It's noteworthy to note that while the recombination kinetics between the different SAMs are of the same order of magnitude, but, interestingly, SAM 2 and the reference show the faster and slower recombination lifetimes, respectively.

(a) (b)

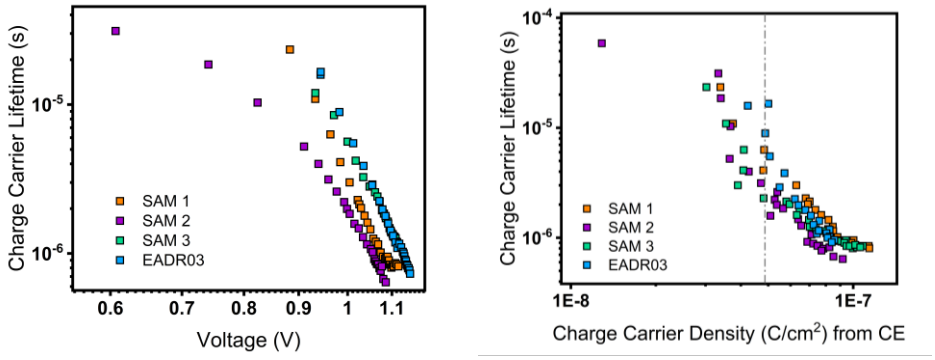

Figure 4.15 TPV measurements versus V_{OC} (a) and versus charge density (b) for the different SAMs.

In addition, the recombination order can also be obtained as $\delta = \lambda + 1$,[76] where δ is a parameter that describes the recombination order of the photovoltaic devices and λ describes the slope of the power law (detailed information is described in Chapter 2).

The devices containing SAM 1, SAM 2, SAM 3, and the EADR03 had the following recombination orders: $\delta = 1.37$, $\delta = 1.38$, $\delta = 1.47$, and $\delta = 1.38$, respectively (see Figure 4.16). The estimated recombination orders are highly similar, verifying that first-order ($\delta = 1$) recombination, which is typically aided by mid-gap impurities governs all devices.[93]

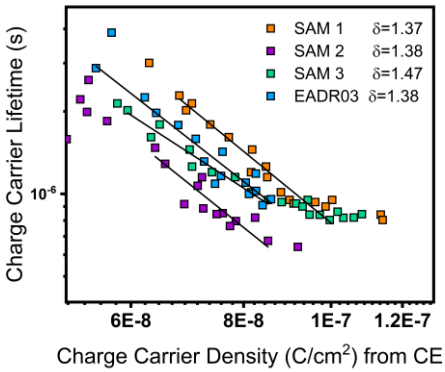

Figure 4.16 Charge carrier lifetime versus charge carrier density indicates the recombination orders.

4.3 Conclusions

In summary, we have successfully synthesized and evaluated three new self-assembled molecules in inverted perovskite solar cells, demonstrating promising power conversion efficiencies. While all SAMs shared a carboxylic acid anchoring group, they differed in the linker (phenyl or biphenyl) and the carbazole core-based functional group. Our findings reveal that SAM 1, containing the phenyl group, outperformed SAM 2 and SAM 3 with the biphenyl group in terms of power conversion efficiency and stability. This suggests that shorter linkers are more favorable in this device structure and molecule type. SAM 1 also exhibited excellent stability comparable to devices with EADR03.

Furthermore, the comparison between SAM 2 and SAM 3 highlights the impact of different terminal groups, despite their similar HOMO energy levels. Notably, the triphenylamine group resulted in smaller grain sizes in the perovskite film. Overall, our study suggests that the linker group in these SAMs has a significant influence on device performance compared to the functional group. These findings provide valuable insights for the future design of new SAMs and the development of efficient and stable inverted perovskite solar cells, offering a promising chemical pathway towards commercialization.

CHAPTER 5

EXPLORING INTERFACE INTERACTIONS: TAILORING CARBAZOLE-BASED SAMS WITH VARYING FUNCTIONAL GROUPS FOR ENHANCED INVERTED PEROVSKITE SOLAR CELLS

Four carbazole-based self-assembled hole transporting materials comprising a carboxylic acid as anchoring group, biphenyl linker and electron-rich side arms as functional groups have been synthesised and used successfully in inverted perovskite solar cells. The new SAMs are obtained from relatively inexpensive starting materials utilising a simple preparation method, avoiding the need for expensive and complex purification techniques. The SAMs are then used as hole-transporting material in inverted perovskite solar cells. A remarkable power conversion efficiency of 19.67 % was achieved using SAM 5.

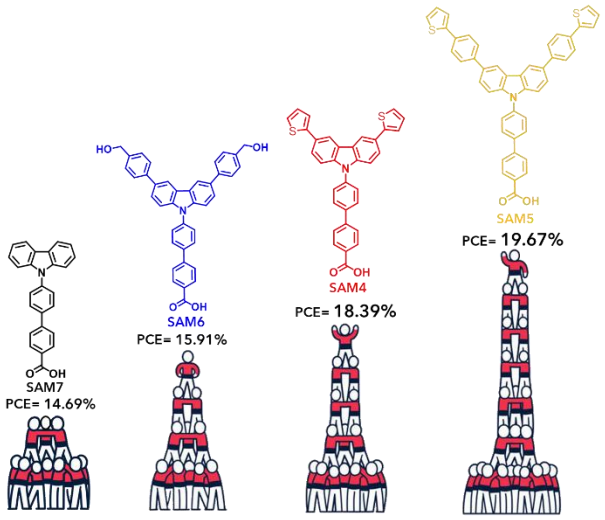

5.1 Introduction

Since the rise of self-assembled molecules as a hole selective layer (HTL) for inverted perovskite solar cells (iPSCs),[94] there has been a significant amount of research focused on novel SAM candidates to gain more insight into the relationship between their molecular structure and iPSC performance.[19,69,75,79,95] To date, many SAMs have been developed and used as HTL in iPSCs.[70,73,75,91,96,97] These include their use in studies at substrate/SAM interfaces to enhance the hole-extraction efficiency,[98,99] modifications of the spacer group to improve charge transport properties and self-assembly behavior,[73,100] the incorporation of different functional groups to fine-tune optoelectronic properties and energy levels alignment,[101–103] among other research. Nevertheless, further research into the interaction at the perovskite/HTL interface is necessary. This will facilitate the design and optimization of the SAM features, assuming that the combination of each group comprising the SAM (such as anchoring, a linker and functional groups) is compatible with the perovskite material, thereby leading to enhanced overall device performance.

Based on the advantages and the significant effect on device performance for SAM2 and SAM3, as reported in the previous section, we were encouraged to continue exploring derivatives of these compounds. In this study, four new carbazole-based compounds were designed by changing the functional group for a deep analysis of the SAM/perovskite interface and to investigate the effects of molecular structure on device performance. Moreover, they were used as selective-contact materials to study their potential use as HTMs in iPSC. These SAMs were synthesized using a simple synthetic strategy (see Chapter 3 for more details on the design and synthesis) and their physical and optoelectronic properties were evaluated by several characterization techniques (including wettability, FESEM, XPS, UV-Vis, PL, TRPL, CE and TPV) to assess their suitability as hole transport layer (HTL) for efficient iPSCs.

5.2 Results and Discussion

Design and Synthesis

The general synthesis scheme for the preparation of SAM4, SAM5, SAM6, and SAM7 is shown in Scheme 5.1. The synthesis begins with the construction of the carbazole core linked with a biphenyl group to a

carboxylic acid (anchoring group) in two steps by Ullmann and Suzuki coupling reactions to obtain **11**. Then, a bromination reaction was carried out using NBS to obtain **12**, which is ready for further borylation, Suzuki, and reduction reactions to yield final SAMs containing carbazole-based engineered donor moieties. Detailed synthetic procedures are fully described in **Chapter 2** methods and procedures and **Chapter 3**, including the measures to verify their chemical structures of the synthesized products by means ^{1}H and ^{13}C NRM spectroscopy. All final SAMs are soluble in common organic solvents such as THF, TOL or alcohols like IPA and MeOH, which are typically used for deposition of self-assembled monolayer in iPSCs. Specifically, **SAM7** was designed to get further information on the addition of different terminal groups (electron rich moieties) to the carbazole-core, and in addition to analyse the influence of carbazole as a functional group in this kind of molecules.

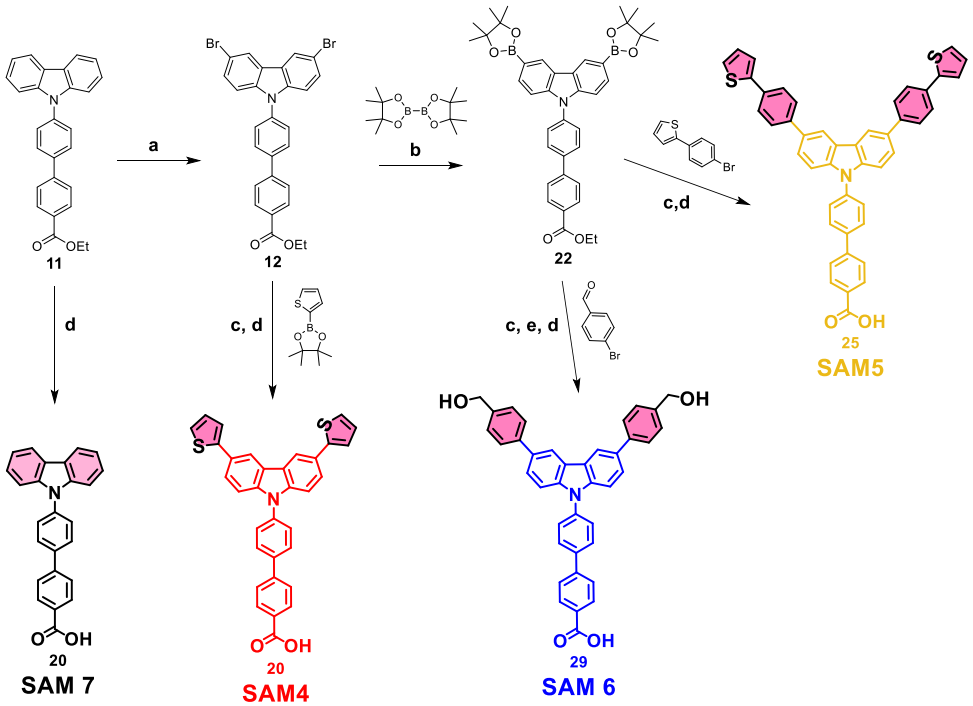

Scheme 5.1 Synthetic route for carbazole-based SAMs. (**a**) NBS/DFM, 0 °C, 12 h, (**b**) $Pd(dppf)Cl_2$, K_2CO_3, 1,4-dioxane 90 °C, 12 h; (**c**) $Pd(PPh_3)_4$ K_2CO_3, THF/H_2O, 90 °C, 24 h; (**d**) KOH, THF/EtOH/H_2O, 100 °C, 1 h; (**e**) $NaBH_4$/THF.

Thermal, Optical and Photophysical Properties

The molecular electrostatic potential (MEP) was used to gain insights into molecular geometries and the SAMs' electronic density distribution. The regions with positive, negative and neutral electrostatic potentials (ESP) are represented with red, blue and green regions, respectively. Figure 5.1 depicts the MEP surface of the SAMs, which shows the partial positive electron density (δ^+) in the C-C and C=C and the negative electron density (δ^-) around -O=C, O-C and -OH bonds. Since all the SAMs have a partial δ^+ and δ^- electron density at the carboxylic acid group (anchoring group), after SAM bonding with ITO, it is expected the formation of a permanent dipole moment (δ^-/δ^+) of SAM on the ITO surface.[104,105] SAM6 possess additional electron density regions on their side arms, benzyl alcohol groups. Notably, the violet-blue area (δ^-) around the oxygen atoms could form interesting chemical interactions with the perovskite.[106] To our knowledge, it is the first time that these groups are used as terminal group in the SAMs.

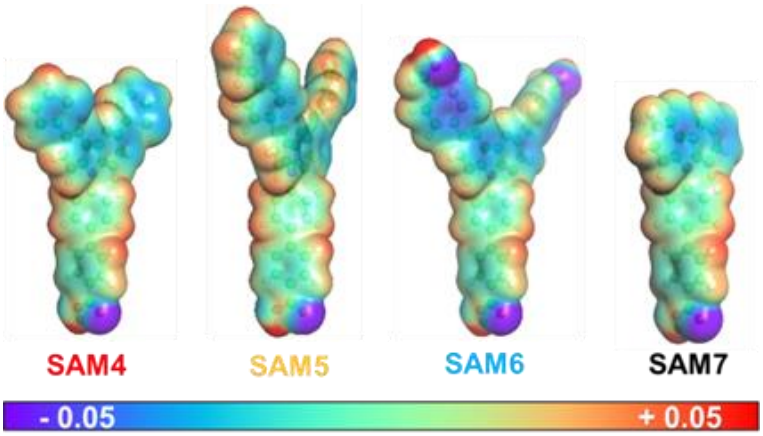

Figure 5.1 The electrostatic potential.

We first determined the thermal properties of the as-synthesized SAMs by thermogravimetric analysis (TGA). The results of the TGA in Figure 5.2a show that the decomposition temperatures (T_{dec}) increased from 146 °C to 286 °C in the following order: SAM7 < SAM6 < SAM5 < SAM4, basically due to the addition of an aromatic substitution, except for SAM5, where the 2-phenylthiophene side arms showed to be less thermally stable than the thiophene group (SAM4). However, all SAMs exhibited good thermal stability up to 120 °C, exceeding the temperature used during the solar

cell fabrication (100 °C)[12] All the decomposition temperatures are summarised in **Table 5.1**, together with the optical properties of SAMs. The normalised UV-Vis absorption and photoluminescence (PL) spectra of **SAM4**, **SAM5**, **SAM6**, and **SAM7** (10^{-3} mM in DCM) are shown in **Figure 5.2b**. It was found that all SAMs show absorption bands in the spectral region, with the maxim absorption wavelength (λ_{abs}) centred at 320 nm (**SAM4**), 332 nm (**SAM5**), 304 nm (**SAM6**), and 319 nm (**SAM7**), which are the bands assigned to the π*-π transitions of the conjugated systems.[69,94] The maximum absorption band was obtained with the addition of 2-phenylthiophene moieties to the carbazole-core (**SAM5**), and it is due to the extended π-conjugation system compared to **SAM4**. The PL emission spectra exhibit one broad emission band in the visible region, ranging from 325 to 600 nm. The rising trend in Stokes shifts (λ_{em} - λ_{abs}) of 77, 151, 182, and 187 nm (for **SAM5**, **SAM7**, **SAM6** and **SAM4**, respectively) resulted in a slightly increasing energy bandgap, suggesting that an electron jump from one level to another will be possible with a lower amount of energy and light.[97] However, **SAM4** shows a higher stoke shift than **SAM5**, suggesting significant changes in the geometrical configuration of the molecule upon excitation.[40] The optical bandgap (E_g) is estimated from the intersection of the corresponding normalised absorbance and PL spectra, which corresponds to E_g of 3.36, 3.15, 3.37 and 3.35 eV for **SAM4**, **SAM5**, **SAM6** and **SAM7**, respectively.

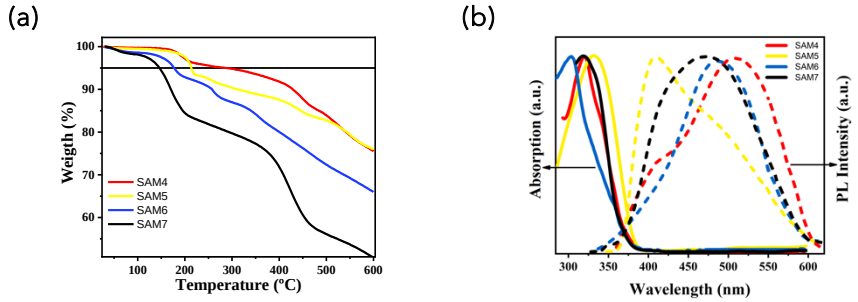

Figure 5.2 Thermal and optical measurements of all SAMs. (**a**) Thermogravimetric analysis (TGA) data with a heating rate of 10 °C min^{-1} under N_2 atmosphere; and (**b**) UV-Vis absorption (solid line) and photoluminescence (dashed line) spectra normalised at the peak value.

Furthermore, ultraviolet photoelectron spectroscopy (UPS) was carried out to evaluate the work function (ϕ) of the ITO modified by adding the SAMs and determine the energy levels of these conjugated SAMs.

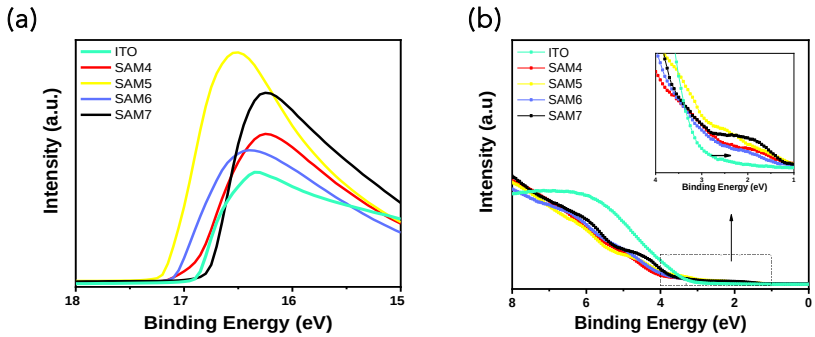

Figure 5.3 UPS measurements: (**a**) secondary electron cutoff and (**b**) valence band onset.

The different work functions were calculated by the minimum energy required to emit an electron from the surface into a vacuum with an excitation energy ($E_{He\ I}$) of 21.22 eV with the equation $\phi = E_{He\ I} - E_{seco}$). The secondary electron cutoff (SECO) values were obtained from the graph in **Figure 5.3a** at the point where the background spectra end abruptly. The UPS results on bare ITO and ITO/SAM films reveal that SAM film is a successful means to adjust the ITO work function from 4.32 to 4.04, 4.0, and 4.08 eV for **SAM4**, **SAM5**, and **SAM6**, respectively, minimizing the energy barrier between the perovskite and the ITO electrode. Except for **SAM7** which slightly increases at 4.38 eV.

Table 5.1 Thermal and optical properties of synthesized compounds.

	T_{dec} (°C)[a]	λ_{abs} (nm)	λ_{em} (nm)	E_g (eV)[b]	SECO (eV)[c]	ϕ (eV)[c]	VB (eV)	E_{HOMO} (eV)[c]	E_{LUMO} (eV)[d]
SAM4	285	320	507	3.36	17.15	4.04	1.11	-5.18	-1.79
SAM5	214	332	409	3.15	17.22	4.00	1.01	-5.01	-1.86
SAM6	177	304	486	3.37	17.13	4.09	1.25	-5.34	-1.97
SAM7	146	319	470	3.35	16.84	4.38	1.19	-5.57	-2.22

[a]Decomposition temperature determined from TGA (5 % weight loss); [b]E_g is calculated as $E_g = 1240/\lambda_{onset}$ (where λ_{onset} is the point where the normalized absorbance and emission spectra overlap); [c]The E_{HOMO}, SECO and the work function (ϕ), were extracted from **Fig 3(a)**. (UPS measurements, with an excitation energy of 21.22 eV); [d]calculated from $E_{LUMO} = E_{HOMO} + E_g$.

Finally, the HOMO level was calculated using the equation $E_{HOMO} = -(E_{He\ I} - SECO + VB)$, where VB (valence band onset) was determined graphically (see **Figure 5.3b**). The E_{HOMO} values are -5.18 (**SAM4**), -5.01 (**SAM5**), -5.34

(SAM6) and -5.57 (SAM7) eV. As expected, the insertion of an additional phenyl ring between carbazole-base and electron-donating moiety stabilised carbazole-core electron-rich via effective charge/electron delocalisation and energy level modulation.[69,73] This modification led to an upshift in the HOMO level for both SAM5 (compared to SAM4) and SAM6 (compared to SAM7). Figure 5.4 illustrates the energy level diagram of ITO/SAMs/CsFAMA/PCBM/BCP/Ag devices. Notice that EADR03 was chosen as a reference in fabricating iPSCs since it demonstrated good performance in devices with similar perovskite composition and band gap.

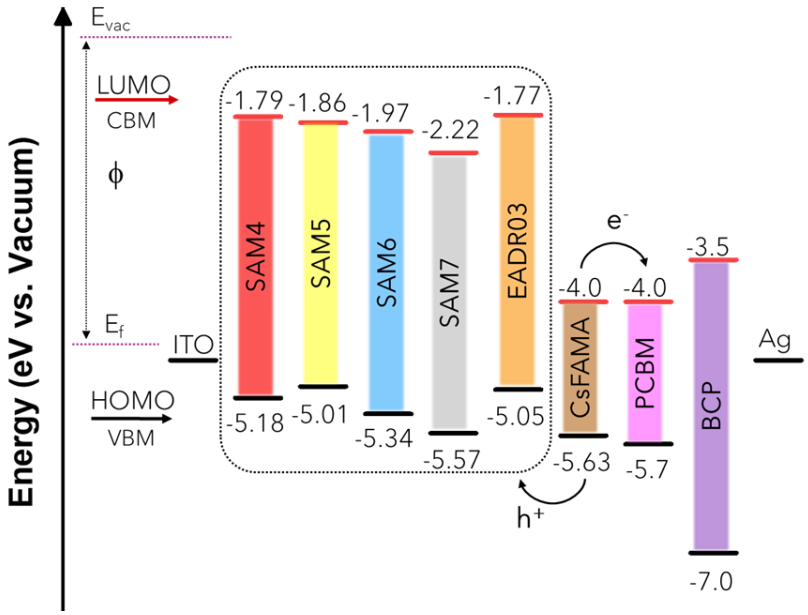

Figure 5.4 Diagram of energy levels.

SAM's Influence on the ITO Surface and the Perovskite Interface

To have a better understanding of the surface modification of ITO substrates before and after SAM deposition by spin-coating, surface wettability was analysed using contact angle in a sessile water drop analysis. Field emission scanning electron microscopy (FESEM) images were recorded to analyse the effects of the SAM molecules on perovskite film (detailed information in Chapter 2). Since all SAMs features similar carbazole-core they should show similar chemical environment being more hydrophobic than EADR03 and bare ITO (after UV-ozone-treatment). Figure 5.5 (top-images) depicts the contact angles of SAM4

(84.34°), SAM5 (80.04°), SAM6 (75.5°) and SAM7 (79.48°), which show a higher hydrophobicity character in comparison to EADR03 estimated at 50°.[107] This trend validates the effect of carbazole derivatives on the hydrophobicity because of electron delocalization.

Moreover, the contact angle of bare ITO after UV-ozone treatment is estimated at 55° (Chapter 2) indicating with this significant difference the presence of SAM on the ITO surface for the ITO/SAMs films, and as expected with higher hydrophobicity. In addition, we also observed a similar perovskite grain size distribution around 305 nm on top of ITO/SAM5 and ITO/SAM7 films whereas the perovskite grain size decreases on top of ITO/SAM4 (281 nm) and slightly increases on top of ITO/SAM6 (317 nm), as shown in FESEM images in Figure 5.5 bottom and grain size distribution summarized in Table 5.2. From Figure 5.5 bottom, we observed that the hydrophobic surface of SAM4 (~84°) leads to a large grain size distribution of the perovskite, while SAM6 (~75°) results in small grain size distribution, this is aligned with what has been reported in the literature.[108]

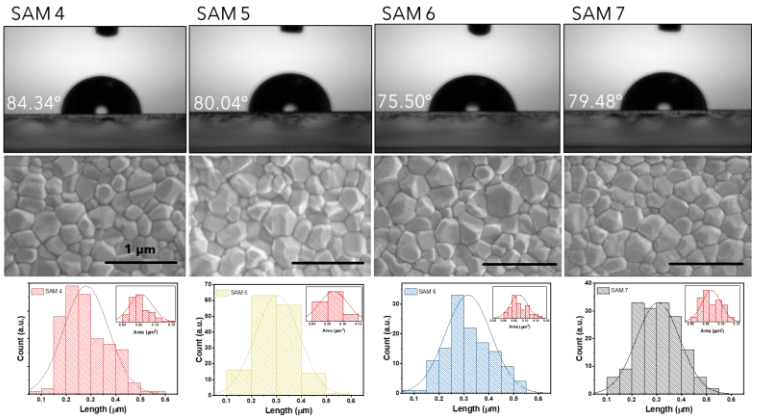

Figure 5.5 Contact angle images of ITO/SAMs (top); FESEM images of CsFAMA surface deposited on ITO/SAMs (middle) and their grain size distribution (bottom). All the scale bars are 1 µm.

In general, the films quality is defined by grain size, crystallinity, and complete surface coverage, where a bigger grain size and smaller grain boundaries can minimize the defect density on the perovskite film, facilitating the charge transfer.[109] According to our results, we corroborated a homogeneous deposition for the perovskite solution on

SAM layers and showing that using alternative SAM structures had influence on perovskite morphology.

Table 5.2 Average grain size of perovskite films determined from FESEM images.

Sample	Mean	
	Length (nm)	Area (nm^2)
ITO/SAM4/CsFAMA	281.0	55.8
ITO/SAM5/CsFAMA	303.6	69.1
ITO/SAM6/CsFAMA	317.1	70.8
ITO/SAM7/CsFAMA	305.8	67.0
ITO/CsFAMA	307.5	66.0

The atomic species on the SAM-coated substrates were identified using X-ray photoelectron spectroscopy (XPS), which also confirmed the formation of SAM anchored to the ITO. Figure 5.6 and Table 5.3 resume the results of the XPS analyses performed on SAMs in the C1s, O1s, and N1s binding energy (BE) regions as previously reported in Chapter 4.

The spectra were fitted and divided into three peaks for C1s assigned to C-H or C–H (around 284 eV), C–O (around 285 eV) and COOH (around 288 eV) bonds. With respect to O1s, the peaks at around 530, 532 and 533 eV, are attributed to C=O, C-O and O-In, respectively. The N1s spectra for all the SAMs show the same peak position about 400 eV assigned to C–N bond, which is not detected on the bare ITO. These results confirm the formation of strong covalent bonds between the carboxylic acid (-CO_2H) group of SAMs and hydroxyl (-OH) group onto the surface of ITO, as well as the successful formation of the self-assembled monolayer of all the SAMs on the ITO.

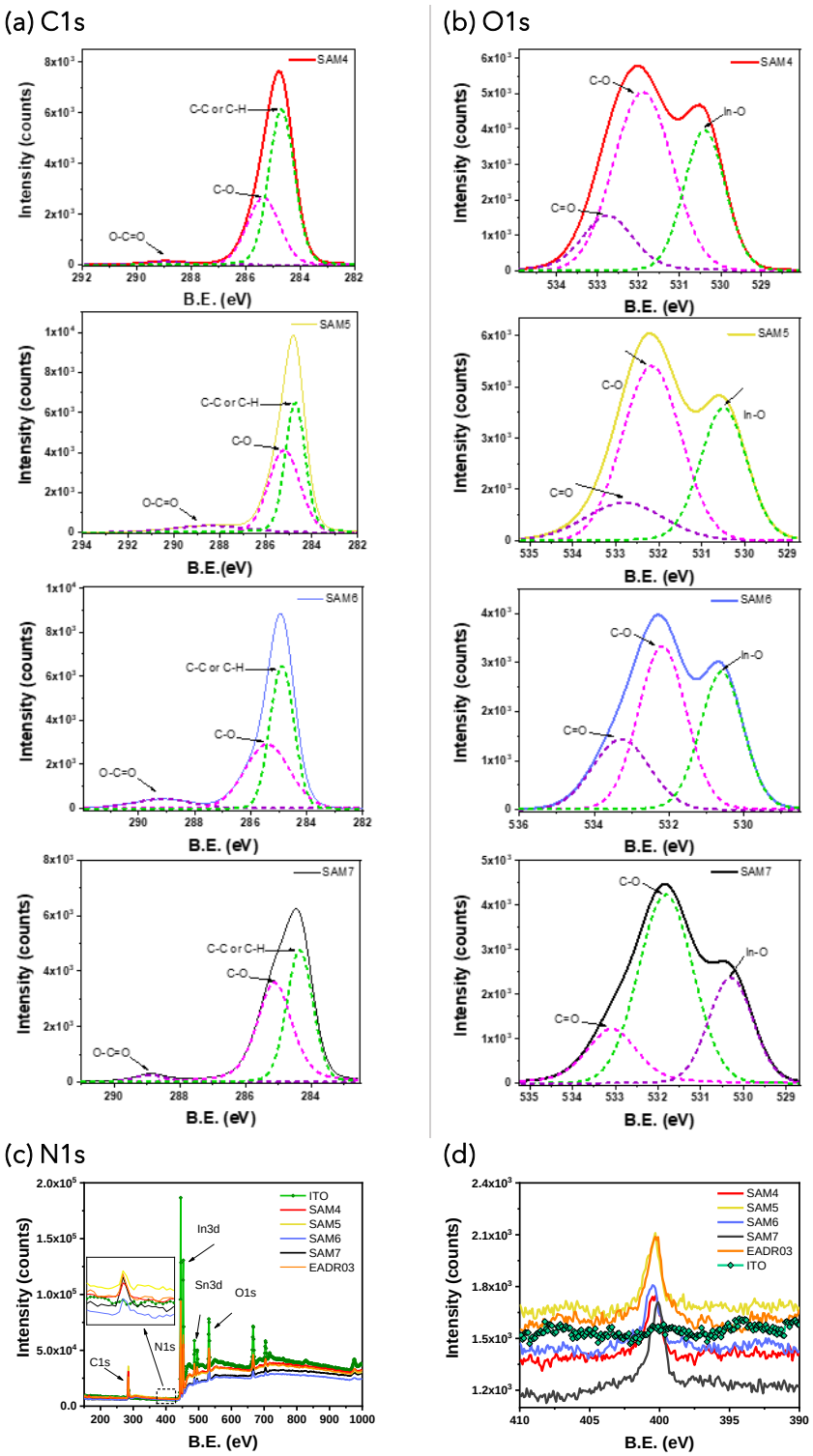

Figure 5.6 High-resolution XPS surface spectra of (a) C1s, (b) O1s, (c) N1s and (d) survey spectrum for bare ITO and the SAMs used in this study.

Table 5.3 Functional groups and their associated binding energies extracted from the XPS spectra of SAM-coated ITO and compared them to cleaned ITO.

Films	C1s (eV)			O1s (eV)			N1s (eV)
	O=C-O	C-O	C-C/ C-H	C=O	C-O	O^{2-} (In)	C-N
SAM4	284.7	285.3	288.9	530.4	531.9	532.8	400.5
SAM5	284.7	285.2	288.4	530.5	532.2	532.8	400.3
SAM6	284.9	285.4	289.2	530.6	532.2	533.3	400.5
SAM7	284.3	285.1	288.9	530.3	531.8	533.1	400.1
ITO	284.7	286.2	288.9	530.4	532.1	533.5	-

Photophysical Properties

The steady-state photoluminescence (PL) and time-resolved photoluminescence (TrPL) analyses were performed to gain insight into the interface processes, in particular, the hole transfer at the perovskite/SAM interface and determine the capability of new SAMs in acting as hole acceptors/transporting within the perovskite-based devices. **Figure 5.7** shows the PL and TrPL of perovskite film deposited on bare ITO and all the new SAMs presented, including the reference EADR03.

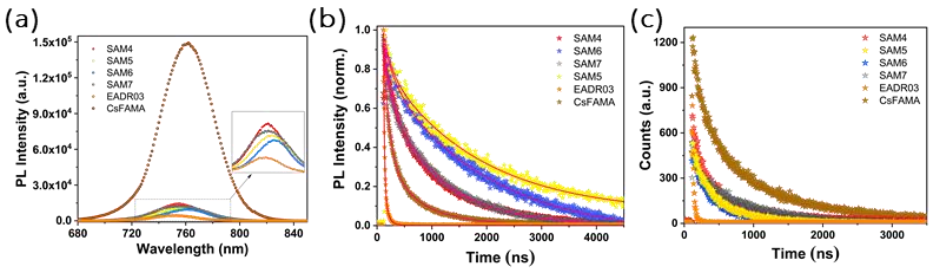

Figure 5.7 (**a**) Steady-state PL spectra and (**b**) normalized time-resolved photoluminescence decays with fixed 5000 acquisition counts (solid lines represent the fit from a bi-exponential function) and, (**c**) PL decay with a fixed time at 300 seconds. The films have been protected with a transparent PMMA layer to prevent degradation or any oxygen/moisture-induced effects. The samples were excited from the glass side (635 nm) and the measurements recorded at the maximum of the perovskite emission band (760 nm).

Figure 5.7a shows the PL spectra of the perovskite films excited at 635 nm from the glass side. Results display that the CsFAMA band-edge emission around 760 nm is quenched in the perovskite films by the SAMs, with negligible differences between samples. This confirms that the injection of holes from the valence band of the CsFAMA layer are transferred to the HOMO of the SAM.[79,96,107] The decay kinetics of emission using time-resolved photoluminescence (TrPL) were explored to further clarify the injection rate of holes. Figure 5.7b shows the decay curves fitted with the biexponential decay model (Equation 7). The fitting parameters are listed in Table 5.4, as already mentioned in Chapter 2, τ_1 and τ_2 are the lifetimes from the fast and the slow components ascribed to charge transfer recombination of CsFAMA to SAM and interface and radiative charge recombination in the perovskite bulk, respectively.[79,91]

Table 5.4 Decay fitting parameters obtained from the TrPL curves.

Films	A_1	τ_1 (μs)	A_2	τ_2 (μs)	Counts[a]
ITO/SAM4/CsFAMA	0.37	218.4	0.58	1089.8	712
ITO/SAM5/CsFAMA	0.14	137.4	0.72	1731.8	600
ITO/SAM6/CsFAMA	0.13	213.4	0.79	1918.1	539
ITO/SAM7/CsFAMA	0.20	104.1	0.68	999.9	508
ITO/CsFAMA	0.68	107.6	0.35	619.4	1237
ITO/EADR03/CsFAMA	1.19	15.7	0.29	61.2	786

[a]Counts collected within a fixed time of 300 s.

Typically, a fast PL decay seems to imply faster hole transfer or quenching of holes in the perovskite absorber, which is common in previous studies (see Chapter 4).[107,110] It should be noted that samples based on our SAMs presented different behaviour than those based on EADR03[107] and ITO/CsFAMA films. Recently, Zhanoning Li et al.,[91] demonstrated that SAMs can help to suppress defect-induced and nonradiative recombination, leading to longer decay processes in the SAM/perovskite films. Later, other study on ITO/SAM/perovskite interface by transient surface photovoltage (SPV) and PL techniques showed that SAMs can strongly influence the passivation and charge transfer kinetics. In another words, SPV-PL allowed to identify electron trapping at the ITO/perovskite and determine the processes of separation and recombination of charge carriers.[96] Having in mind that, as it has been described, SAM promotes

hole injection into the ITO, reduce the buried interface defects of perovskite and charge recombination loss. This could be one of the reasons why our SAMs exhibit a higher PL decay in comparison to EADR03. Furthermore, the transition from PL decay to a single-exponential decay can be explained by examining the early stages of the TrPL mainly when the PL decay is dominated by fast hole injection and recombination among others. Thus, we monitored the charge dynamics by using TrPL with a fixed time of 300 s as shown in Figure 5.7c. The perovskite/SAMs show a reduction of the PL signal with respect to the pristine perovskite film, this confirms that interfacial hole transfer happens and quenches the PL signals.

Photovoltaic Properties

Since the interfaces of ITO/SAM and SAM/perovskite films have already been investigated, the next concern will be the effect and performance of the whole solar cell. To analyse the function, effect and efficacy of the new carbazole derivatives, iPSCs were fabricated. In brief, optimized devices with the following configuration were employed: ITO/SAM/CsFAMA/PCBM/BCP/Ag as already reported in Chapter 4. More information on device fabrication is available in Chapter 2. The SAM layer was applied by spin-coating at 3000 rpm for 30 s with an acceleration of 2000 rpm s^{-1} on the bare ITO UV-O_3 treated and the concentration of SAM solution was optimized to 0.1 M in THF anhydrous. In addition, by controlling the processing conditions and interactions between SAMs and the substrate, the coverage ratio of SAMs on top of the substrate can be regulated.

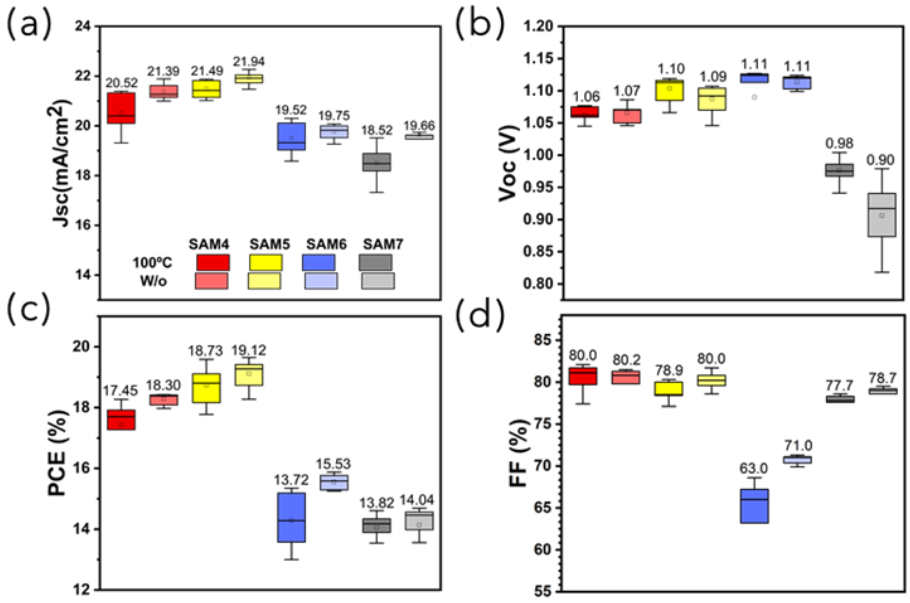

Figure 5.8 Statistical distribution of the cell parameters of more than 20 devices on iPSCs using SAMs with annealing at 100 °C for 10 minutes and without annealing (w/o).

Among all the parameters, the post-annealing treatment was studied to provide a better interlayer for the smooth growth of the perovskite layer. Figure 5.8 shows the statistical distribution of the solar cell parameters obtained. We can observe that devices based on SAMs without thermal treatment exhibit better performance than those with annealing. We can attribute these results to the crystallization of SAMs and the decreased of wettability, resulting in a poor deposition and consequently an inhomogeneous perovskite layer. For those reasons, the thermal treatment was not used in further devices.

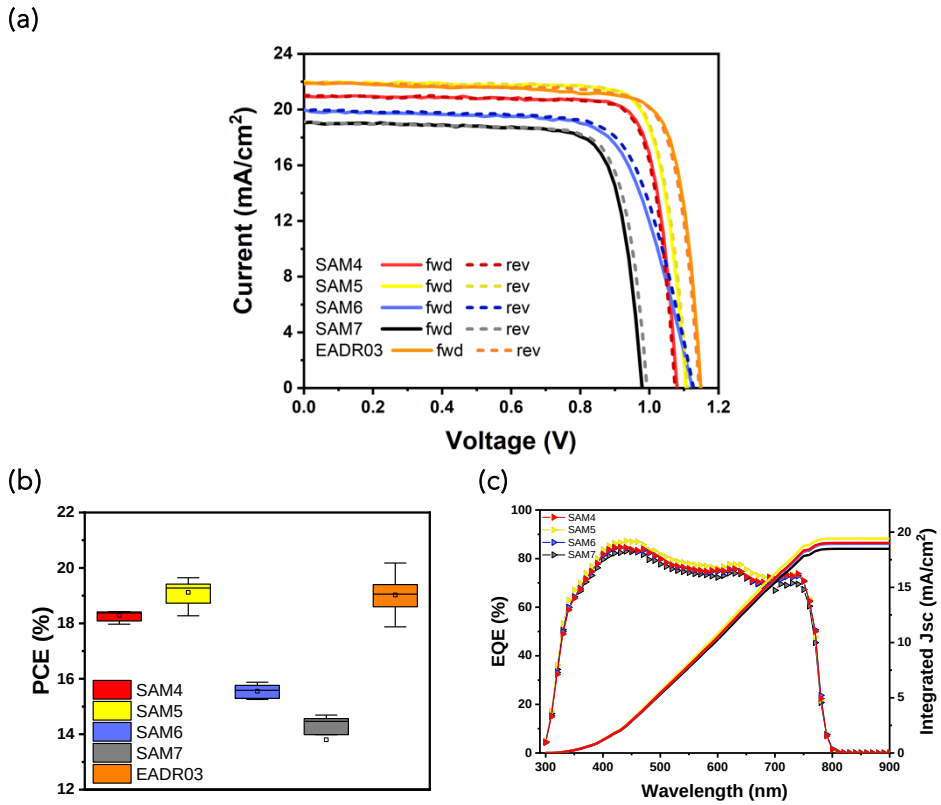

Figure 5.9 (a) J-V curves of champion devices based on SAM4, SAM5, SAM6, SAM7, and EADR03 as the reference. The curves were recorded under 1 sun condition (100 mW·cm^{-2}, AM 1.5G) scanning at 80 mV·s^{-1}. (b) statistical distribution of iPSCs and (c) EQE spectra of devices with the new SAMs.

Figure 5.9a shows the best J-V characteristics of iPSCs with SAM 4, SAM5, SAM6, SAM7 and EADR03 (used as a reference) under 1sun simulated illumination (100 mW·cm^{-2}, AM 1.5G). The J-V characteristics were collected by forward (fwd) and reverse (rev) scans at 80 mV·s^{-1} in 0 to 1.2 V range (and the other way around). Table 5.5 summarizes the detailed photovoltaic parameters (Jsc, Voc, FF and PCE) and the statistics extracted from J-V curves. The mean and standard deviation values of at least 10 devices were tested for reliable data and acceptable comparability (Figure 5.9b).

Table 5.5 Photovoltaic parameters of the champion cells and the statistics of an average of 10 devices.

	Scan direction	Jsc (mA/cm^2)	Voc (V)	FF (%)	Efficiency (%)
	fwd	21.89	1.086	77.3	18.39
SAM 4		21.38 ± 0.30	1.066 ± 0.14	80 ± 1.5	18.29 ± 0.18
	rev	22.05	1.083	78	18.63
	fwd	21.99	1.070	80.8	19.67
SAM 5		21.93 ± 0.36	1.087 ± 0.019	80.1 ± 1.0	19.11 ± 0.44
	rev	21.95	1.110	81.3	19.80
	fwd	19.92	1.121	71.1	15.91
SAM 6		19.76 ± 0.30	1.113 ± 0.010	70.7 ± 0.7	15.03 ± 0.81
	rev	19.94	1.128	72.3	16.27
	fwd	19.09	0.979	78.6	14.69
SAM 7		19.64 ± 0.56	0.906 ± 0.051	77.3 ± 0.04	13.80 ± 1.40
	rev	19.1	0.992	78.8	14.93
	fwd	21.89	1.149	80.2	20.18
EADR03		20.78 ± 0.48	1.13 ± 0.006	80.3 ± 1.60	19.02 ± 0.56
	rev	21.83	1.144	80.6	20.15

The results show excellent performances for SAM4 and SAM5 of 18.39% and 19.67%, respectively. They exhibit a Voc over 1.1 V and a Jsc of more than 21 mA·cm^{-2}, with a relative difference in the FF of 3%, showing comparable performance. The results are pretty close to EADR03 champion cell performance, achieving 20.18% PCE, and are comparable to those reported in the literature.[107] This suggests that our device fabrication process is reliable for valid comparisons. In contrast, SAM6 and SAM7 show PCEs of 15.91% and 14.69% respectively, due to a lower Jsc, most likely because of the energy levels alignment resulting in greater charge recombination. Despite its low efficiency, SAM6 achieved a Voc of 1.128 V, making this terminal group (-OH) attractive for future SAM designs in which energy levels might be controlled. The most remarkable aspect in the performance of iPSCs is that all the SAMs present a negligible J-V hysteresis, as can be observed in Figure 5.9a. This small hysteresis indicates that all the SAMs can reduce the ion migration in

iPSCs, which is one of the leading causes of hysteresis and it has been well documented in the literature.[28,111]

Jsc and Voc dependency of the light

Considering the aforementioned experimental results, it is evident that the significant differences in the performance of SAMs are mainly related to both Voc and Jsc values. The next step was to explore the effect of light intensity using various optical filters to gain insight into the influence of the underlying self-assembled molecules on the Jsc and Voc parameters. Specifically, the Jsc and Voc parameters can provide recombination information within the devices.[73] In Figure 5.10 we can see the J-V curves obtained at various light intensities (P_{light}).

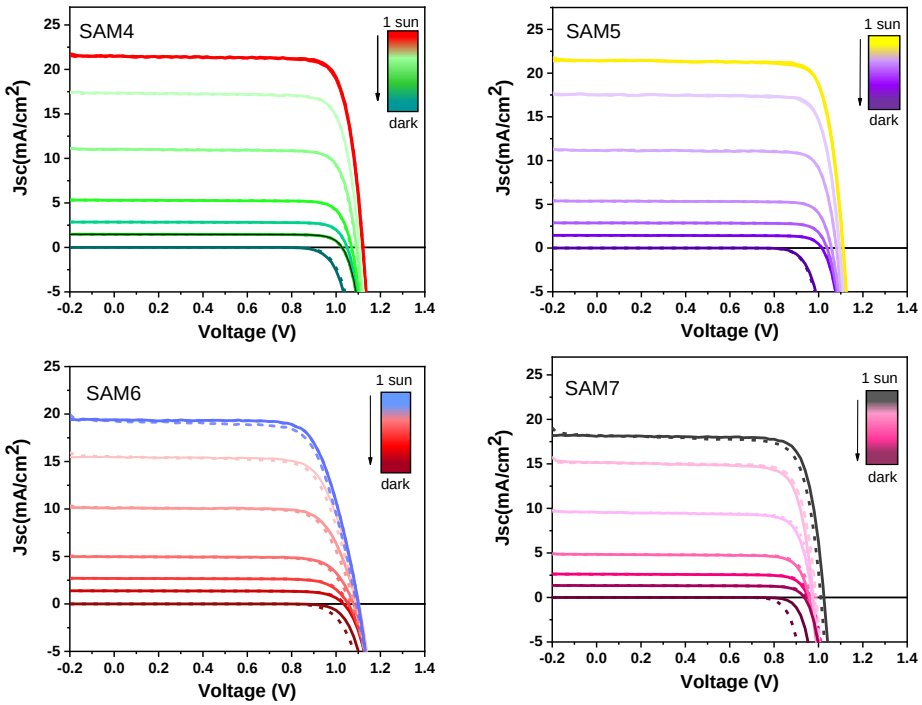

Figure 5.10 The J-V curves in forward (solid line) and reverse (dash line) of the devices based on SAMs over different light intensities from 1 sun to dark (100, 81.3, 51.5, 25.2, 12.6, 5.1 mW/cm^2).

We first analysed the Jsc dependence with light with a power-law formula of Jsc proportional to $P_{light}\,\alpha^{-1}$, in which α is the exponential factor related to biomolecular recombination degree.

From the data collected from J-V curves versus light intensity (Figure 5.10), the fitted α values for SAM4, SAM5, SAM6, and SAM7 were 0.998, 0.972,

0.958, and 0.95, respectively and 1.02 for EADR03 (Figure 5.11a). The α values were closer to unity (α ≈ 1), as aforementioned in Chapter 2, it can be indicated that the ratio of photons to electrons remained constant with decreasing light intensity, meaning that there are no significant photocurrent losses at these conditions and the SAMs suppress the biomolecular recombination.[104,112] In this context, SAM4 and SAM5 can effectively suppress the recombination and trap states at the interfaces, which is consistent with the improvement in Jsc, the small drop in the α of SAM6 and SAM7, on the other hand, exhibits a significant decrease in the Jsc. Then, we evaluated Voc dependence with P_{light} (Figure 5.11b) and the liner fit follows equation 1:

$$V_{oc} = \frac{K_B T}{n_{id} q} In\ P_{light} \qquad (1)$$

where n_{id} is the ideality factor which indicates how far the solar cell deviates from ideal diode performance (see Chapter 2). The $n_{id} \cong 1$ is attributed to band-to-band recombination, while $n_{id} = 2$ suggests that trap-assisted recombination (monomolecular recombination) is predominant in the device.[113,114] The highest value of $n_{id} = 1.28$ was found for EADR03 in comparison with the values for SAM4, SAM5, SAM6 and SAM7 (1.18, 1.19, 1.01 and 1.06, respectively), suggesting that our SAMs minimise defect-related to Shockley-Read-Hall (SRH) recombination.[115] Moreover, SAM5 device has the lowest dark current compared to other counterparts (Figure 5.11c), including the reduced nonradiative recombination at SAM5 and perovskite interface.

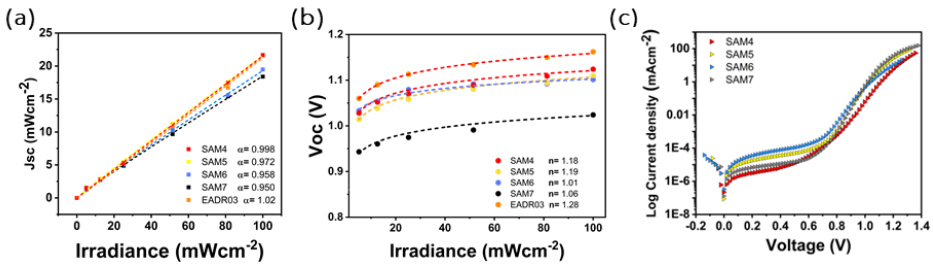

Figure 5.11 Device performance parameters: (a) current density and (b) open-circuit voltage versus light intensity. (c) Current density under dark of the best cells with each SAM. The data were extracted from the *J-V* curves versus light shown in Figure 5.10.

Optoelectronic transient techniques

After that, **SAM4**, **SAM5**, **SAM6**, **SAM7** and the reference EADR03 self-assembled molecules were also further analysed by CE and TPV as previously reported in **Chapter 4**. CE technique was also validated for all the self-assembled molecules by comparing the CE and TPV decays at 1 Sun illumination conditions (see **Fig. 5.12** and **Table 6**).

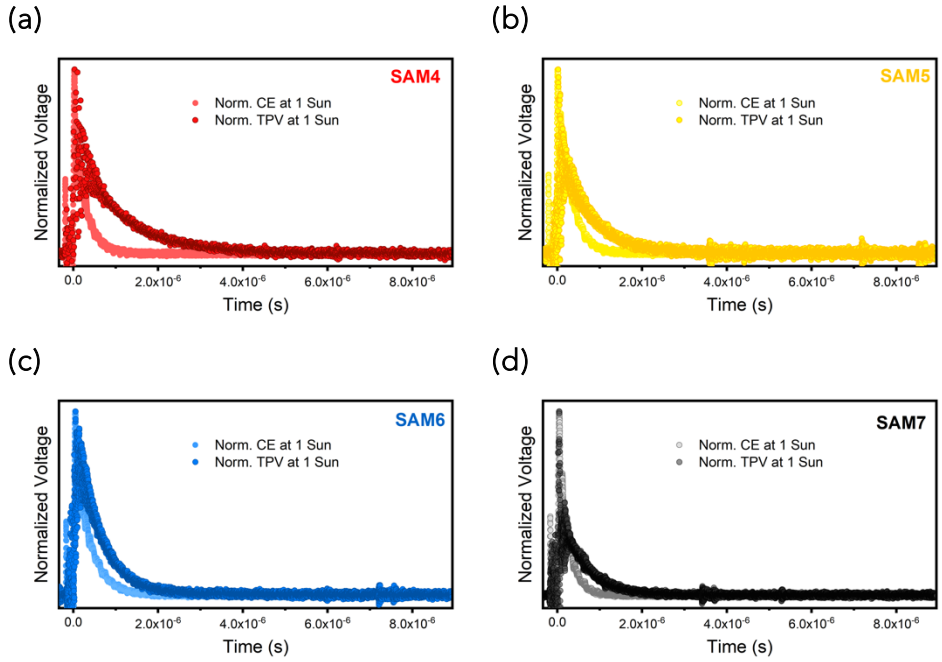

Figure 5.12 The CE and TPV decays under 1 Sun illumination conditions for **SAM4** (**a**), **SAM5** (**b**), **SAM6** (**c**) and **SAM7** (**d**).

Table 5.6 CE and TPV decays lifetime at 1 Sun illumination conditions. Two diodes of every molecule are shown, indicating reproducible results.

	CE (μs)	TPV (μs)
SAM4	0.24	1.15
SAM4_b	0.308	0.593
SAM5	0.326	0.827
SAM5_b	0.294	0.792
SAM6	0.416	0.696
SAM6_b	0.365	0.598
SAM7	0.224	0.761
SAM7_b	0.214	1.09
EADR03	0.226	0.785
EADR03_b	0.341	0.662

Figure 5.13 shows the photo-generated charges for the different devices. The charges in the bulk (solid lines) present a more pronounced slope at lower voltages for SAM4, SAM5, SAM6, and SAM7, in comparison to EADR03, meaning that the energy offsets concerning the perovskite valence band (VB) are better aligned for EADR03.

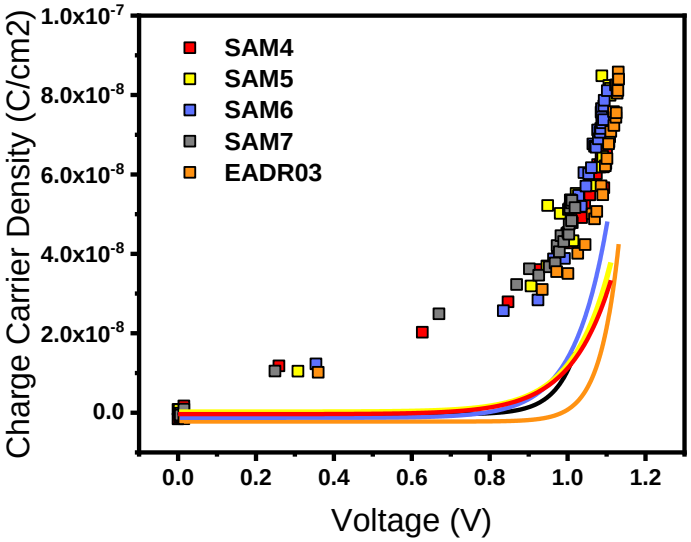

Figure 5.13 Charge density under different open circuit voltages due to the various illumination conditions with Cgeo and without Cgeo. The solid lines at the bottom are the experimental part of the fits: y= Be^{Cx} (chemical capacitance) after subtracting the Cgeo (linear part).

Figure 5.14 show the carrier lifetime versus V_{OC} and charge. The dashed vertical black line in Figure 5.14b compares the differences in carrier lifetime at an equal charge value. The recombination kinetics between the different self-assembled molecules is inside the same order of magnitude. Still, interestingly, SAM7 and EADR03 show faster and slower recombination lifetimes, respectively, as observed in J-V measurements.

As shown in Chapter 4, δ is a parameter that describes the recombination order of the photovoltaic devices. From Figure 5.15, we obtained the recombination orders of the devices containing different self-assembled molecules: δ(SAM4) = 1.40, δ(SAM5) = 1.45, δ(SAM6) = 1.27, δ(SAM7) = 1.31, and δ(EADR03) = 1.38. The deduced recombination orders are once again very alike and confirm that devices are all ruled by first-order (δ=1) which corresponds to the trap-assisted recombination.

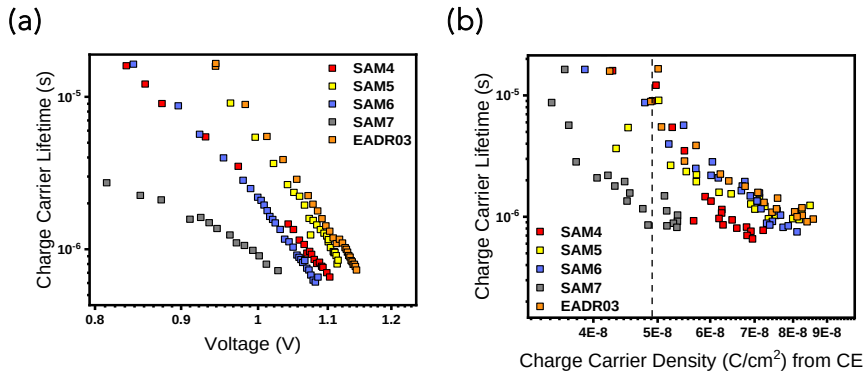

Figure 5.14 TPV measurements versus V_{OC} (**a**) and versus charge density (**b**) for the different self-assembled molecules.

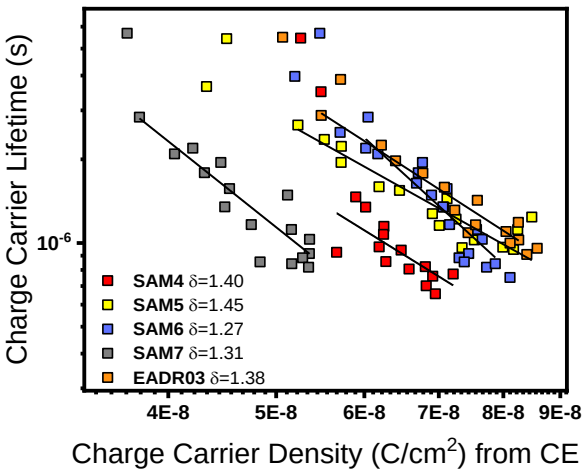

Figure 5.15 Charge carrier lifetime versus charge carrier density indicates the recombination orders.

Effect of PEAI as interlayer on SAM and perovskite interfaces

Finally, for further tests to analyse the effect of the terminal group at the SAM/perovskite interface, we introduced the phenethylammonium iodide (PEAI) cation as an interlayer at both HTL/perovskite and perovskite/ETL interfaces. The PEAI has been previously reported for this type of structure device,[107,116] since it induces high-quality film formation on top of the HTM, improving the cells performance.[117,118] A set of devices based on the champion molecule (SAM5) with and without PEAI as an interlayer were fabricated without further optimisation. For the PEAI interlayer, we adopted the strategy developed by Degani M. et al.,[116] who used a low concentration of PEAI (0.5 mM) in the pre-wash and antisolvent steps, which is already present in the device fabrication of reference devices.

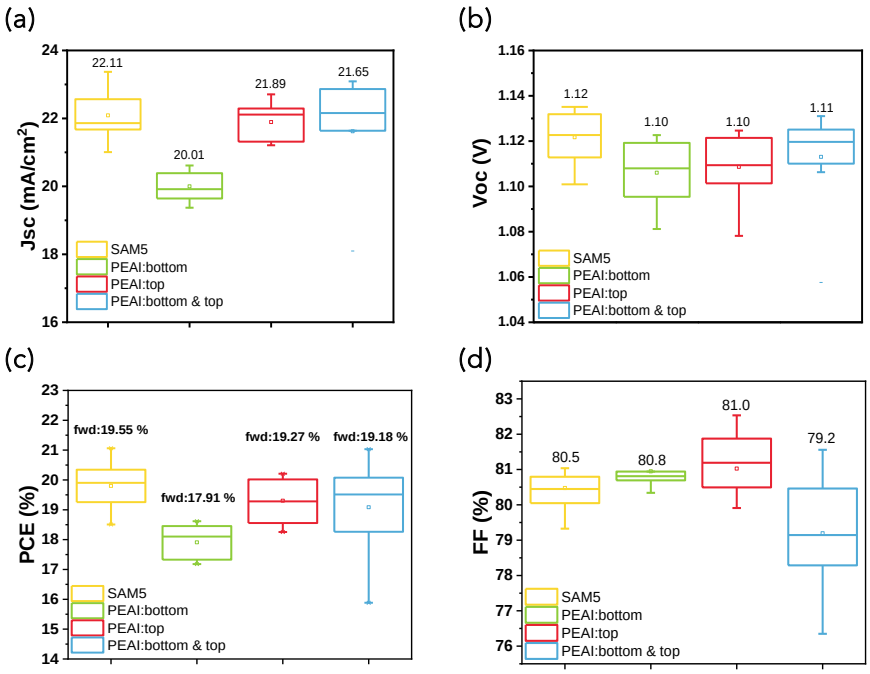

Figure 5.16 Statistical distribution of the photovoltaic parameters obtained for perovskite devices with SAM5 as HTM and with PEAI deposited at different solar cell interfaces. J-V curves were measured under 1 Sun conditions.

In Figure 5.16, a statistical distribution of the devices based on the incorporation of PEAI at the bottom (PEAI-b), top (PEAI-t) and both (PEAI-bt) interfaces of the CsFAMA layer. For this analysis, we used the values obtained from the forward scan of the J-V curves since these devices exhibited too low hysteresis. By comparing the different parameters obtained from the J-V curves, the PCE, Jsc, and Voc showed a similar trend (SAM5 < PEAI-t ≈ PEAI-b < PEAI-bt). On the other hand, a slight enhancement is observed in the FF when the PEAI-t is introduced to the perovskite layer. This improvement can be attributed to the enhanced perovskite/ETM interface, as shown by the fact that the values decline when the PEAI is deposited above and below the perovskite. These findings suggest a potential correlation between the functional group of SAM5 and the perovskite, which contributes to the overall performance of the solar cell. In addition, this topic has been thoroughly examined where the S atoms on the thiophene ring are expected to bond with the Pb atoms to the perovskite layer.[104,112] However, further studies are required to demonstrate their interaction.

5.3 Conclusions

In summary, various new carbazole-based SAMs with functional group-engineered substituents were synthesised efficiently and effectively. SAMs are obtained in a few scalable synthetic procedures from simple and affordable starting materials, potentially resulting in decreased production costs compared to the most widely used PTAA. The HOMO and LUMO energy levels of each SAM were determined based on the UPS measurements, the UV-Vis and PL spectra, and they agreed with the perovskite material's energy levels. Self-assembled molecules proved to be useful as an assistant in reducing the charge recombination where the α and n_{id} values close to 1 indicate that hole injection from the valence band of perovskite into the HOMO of SAMs which is in pair with that of EADR03. Moreover, the photoluminescence quenching observed corresponds to an efficient hole transfer which is correlated with the performance of the iPSC. However, a deeper analysis of the photovoltaic parameters leads to the finding that different moieties in carbazole-based compounds had an essential effect on iPCE performance. A power conversion efficiency of 19.8% was achieved utilising SAM5 as HTM with the inverted configuration ITO/SAM/CsFAMA/PCBM/BCP/Ag, comparable to EADR03 efficiency (20.18%). When we integrated an extended π-conjugation system into the functional group, it creates an energetically well-suited interface to the perovskite absorber. This enables efficient hole transport, electron blocking and surface passivation of the perovskite, minimising the energy losses. We can confirm that adding a phenyl spacer between the carbazole-core and terminal group in SAM5 improves performance due to all the aforementioned features. The current findings pave the way for developing low-cost and efficient self-assembled molecules based on the carbazole building block for iPSCs with improved efficiency.

More importantly, our detailed analysis allows us to determine differences in passivation quality, selectivity, and hole transfer rate depending on the structure of the SAM, especially in the terminal group.

CHAPTER 6

Exploring the Influence of Organic Hole Transport Materials with Diverse Terminal Groups by Extending the Conjugation in Thiophene-core for Their Use in Perovskite Solar Cells

Herein we present a new family of small molecules derived from carbazole moieties with thiophene or bithiophene as the core, designed for utilization as hole transporting materials in regular perovskite solar cells. HTM-1, HTM-2, HTM-3 and HTM-4 were designed and synthesized using a straightforward synthetic route with a simple purification procedure. The characterization of their thermal, optical, and electrochemical properties highlights their potential as promising hole transporting materials for efficient perovskite solar cells. Particularly, HTM-1 demonstrates a power conversion efficiency of 16% with the use of dopants and 11% without dopants.

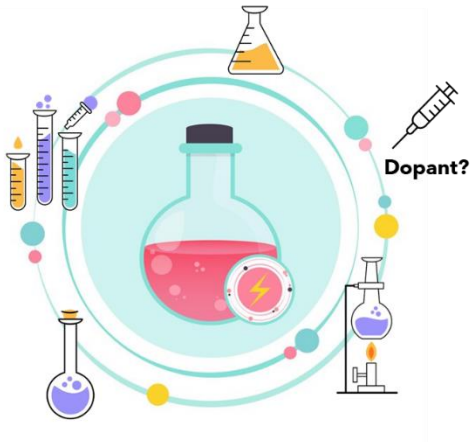

CHAPTER 6

6.1 Introduction

The efficiency of perovskite solar cells (PSCs) has notably improved in recent years, owing to the advancements in the perovskite semiconducting materials and the charge transporting materials used in the devices. These progressions are particularly associated with the materials that compose the hole-transporting layer for charge extraction, known as hole-transporting materials (HTMs), among other material components.[21] To date, 2,2′,7,7′-tetrakis[N,N-di(4-methoxyphenyl)amino]-9,9′-spirobifluorene (spiro-OMeTAD) stands out as the most widely used HTM in regular PSCs, traditionally applied heavily doped. However, the use of dopants and additives promote the chemical degradation of the devices due to their hygroscopic nature. Moreover, the cost of spiro-OMeTAD is high due to its multi-step synthetic procedure, as well as the need to use it combined with dopants and additives, making it challenging for scalable production.[32,119] Despite significant efforts to develop new alternatives to spiro-OMeTAD, a fundamental study is needed in establishing criteria that define the relationship between structure of HTMs and the required properties, especially in conjunction with its surrounding layers. A promising strategy to solve these challenges involves the design of organic dopant-free HTMs by a simple synthetic procedure, featuring special groups that act as a protective barrier against moisture. Additionally, this approach serves to enhance the understanding of the correlation between the structure of the HTM, its influence on the interface with the surrounding layers, as well as the performance of the device.

In this study, four new small molecules (SMs) with the structure donor-π-core-donor (D-π-D) type have been designed as HTMs. The structure is made of thiophene or bithiophene as a central core (π) linked to different carbazole-based electron donor side arms (D) and they are synthesised by relatively simple synthetic procedures. Moreover, these molecules present good solubility in common organic solvents, as well as thermal, electrochemical and photochemical stability. Finally, we have applied these molecules as HTMs in regular PSCs to study the effect on device performance.

6.2 Results and Discussion

Design and Synthesis

The previous Chapter reports the use of carbazole derivatives with electron-donor groups with strong electron-donating character and good hole-transporting properties. In this study, we employed a similar strategy by synthesizing two carbazole-based units functionalized with electron-rich groups. The molecular structures are depicted in Figure 6.1 comparing to the fragment unit of spiro-OMeTAD. Firstly, we synthesized compound **35**, which displays a structure similar to the electron donating fragment of spiro-OMeTAD (*p*-methoxydiphenylamine), which has been extensively used as hole-transporting molecules.[65,120,121] On the other hand, 2,4-dimethoxybenzene-subtituted carbazole **42**, was also selected due to its ability to tune optical and electrical properties, enhancing the perovskite film, among other discoveries from our previous studies.[70,76] Both compounds were easily synthesized from commercially available starting materials, in a good agreement with previous report (detailed information can be found in Chapter 3).

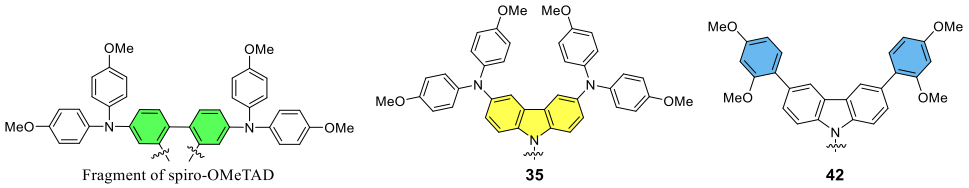

Figure 6.1 Electron donor derivatives units from spiro-OMeTAD and those employed in this work

Furthermore, to use them as the final HTMs, we incorporated a thiophene or bithiophene bridge in the structure. The aim was to improve the HTM layer by reducing the random distribution due to strong intermolecular interaction between S---Pb, as observed in our previous work reported in Chapter 5 and documented in the literature.[104]

In this work, the hole-transporting molecules are classified based on the aforementioned electron-donor units (**35** and **42**), namely, Group I) **HTM-1** and **HTM-2**; and Group II) **HTM-3** and **HTM-4**. It is worth mentioning that in this study, we initially synthesized and tested **HTM-1** and **HTM-2** (group I) in PSCs. Encouraged by the preliminary results, we subsequently proceeded to synthetise **HTM-3** and **HTM-4** (group II). The division into

groups is based on this progression. The general procedure for the synthesis of HTM-1, HTM-2, HTM-3 and HTM-4, shown in Scheme 6.1, employs a one-step Buchwald-Hartwig coupling reaction. The detailed synthesis is provided in Chapter 3. All the final SMs are soluble in common organic solvents, facilitating their deposition in the PSCs.

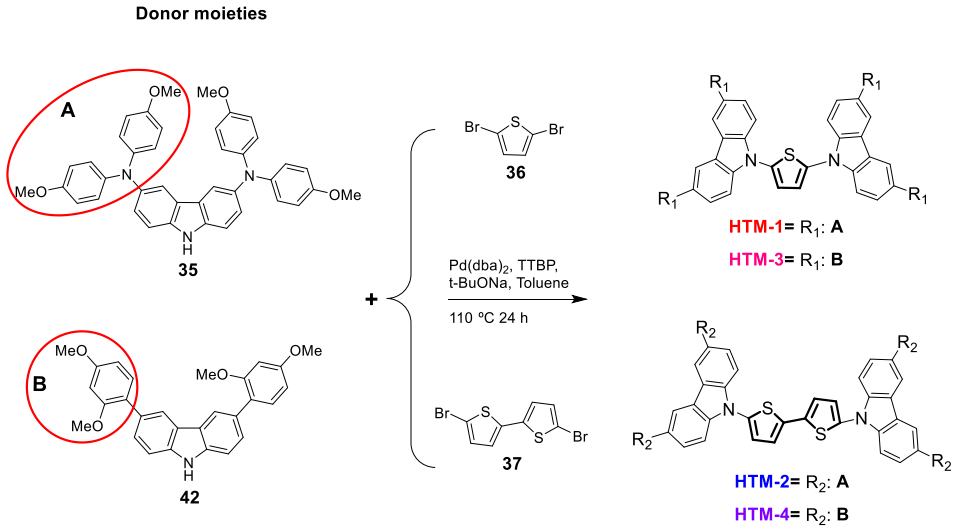

Scheme 6.1 Simplified synthesis route for the new compounds as linear D-π-D HTMs.

Thermal, Optical and Electrochemical Properties

First, the electronic structures of HTM-1, HTM-2, HTM-3 and HTM-4 were determined by using electrostatic surface potential (ESP). As is well known, this kind of compounds form a layer of randomly deposited molecules, playing a pivotal role the molecular geometries and charge distribution. For the purpose of better visualising ESP, the images are not displayed horizontally but rather according to their planarity, which in these compounds is pretty similar.

As displayed in ESP (Figure 2), the red, blue and green regions represent positive, negative and neutral charges, respectively. As can be seen, the partial positive electron density (δ^+) are located in the C–C, C=C, C-H (from thiophene group) and CH_3– (from methoxy group), while the negative electron density (δ^-) is around on carbazole unit and oxygen atoms of methoxy group. It is worth noting that carbazole unit has more negative charges in group II compared with group I, which could result in different stacking modes at the perovskite surface.

In relation to the same donor unit, group II have a more partial δ^+ and δ^- electron density along their structure, after S---Pb interact, is expected the formation of a dipole moment (δ^-/δ^+) of HTM on the perovskite surface.[122,123]

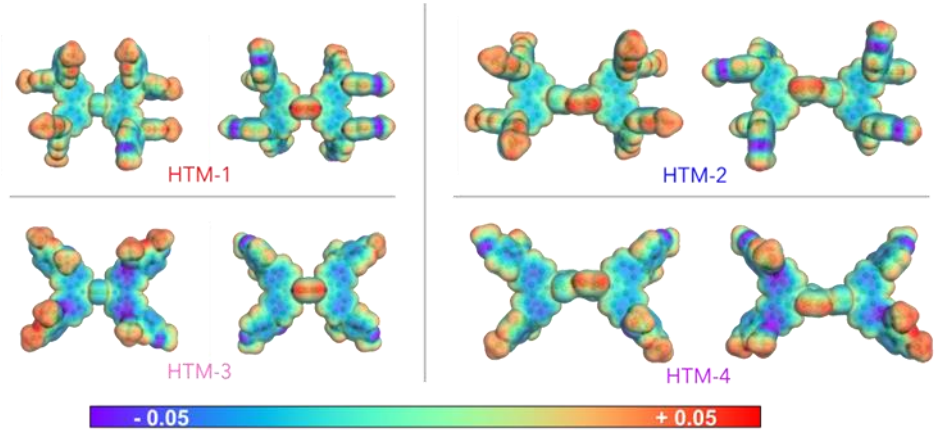

Figure 6.2 Tops view of electrostatic surface potential images of all the HTMs.

The thermal characteristics of the synthesized HTMs were determined by thermogravimetric analysis (TGA) and differential scanning calorimetry (DSC) measurements (**Figure 6.3**). All HTMs exhibit good thermal stability, showing relatively high decomposing temperature (T_{dec}), defined as the temperature where the weight loss is of 5%, above of 430 °C (**Figure 6.3a**). Moreover, it can be observed a slight increase in the T_{dec} of the molecules with variations in the donor moiety of the HTMs, following the trend **HTM-1≈HTM-2<HTM-3≈HTM-4** (Group I < Group II).

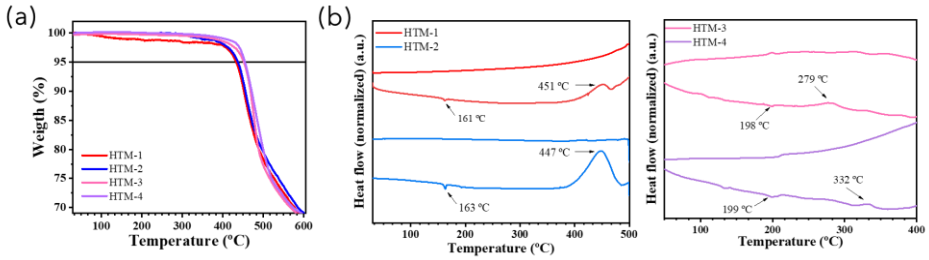

Figure 6.3 Thermal measurements of all HTMs. (**a**) Thermogravimetric analysis (TGA) data obtained with a heating rate of 10 °C/min under N_2 atmosphere; and (**b**) Differential scanning calorimetry (DSC) second heating curves, obtained with scan rate 5 °C/min under N_2 atmosphere.

The thermal transitions of the HTMs were studied by DSC (Figure 6.3b). During the second heating scan, both glass transition (T_g) and crystallization (T_{cr}) process were observed for all the compounds. This indicates that all the compounds exhibit stabilized amorphous states at the temperature range where the devices are prepared. Furthermore, a similar effect to that observed in T_{dec} is noted, with an increase in T_g ranging from 160 to 190 °C attributed to variations in the donor moiety(Group I < Group II).

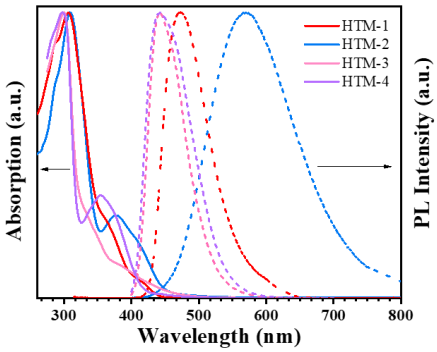

Figure 6.4 UV-Vis absorption (solid line) and photoluminescence (dashed line) spectra normalised at the peak value of all the synthesized HTMs (10^{-3} mM in DCM).

The normalised UV-Vis absorption and emission curves of the synthesised HTMs are shown in Figure 6.4. The absorption maxima bands (λ_{abs}) are centred around 300 nm. As expected, an extra π-π^* transition is induced by introducing a bithiophene-core (HTM-2 and HTM-4), where an additional shoulder is noticed, making the absorption of this derivatives broad. Emission spectra show maxima centred at 471 nm for HTM-1 and 442 nm for HTM-3 and HTM-4. In contrast, HTM-2 exhibits relatively large PL emission at 568 nm, suggesting significant changes in geometrical configuration of the molecules upon excitation. Additionally, the Group II (HTM-3 and HTM-4) increased the bandgap, implying that an electron moves with less energy and light.[120,124] The optical bandgap (E_g) was estimated at the intersection of normalised UV-Vis and PL spectra for each molecule (λ_{onset}). All the aforementioned thermal and optical properties of the new compound are summarized in the table below.

Table 6.1 Thermal and optical properties of the synthetised HTMs

	T_{dec} (°C)[(a)]	T_g (°C)[(b)]	T_{cr} (°C)[(b)]	λ_{abs} (nm)[(c)]	λ_{em} (nm)[(c)]	E_g [(d)]
HTM-1	433	161	451	307	473	2.93
HTM-2	437	163	447	309	570	2.78
HTM-3	451	198	279	300	443	3.04
HTM-4	455	199	332	298	442	3.06

[(a)] Decomposition temperature determined from TGA (5 % weight loss); [(b)] T_g and T_{cr} are extracted from the second heating curve of DSC; [(c)] UV-Vis absorption and emission spectra normalized at the peak value; [(d)] E_g is calculated as $E_g = 1240/\lambda_{onset}$ (where λ_{onset} is the point where the normalized absorbance and emission spectra overlap).

As discussed in previous chapters, the alignment of the molecular energy levels is a crucial step in the design of new HTMs. The electrochemical properties of the new HTMs were studied using cyclic voltammetry (CV) to determine the HOMO levels. As illustrated in **Figure 6.5**, the voltammogram of each group show similar oxidation waves. Both groups exhibit two reversible oxidation waves attributed to the oxidation process of the carbazole units and central core. Whereas Group I (**HTM-1** and **HTM-2**), displays an additional wave assigned to the diphenylamine units. The HOMO levels were estimated from the first half-wave oxidation potential ($E_{1/2}$) vs Fc^+/Fc and all the data are collected in **Table 6.2**. The molecules present an almost identical HOMO around 4.9 eV with a small ~5 meV difference that rarely influences the hole transfer from the perovskite (5.63 eV)[79] to the HTM. However, the different arrangements of both the thiophene-core and the entire molecule may result in final molecules exhibiting varied steric effects, consequently influencing their behaviour in the performance of PSCs. Finally, the estimated LUMO level are found to be -2.00 eV, -2.14 eV, -1.94 eV and -1.92 eV for **HTM-1**, **HTM-2**, **HTM-3** and **HTM-4**, respectively. Detailed information of the calculation of the HOMO and LUMO energy levels can be found in **Chapter 2**.

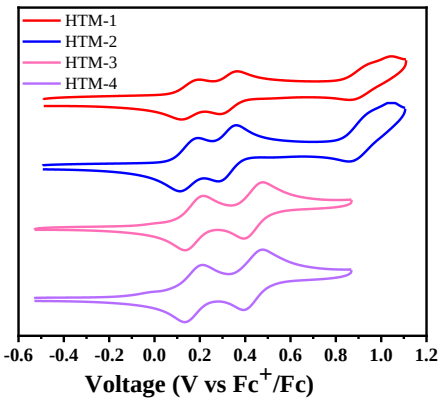

Figure 6.5 (a) Cyclic voltammograms of carbazole-based HTMs with Fc^{+}/Fc as an internal standard.

Table 6.2 Oxidation potential, HOMO and LUMO energy levels of new HTMs.

	$E_{p\text{-doping}}$ [a] (V)	$E_{p\text{-dedoping}}$ [b] (V)	$E_{1/2}$ [c] (V)	HOMO [d] (eV)	LUMO [e] (eV)
HTM-1	0.16/0.32/0.99	0.084/0.25/0.82	0.12	-4.92	-2.00
HTM-2	0.16/0.33/1.01	0.083/0.25/0.83	0.12	-4.92	-2.14
HTM-3	0.21/0.48	0.14/0.40	0.17	-4.97	-1.94
HTM-4	0.21/0.49	0.13/0.39	0.17	-4.97	-1.92

[a]$E_{p\text{-doping}}$ and [b]$E_{p\text{-dedoping}}$ are extracted graphically from p-doping and p-dedoping CV reversible curves; [c]$E_{1/2}$, first half-wave potential [d] estimated from $E_{HOMO} = -(E_{1/2}$ vs $E_{Fc} + 4.8)$ [e]calculated from $E_{LUMO} = E_{HOMO} + E_g$.

Hole Mobility Measurements

To demonstrate the ability of **HTM-1** and **HTM-2** act as HTMs, first we evaluated the hole mobility by Space-Charge Limited Current (SCLC) method. For this purpose, SCLC measurements were performed using a hole-only device structure: ITO/PEDOT:PSS/HTM/Au, in comparison to the reference spiro-OMeTAD. The hole mobility (μ) values of **HTM-1** and **HTM-2** were obtained using the modified Mott-Gurney equation:

$$J_{SCLC} = \left(\frac{9}{8}\right)\varepsilon_0\varepsilon_r \cdot \mu\left(\frac{V_{eff}}{d^3}\right) \qquad \text{EQUATION 20}$$

Where, d represents the thickness of HTMs (~100 nm), V_{eff} denotes the effective applied voltage (ranging from 1 to 5 V) and the dielectric

constant ($\varepsilon_0\varepsilon_r$) is chosen as 3, based on literature values for organic semiconductors.[125,126] The current-voltage (J-V) curve and the corresponding calculated μ are show in Figure 6.6. Instead of relying on the hole recombination, the concentration of charge carriers and the dielectric field in the device are estimated based on hole mobility. The values obtained without chemical dopants for HTM-1 and HTM-2 were 2.14 E^{-5} $cm^2/V{\cdot}s$ and 2.02 E^{-4} $cm^2/V{\cdot}s$, respectively. This indicates enhanced charge transport properties of the bithiophene-based HTM (HTM-2), similar to those of spiro-OMeTAD (1.96 E^{-4} $cm^2/V{\cdot}s$).

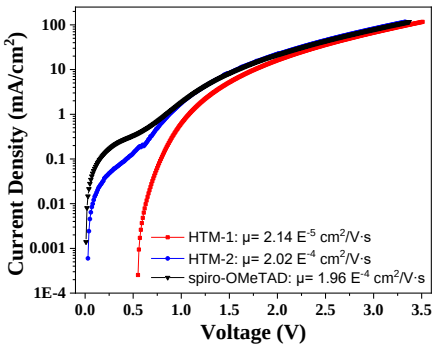

Figure 6.6 Mobility measurements for HTM-1, HTM-2 and spiro-OMeTAD using the SCLC method.

Photovoltaic Performance

Finally, the photovoltaic performance was evaluated in regular PSC to study the impact of HTM-1 and HTM-2 with and without doping. The effective operation of PSCs relies significantly on the precise alignment of energy levels of the components. This alignment is crucial for facilitating charge transport, extraction and minimizing interface recombination, thereby optimizing the overall performance.[127]

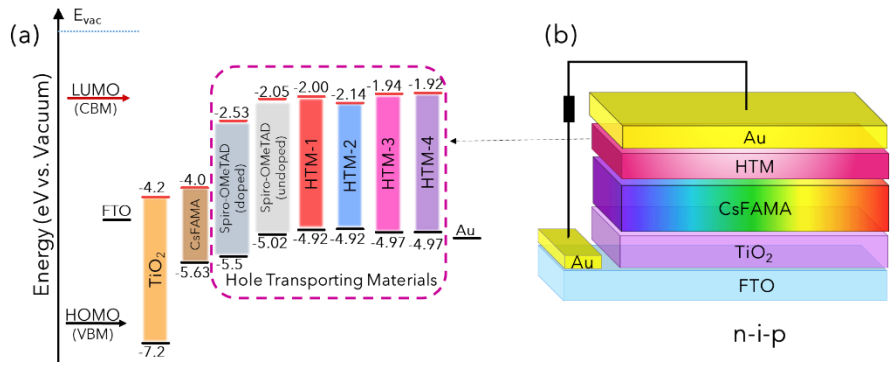

Figure 6.7 (a) Energy levels of the components in the PSC devices employing spiro-OMeTAD for comparison purpose and (b) the device structure scheme in the n-i-p configuration. The energy level values for the CsFAMA, spiro-OMeTAD (doped and undoped), TiO_2, FTO and Au values are extracted from the literature.[79,128]

In **Figure 6.7a**, the energy levels of components are illustrated within the PSC. It is evident that the HOMO energy values of the synthetised HTMs are closely aligned with those of undoped spiro-OMeTAD. Moreover, The HTMs exhibit higher energy levels upon comparing their HOMO levels with the valence band of CsFAMA (-5.63 eV), facilitating the hole transfer from the perovskite to the HTM.

The devices were fabricated with the following structure: FTO/c-TiO_2 & m-TiO_2/LiTSI/$(Cs_{0.05}(FA_{0.85}MA_{0.15})_{0.95}Pb(I_{0.85}Br_{0.15})_3$ (CsFAMA)/HTMs/Au (**Figure 6.7b**). We prepared and compared the devices prepared with HTMs with spiro-OMeTAD (doped) under the same fabrication conditions (see for details **Chapter 2,**). The performance parameters of the PSCs were extracted from the current-voltage curves measured under 1 Sun illumination (100 mW/cm^2) at scan rate of 40 mV/s and are summarized in **Table 6.3**. As depicted in **Figure 6.8**, the J-V curves present hysteresis behaviour, wherein the PCE is higher in the forward scan (fwd) than in the reverse scan (rev). This result suggests the existence of the ion migration or recombination in PSCs,[111,129] indicating a need for further investigation into hysteresis behavior. The best PCE of the **HTM-1** and **HTM-2** are 16.3% and 15.1% respectively, showing a slight lower performance than the reference prepared with spiro-OMeTAD (19.8%). To further improve the device performance, the concentration and solvents of the synthetised HTMs will be optimized to obtain better and uniform films.

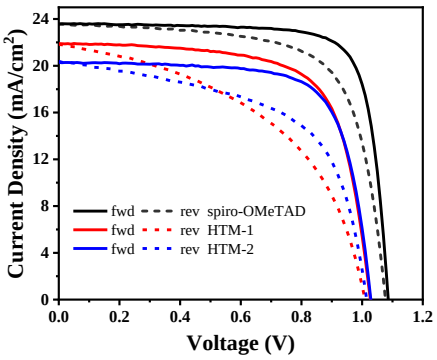

Figure 6.8 Best J-V curves measurements from preliminary studies on **HTM-1** and **HTM-2**, utilizing the same solution concentration and chemical dopants as spiro-OMeTAD for comparison.

Table 6.3 The preliminary solar cells performance parameters extracted from the J-V curves in **Figure 6.8.**

HTM	Sweep	J_{sc} (mA/cm^2)	V_{OC} (V)	FF (%)	PCE (%)
HTM-1	rev	22.97	1.010	48	11.1
	fwd	22.82	1.027	69	16.3
HTM-2	rev	20.40	1.015	56	11.6
	fwd	20.30	1.029	72	15.1
Spiro-OMeTAD	rev	23.83	1.077	69	17.8
	fwd	23.44	1.086	78	19.8

*HTMs are under the same solution conditions and dopants as spiro-OMeTAD.

One of the objectives is to comprehend the impact of the HTM/perovskite interface by examining the modifications in the structures of HTMs. For this purpose, it is crucial to understand the behavior of PSC devices without doping. We selected the **HTM-1** as the most efficient HTM of the series and prepared PSCs by employing **HTM-1** with and without doping, as well as using spiro-OMeTAD as reference. Summarized device performance parameters are reported in **Table 6.4** extracted from the J-V curves data in **Figure 6.9 (a)** and **(b)**. The maximum PCE of the prepared devices with doped HTM-1 and doped spiro-OMeTAD was 15.6% and 18.9% respectively, whereas undoped **HTM-1** was 5.5%. However, a high hysteresis was observed for all HTMs. Generally, the device performance improves after some days, due to the reduction of both ion migration or

recombination and oxidized species, particularly at the charge transporting materials and perovskite interfaces.[130-132] For the aforementioned, the performance was measured after three and eight days after their elaboration. The undoped **HTM-1** showed an impressive improvement with PCE from 5.5% to 11.5%. In addition, all the HTMs present less hysteresis.

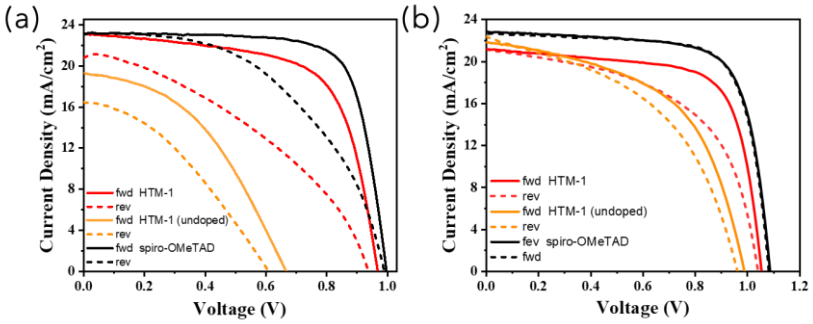

Figure 6.9 The best J-V curves of PSCs based on **HTM-1**, both doped and undoped, using spiro-OMeTAD as reference under the same solution condition, measured (a) after 3 days, and (b) after 8 days.

Table 6.4 The photovoltaic parameters of the champion cells of devices based on **HTM-1** with and without doping, using spiro-OMeTAD for comparison, measured 3 and 8 days after fabrication.

HTM	Day	Sweep	J_{sc} (mA/cm^2)	V_{OC} (mV)	FF (%)	PCE (%)
HTM-1	3	fwd	22.93	985	49	11.1
		rev	22.85	1008	68	15.6
	8	fwd	**21.12**	**1043**	**54**	**12.0**
		rev	**21.14**	**1056**	**70**	**15.7**
HTM-1 (undoped)	3	fwd	16.36	610	37	3.7
		rev	19.28	668	43	5.5
	8	fwd	**22.36**	**964**	**47**	**10.1**
		rev	**21.81**	**990**	**53**	**11.5**
Spiro-OMeTAD	3	fwd	23.13	1055	62	15.2
		rev	23.32	1069	76	18.9
	8	fwd	**22.83**	**1089**	**73**	**18.1**
		rev	**22.64**	**1084**	**74**	**18.1**

*HTM-1 and spiro-OMeTAD are doped under the same solution conditions

As a previously mentioned, the synthesis of group II (HTM-3 and HTM-4) was inspired by these preliminary results obtained from the first group (HTM-1 and HTM-2). This was done to further investigate the molecular structure, specifically examining the impact of donor moieties and the core. The device fabrication is still under optimization, as well as the layer preparation of the new compounds. Once these optimizations are completed, further studies will analyse the impact of HTMs on their surrounding layers.

6.3 Conclusions

In this study, we designed and synthesised four new small molecules based on carbazole-derivatives moieties with thiophene or bithiophene as the core. These new compounds are easy to obtain through a straightforward synthetic route with a simple purification procedure, making them candidates for cost-effective upscaling. Their thermal, optical and electrochemical properties were characterized, demonstrating their potential as good HTM candidates for efficient PSCs. Based upon these preliminary findings, we have obtained a promising PCE of ~16, and ~15% for HTM-1 and HTM-2, respectively, all under identical conditions. Notably, undoped HTM-1 achieved a PCE of 11.5% which is comparable to its counterpart with doping. Based on the above findings, we have observed how the molecular structure plays a pivotal role to modulate the optoelectronic properties of the HTMs, which in turn affects the interfacial charge transfer in PSCs. In this sense, the di(4-methoxyphenyl) amine derivative provides higher photocurrent, although similar V_{oc} and lower FF, than the 2,4-dimethoxy phenyl substituent. Both HTM-1 and HTM-2 show similar HOMO levels, but HTM-2 has higher hole mobility which is not translated into higher efficient devices. Therefore, further characterization of the interface will be required to fully understand the relationship between structure and performance.

CHAPTER 7

General Conclusions

The main objective of this thesis was to develop new organic small molecules to be applied as hole transporting materials in perovskite solar cell devices. Through judicious design and molecular engineering, new hole transporting molecules have been synthesised, characterised, and applied in inverted or regular perovskite solar cells. These materials have been used to study the complex relationship between their molecular structure and its surrounding layers, in particular the perovskite layer. The research aim was to gain a fundamental understanding of the essential characteristics required for an effective hole-transporting material, through molecular modifications of different carbazole-based hole-transporting materials in order to tune their diverse properties and facilitate their operation in efficient perovskite solar cells.

SUMMARY

This section will provide a concise explanation of the thesis' overall conclusion for each chapter.

In Chapter 4, we have successfully synthesized and characterised three new carbazole-based self-assembled molecules, featuring different linker and functional groups. These compounds were evaluated using various techniques such as TGA, UV-vis, CV and PL measurements, followed by testing in inverted perovskite solar cells, where they demonstrated promising power conversion efficiencies. Notably, SAMs containing the phenyl linker group (SAM 1) exhibited the best device performance, achieving an efficiency of 18.9% and excellent stability. Furthermore, we investigated the impact of different side arms into the carbazole-core on the chemical, physical properties of the SAMs, establishing a clear relationship between the SAM molecular structure and device performance Thus, the triphenylamine derivatives produce smaller grain size distributions in the perovskite layer which did not resulted in higher efficiencies than the other derivatives.

Finally, all the new compounds were utilised to study the interfaces between ITO/SAM and SAM/perovskite, providing valuable insights for the future design of SAMs and the fabrication of efficient perovskite solar cells.

In Chapter 5, we have further employed ethyl 4'-(*9H*-carbazol-9-yl)-[1,1'-biphenyl]-4-carboxylate as a starting molecule functionalized with different electron-rich groups attached to the carbazole-core in a simple two or three synthetic steps, potentially resulting in decreased production costs compared to the widely used PTAA in inverted perovskite solar cells. The energy levels of the SAMs were determined using UPS measurements, UV-Vis, and PL spectra, aligning well with the energy levels of the perovskite material. Furthermore, it was shown that the integration of an extended π-conjugation system into the functional group facilitated an energetically well-matched interface with the perovskite absorber, allowing efficient hole transport, electron blocking, and surface passivation, thus minimising energy losses. Deeper analysis revealed that different units in the carbazole-based compounds significantly affected device performance, where a power conversion efficiency of 18.4% and

19.8% was achieved utilising thiophene (SAM4) and 2-phenylthiophene (SAM5) as electron-donor units, respectively. Although through photoluminescence and optoelectronic analysis, it was found that all the SAMs facilitate efficient hole transfer and assist in reducing charge recombination, the thiophene derivatives passivate the vacancies in the perovskite layer leading to higher efficiencies. Our detailed analysis enables us to identify differences in passivation quality, selectivity, and hole transfer rate as dependent on SAM structure, particularly in the terminal group. These findings pave the way for the development of efficient and low-cost carbazole-based SAMs for the improvement of solar cell technology.

In Chapter 6, we describe four new compounds featuring one or two thiophene central cores (π) linked to different carbazole-based (D) moieties through a straightforward synthetic pathway and simple purification procedure. From characterisation of their thermal, optical and electrochemical properties, we found that they have promising properties as a dopant-free hole-transporting material for regular perovskite solar cells. Based on these first results, we were able to acquire a promising PCE of 11.5% with undoped HTM based on thiophene-core (HTM-1), which is similar to that of the doped counterpart. This suggests that the bithiophene unit has an additional interaction with the perovskite.

Despite HTMs based on different central cores exhibiting comparable HOMO levels, those with a bithiophene core demonstrated higher hole mobility. However, this increase in hole mobility did not necessarily translate into more efficient devices. To properly understand the connection between structure in this kind of compounds and the performance in regular architecture devices, more interface characterisation is currently under the progress. Similarly, the optimisation of both HTM solutions and HTM layer are being studied

In summary, the thesis presents a variety of molecules, demonstrating how minor modifications to the molecular structure, such as substituting electron donor groups or adjusting the length of the π-conjugated system by incorporating phenyl groups, can have a substantial impact on the material's properties and enhance photovoltaic performance. To achieve high-performance in perovskite solar cells, it is necessary to tune several

desirable characteristics of the hole transporting materials, including steric effects, well-aligned energy levels, hydrophobicity, and stability. The thesis presents strategies for rational design using simple synthetic schemes with straightforward procedures. These findings contribute to the development of various materials that are the starting point for even more efficient materials and facilitate the commercialization of advanced solar cell technologies.

REFERENCES

1. Bariloche, F. *SCIENCE AND ACADEMIA AEE-Institute for Sustainable Technologies (AEE-INTEC) Council on Energy, Environment and Water (CEEW)*.
2. Nayak, P. K., Mahesh, S., Snaith, H. J. & Cahen, D. Photovoltaic solar cell technologies: analysing the state of the art. *Nat Rev Mater* **4**, 269–285 (2019).
3. Wilson, G. M. *et al.* The 2020 photovoltaic technologies roadmap. *Journal of Physics D: Applied Physics* vol. 53 Preprint at https://doi.org/10.1088/1361-6463/ab9c6a (2020).
4. Snaith, H. J. Perovskites: The emergence of a new era for low-cost, high-efficiency solar cells. *Journal of Physical Chemistry Letters* **4**, 3623–3630 (2013).
5. Kojima, A., Teshima, K., Shirai, Y. & Miyasaka, T. Organometal Halide Perovskites as Visible-Light Sensitizers for Photovoltaic Cells. *J Am Chem Soc* **131**, 6050–6051 (2009).
6. Park, J. *et al.* Controlled growth of perovskite layers with volatile alkylammonium chlorides. *Nature* **616**, 724–730 (2023).
7. Renewable Energy Lab, N. *NREL Best Research Cell Efficiencies Chart*. https://www.nrel.gov/pv/cell-efficiency.html.
8. Liang, Z. *et al.* Homogenizing out-of-plane cation composition in perovskite solar cells. *Nature* **624**, 557–563 (2023).
9. Szabó, G., Park, N. G., De Angelis, F. & Kamat, P. V. Are Perovskite Solar Cells Reaching the Efficiency and Voltage Limits? *ACS Energy Letters* vol. 8 3829–3831 Preprint at https://doi.org/10.1021/acsenergylett.3c01649 (2023).
10. Qiu, L. *et al.* Interfacial engineering of halide perovskites and two-dimensional materials. *Chem Soc Rev* **52**, 212–247 (2022).
11. Mohd Yusoff, A. R. Bin *et al.* Passivation and process engineering approaches of halide perovskite films for high efficiency and stability perovskite solar cells. *Energy and Environmental Science* vol. 14 2906–2953 Preprint at https://doi.org/10.1039/d1ee00062d (2021).
12. Saliba, M. *et al.* Cesium-containing triple cation perovskite solar cells: Improved stability, reproducibility and high efficiency. *Energy Environ Sci* **9**, 1989–1997 (2016).
13. Jena, A. K., Kulkarni, A. & Miyasaka, T. Halide Perovskite Photovoltaics: Background, Status, and Future Prospects. *Chem Rev* **119**, 3036–3103 (2019).

14. Puerto Galvis, C. E., González Ruiz, D. A., Martínez-Ferrero, E. & Palomares, E. Challenges in the design and synthesis of self-assembling molecules as selective contacts in perovskite solar cells. *Chemical Science* Preprint at https://doi.org/10.1039/d3sc04668k (2023).
15. Roose, B., Wang, Q. & Abate, A. The Role of Charge Selective Contacts in Perovskite Solar Cell Stability. *Adv Energy Mater* **9**, 1–20 (2019).
16. Li, Y., Xie, H., Lim, E. L., Hagfeldt, A. & Bi, D. Recent Progress of Critical Interface Engineering for Highly Efficient and Stable Perovskite Solar Cells. *Adv Energy Mater* **12**, (2022).
17. Stolterfoht, M. *et al.* The impact of energy alignment and interfacial recombination on the internal and external open-circuit voltage of perovskite solar cells. *Energy Environ Sci* **12**, 2778–2788 (2019).
18. Liu, S., Biju, V. P., Qi, Y., Chen, W. & Liu, Z. Recent progress in the development of high-efficiency inverted perovskite solar cells. *NPG Asia Materials* vol. 15 Preprint at https://doi.org/10.1038/s41427-023-00474-z (2023).
19. Ali, F., Roldán-Carmona, C., Sohail, M. & Nazeeruddin, M. K. Applications of Self-Assembled Monolayers for Perovskite Solar Cells Interface Engineering to Address Efficiency and Stability. *Adv Energy Mater* **10**, 1–24 (2020).
20. Lin, X. *et al.* Efficiency progress of inverted perovskite solar cells. *Energy Environ Sci* **13**, 3823–3847 (2020).
21. Isikgor, F. H. *et al.* Molecular engineering of contact interfaces for high-performance perovskite solar cells. *Nature Reviews Materials* vol. 8 89–108 Preprint at https://doi.org/10.1038/s41578-022-00503-3 (2023).
22. Lyu, B., Yang, L., Luo, Y., Zhang, X. & Zhang, J. Counter electrodes for perovskite solar cells: materials, interfaces and device stability. *Journal of Materials Chemistry C* vol. 10 10775–10798 Preprint at https://doi.org/10.1039/d2tc02182j (2022).
23. Deepika, Singh, A., Verma, U. K. & Tonk, A. Device Structures of Perovskite Solar Cells: A Critical Review. *Physica Status Solidi (A) Applications and Materials Science* vol. 220 Preprint at https://doi.org/10.1002/pssa.202200736 (2023).
24. Zhao, Y. *et al.* Recent Progress in High-efficiency Planar-structure Perovskite Solar Cells. *Energy and Environmental Materials* vol. 2 93–106 Preprint at https://doi.org/10.1002/eem2.12042 (2019).
25. Liao, J. F., Wu, W. Q., Jiang, Y., Kuang, D. Bin & Wang, L. Maze-Like Halide Perovskite Films for Efficient Electron Transport Layer-Free Perovskite Solar Cells. *Solar RRL* **3**, (2019).

26. Said, A. A., Xie, J. & Zhang, Q. Recent Progress in Organic Electron Transport Materials in Inverted Perovskite Solar Cells. *Small* vol. 15 Preprint at https://doi.org/10.1002/smll.201900854 (2019).
27. Pan, H. *et al.* Advances in design engineering and merits of electron transporting layers in perovskite solar cells. *Mater Horiz* **7**, 2276–2291 (2020).
28. Rakstys, K., Igci, C. & Nazeeruddin, M. K. Efficiency *vs.* stability: dopant-free hole transporting materials towards stabilized perovskite solar cells. *Chem Sci* **10**, 6748–6769 (2019).
29. Rodríguez-Seco, C., Cabau, L., Vidal-Ferran, A. & Palomares, E. Advances in the Synthesis of Small Molecules as Hole Transport Materials for Lead Halide Perovskite Solar Cells. *Acc Chem Res* **51**, 869–880 (2018).
30. Yin, X., Song, Z., Li, Z. & Tang, W. Toward ideal hole transport materials: A review on recent progress in dopant-free hole transport materials for fabricating efficient and stable perovskite solar cells. *Energy and Environmental Science* vol. 13 4057–4086 Preprint at https://doi.org/10.1039/d0ee02337j (2020).
31. Urieta-Mora, J., García-Benito, I., Molina-Ontoria, A. & Martín, N. Hole transporting materials for perovskite solar cells: a chemical approach. *Chem Soc Rev* **47**, 8541–8571 (2018).
32. Nakka, L., Cheng, Y., Aberle, A. G. & Lin, F. Analytical Review of Spiro-OMeTAD Hole Transport Materials: Paths Toward Stable and Efficient Perovskite Solar Cells. *Advanced Energy and Sustainability Research* vol. 3 Preprint at https://doi.org/10.1002/aesr.202200045 (2022).
33. Mahapatra, A. *et al.* A review of aspects of additive engineering in perovskite solar cells. *J Mater Chem A Mater* **8**, 27–54 (2020).
34. Kim, H. S. *et al.* Lead iodide perovskite sensitized all-solid-state submicron thin film mesoscopic solar cell with efficiency exceeding 9%. *Sci Rep* **2**, (2012).
35. Wu, T. *et al.* The Main Progress of Perovskite Solar Cells in 2020–2021. *Nanomicro Lett* **13**, 1–18 (2021).
36. Choi, K. *et al.* A Short Review on Interface Engineering of Perovskite Solar Cells: A Self-Assembled Monolayer and Its Roles. *Solar RRL* **4**, 1–20 (2020).
37. Guo, Z., Jena, A. K., Kim, G. M. & Miyasaka, T. The high open-circuit voltage of perovskite solar cells: a review. *Energy Environ Sci* **15**, 3171–3222 (2022).
38. Kim, S. Y., Cho, S. J., Byeon, S. E., He, X. & Yoon, H. J. Self-Assembled Monolayers as Interface Engineering Nanomaterials in Perovskite Solar Cells. *Advanced Energy Materials* vol. 10 Preprint at https://doi.org/10.1002/aenm.202002606 (2020).

39. Ameen, S. *et al.* Perovskite Solar Cells: Influence of Hole Transporting Materials on Power Conversion Efficiency. *ChemSusChem* **9**, 10–27 (2016).
40. Daskeviciute-Geguziene, S. *et al.* Green-Chemistry-Inspired Synthesis of Cyclobutane-Based Hole-Selective Materials for Highly Efficient Perovskite Solar Cells and Modules. *Angewandte Chemie - International Edition* **61**, (2022).
41. Hawash, Z., Ono, L. K. & Qi, Y. Recent Advances in Spiro-MeOTAD Hole Transport Material and Its Applications in Organic–Inorganic Halide Perovskite Solar Cells. *Advanced Materials Interfaces* vol. 5 Preprint at https://doi.org/10.1002/admi.201700623 (2018).
42. Magomedov, A. *et al.* Self-Assembled Hole Transporting Monolayer for Highly Efficient Perovskite Solar Cells. *Adv Energy Mater* **8**, 1801892 (2018).
43. Jeon, N. J. *et al.* O-methoxy substituents in spiro-OMeTAD for efficient inorganic-organic hybrid perovskite solar cells. *J Am Chem Soc* **136**, 7837–7840 (2014).
44. Hammett, L. P. The Effect of Structure upon the Reactions of Organic Compounds. Benzene Derivatives. *J Am Chem Soc* **59**, 96–103 (1937).
45. Franckevičius, M. *et al.* A dopant-free spirobi[cyclopenta[2,1-b:3,4-b′]dithiophene] based hole-transport material for efficient perovskite solar cells. *Mater Horiz* **2**, 613–618 (2015).
46. Saliba, M. *et al.* A molecularly engineered hole-transporting material for efficient perovskite solar cells. *Nat Energy* **1**, 15017 (2016).
47. Xu, B. *et al.* A low-cost spiro[fluorene-9,9′-xanthene]-based hole transport material for highly efficient solid-state dye-sensitized solar cells and perovskite solar cells. *Energy Environ Sci* **9**, 873–877 (2016).
48. Xie, L. H. *et al.* Unexpected one-pot method to synthesize spiro[fluorene-9,9′-xanthene] building blocks for blue-light-emitting materials. *Org Lett* **8**, 2787–2790 (2006).
49. Song, Y. *et al.* Energy level tuning of TPB-based hole-transporting materials for highly efficient perovskite solar cells. *Chemical Communications* **50**, 15239–15242 (2014).
50. Rakstys, K. Molecularly Engineered Hole Transporting Materials for High Performance Perovskite Solar Cells. 15–17 (2018).
51. Malinauskas, T. *et al.* Branched methoxydiphenylamine-substituted fluorene derivatives as hole transporting materials for high-performance perovskite solar cells. *Energy Environ Sci* **9**, 1681–1686 (2016).
52. Sung, S. Do *et al.* 14.8% perovskite solar cells employing carbazole derivatives as hole transporting materials. *Chemical Communications* **50**, 14161–14163 (2014).

53. Lu, C., Choi, I. T., Kim, J. & Kim, H. K. Simple synthesis and molecular engineering of low-cost and star-shaped carbazole-based hole transporting materials for highly efficient perovskite solar cells. *J Mater Chem A Mater* **5**, 20263–20276 (2017).
54. García-Benito, I., Urieta-Mora, J., Molina-Ontoria, A. & Martín, N. Chalcogen-containing hole transporting materials. *Bulletin of the Chemical Society of Japan* vol. 94 1311–1323 Preprint at https://doi.org/10.1246/bcsj.20210032 (2021).
55. Kim, G. W. *et al.* Hole Transport Materials in Conventional Structural (n–i–p) Perovskite Solar Cells: From Past to the Future. *Advanced Energy Materials* vol. 10 Preprint at https://doi.org/10.1002/aenm.201903403 (2020).
56. Liu, X. *et al.* A star-shaped carbazole-based hole-transporting material with triphenylamine side arms for perovskite solar cells. *J Mater Chem C Mater* **6**, 12912–12918 (2018).
57. Zhang, J. *et al.* Constructive Effects of Alkyl Chains: A Strategy to Design Simple and Non-Spiro Hole Transporting Materials for High-Efficiency Mixed-Ion Perovskite Solar Cells. *Adv Energy Mater* **6**, (2016).
58. Zhang, J. *et al.* Strategy to Boost the Efficiency of Mixed-Ion Perovskite Solar Cells: Changing Geometry of the Hole Transporting Material. *ACS Nano* **10**, 6816–6825 (2016).
59. Li, X. *et al.* A comparative study of o, p -dimethoxyphenyl-based hole transport materials by altering π-linker units for highly efficient and stable perovskite solar cells. *J Mater Chem A Mater* **5**, 10480–10485 (2017).
60. Liu, P. *et al.* Design, synthesis and application of a π-conjugated, non-spiro molecular alternative as hole-transport material for highly efficient dye-sensitized solar cells and perovskite solar cells. *J Power Sources* **344**, 11–14 (2017).
61. Leijtens, T. *et al.* Hydrophobic Organic Hole Transporters for Improved Moisture Resistance in Metal Halide Perovskite Solar Cells. *ACS Appl Mater Interfaces* **8**, 5981–5989 (2016).
62. Zhang, F. *et al.* Over 20% PCE perovskite solar cells with superior stability achieved by novel and low-cost hole-transporting materials. *Nano Energy* **41**, 469–475 (2017).
63. Sathiyan, G., Sivakumar, E. K. T., Ganesamoorthy, R., Thangamuthu, R. & Sakthivel, P. Review of carbazole based conjugated molecules for highly efficient organic solar cell application. *Tetrahedron Letters* vol. 57 243–252 Preprint at https://doi.org/10.1016/j.tetlet.2015.12.057 (2016).

64. Gratia, P. *et al.* A Methoxydiphenylamine-Substituted Carbazole Twin Derivative: An Efficient Hole-Transporting Material for Perovskite Solar Cells. *Angewandte Chemie International Edition* **54**, 11409–11413 (2015).
65. Magomedov, A. *et al.* Diphenylamine-Substituted Carbazole-Based Hole Transporting Materials for Perovskite Solar Cells: Influence of Isomeric Derivatives. *Adv Funct Mater* **28**, (2018).
66. Yalcin, E. *et al.* Semiconductor self-assembled monolayers as selective contacts for efficient PiN perovskite solar cells. *Energy Environ Sci* **12**, 230–237 (2019).
67. Al-Ashouri, A. *et al.* Conformal monolayer contacts with lossless interfaces for perovskite single junction and monolithic tandem solar cells. *Energy Environ Sci* **12**, 3356–3369 (2019).
68. Li, E. *et al.* Bonding Strength Regulates Anchoring-Based Self-Assembly Monolayers for Efficient and Stable Perovskite Solar Cells. *Adv Funct Mater* **31**, (2021).
69. Jiang, W. *et al.* π-Expanded Carbazoles as Hole-Selective Self-Assembled Monolayers for High-Performance Perovskite Solar Cells. *Angewandte Chemie - International Edition* **61**, (2022).
70. Aktas, E. *et al.* Understanding the perovskite/self-assembled selective contact interface for ultra-stable and highly efficient p-i-n perovskite solar cells. *Energy Environ Sci* **14**, 3976–3985 (2021).
71. Al-Ashouri, A. *et al.* Monolithic perovskite/silicon tandem solar cell with >29% efficiency by enhanced hole extraction. *Science (1979)* **370**, 1300–1309 (2020).
72. González, D. A. *et al.* Influence of the carbazole moiety in self-assembling molecules as selective contacts in perovskite solar cells: interfacial charge transfer kinetics and solar-to-energy efficiency effects. *Nanoscale Adv* **5**, 6542–6547 (2023).
73. Zhang, S. *et al.* Conjugated Self-Assembled Monolayer as Stable Hole-Selective Contact for Inverted Perovskite Solar Cells. *ACS Mater Lett* **4**, 1976–1983 (2022).
74. Wang, S., Guo, H. & Wu, Y. Advantages and challenges of self-assembled monolayer as a hole-selective contact for perovskite solar cells. *Materials Futures* vol. 2 Preprint at https://doi.org/10.1088/2752-5724/acbb5a (2023).
75. Arkan, E. *et al.* Effect of functional groups of self assembled monolayer molecules on the performance of inverted perovskite solar cell. *Mater Chem Phys* **254**, 123435 (2020).

76. Rodríguez-Seco, C. *et al.* Minimization of Carrier Losses for Efficient Perovskite Solar Cells through Structural Modification of Triphenylamine Derivatives. *Angewandte Chemie* **132**, 5341–5345 (2020).
77. Kumari, S. *et al.* Self-assembled molecules as selective contacts in $CsPbBr_3$ nanocrystal light emitting diodes. *J Mater Chem C Mater* **11**, 3788–3795 (2023).
78. Deng, X. *et al.* Co-assembled Monolayers as Hole-Selective Contact for High-Performance Inverted Perovskite Solar Cells with Optimized Recombination Loss and Long-Term Stability. *Angewandte Chemie - International Edition* **61**, (2022).
79. Li, W., Cariello, M., Méndez, M., Cooke, G. & Palomares, E. Self-Assembled Molecules for Hole-Selective Electrodes in Highly Stable and Efficient Inverted Perovskite Solar Cells with Ultralow Energy Loss. *ACS Appl Energy Mater* **6**, 1239–1247 (2023).
80. Elgrishi, N. *et al.* A Practical Beginner's Guide to Cyclic Voltammetry. *J Chem Educ* **95**, 197–206 (2018).
81. Riordan, C. & Hulstron, R. What is an air mass 1.5 spectrum? (solar cell performance calculations). in *IEEE Conference on Photovoltaic Specialists* 1085–1088 (IEEE). doi:10.1109/PVSC.1990.111784.
82. Wang, C. *et al.* Spiro-Linked Molecular Hole-Transport Materials for Highly Efficient Inverted Perovskite Solar Cells. *Solar RRL* **4**, (2020).
83. Shi, Y. *et al.* Interfacial Engineering via Self-Assembled Thiol Silane for High Efficiency and Stability Perovskite Solar Cells. *Solar RRL* **5**, (2021).
84. Tan, F. *et al.* Dual Coordination of Ti and Pb Using Bilinkable Ligands Improves Perovskite Solar Cell Performance and Stability. *Adv Funct Mater* **30**, (2020).
85. Zhou, Z. *et al.* Heteroatom effect on linear-shaped dopant-free hole transporting materials for perovskite solar cells. *Solar Energy* **221**, 323–331 (2021).
86. Shariatinia, Z. & Sarmalek, S. I. Molecular engineering of several butterfly-shaped hole transport materials containing dibenzo[b,d]thiophene core for perovskite photovoltaics. *Sci Rep* **12**, (2022).
87. Rombach, F. M., Haque, S. A. & Macdonald, T. J. Lessons learned from spiro-OMeTAD and PTAA in perovskite solar cells. *Energy and Environmental Science* vol. 14 5161–5190 Preprint at https://doi.org/10.1039/d1ee02095a (2021).
88. Jiang, Q. *et al.* Surface reaction for efficient and stable inverted perovskite solar cells. *Nature* **611**, 278–283 (2022).

89. Zhang, S. *et al.* Conjugated Self-Assembled Monolayer as Stable Hole-Selective Contact for Inverted Perovskite Solar Cells. *ACS Mater Lett* **4**, 1976–1983 (2022).
90. Arkan, E. *et al.* Influence of end groups variation of self assembled monolayers on performance of planar perovskite solar cells by interface regulation. *Mater Sci Semicond Process* **123**, 105514 (2021).
91. Li, Z. *et al.* Simple and robust phenoxazine phosphonic acid molecules as self-assembled hole selective contacts for high-performance inverted perovskite solar cells. *Nanoscale* **15**, 1676–1686 (2023).
92. Maurano, A. *et al.* Transient optoelectronic analysis of charge carrier losses in a selenophene/fullerene blend solar cell. *Journal of Physical Chemistry C* **115**, 5947–5957 (2011).
93. Wolff, C. M., Caprioglio, P., Stolterfoht, M. & Neher, D. Nonradiative Recombination in Perovskite Solar Cells: The Role of Interfaces. *Advanced Materials* **31**, (2019).
94. Magomedov, A. *et al.* Self-Assembled Hole Transporting Monolayer for Highly Efficient Perovskite Solar Cells. *Adv Energy Mater* **8**, (2018).
95. Al-Ashouri, A. *et al.* Conformal monolayer contacts with lossless interfaces for perovskite single junction and monolithic tandem solar cells. *Energy Environ Sci* **12**, 3356–3369 (2019).
96. Levine, I. *et al.* Charge transfer rates and electron trapping at buried interfaces of perovskite solar cells. *Joule* **5**, 2915–2933 (2021).
97. Aktas, E. *et al.* Role of Terminal Group Position in Triphenylamine-Based Self-Assembled Hole-Selective Molecules in Perovskite Solar Cells. *ACS Appl Mater Interfaces* **14**, 17461–17469 (2022).
98. Liu, H. *et al.* Self-Assembled Donor-Acceptor Dyad Molecules Stabilize the Heterojunction of Inverted Perovskite Solar Cells and Modules. *ACS Appl Mater Interfaces* **14**, 6794–6800 (2022).
99. Li, E. *et al.* Bonding Strength Regulates Anchoring-Based Self-Assembly Monolayers for Efficient and Stable Perovskite Solar Cells. *Adv Funct Mater* **31**, (2021).
100. Truong, M. A. *et al.* Tripodal Triazatruxene Derivative as a Face-On Oriented Hole-Collecting Monolayer for Efficient and Stable Inverted Perovskite Solar Cells. *J Am Chem Soc* **145**, 7528–7539 (2023).
101. Guo, R. *et al.* Tailoring Multifunctional Self-Assembled Hole Transporting Molecules for Highly Efficient and Stable Inverted Perovskite Solar Cells. *Adv Funct Mater* **33**, (2023).
102. You, S. *et al.* Bifunctional hole-shuttle molecule for improved interfacial energy level alignment and defect passivation in perovskite solar cells. *Nat Energy* **8**, 515–525 (2023).

103. You, S. *et al.* Bifunctional hole-shuttle molecule for improved interfacial energy level alignment and defect passivation in perovskite solar cells. *Nat Energy* **8**, 515–525 (2023).
104. Zhang, J. & Yu, H. Reduced energy loss enabled by thiophene-based interlayers for high performance and stable perovskite solar cells. *J Mater Chem A Mater* **9**, 4138–4149 (2021).
105. Zuo, L. *et al.* Enhanced photovoltaic performance of CH3NH3PbI3 perovskite solar cells through interfacial engineering using self-assembling monolayer. *J Am Chem Soc* **137**, 2674–2679 (2015).
106. Kulkarni, A. *et al.* A Universal Strategy of Perovskite Ink-Substrate Interaction to Overcome the Poor Wettability of a Self-Assembled Monolayer for Reproducible Perovskite Solar Cells. *Adv Funct Mater* (2023).
107. Aktas, E. *et al.* Understanding the perovskite/self-assembled selective contact interface for ultra-stable and highly efficient p-i-n perovskite solar cells. *Energy Environ Sci* **14**, 3976–3985 (2021).
108. Bi, C. *et al.* Non-wetting surface-driven high-aspect-ratio crystalline grain growth for efficient hybrid perovskite solar cells. *Nat Commun* **6**, (2015).
109. Arkan, E. *et al.* Influence of end groups variation of self assembled monolayers on performance of planar perovskite solar cells by interface regulation. *Mater Sci Semicond Process* **123**, (2021).
110. Yalcin, E. *et al.* Semiconductor self-assembled monolayers as selective contacts for efficient PiN perovskite solar cells. *Energy Environ Sci* **12**, 230–237 (2019).
111. Tumen-Ulzii, G. *et al.* Hysteresis-less and stable perovskite solar cells with a self-assembled monolayer. *Commun Mater* **1**, (2020).
112. Ullah, A. *et al.* Versatile Hole Selective Molecules Containing a Series of Heteroatoms as Self-Assembled Monolayers for Efficient p-i-n Perovskite and Organic Solar Cells. *Adv Funct Mater* **32**, (2022).
113. Jiménez-López, J., Cambarau, W., Cabau, L. & Palomares, E. Charge Injection, Carriers Recombination and HOMO Energy Level Relationship in Perovskite Solar Cells. *Sci Rep* **7**, (2017).
114. Castro-Chong, A. *et al.* Illumination Intensity Dependence of the Recombination Mechanism in Mixed Perovskite Solar Cells. *Chempluschem* **86**, 1347–1356 (2021).
115. Ullah, A. *et al.* Novel Phenothiazine-Based Self-Assembled Monolayer as a Hole Selective Contact for Highly Efficient and Stable p-i-n Perovskite Solar Cells. *Adv Energy Mater* **12**, (2022).
116. Degani, M. *et al.* 23.7% Efficient inverted perovskite solar cells by dual interfacial modification. *Sci Adv* **7**, 1–10 (2021).

117. Tien, C. H., Lin, W. C. & Chen, L. C. Efficient Perovskite Solar Cells via Phenethylamine Iodide Cation-Modified Hole Transport Layer/Perovskite Interface. *ACS Omega* **7**, 37359–37368 (2022).
118. Wang, Z. *et al.* Suppressed phase segregation for triple-junction perovskite solar cells. *Nature* **618**, 74–79 (2023).
119. Tumen-Ulzii, G., Matsushima, T. & Adachi, C. Mini-Review on Efficiency and Stability of Perovskite Solar Cells with Spiro-OMeTAD Hole Transport Layer: Recent Progress and Perspectives. *Energy and Fuels* vol. 35 18915–18927 Preprint at https://doi.org/10.1021/acs.energyfuels.1c02190 (2021).
120. Zhu, W. *et al.* Rational design of small molecule hole-transporting materials with a linear π-bridge for highly efficient perovskite solar cells. *Physical Chemistry Chemical Physics* (2022) doi:10.1039/d2cp02036j.
121. Yu, W. *et al.* Simple Is Best: A p-Phenylene Bridging Methoxydiphenylamine-Substituted Carbazole Hole Transporter for High-Performance Perovskite Solar Cells. *ACS Appl Mater Interfaces* **11**, 30065–30071 (2019).
122. Ok, S. A. *et al.* Management of transition dipoles in organic hole-transporting materials under solar irradiation for perovskite solar cells. *Nat Commun* **9**, (2018).
123. Wu, N. *et al.* Efficient furan-bridged dibenzofulvene-triphenylamine hole transporting materials for perovskite solar cells. *Mater Adv* **4**, 515–522 (2022).
124. Idrissi, A. *et al.* Thiophene-based molecules as hole transport materials for efficient perovskite solar cells or as donors for organic solar cells. *Mater Chem Phys* **293**, (2023).
125. Montcada, N. F., Cabau, L., Kumar, C. V., Cambarau, W. & Palomares, E. Indoline as electron donor unit in 'push-Pull' organic small molecules for solution processed organic solar cells: Effect of the molecular π-bridge on device efficiency. *Org Electron* **20**, 15–23 (2015).
126. Rodríguez-Seco, C., Biswas, S., Sharma, G. D., Vidal-Ferran, A. & Palomares, E. Benzothiadiazole Substituted Semiconductor Molecules for Organic Solar Cells: The Effect of the Solvent Annealing over the Thin Film Hole Mobility Values. *Journal of Physical Chemistry C* **122**, 13782–13789 (2018).
127. Canil, L. *et al.* Tuning halide perovskite energy levels. *Energy Environ Sci* **14**, 1429–1438 (2021).
128. Sánchez, J. G. *et al.* Increasing the stability of perovskite solar cells with dibenzofulvene-based hole transporting materials. *Electrochim Acta* **432**, (2022).

129. Jiménez-López, J., Puscher, B. M. D., Guldi, D. M. & Palomares, E. Improved Carrier Collection and Hot Electron Extraction across Perovskite, C60, and TiO2 Interfaces. *J Am Chem Soc* **142**, 1236–1246 (2020).
130. Snaith, H. J. *et al.* Anomalous hysteresis in perovskite solar cells. *Journal of Physical Chemistry Letters* **5**, 1511–1515 (2014).
131. Kasparavicius, E. *et al.* Oxidized Spiro-OMeTAD: Investigation of Stability in Contact with Various Perovskite Compositions. *ACS Appl Energy Mater* **4**, 13696–13705 (2021).
132. Habisreutinger, S. N., Noel, N. K. & Snaith, H. J. Hysteresis Index: A Figure without Merit for Quantifying Hysteresis in Perovskite Solar Cells. *ACS Energy Lett* **3**, 2472–2476 (2018).

APPENDIX

^{1}H AND ^{13}C SPECTRA

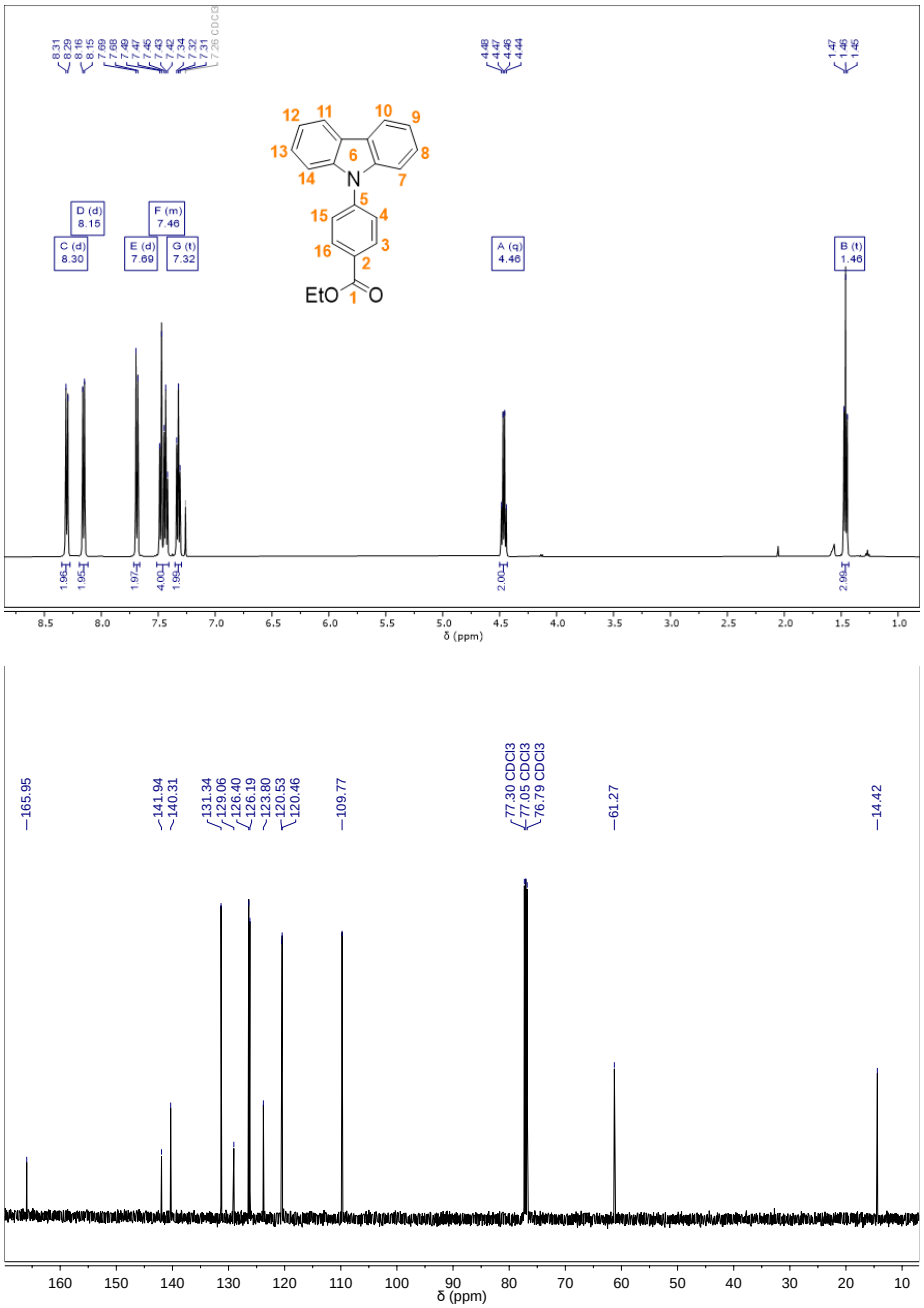

Figure A1. ^{1}H and ^{13}C NMRs of 3.

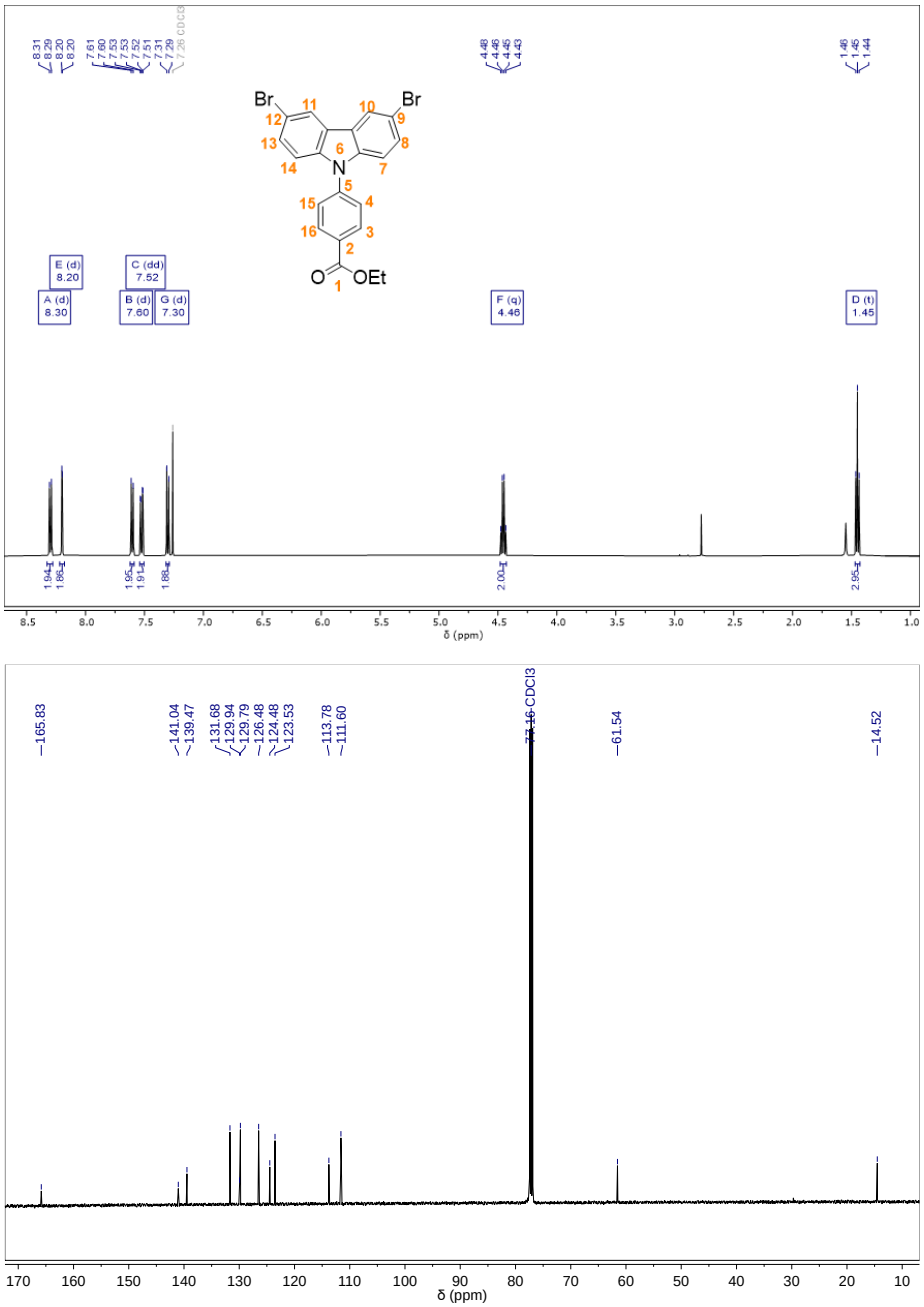

Figure A2. ^{1}H and ^{13}C NMRs of **4**.

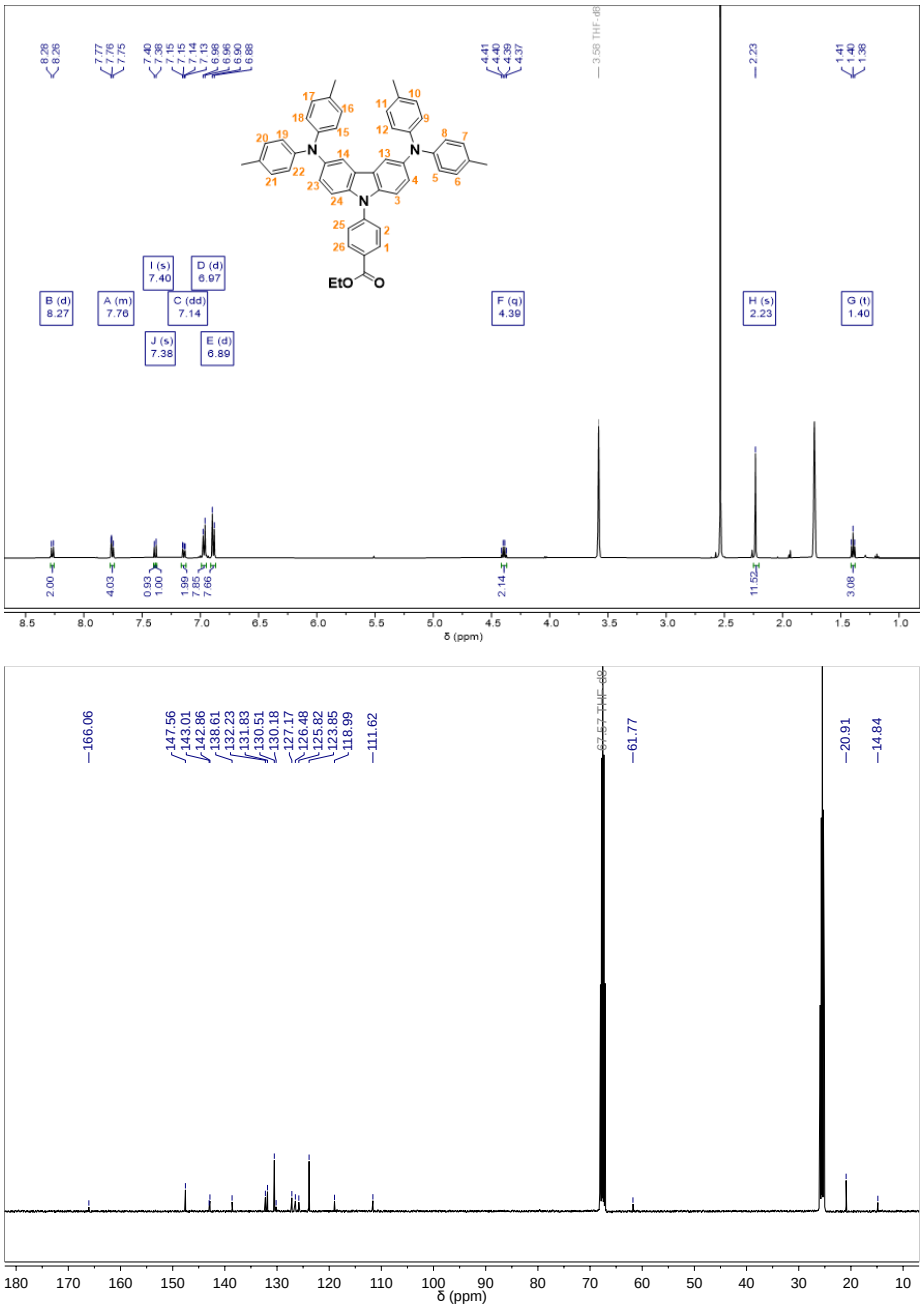

Figure A3. ^{1}H and ^{13}C NMRs of **6**.

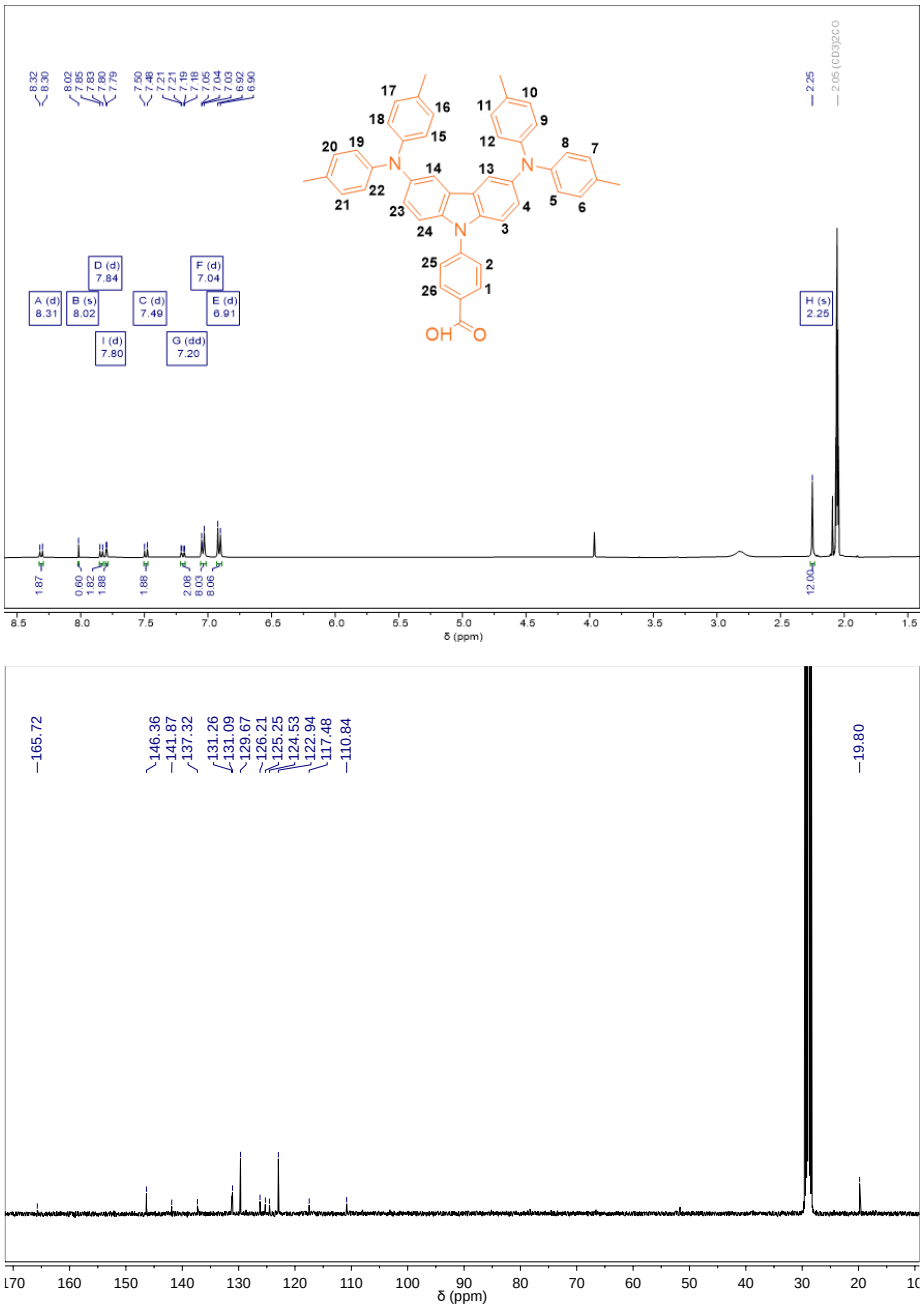

Figure A4. ^{1}H and ^{13}C NMRs of **7, SAM 1.**

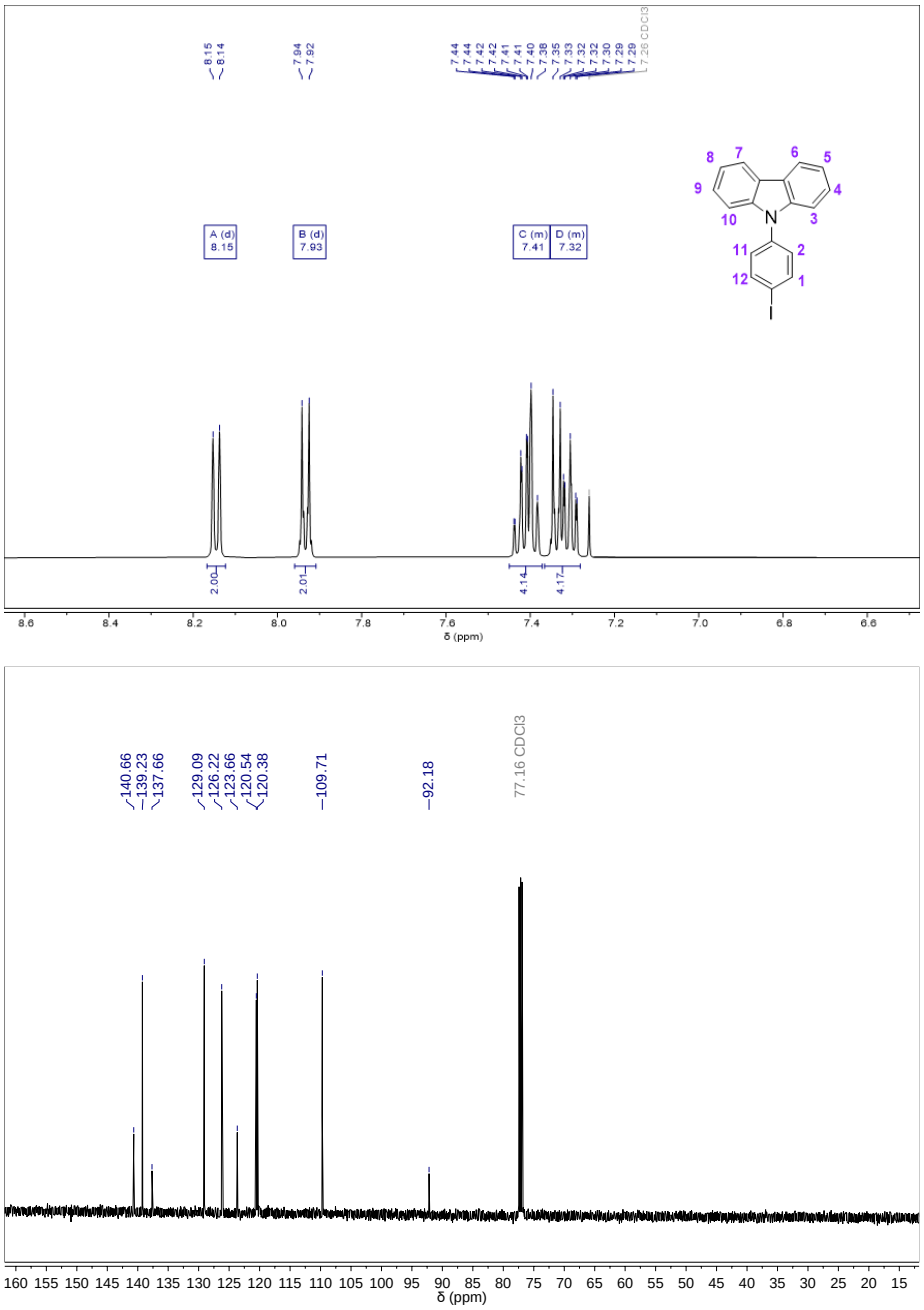

Figure A5. ^{1}H and ^{13}C NMRs of **9**.

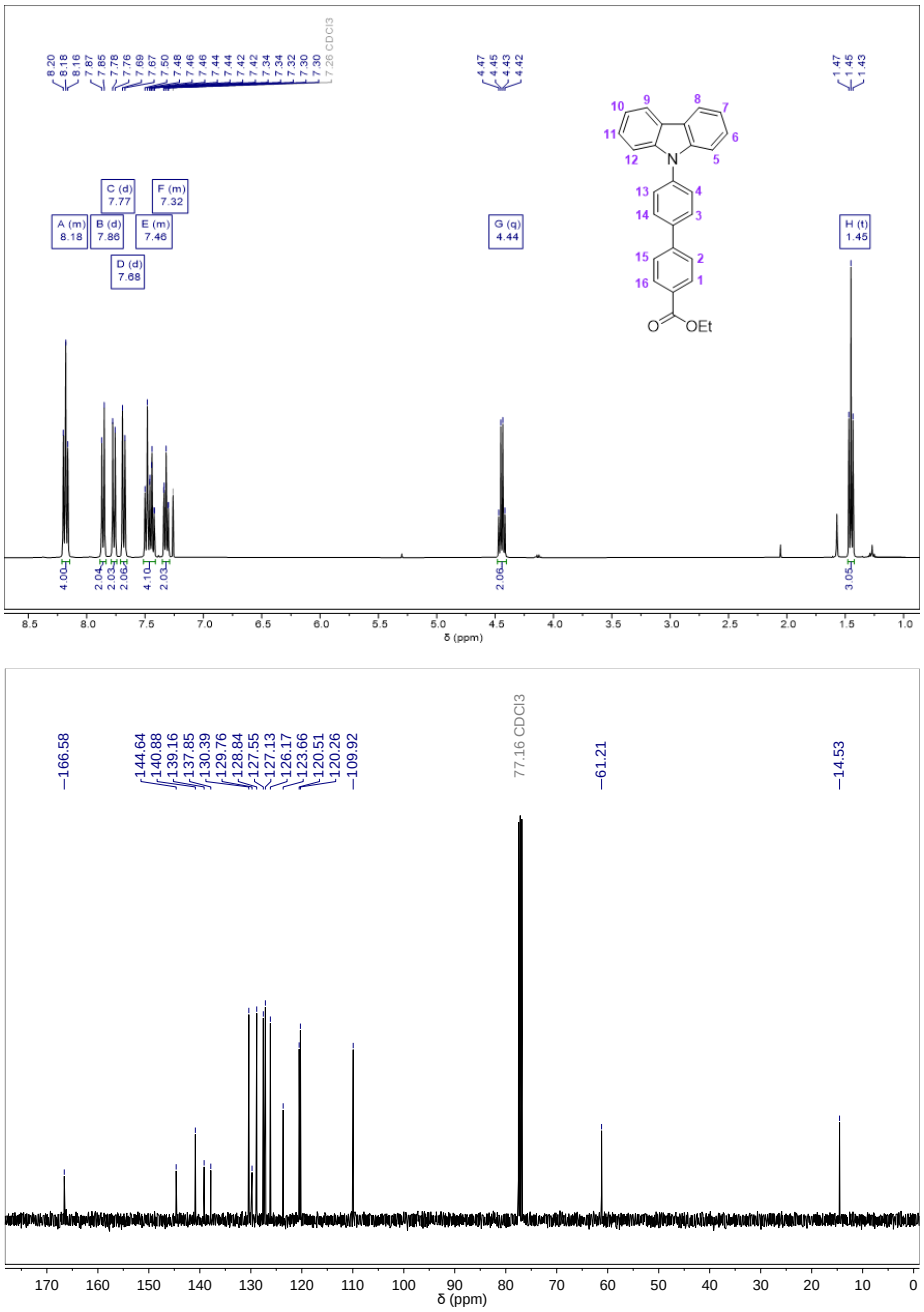

Figure A6. ^{1}H and ^{13}C NMRs of **11**.

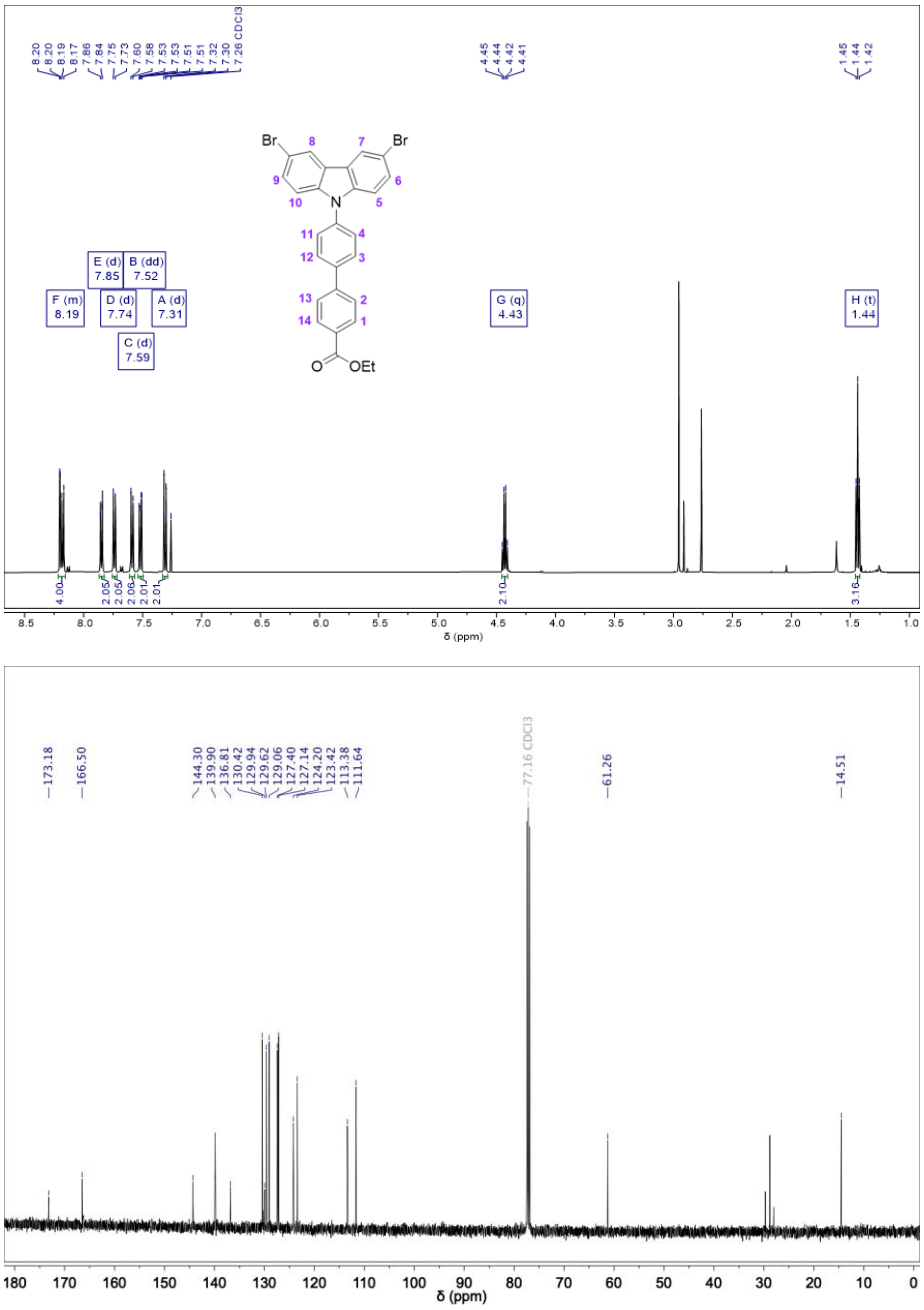

Figure A7. ^{1}H and ^{13}C NMRs of 12.

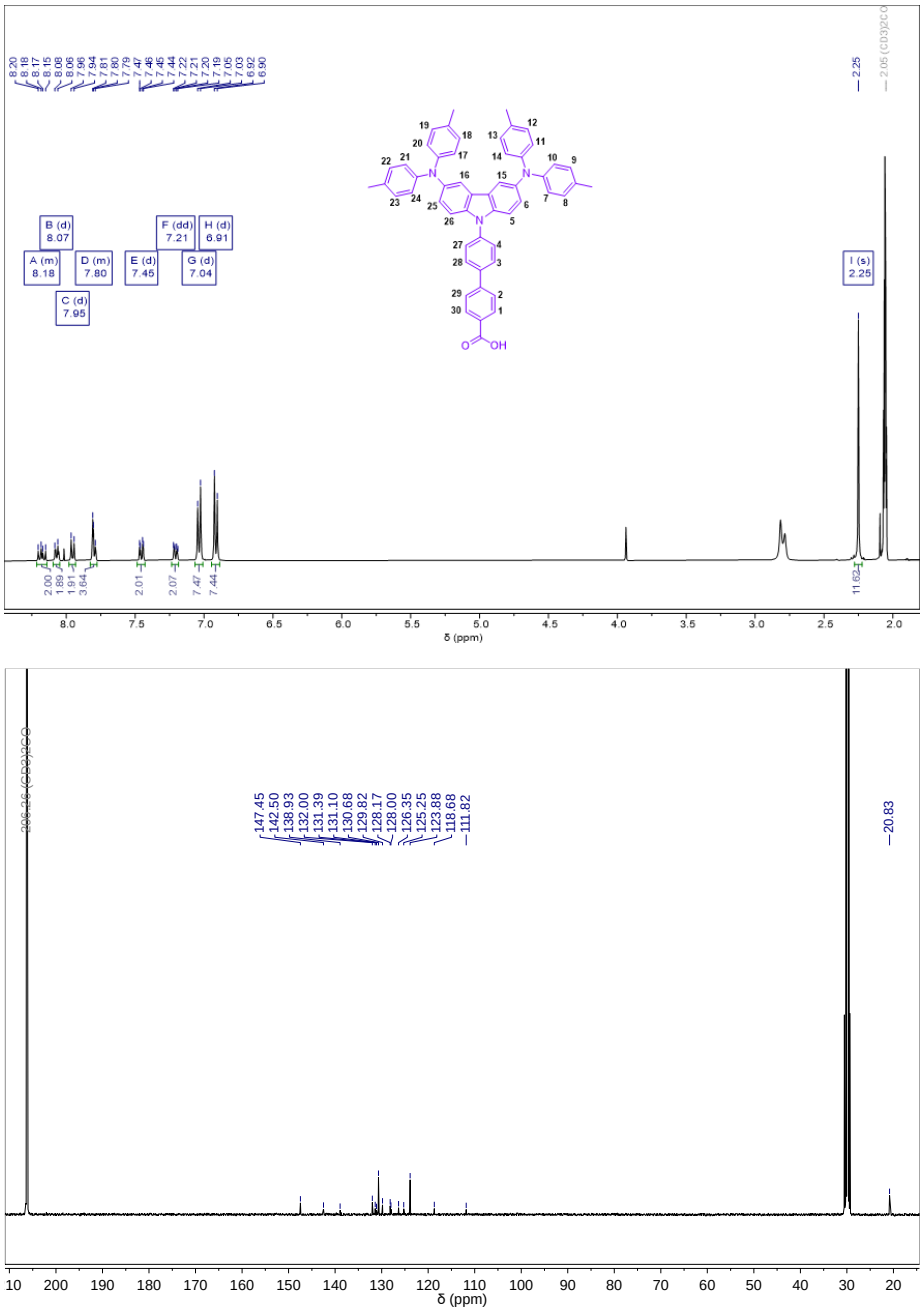

Figure A8. ^{1}H and ^{13}C NMRs of **14, SAM 2.**

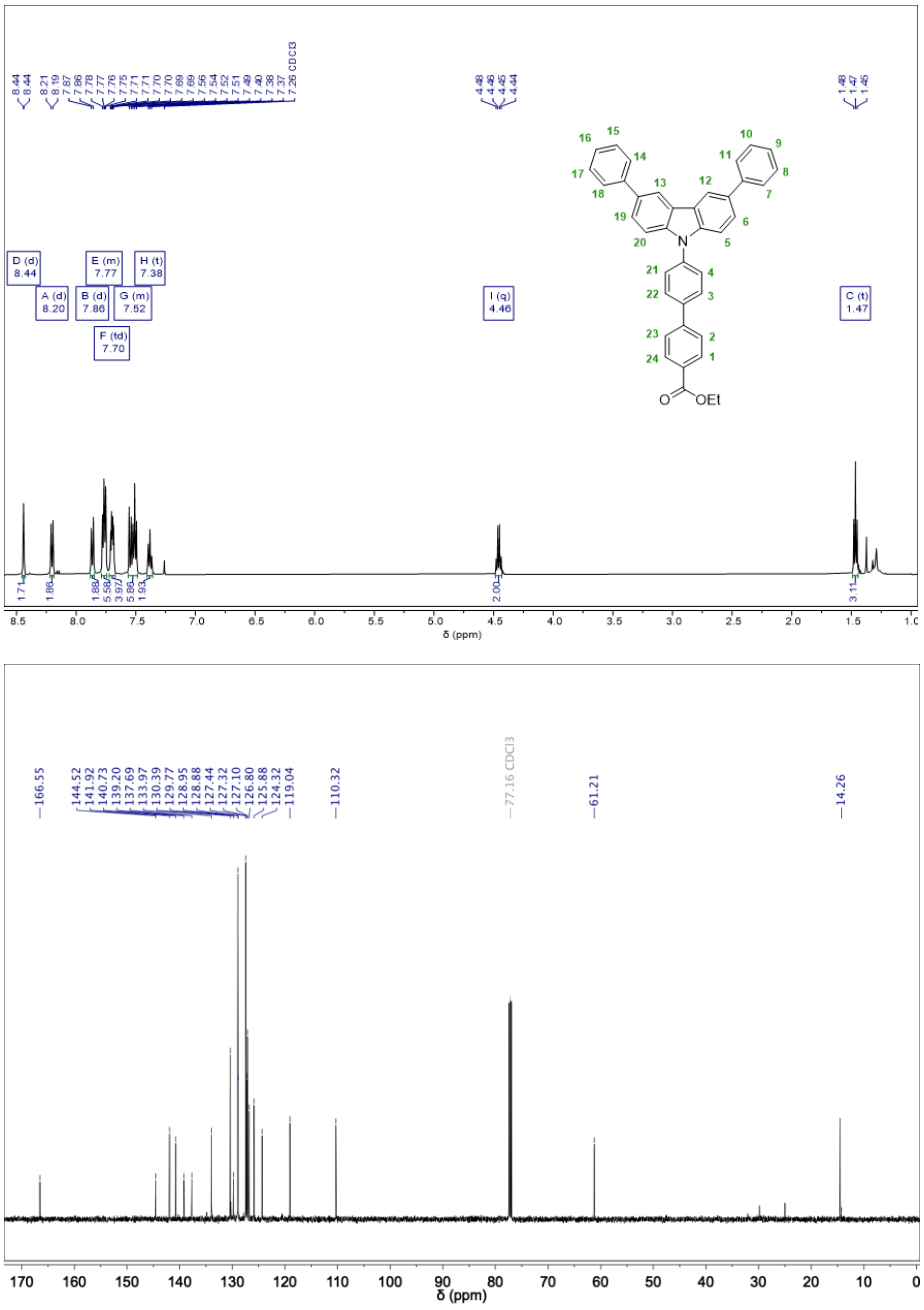

Figure A9. ^{1}H and ^{13}C NMRs of **16**.

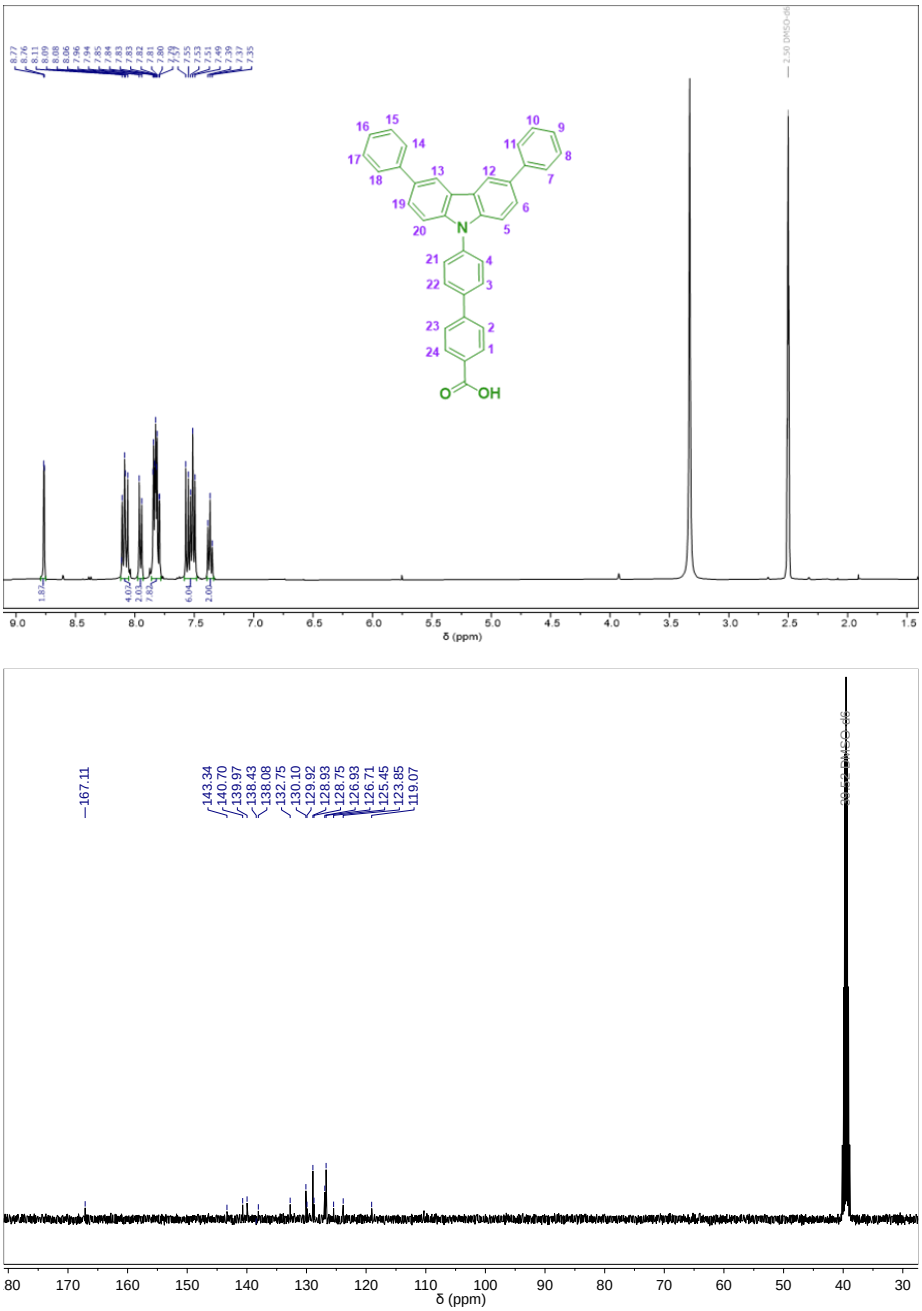

Figure A10. ^{1}H and ^{13}C NMRs of 17, SAM 3.

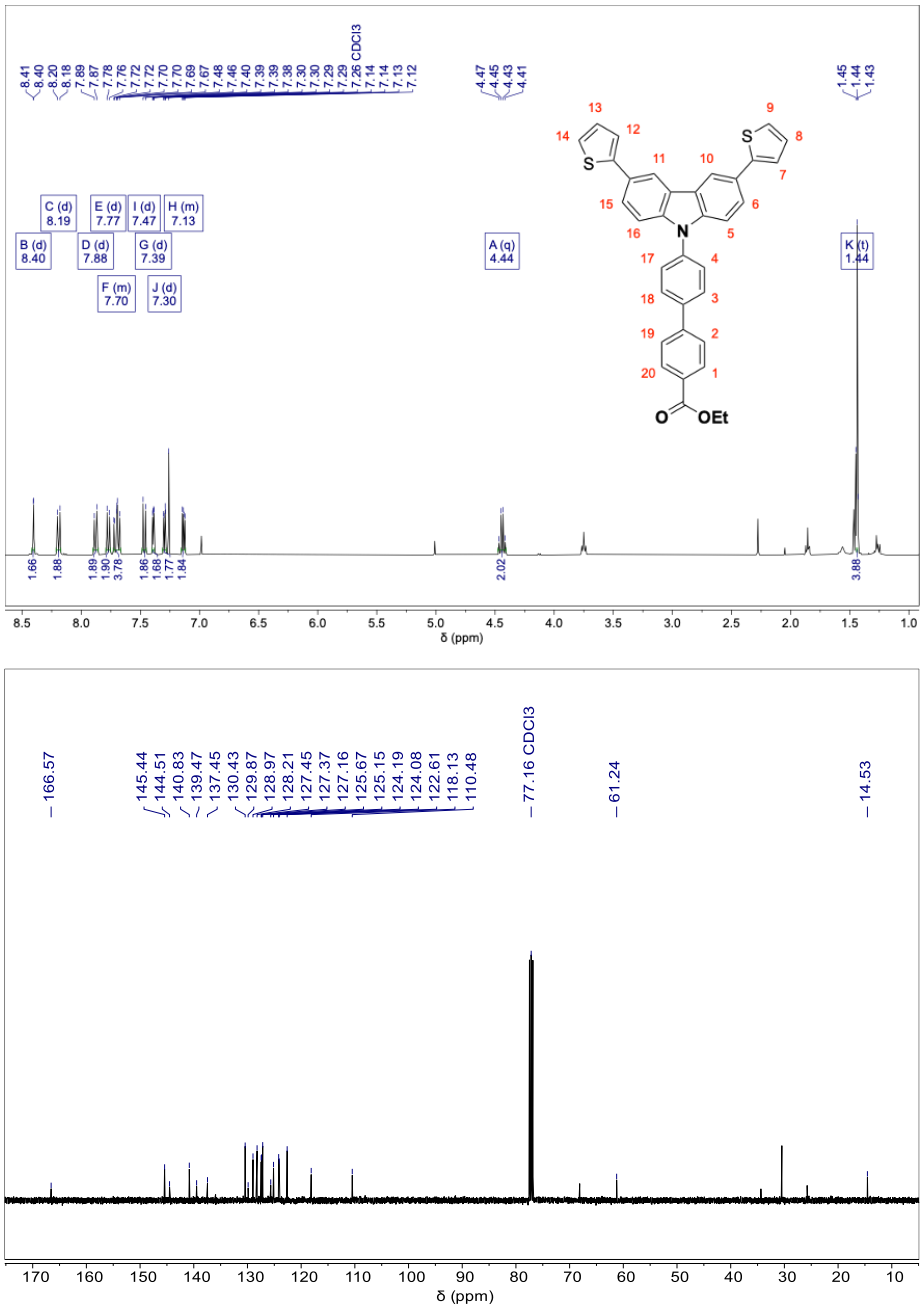

Figure A11. ^{1}H and ^{13}C NMRs of **19**.

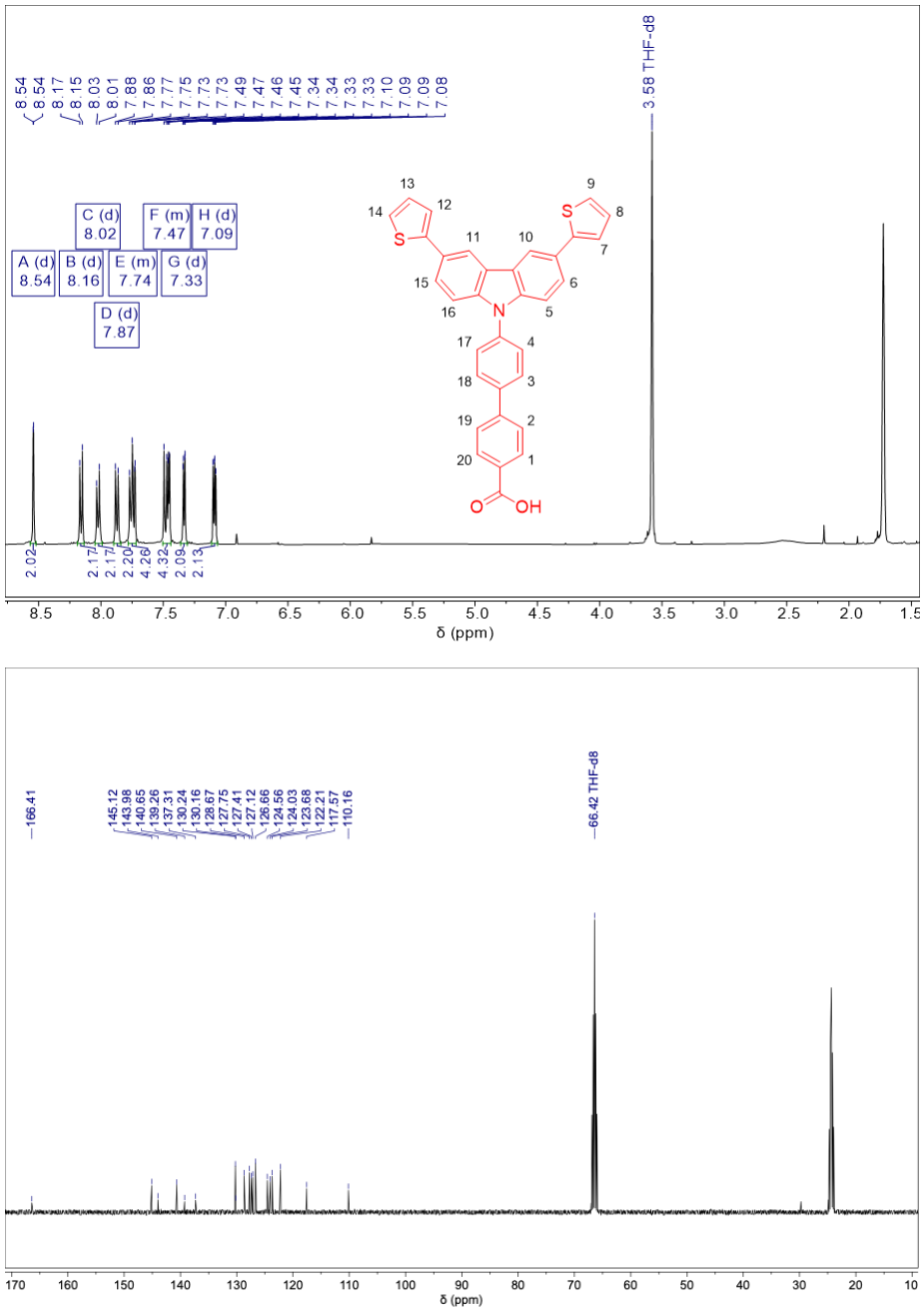

Figure A12. ^{1}H and ^{13}C NMRs of **20**, **SAM 4**.

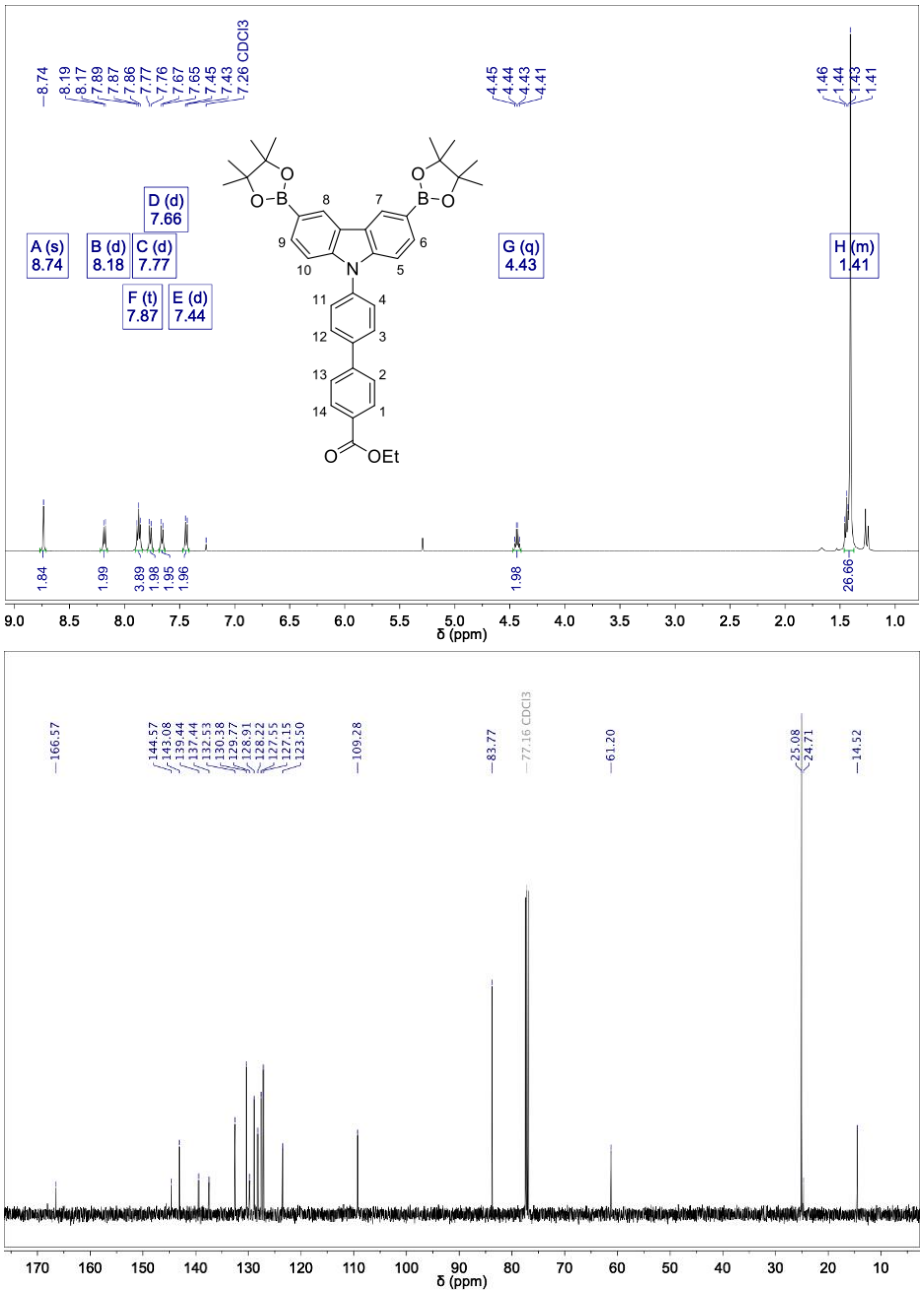

Figure A13. ^{1}H and ^{13}C NMRs of **22**.

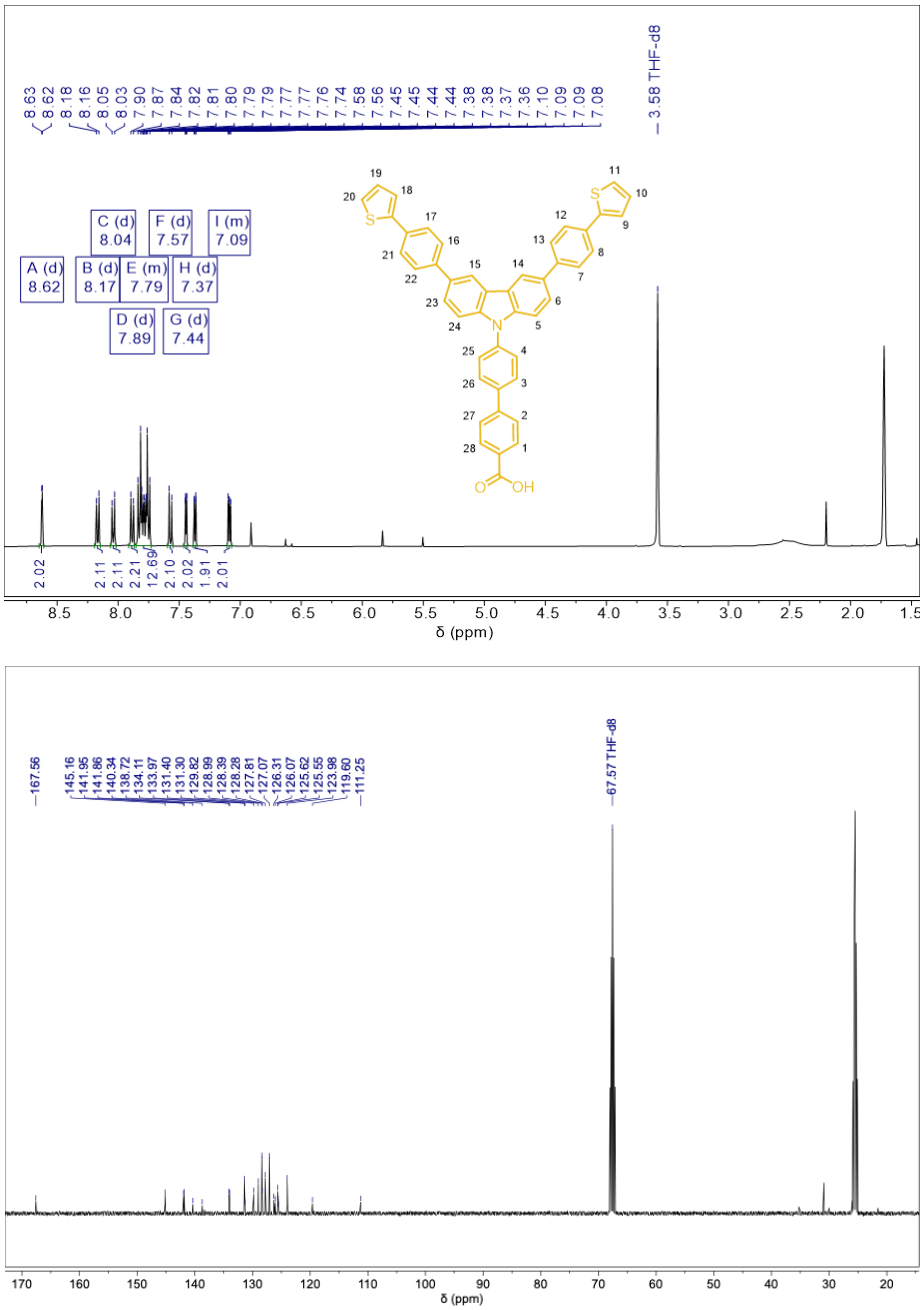

Figure A14. ^{1}H and ^{13}C NMRs of **25**, **SAM 5.**

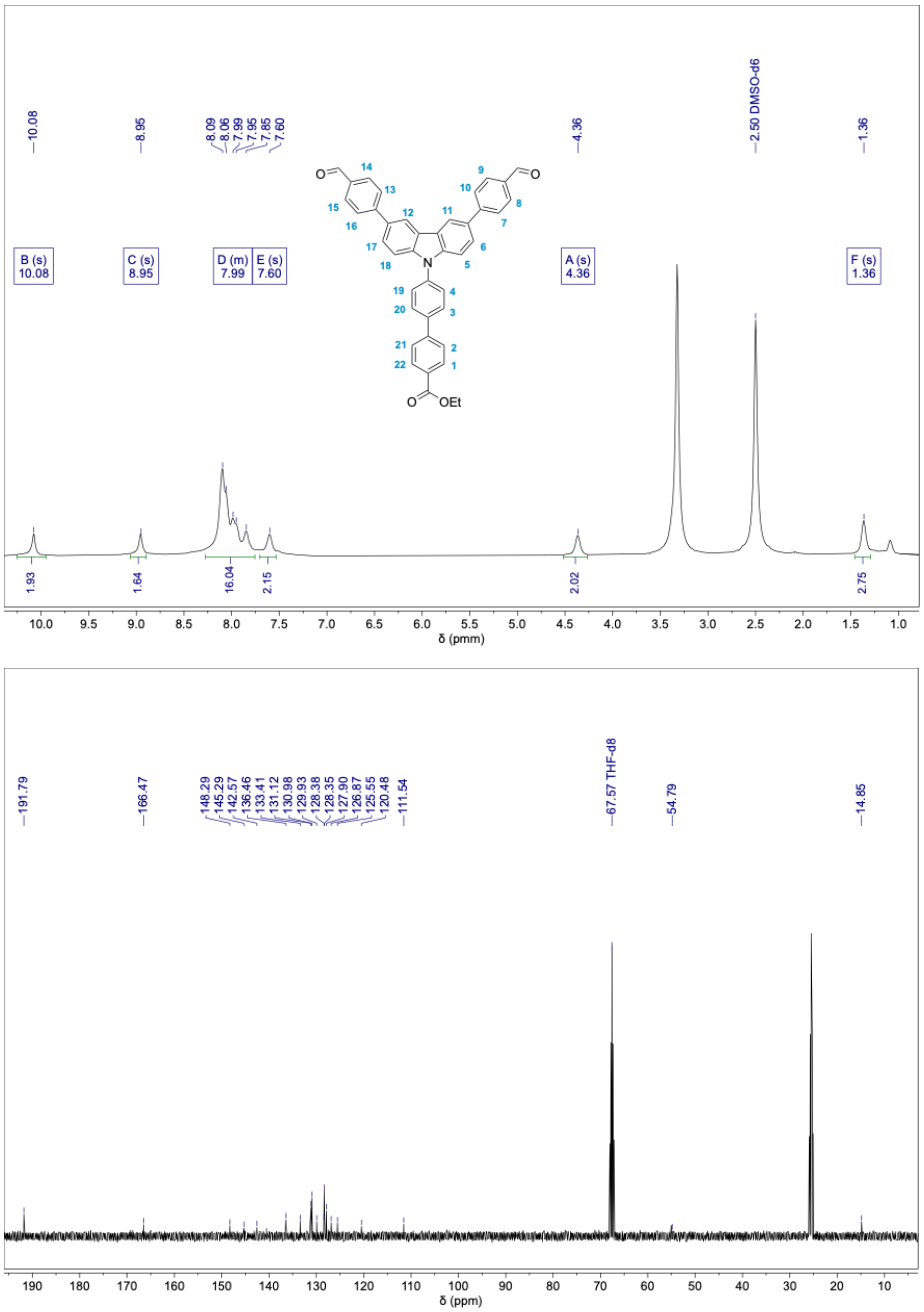

Figure A15. ^{1}H and ^{13}C NMRs of **27**.

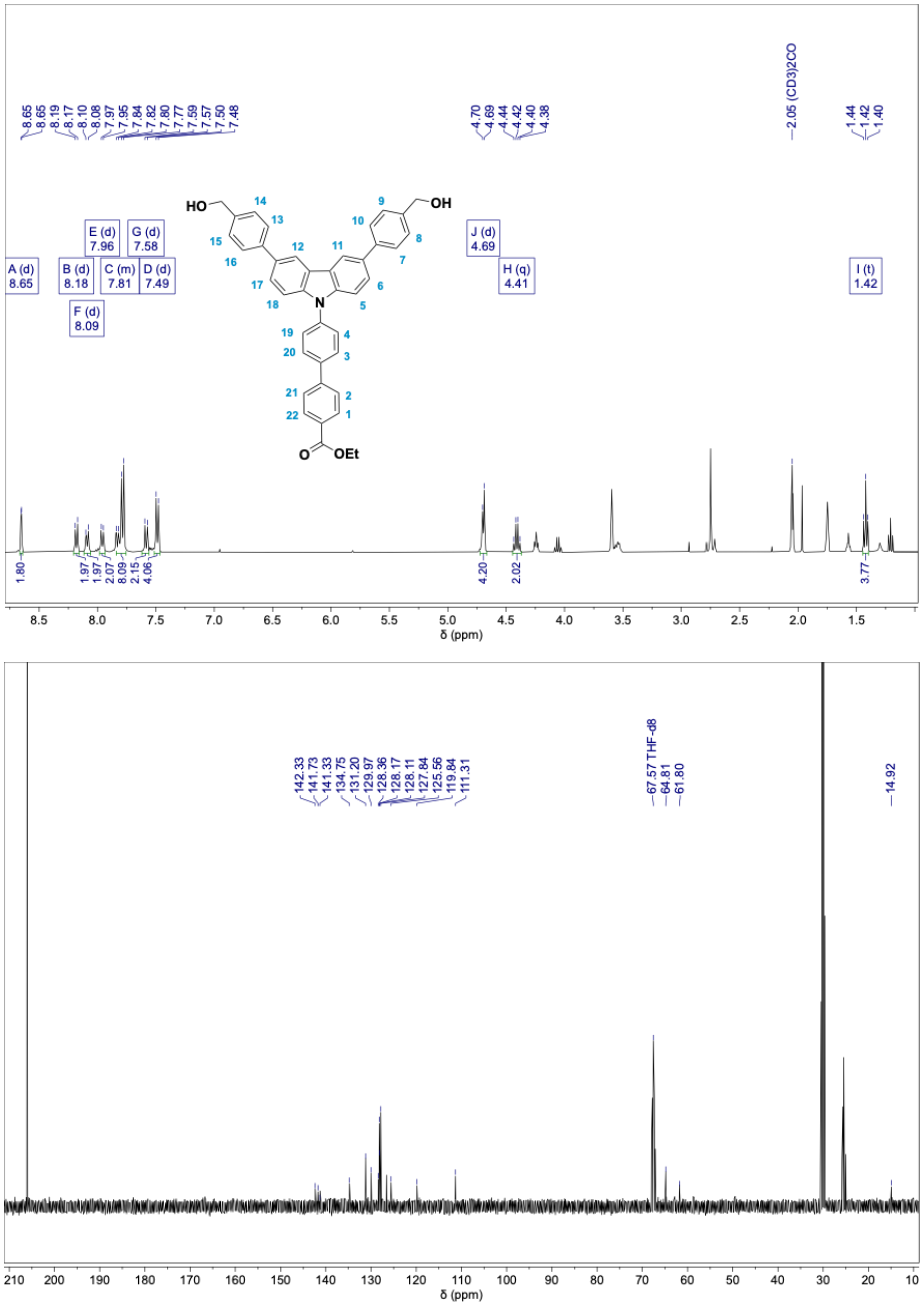

Figure A16. ^{1}H and ^{13}C NMRs of **28**.

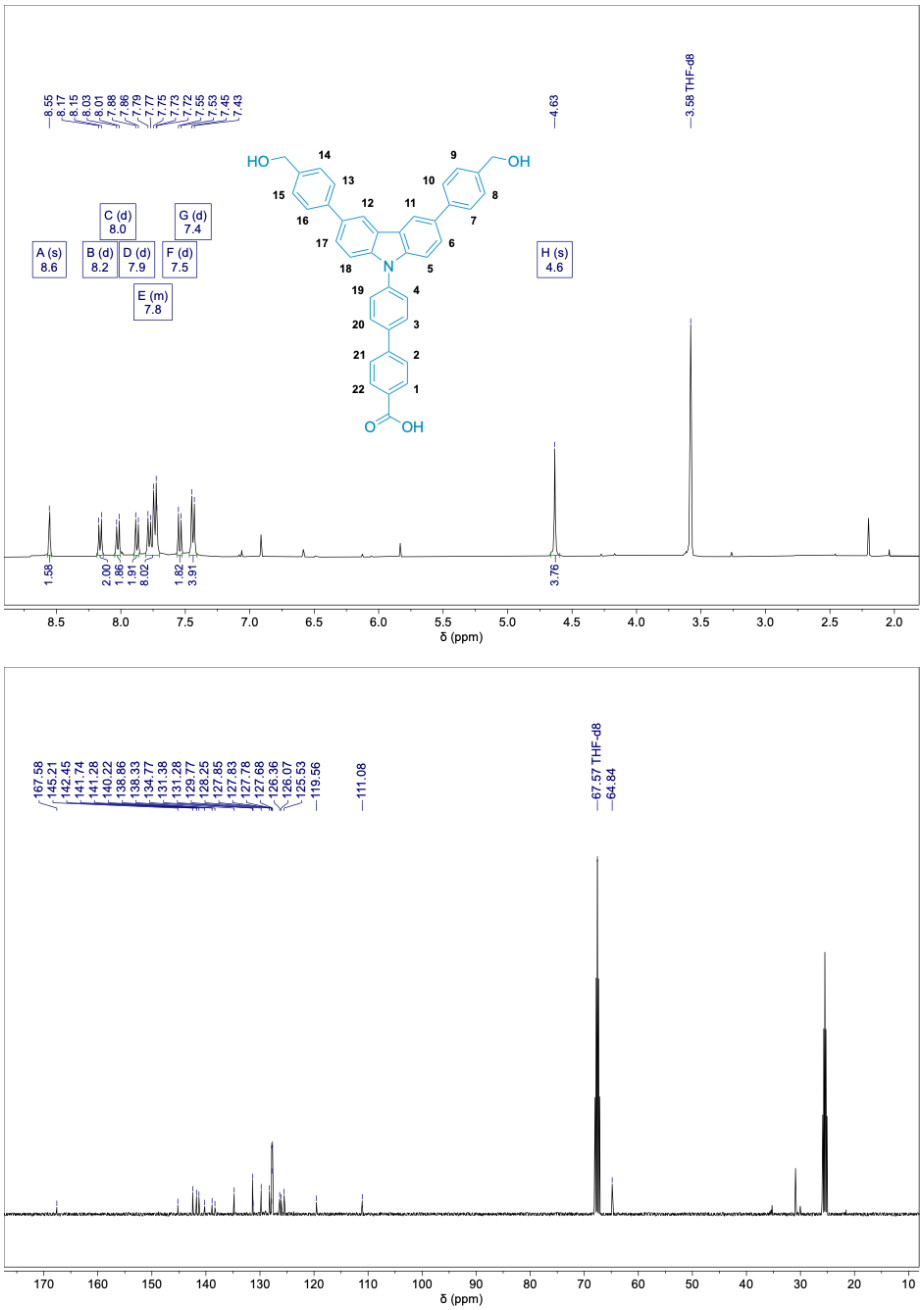

Figure A17. ^{1}H and ^{13}C NMRs of **29**, **SAM 6.**

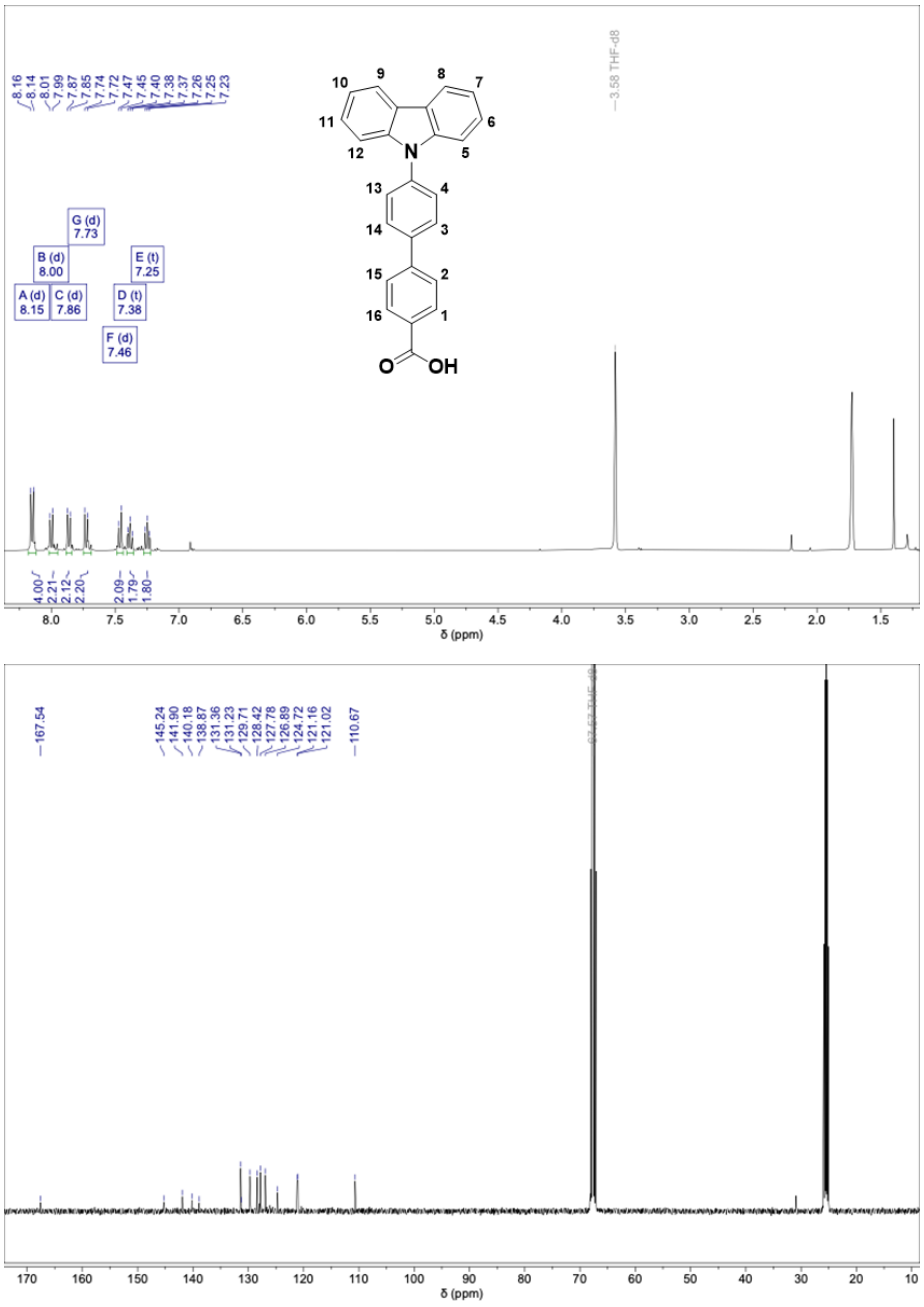

Figure A18. ^{1}H and ^{13}C NMRs of **30**, **SAM 7**.

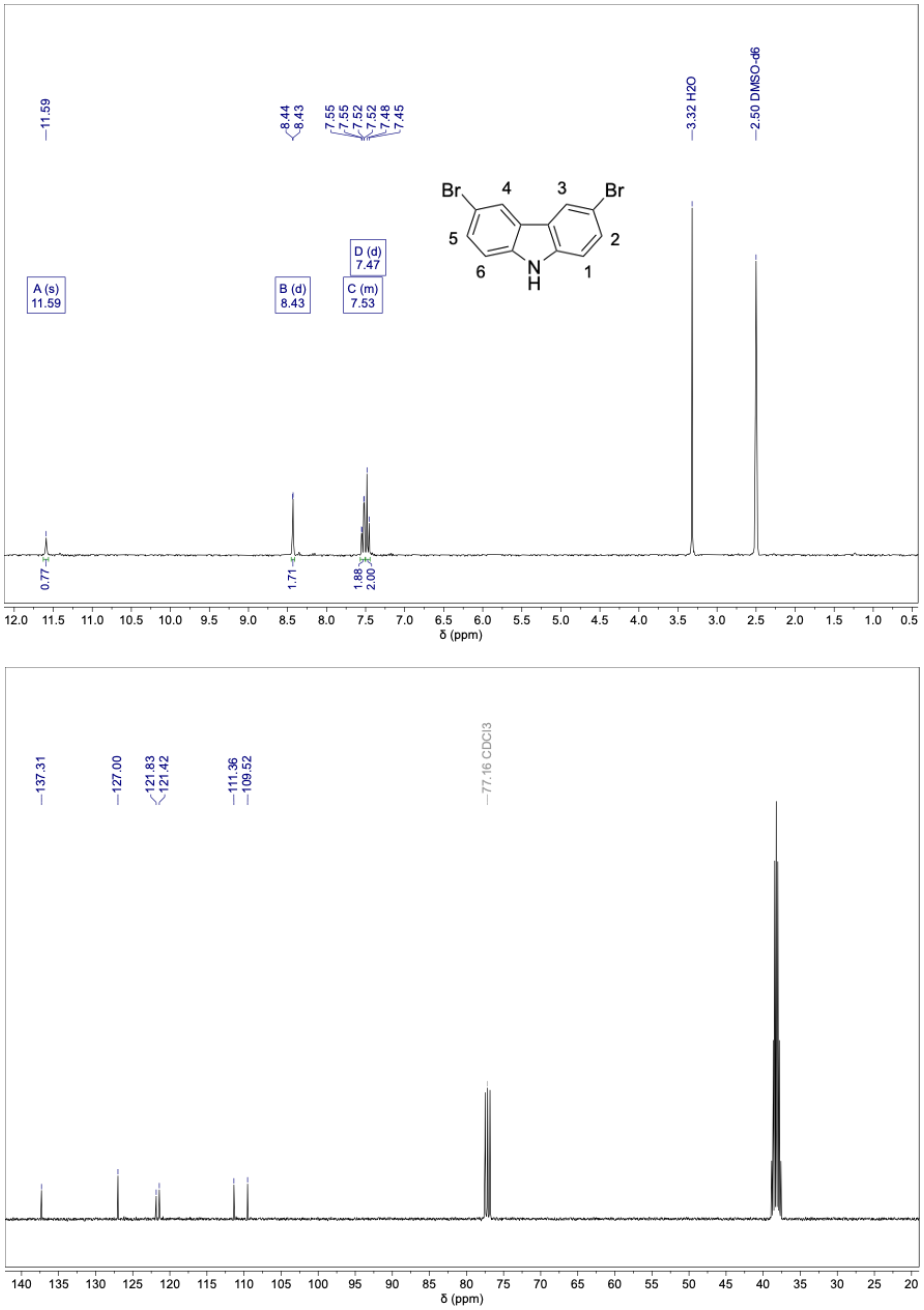

Figure A19. ^{1}H and ^{13}C NMRs of 31.

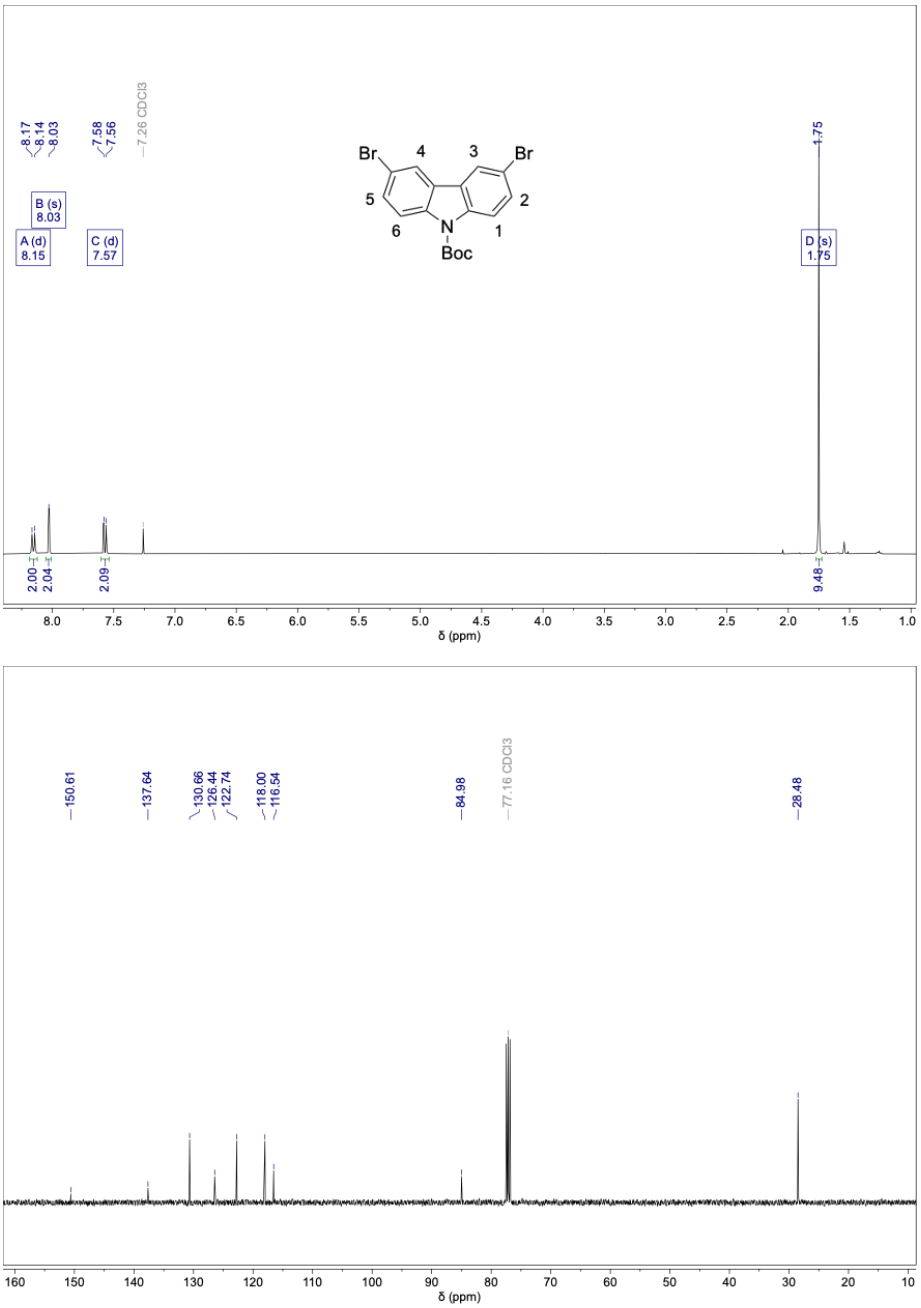

Figure A20. ^{1}H and ^{13}C NMRs of **32**.

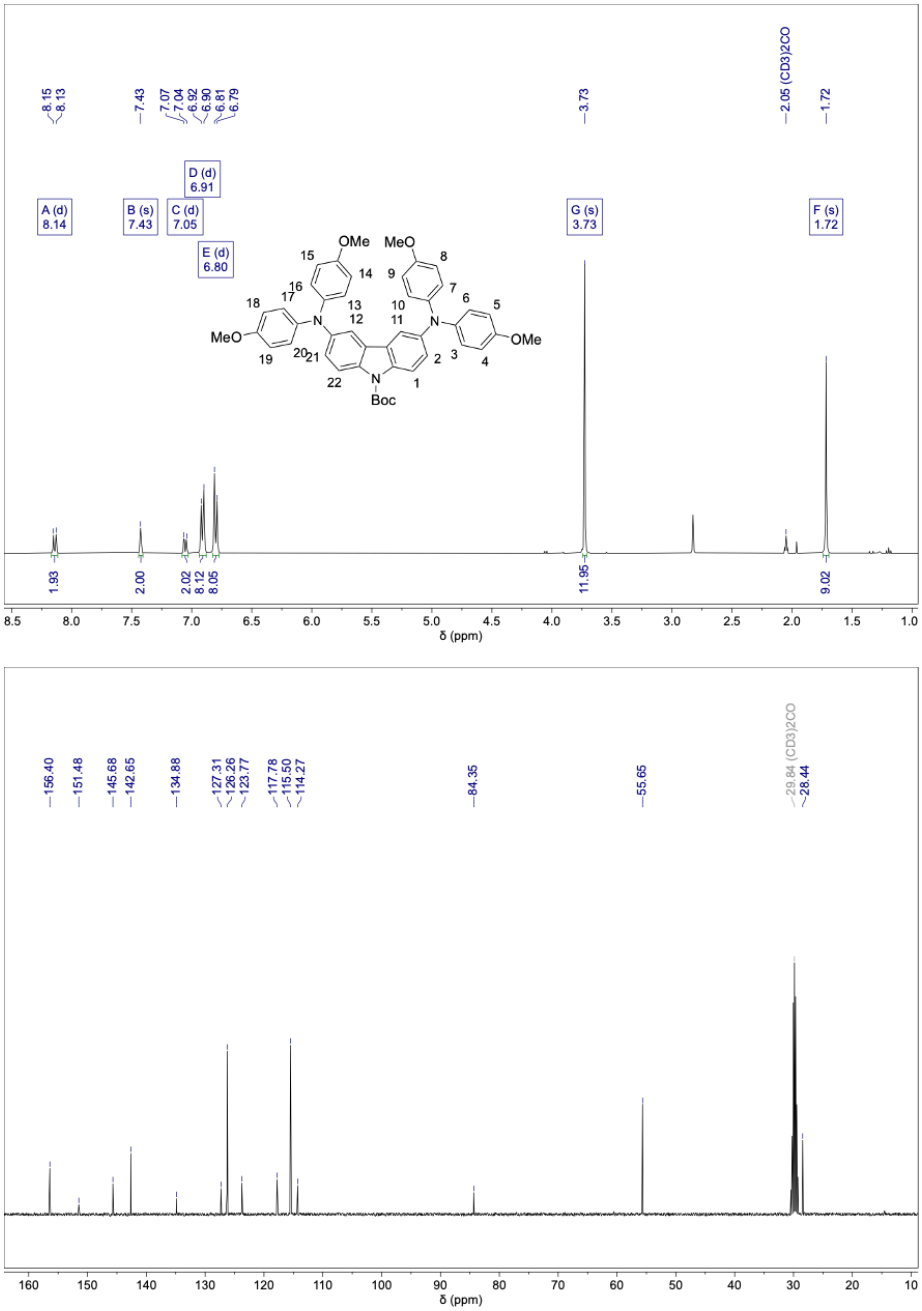

Figure A21. ^{1}H and ^{13}C NMRs of **34**.

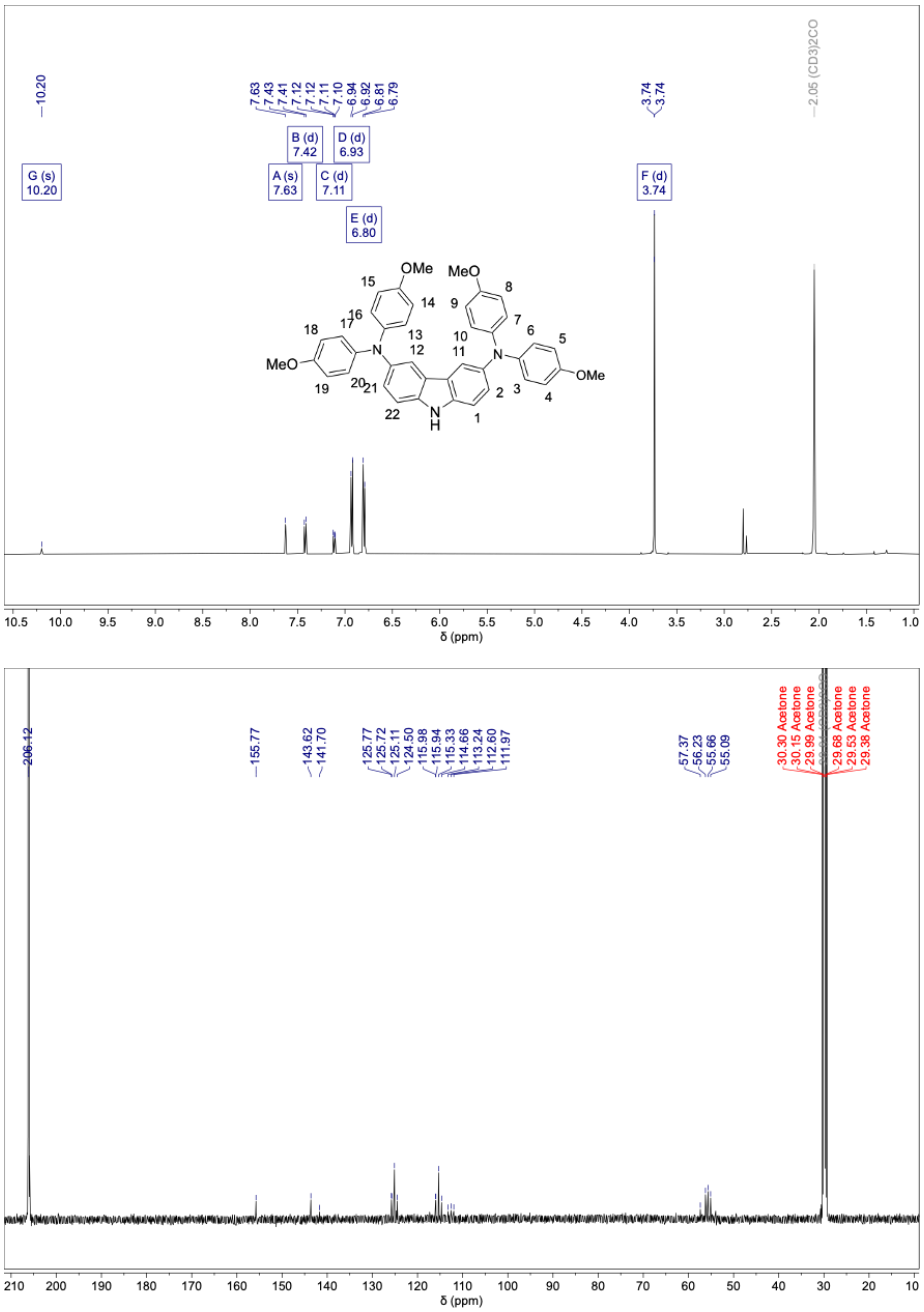

Figure A22. ^{1}H and ^{13}C NMRs of **35**.

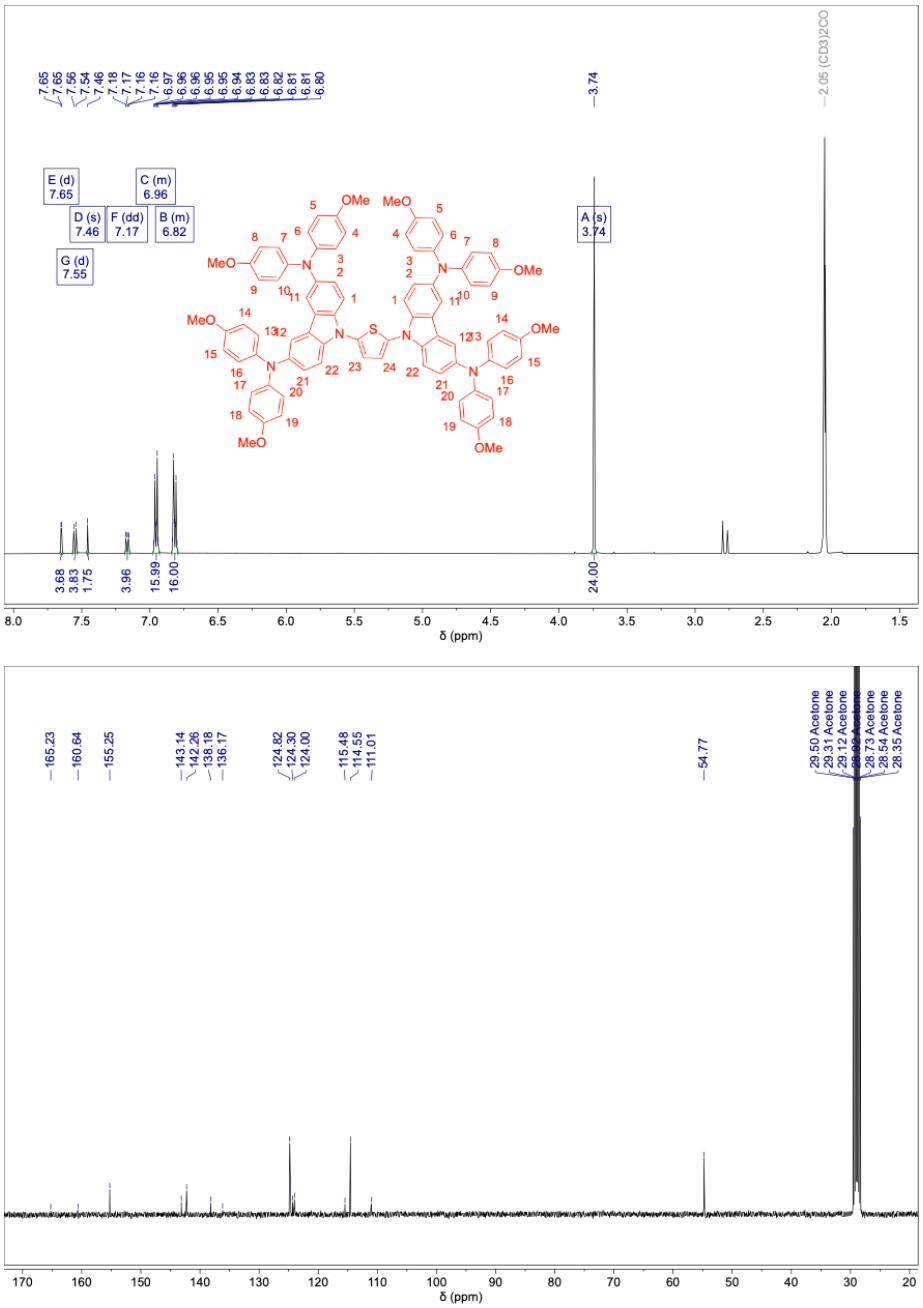

Figure A23. ^{1}H and ^{13}C NMRs of **37, HTM-1.**

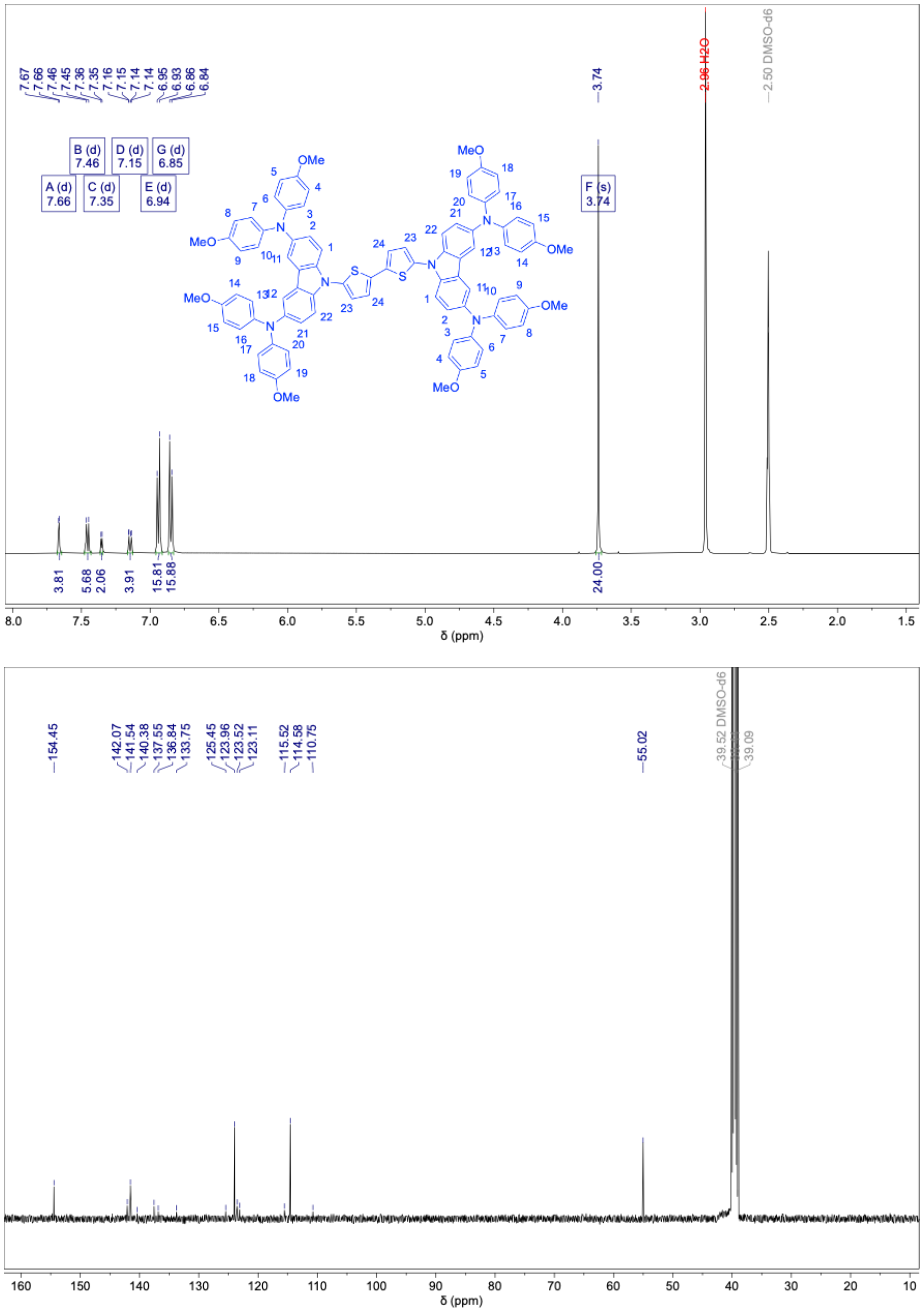

Figure A24. ^{1}H and ^{13}C NMRs of 39, HTM-2.

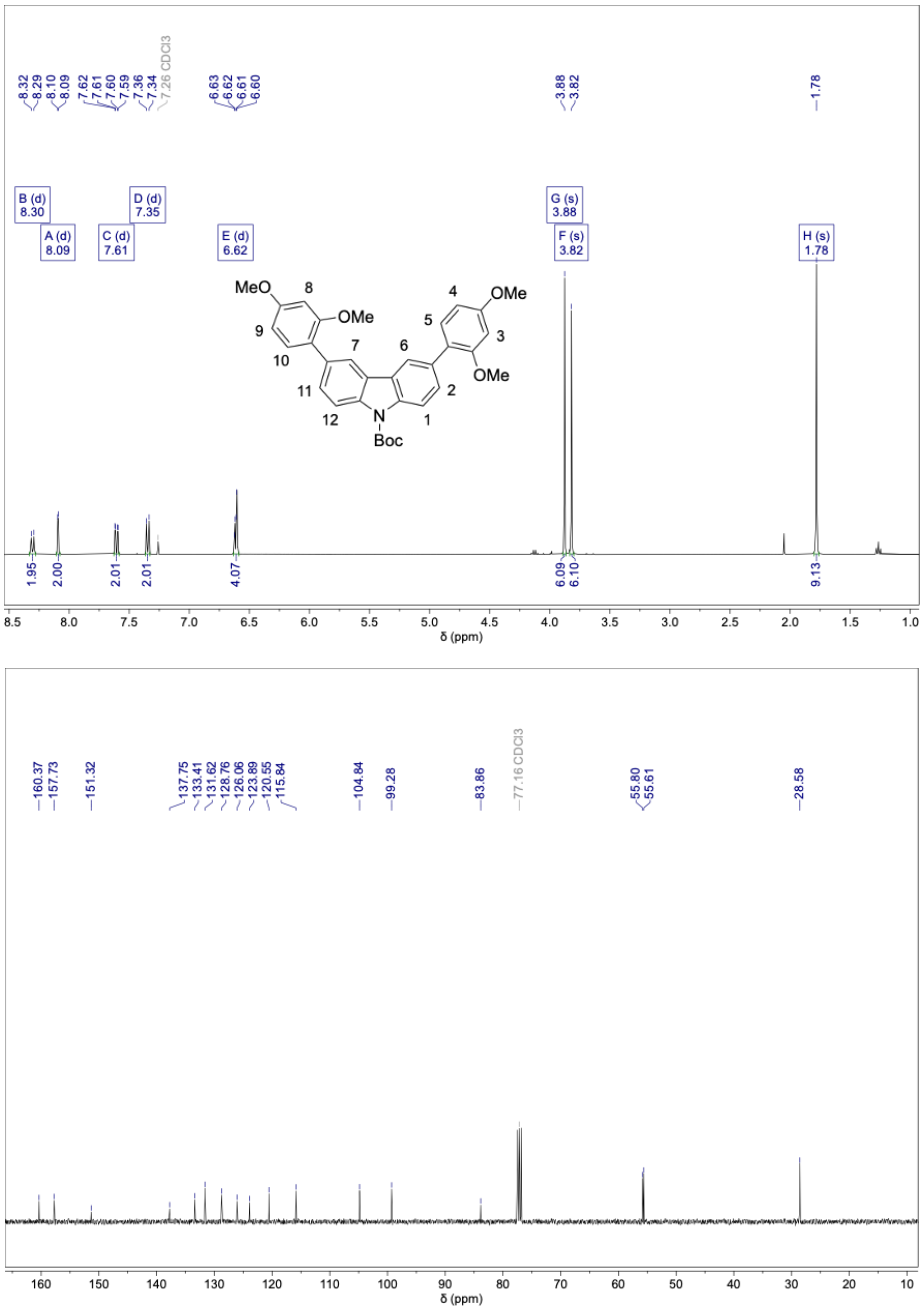

Figure A25. ^{1}H and ^{13}C NMRs of **41**.

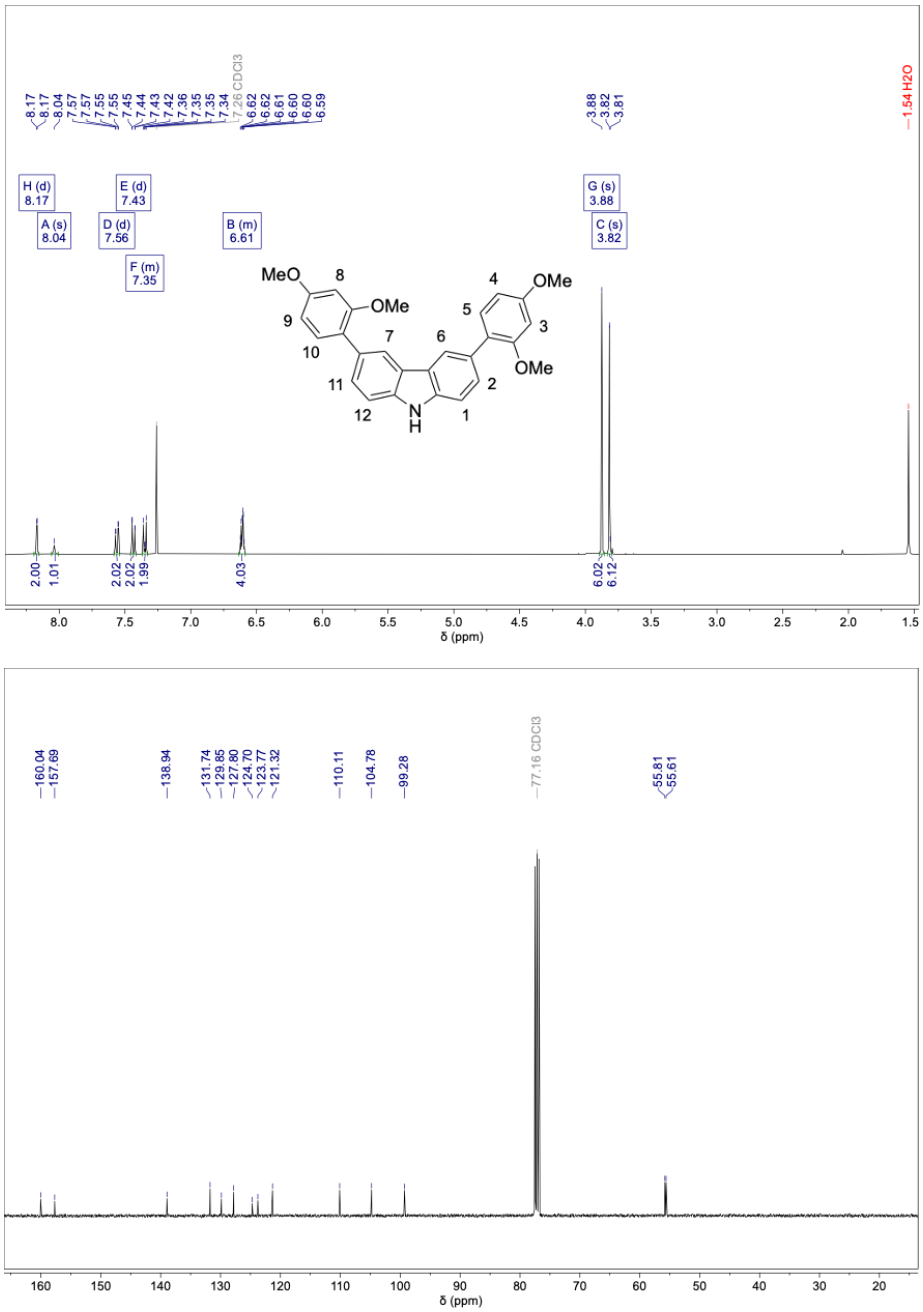

Figure A26. ^{1}H and ^{13}C NMRs of **42**.

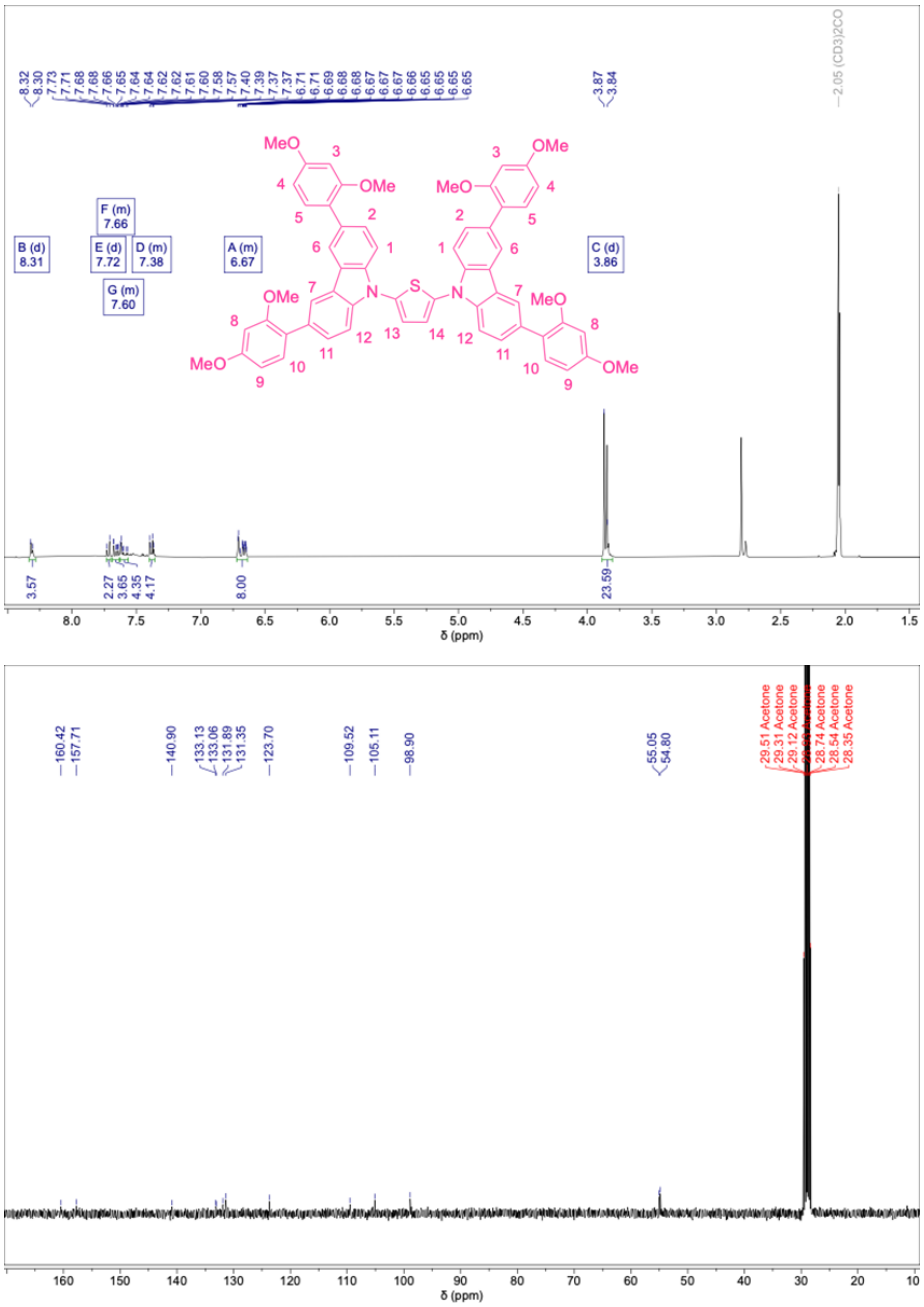

Figure A27. ^{1}H and ^{13}C NMRs of **43**, **HTM-3**.

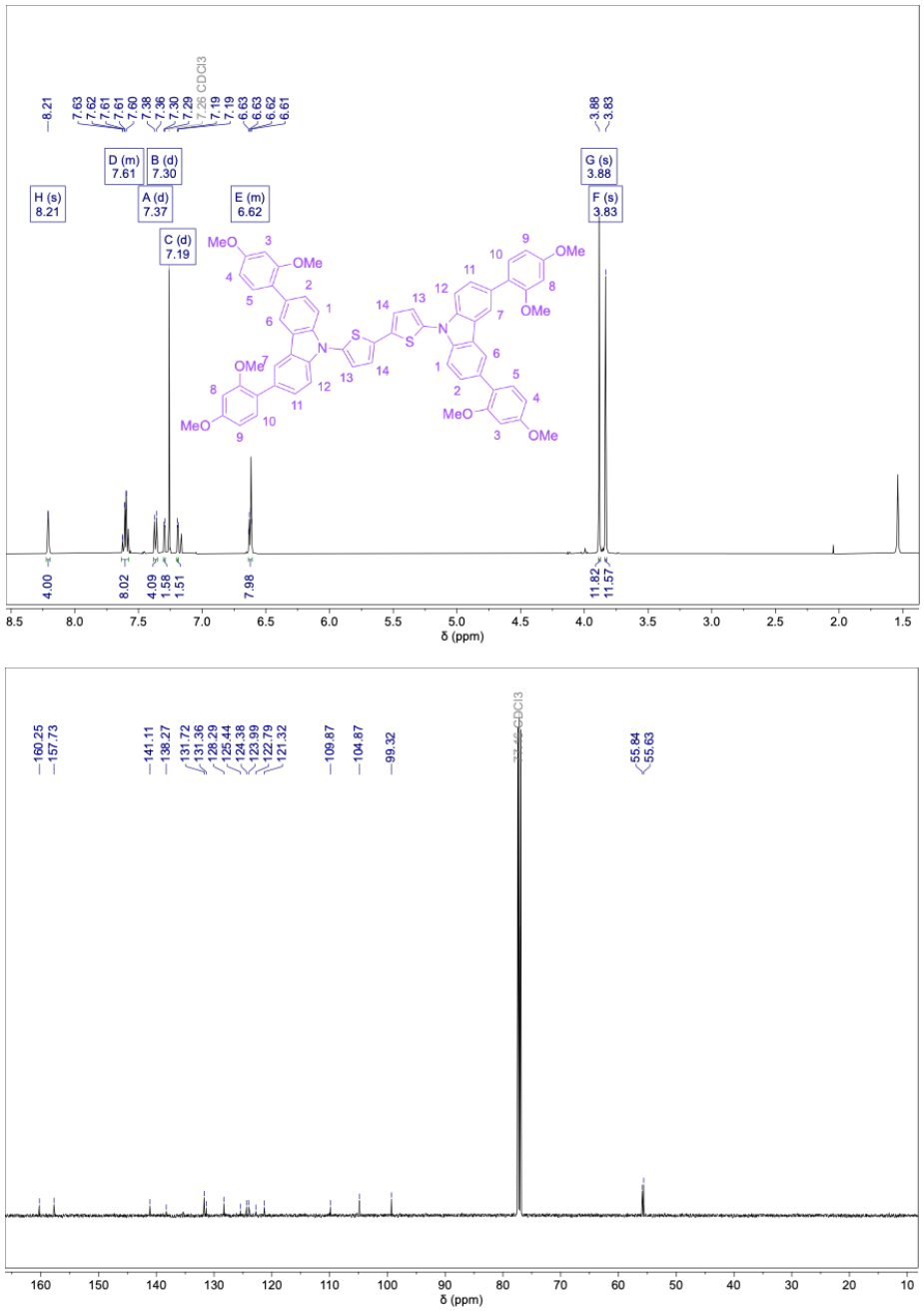

Figure A28. ^{1}H and ^{13}C NMRs of **44**, **HTM-4**.

MASS SPECTRUM SPECTRA

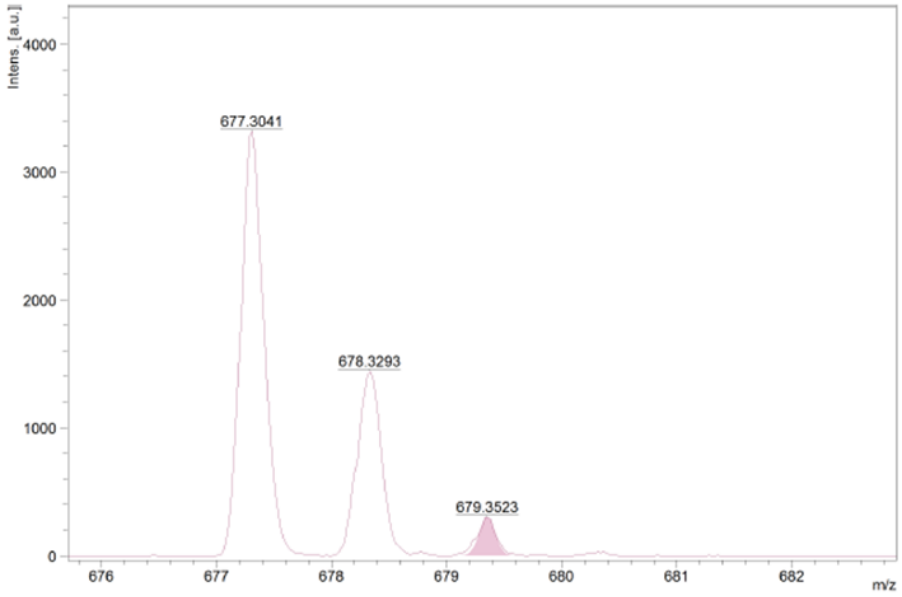

Figure A29. MS spectra of **SAM 1** (**7**).

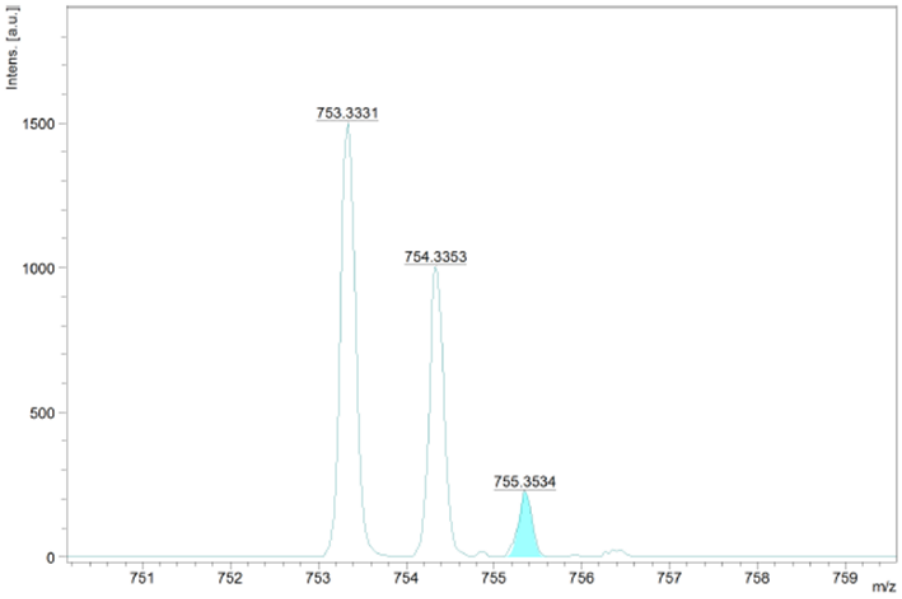

Figure A30. MS spectra of **SAM 2** (**14**).

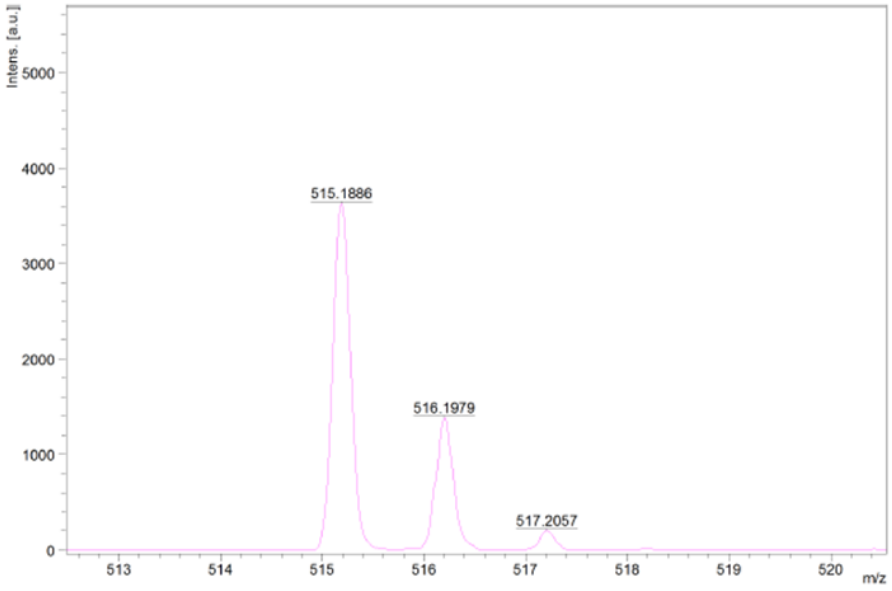

Figure A31. MS spectra of SAM 3 (17).

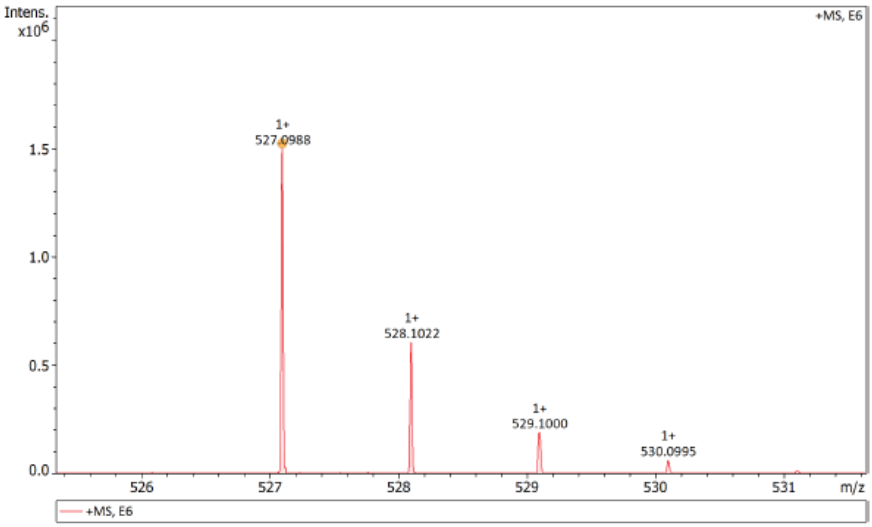

Meas. m/z	Ion Formula	m/z	err [ppm]	err [mDa]	mSigma	e¯ Conf	z
527.0988	C33H21NO2S2	527.1008	3.9	2.0	20.3	odd	1+
	C32H17NO7	527.1000	2.2	1.2	37.8	odd	1+

Figure A32. MS spectra of SAM 4 (20).

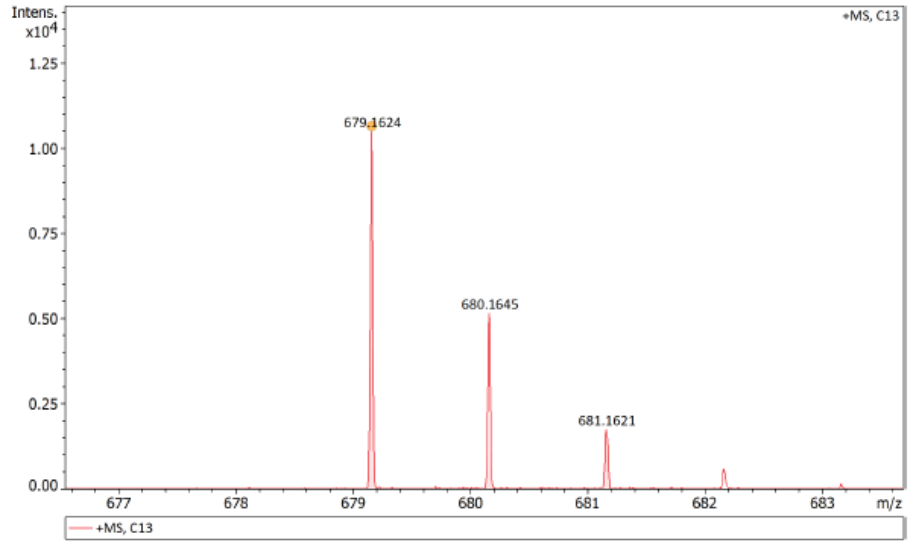

Meas. m/z	Ion Formula	m/z	err [ppm]	err [mDa]	mSigma	e¯ Conf	z
679.1624	C44H25NO7	679.1626	0.3	0.2	22.0	odd	1+
	C43H19N8O2	679.1625	0.3	0.2	23.0	even	1+
	C43H27N4OS2	679.1621	-0.4	-0.3	36.8	even	1+
	C45H29NO2S2	679.1634	1.6	1.1	40.9	odd	1+

Figure A33. MS spectra of SAM 5 (25).

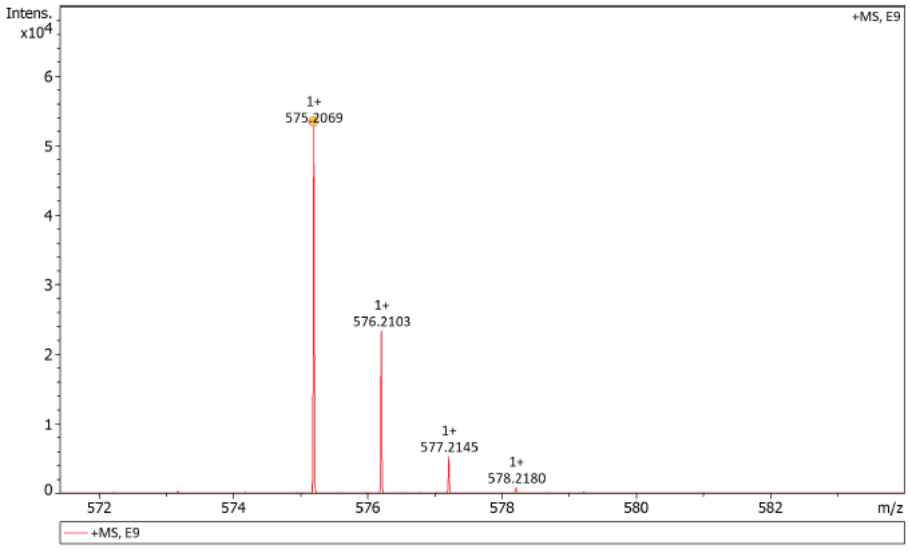

Meas. m/z	Ion Formula	m/z	err [ppm]	err [mDa]	mSigma	e¯ Conf	z
575.2069	C39H29NO4	575.2091	3.9	2.2	6.5	odd	1+
	C37H27N4O3	575.2078	1.5	0.9	12.8	even	1+
	C36H31O7	575.2064	-0.8	-0.5	24.3	even	1+

Figure A34. MS spectra of SAM 6 (29).

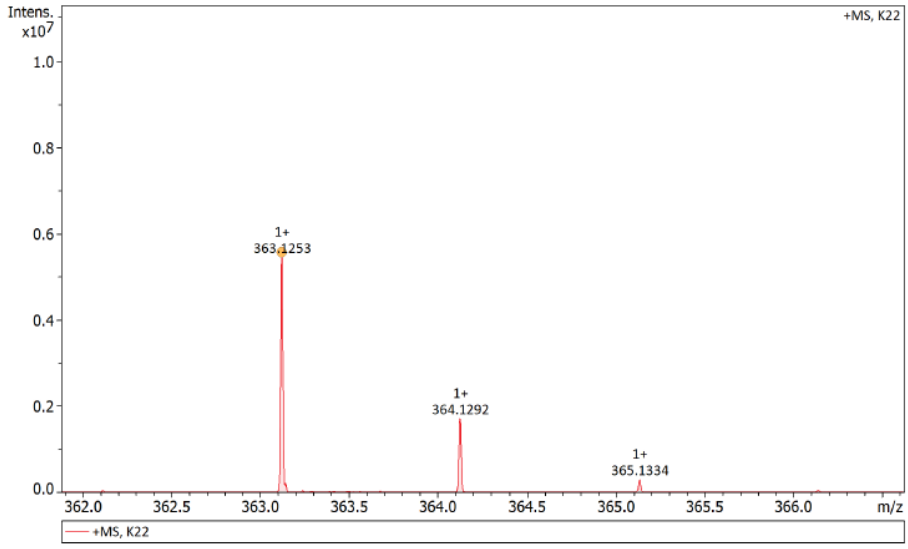

Meas. m/z	Ion Formula	m/z	err [ppm]	err [mDa]	mSigma	e¯ Conf	z
363.1253	C25H17NO2	363.1254	0.2	0.1	23.2	odd	1+
	C23H15N4O	363.1240	-3.5	-1.3	30.3	even	1+

Figure A35. MS spectra of SAM 7 (30).

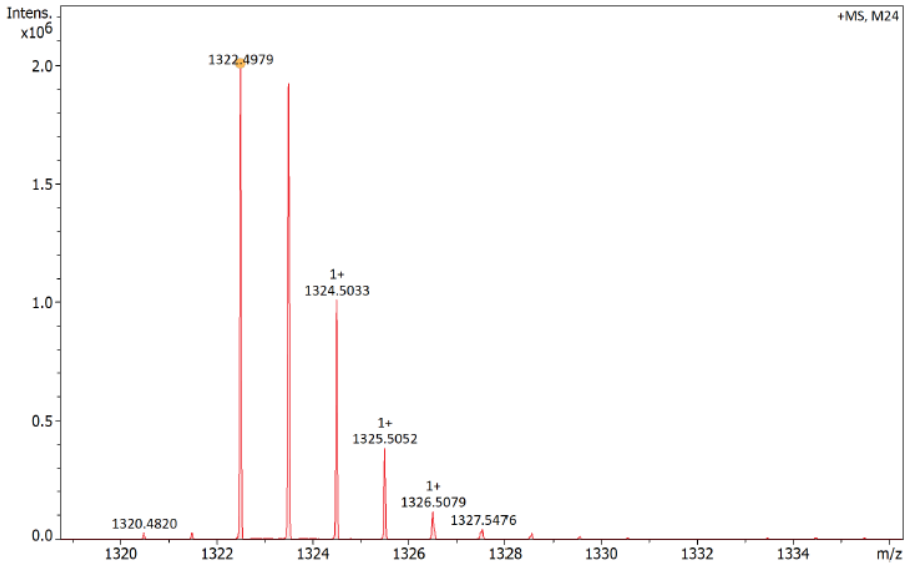

Meas. m/z	Ion Formula	m/z	err [ppm]	err [mDa]	mSigma	e¯ Conf	z
1322.4979	C84H70N6O8S	1322.4970	-0.7	-0.9	7.7	odd	1+

Figure A36. MS spectra of HTM-1 (37).

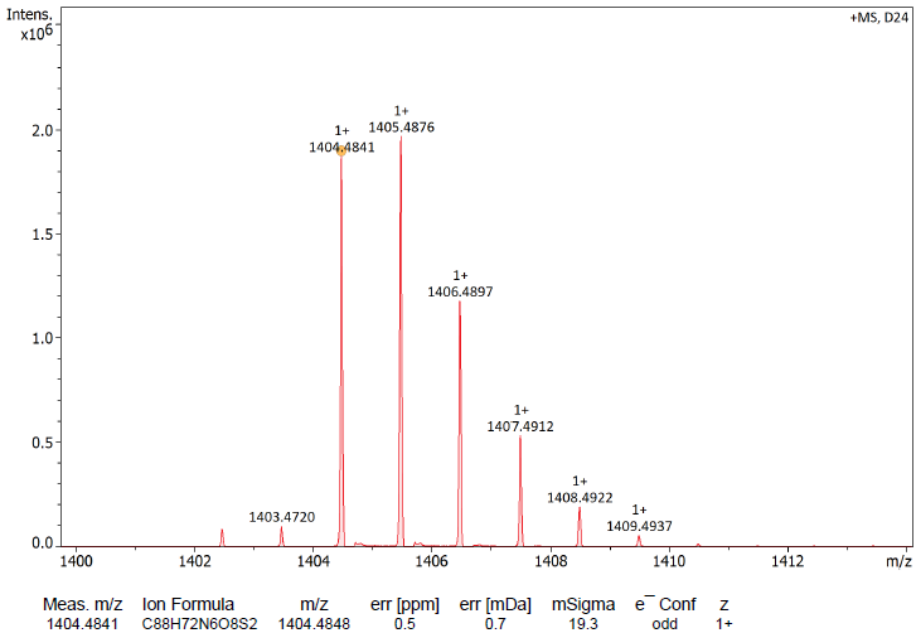

Figure A37. MS spectra of HTM-2 (39).

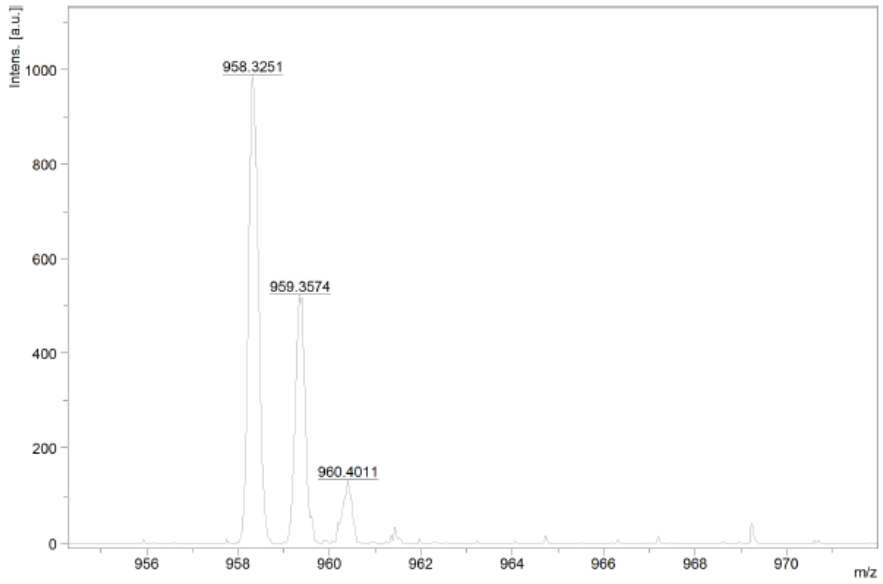

Figure A38. MS spectra of HTM-3 (43).

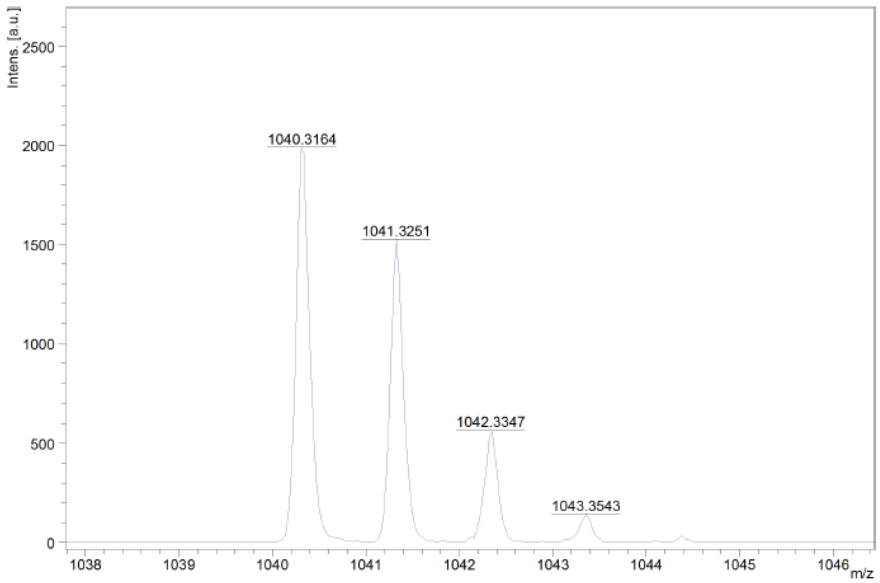

Figure A39. MS spectra of HTM-4 (44).

UNIVERSITAT ROVIRA I VIRGILI
SYNTHETIC APPROACHES FOR THE DEVELOPMENT OF ORGANIC MOLECULES AND THEIR APPLICATION IN SOLAR CELLS
Dora Alejandra González Ruiz

UNIVERSITAT
ROVIRA i VIRGILI

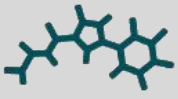

ICIQ

Institut
Català
d'Investigació
Química